Material Development of Cost-Effective Electrocatalysts for Water Oxidation Reactions

D Belami

PhD 2024

Material Development of Cost-Effective Electrocatalysts for Water Oxidation Reactions

Debora Belami

A thesis submitted in partial fulfilment of the requirements of
Manchester Metropolitan University for the Degree of
Doctor of Philosophy

Department of Natural Sciences

Manchester Metropolitan University

2024

Declaration

I, Debora Belami, confirm that the material contained in this thesis is my own, has not been submitted for any other academic award. Where information has been derived from other sources, I confirm that this has been indicated in the thesis.

Abstract

Proton exchange membrane (PEM) electrolysis is a promising technology that can produce high purity, desirable products such as hydrogen and hydrogen peroxide via electrolysis. However, the large-scale commercialisation of PEM electrolysers is hindered due to the expensive and non-selective catalysts necessary for 2-electron (2e-WOR) and 4-electron (4e-WOR) water oxidation reactions. This work aims to develop supported electrocatalysts to address the need for cost-effective and high performing electrocatalysts for the WORs.

The use of high surface area catalyst supports can enhance the intrinsic activity of Ir at low loadings (< 75 wt%). Sn and Ti oxides have been widely used as catalyst-supports due to their abundance and stability in corrosive WOR environments. However, Sn and Ti oxides suffer from low conductivity, hindering electrocatalytic activity. In this work, M-doped-SnO_2 (where M = Sb, Ta, Mo and Nb) and AuPd coated TiO_2 were synthesised and characterised to investigate the influence of their physical properties on the 4e-WOR. Additionally, Ir deposition syntheses (polyol and acid modified polyol) were investigated and found that the surface charge on the support has significant influence on the Ir loading. Furthermore, the presence of dopants in the supports rendered them unstable while the addition of AuPd to TiO_2 supports enhances the electrochemical activity and stability. These trends were consistent across the three-electrode rotating disk electrode and in a 5 cm^2 membrane electrode assembly testing for activity and durability.

The second part of this work focused on the development of electrocatalysts with a selectivity towards hydrogen peroxide (H_2O_2). Thin films and nanopowders of metal stannates (Ca-SnO_3, Ba-SnO_3 and Au-$CaSnO_3$) were synthesised to generate H_2O_2 through the electrochemical pathway. The activity and selectivity for H_2O_2 are encouraging despite being relatively low due to lack of conductivity and rapid catalyst degradation. This work will continue in the future to optimise the electrocatalytic activities and selectivities and dissolved catalyst quantification techniques.

Acknowledgements

Firstly, I would like to thank the people who made this PhD possible in the first place, Prof. Laurie King and Dr. Yagya Regmi for choosing me, an inexperienced chemist into their group and plying me with all their electrochemistry and materials science knowledge. Most importantly, their kindness, patience and critical feedback which made me think outside of the box. This thesis wouldn’t have been possible without them.

A big part of my work would also have not been possible without the technicians, academic staff and collaborators who helped me along the way. Specifically, Gary, Hayley, Matt and Lubomira who characterised most of the work in this thesis. Additionally, to the funding bodies (RSc, MMU and Henry Royce Institute) who made it possible for me to travel to conferences and share my work with international members of my field.

To all the members of the King-Regmi group from Post-docs, PhDs, MSc and summer interns who I’ve met over the years – thank you for the additional knowledge, support and general advice but most of all the laughs that made each day just a little brighter. Special thank you to Hessan for his calming influence when things felt overwhelming and Fahmida for expanding my taste buds by making me try all the Manchester food spots around Oxford Road, and the witty banter that got me through the last 2 years. I would also like to thank the members of the surface engineering group, for inadvertently teaching me about magnetron sputtering, sharing the most random conversations and laughs over lunch and the weekly Durak tournaments. Especially Kath for staying after hours during long experiments, being my sounding board, engineer teacher and my favourite go-to person on the 5th floor. Looking forward to our adventures outside of the lab! I also can’t forget the members of the 7th floor who kept me up to date with all the lab gossip and their help when I was looking for equipment in the wrong places.

To all my friends outside the lab, thank you for keeping me sane, buying all the drinks and giving me respite from science on weekends with our weekly outings.

Last but not least, to my family for their unwavering support (financial and emotional), especially my dad who would look forward to me explaining my

experiments even though he had no clue what I was saying the majority of the time.

It’s been a rollercoaster of a journey and none of this would have been possible without the support, understanding and patience of all who are mentioned here and for that I will be forever grateful to all of you.

List of Publications

D. Belami, M. Lindley, U. Jonnalagadda, A. M. Goncalves Bullock, W. Fan, P. Liu, S. Haigh, J. Kwan, Y. Regmi, L. King, “Active and durable supported catalysts for proton exchange membrane electrolysers”, *Submitted.*

D. Belami, Y. Regmi, L. King, “The Activity and Stability of Tin Oxide Based Supports for the Oxygen Evolution Reaction in Proton Exchange Membrane Electrolysers”, *In preparation.*

Glossary

2e-WOR	2-electron water oxidation
4e-WOR	4-electron water oxidation
AEM	Adsorbate evolution mechanism
A-FTO	Annealed fluorine doped tin oxide
AMP	Acid modified polyol
ASF	Activity-stability factor
AST(s)	Accelerated stress test(s)
ATO	Antimony doped tin oxide
BET	Brunauer-Emmett-Teller
BoL	Beginning of life
CA	Chronoamperometry
CE	Counter electrode
CP	Chronopotentiometry
CV	Cyclic voltammetry
EDX	Electron dispersive x-ray
EoL	End of life
FE	Faradaic efficiency
FTO	Fluorine doped tin oxide
HAADF	High angle annular dark field
HEA(s)	High entropy alloy(s)
HR-TEM	High resolution transmission electron microscopy
ICP-MS	Inductively coupled plasma – mass spectrometry
LOEM	Lattice oxygen evolution mechanism
LSV	Linear sweep voltammetry
MEA	Membrane electrode assembly
MoTO	Molybdenum doped tin oxide
NbTO	Niobium doped tin oxide
OER	Oxygen evolution reaction
ORR	Oxygen reduction reaction
(P)EIS	(Potentiostatic) electrochemical impedance spectroscopy
PEM	Proton exchange membrane
PEM-WE(s)	Proton exchange membrane water electrolyser(s)

PGM	Platinum group metals
ppm	Parts per million
RDE	Rotating disk electrode
RE	Reference electrode
RHE	Reversible hydrogen electrode
SEM	Scanning electron microscopy
S-number	Stability number
(S)TEM	(Scanning) transmission electron microscopy
TaTO	Tantalum doped tin oxide
UA-FTO	Unannealed fluorine doped tin oxide
WE	Working electrode
WH1	1% Gold palladium coated onto titanium dioxide
WH5	5% Gold palladium coated onto titanium dioxide
WOR(s)	Water oxidation reaction(s)
XPS	X-ray photoelectron spectroscopy
XRD	X-ray diffraction
XRF	X-ray fluorescence

Table of Contents

List of Figures

List of Tables

1 Introduction

1.1 Motivation

The rise of greenhouse gases such as carbon dioxide (CO_2) in the atmosphere due to our consumption of fossil fuels, has led to detrimental effects on climate and health.[1] Alongside the health and climate effects, it is estimated that the Earth only has enough fossil fuels to last ~ 50 years.[2] As of 2019, the UK and several European countries have committed to achieving net-zero carbon emissions by 2050.[3] Renewable energies (e.g. photovoltaics, wind turbines) offer a critical route to net-zero carbon emissions due to their natural abundance and use of sustainable resources. However, storing the energy generated from renewable technologies has remained difficult due to their intermittent and fluctuating nature which does not match current energy demands.[4] Therefore, energy storage is required for renewable energies to be dependable. A promising pathway to this solution has been the development of hydrogen production via electrolysis.

Hydrogen is a non-toxic gas that can be stored in pressurised tanks as a gas or liquid.[5] Hydrogen has recently attracted significant attention owing to its ability to act as an energy carrier.[6] As an energy carrier, hydrogen has the potential to support the electrical grid by supplying stored energy at times of high demand.[7]

In 2021, 95% of global hydrogen production was produced from hydrocarbon reforming which emitted approximately 900 Mt of CO_2.[8–10] There are several alternative pathways to produce hydrogen such as biological and thermochemical processes using biomass materials[11], but the most common pathway is electrolysis powered by a renewable energy sources.[12,13] Electrolysers use electricity to produce hydrogen from water. When the hydrogen generation is coupled with a renewable energy source, hydrogen acts as a sustainable energy carrier. This hydrogen can then be stored and used to generate power or heat when needed.[14] However, electrolysis is an expensive process attributed to the expensive materials required to split water.

To reach the commitment of achieving net-zero carbon by 2050, we must also decarbonise chemical industries. The production of hydrogen peroxide (H_2O_2), an environmentally friendly, oxidising agent, is widely utilised in the chemical industry for wastewater treatment, chemical synthesis and as a disinfectant.[15] As of 2020, 5.5 million metric tonnes of H_2O_2 was produced worldwide through a large scale anthraquinone process.[16] The anthraquinone process involves the hydrogenation of 2-alkylanthraquinone to alkylanthrahydroquinone (AHQ) using a Pd catalyst, the AHQ is oxidised back to its original reagent and forms H_2O_2 in the process.[17] The anthraquinone process has significant drawbacks due to the highly concentrated H_2O_2 which is explosive in nature, large amounts of organic solvents required in the synthesis and the high energy required to produce up to 70 wt% H_2O_2.[15,18] Therefore, the decarbonisation of H_2O_2 production requires a cost-effective technology that can also reduce the safety concerns.

The electrochemical production of H_2O_2 is an economic and environmentally friendly route to generate highly concentrated H_2O_2.[19] Currently, research has focused on two electron oxygen reduction reaction (ORR, (equation. 1.1) to produce H_2O_2,[20–22] however the use of gas diffusion electrodes and expensive precious metal electrodes alongside the low efficiency of H_2O_2 production makes ORR produced H_2O_2 unfavourable.[18] Two electron water oxidation (2e-WOR, (equation. 1.2) has recently shown promise as the reactant used is water and thus not dependant on the solubility of O_2 in the water as seen in ORR and thus likely to be more efficient for H_2O_2 production.[16] However, catalysts for the 2e-WOR exhibit low selectivity and activity for H_2O_2 hindering its' development.

ORR: $O_2 + 2H^+ + 2e^- \rightarrow H_2O_2$ (equation. 1.1)

2e-WOR: $2H_2O \rightarrow H_2O_2 + 2H^+ + 2e^-$ (equation. 1.2)

1.2 Water Electrolysis

Electrolysis is an endothermic process which requires electrical energy to occur.[9]. A typical electrolysis setup involves an anode and a cathode immersed in an electrolyte. Once an electrical current is applied, the water is split into oxygen at the anode and hydrogen at the cathode (Table *1.1*).[11,23] When the electricity source comes from a renewable energy technology, the hydrogen produced can be labelled "green hydrogen". Alongside the advantage of producing green hydrogen, electrolysis is beneficial owing to the generation of highly pure hydrogen.[24]

Table 1.1: The 4-electron water oxidation reactions in acidic and alkaline environments.

	Acidic Environment	**Alkaline Environment**
Anode	$2H_2O \rightarrow O_2 + 4H^+ + 4e$	$4OH^- \rightarrow O_2 + 2H_2O + 4e^-$
Cathode	$4H^+ + 4e^- \rightarrow 2H_2$	$4H_2O + 4e^- \rightarrow 2H_2 + 4OH^-$
Water Splitting	$2H_2O \rightarrow 2H_2 + O_2$	

1.3 Types of Electrolysers

Today, a range of technologies (Table 1.2) exist for electrochemical hydrogen generation at low (< 200 °C) and high temperatures (> 500 °C) including solid oxide electrolysers (SOEC), alkaline electrolysers, proton exchange membrane (PEM) and anionic exchange membrane electrolysers. The majority of currently deployed large-scale electrolysers are the alkaline electrolysers.[25] Advancements in PEM research has boosted the capabilities of PEM electrolysers to become available at 50 – 200 kW scale, with a limited number available at MW scale.[26,27] Anionic exchange membrane electrolysers and SOEC are still in the early stages of development but are projected to play prominent roles in the decarbonisation of industrial processes.[9] Alternative electrolysers such as microbial[28,29], seawater[30,31], CO_2 reduction[32] are also being investigated to produce hydrogen and other valuable products such as fuels and chemicals.

Table 1.2: Characteristics of low temperature electrolysers adapted from Chi. J et al.[24]

Environment	**Alkaline Electrolysis**		**Acid Electrolysis**
Name	***Alkaline Water***	***Anion Exchange Membrane***	***Proton Exchange Membrane***
Anodic Reaction	$4OH^- \rightarrow 2H_2O + O_2 + 4e^-$	$4OH^- \rightarrow 2H_2O + O_2 + 4e^-$	$2H_2O \rightarrow 2H_2 + O_2 + 4e^-$

Electrolyte	Liquid	Solid Polymer	Solid Polymer
Charge Carrier	OH^-	OH^-	H^+
Temperature (°C)	20 - 80	20-200	20-200
Anodes	Perovskites, Ni, Co and Fe oxides	Ni-Based	Ir and Ru based and their oxides
Efficiency (%)	59-70	-	65-82
Commercialisation	Commercial	Lab scale	Commercial
Advantages	Low capital cost, stable, mature technology	Combination of alkaline and acid electrolysis	Compact design, high purity H_2, high efficiency at low current densities
Disadvantages	Corrosive electrolyte, slow dynamics	Low conductivity and stability of membranes	Expensive technology, acidic environment requires expensive anodes

1.4 Proton Exchange Membrane Electrolysers

PEM water electrolysers (PEM-WEs) have received significant attention recently as they can operate at higher current densities (up to 2 A/cm^2) and produce highly pure gases due to low gas crossover.[25] PEM-WEs can also operate at low loads with low hydrogen permeability through the thin membrane (approx. 20 -300 μm thick). Further advantages include, compact design, high efficiency at low current densities, small footprint and the ability to produce oxygen as a by-product.[33,29]

At the heart of an electrolyser cell is the membrane electrode assembly (MEA). For PEM-WEs, an MEA consists of an acidic, polymer membrane made from perfluorosulfonic acid commercially known as Nafion®.[34] As Nafion is acidic in nature, PEM-WEs have an acidic environment. The membrane separates the anode from the cathode and is typically coated with a catalyst on either side of the membrane (catalyst coated membrane, CCM). The CCM is placed between a porous transport layer (PTL) on the anode and gas diffusion layer (GDL) on the cathode to allow for water and gases to flow through the cell, respectively.

A typical PEM-WEs (Figure 1.1) splits water into hydrogen and oxygen at the cathode and anode, respectively. A reaction occurring at the anode is the OER and the hydrogen evolution reaction (HER) occurs at the cathode. Water is pumped through the anode and potential is applied, splitting the water into protons, oxygen and electrons (Table 1.1)[35] The protons formed at the anode are transported through the proton conductive membrane to the cathode. The electrons are recombined with the protons at the cathode leading to a reduction reaction forming hydrogen (Table 1.1).[29] When water splitting occurs at optimum temperature and pressure, a minimum energy of 1.23 V is required.[36]

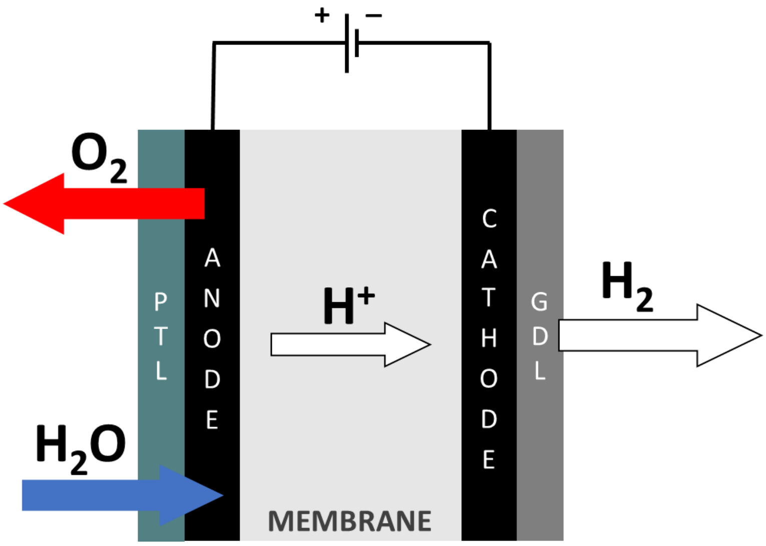

Figure 1.1: Schematic of a 4e-water oxidation reaction PEM-WE where the porous transport layer and gas diffusion layer are ascribed as PTL and GDL, respectively.

During 2e-water oxidation reaction (WOR) under an acidic environment, an electrolyser works in a similar way to 4e-WOR, however instead of O_2 being produced at the anode H_2O_2 is produced when a minimum energy of 1.76 V is reached (equation. 1.2).[37] The proton produced from the oxidised H_2O flows through the membrane and is reduced to form hydrogen.

1.5 Electrochemical Water Oxidation Mechanisms

There are several pathways available for electrochemical water oxidation (Figure 1.2). The most favourable process is the 4-electron water oxidation reaction (4e-WOR) also known as the oxygen evolution reaction (OER). However, water oxidation can also occur via 2-electron (2e-WOR) and one electron pathway producing H_2O_2 and OH radicals ($OH^{\bullet}$), respectively.[38] Electrochemical water oxidation can occur under acidic or alkaline conditions.[39,40] However, the combination of highly oxidising and acidic environment rapidly degrades the catalysts required to lower overpotentials. Therefore, more research is required to develop cost-effective, active and stable electrocatalysts for PEM-WEs under acidic conditions. In this thesis, we will be discussing the 4e-WOR and 2e-WOR and their reaction mechanisms under acidic conditions.

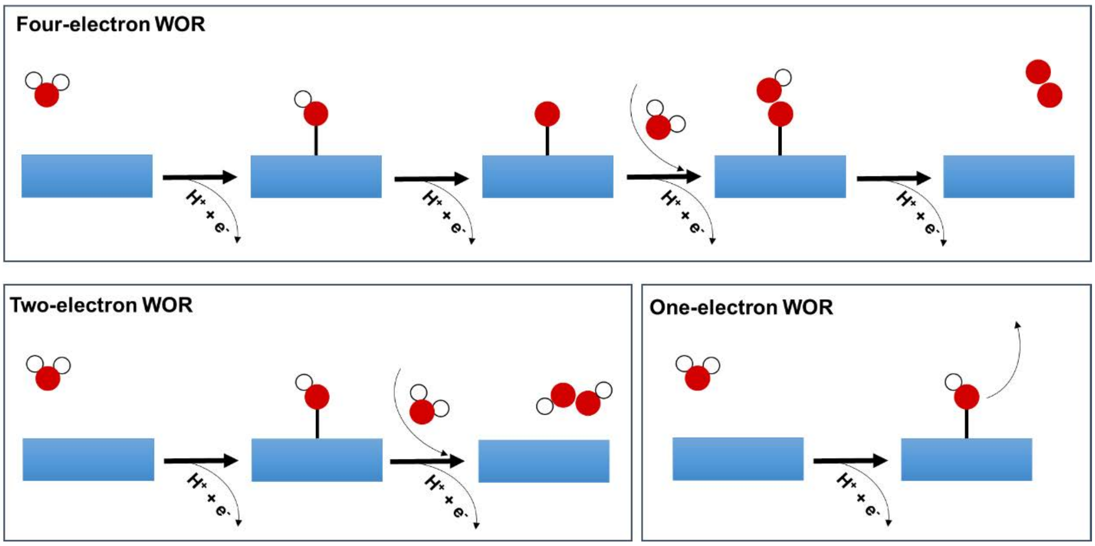

Figure 1.2: Schematic of the three reaction pathways for water oxidation adapted from ref. [41].

1.5.1 4-electron Water Oxidation

The 4e-WOR as shown in Table 1.1 is the most favourable water oxidation reaction due to its lower thermodynamic potential of 1.23 V_{RHE} compared to the thermodynamic potential of 2e-WOR (1.76 V_{RHE}).[41]

The acidic OER mechanism is known to occur through two possible mechanisms known as adsorbate evolution mechanism (AEM) and lattice oxygen evolution mechanism (LOEM). For the AEM, the water molecules are adsorbed onto the surface of the catalyst leading to dissociation of a proton to form *OH (equation. 1.3). The *OH undergoes deprotonation to form *O (equation. 1.4), the second H_2O molecule undergoes nucleophilic attack on *O (equation. 1.5) and generates *OOH which undergoes deprotonation to form desorbed O_2 and an exposed active site on the catalyst (denoted with *) (equation. 1.6).[42]

$$H_2O + * \rightarrow H^+ + {*OH} + e^- \qquad \text{(equation. 1.3)}$$

$$*OH \rightarrow {*O} + H^+ + e^- \qquad \text{(equation. 1.4)}$$

$$H_2O + {*O} \rightarrow {*OOH} + H^+ + e^- \qquad \text{(equation. 1.5)}$$

$$*OOH \rightarrow * + O_2 + H^+ + e^- \qquad \text{(equation. 1.6)}$$

However, some catalysts do not follow the AEM. Indeed, the LOEM is an alternate mechanism proposed in which lattice oxygen present on the catalysts surface participate in the OER.[43,44] The LOEM begins with the adsorption of H_2O (equation. 1.7) and deprotonation similar to the AEM (equation. 1.8). However, after deprotonation the lattice oxygen (O_L) from H_2O binds with *O (equation. 1.9) and O_2 is released and thus forming oxygen vacancies (V_o) in the catalyst. The vacancies on the catalyst surface are filled with water molecules to form *OH (equation. 1.10). A deprotonation occurs from the active site leaving the active site exposed (equation. 1.11).

$$H_2O + * \rightarrow H^+ + {*OH} + e^- \qquad \text{(equation. 1.7)}$$

$$*OH \rightarrow {*O} + H^+ + e^- \qquad \text{(equation. 1.8)}$$

$$*O + O_L \rightarrow O_2 + V_o \qquad \text{(equation. 1.9)}$$

$$V_o + H_2O \rightarrow {*OH} + H^+ + e^- \qquad \text{(equation. 1.10)}$$

$$*H \rightarrow * + H^+ + e^- \qquad \text{(equation. 1.11)}$$

The LOEM induces increased activity due to the minimum overpotential being lower than AEM by ~ 0.1 V.[45] However, it's been hypothesised that LOEM weakens the bonding in the catalyst and thus increases catalyst dissolution.[46] The oxygen evolution reaction mechanisms highlight that the activity of the catalyst is dependent on the binding energy of the oxygen intermediates and active site. Surfaces that bind too strongly to oxygen are limited by the formation of *OOH however, for surfaces that bind weakly to oxygen, the activity is limited by the *OH.[43] To obtain the best activity, the catalyst and *O must have an appropriate binding strength that binds the adsorbate neither too strongly or too weakly.

For IrO_2 based catalysts, both OER mechanisms can occur.[47–49] The morphology and structure of IrO_2 determines which reaction mechanism occurs during OER.[50,51] The introduction of defects can enhance the likelihood of LOEM which leads to improved OER activity but lower stability compared to AEM.[52,53] To confirm the reaction mechanism ongoing, computational methods such as density-functional theory or isotope labelling must be conducted.[46,48,54]

1.5.2 2-electron Water Oxidation

The 2e-WOR is an attractive route to produce H_2O_2, as it can be coupled with hydrogen evolution reaction to produce H_2O_2 and H_2 simultaneously with water as the main source.[38] However, 2e-WOR competes with the thermodynamically favourable 4e-WOR and one electron oxidation for $OH^{\bullet}$. The overall 2e-WOR has a thermodynamic potential of 1.76 V_{RHE} (equation. 1.2) [17] The H_2O is adsorbed onto the catalyst surface and undergoes an oxidation step to generate adsorbed $^*OH$ on the catalyst surface (equation. 1.12). If the binding free energy of $^*OH$ (ΔG_{*OH}) is < 2.38 eV the adsorbed *OH is further oxidised to H_2O_2 (equation. 1.13).[55] A strong OH binding energy leads to *OH oxidising to *O and *OOH which forms the 4e-WOR, however too weak binding energy leads to high activation energies reducing the reaction rate.[56]

$$* + H_2O \rightarrow OH^* + H^+ + e^- \qquad \text{(equation. 1.12)}$$

$$OH^* + H_2O \rightarrow H_2O_2 + H^+ + e^- + * \qquad \text{(equation. 1.13)}$$

In both 2e-WOR and 4e-WOR, the activity determining step is the ΔG_{*OH} whereas the ΔG_{O*} determines the selectivity.[41,55] These factors can determine the catalysts with specific selectivity and activity for the desired WOR.

1.6 Electrocatalysts for Water Oxidation

1.6.1 4e- WOR

For the acidic OER, the number of materials that can withstand the corrosive and highly oxidising potentials required for the OER in a PEM-WE is very limited.[57] Currently, noble metals (IrO_2) are the only commercially viable catalysts that achieve both high activity and stability during OER. A high overpotential is required to overcome the high energy barriers compared to those required for the HER.[58] Therefore, high mass loadings of iridium (> 2 mg/cm^2) are necessary.[59] The high mass loadings, scarcity and high-cost of Ir limits the deployment of PEM-WEs to 2 GW/yr which results in ~ 200-fold reduction in H_2 production compared to current global demands (~ 400 GW/yr).[60] The increased demand for PEM-WEs strains the current Ir supply therefore, there is a need to design improved and economic PEM-WE anode electrocatalysts. The anode electrocatalyst must be able to withstand the aggressive environments whilst also having low overpotential and mass loading at highly oxidising potentials.[4,57]

1.6.2 2e-WOR

The 2e-WOR is a challenging reaction owing to the high current densities required hindering the scaling up of H_2O_2 production[17] and the competing 4e-WOR previously discussed in Section 1.51 where the thermodynamic potential for 4e-WOR is lower than 2e-WOR. Additionally, the electrochemical degradation of H_2O_2 occurs at 0.67 V_{RHE}, leading to H_2O_2 being directly oxidised to H^+ and O_2.[61] Thus, lowering the yield of H_2O_2 and lowering the efficiency towards 2e-WOR. Ideal 2e-WOR electrocatalysts will bind H_2O_2 weakly to reduce any further oxidation,[19] obtain low overpotentials at high current densities and be able to withstand high current densities (> 100 mA/cm^2) for long periods of time.[61]

Over the last few years, significant research has focused on scaling up PEM-WEs.[13] However, PEM-WEs require cost-effective and selective electrocatalysts for WOR.[9]

1.7 Electrocatalyst Properties

There are three main characteristics that are typically investigated during the development of electrocatalysts – activity, stability and selectivity. It is vital for all three characteristics to be met to increase the efficiency of an electrolyser.

1.7.1 Activity

One of the essential characteristics of a catalyst is that it should have high activity. The activity is determined by the catalysts' ability to increase the rate of reaction and thus lower the overpotential. To achieve high activity, the Sabatier Principle can be used as a guiding principle (Figure 1.3) – a heterogeneous catalyst must adsorb reactants, reaction intermediates and products with the appropriate binding energy to enable chemical bonds to break and thus the reaction to proceed.[62] Weak adsorption between reactant and the catalyst leads to an easily desorbed reactant. However, if the adsorption is too strong, this can prevent product desorption thus blocking the active sites. A highly active catalyst can adsorb the reactant with enough strength to allow the reaction to reach completion and bind the product not too strongly to be desorbed.[63]

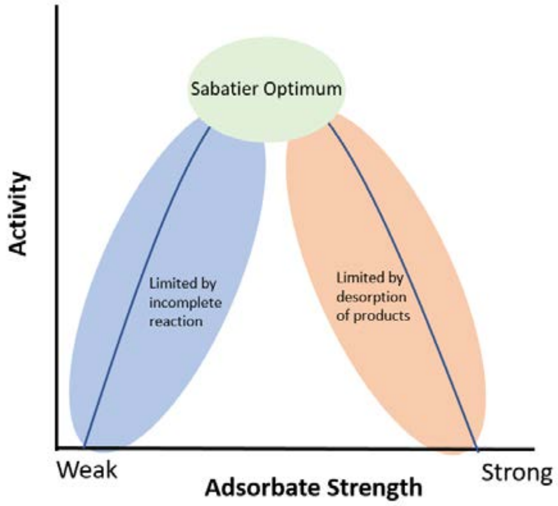

Figure 1.3: Graphical representation of the Sabatier Principle.[64]

Activity in OER electrocatalysis is typically assessed using five parameters:[63,65]

1. Geometric current density (J_g, mA/cm_{geo}^2) – the current density normalised to the geometric area of the working electrode (WE) irrespective of the catalyst loading.
2. Mass activity (A/g_{Ir}) – the current produced normalised to the mass of Ir present on the working electrode.
3. Overpotential (η) – the difference between the thermodynamic potential of the half-cell reaction, i.e. 1.23 V_{RHE} and the potential at which the current density turns on. The overpotentials are typically reported at specific current densities (e.g. 0.1 mA/cm^2, 1 mA/cm^2, 10 mA/cm^2).[65]
4. Specific activity (J_s, mA/cm^2) – the current density at a given overpotential normalised for electrochemically active surface area (ECSA) of the catalyst.
5. Turnover frequency (TOF) – often considered as a proxy for intrinsic activity is the number of moles of O_2 generated per second per active site.

The activity parameters used in this thesis are geometric current density and mass activity as it allows for comparison of the synthesised electrocatalysts from this work against literature in the field. An additional parameter often discussed in the field and within this work to assess catalyst performance is the Tafel slope, a kinetic parameter that relates rate of the reaction to the overpotential. Although Tafel slope measurements alone cannot be used to assess the efficacy of an electrocatalyst, it is an important indicator if used in conjunction with the other parameters.[66]

1.7.2 Stability

Another critical characteristic of a catalyst is stability. Stability reflects the ability of the catalyst to withstand harsh operating environments, such as acidic media, temperatures and highly oxidising potentials over time. Durability is a major challenge particularly in PEM electrolysis where very few materials have sufficient stability under the relevant pH and applied potentials to be considered commercially relevant.[63] Poor stability leads to rapid catalyst degradation, which in turn, decreases the lifespan of the electrolyser.[63]

Activity-stability factor (ASF) is the ratio of rate of oxygen generated at a specific overpotential to the rate of metal dissolution, providing an indicator for activity-stability relationship of a catalyst.[67] Another measure of stability that is used without the need to quantify the catalyst surface area or catalyst loading is the stability number (S-number), defined as the ratio of moles of evolved oxygen to moles of dissolved metal.[65] S-number allows for insight regarding the relationship between activity and catalyst dissolution. The higher the S-number the more stable the electrocatalyst.[46] Stability is typically assessed by chronoamperometry (constant applied potential - CA) or chronopotentiometry (constant applied current - CP). The rate of catalyst dissolution can be measured either *ex-situ* by taking aliquots of electrolyte at regular time intervals or *in-situ* flow-cell coupled to an analyser. The electrolyte solution is typically analysed using inductively coupled plasma mass spectroscopy (ICP-MS) or optical emission spectroscopy (ICP-OES).

1.7.3 Selectivity

Selectivity describes the ability of a catalyst to produce a specific product from a reaction with multiple thermodynamically feasible products.[68] The difference in activation energy for the desired and undesired product determines the reactions selectivity.[69] Specifically, the activation energy for the desired product must be lower than the undesired products in order for the desired product to be formed.[70]

Selectivity is affected by structural and electronic properties.[71] Other factors which affect selectivity are the reaction conditions (e.g. pH of electrolyte, applied potential or current to electrode, temperature, pressure).[65] Such reaction conditions can alter the binding energies of the reaction intermediates and the surface of the catalyst. By tuning each of these factors from the molecular level to the reaction conditions we can influence the reaction selectivity.

1.8 Reducing Iridium Content in 4-electron Water Oxidation Catalysts

Currently, commercial proton exchange membrane water electrolysers (PEM-WEs) require IrO_x-based materials for the oxygen evolution reaction (OER). Several strategies have been explored as methods for reducing iridium loading in PEM-WEs. These strategies include the formation of mixed metal oxides and non-platinum group metals (PGM), altering electrocatalysts morphology to create core-shells and supporting the iridium on stable metal oxides to form supported catalysts. These strategies can improve mass activity of low Ir loadings due to the physical and electronic properties. This chapter provides an overview of the primary literature strategies that have been explored for reducing Ir content for the acidic OER. Although, ruthenium-based (Ru) catalysts have superior activity to iridium, Ru has significantly inferior stability compared to IrO_x.[54] Therefore, this section will mainly focus on Ir-based catalysts.

1.8.1 Mixed Metal Oxides

Perovskites have a formula of ABO_3 where A has large radii, typically alkaline/rare earth metals with 12 co-ordination to oxygen ions whilst B has 6 co-ordinations to oxygen ions.[72, 73] Pyrochlores have a formula of $A_2B_2O_7$ where A is either a rare earth, alkaline earth or p-block metal and B are transition metals (Figure *1.4*Figure *1.4*).[74,75] In both structures, the B site can contain Ir or Ru which have in many cases shown promising activities and stability for the OER. These structures enable “tuneable” stoichiometry of A and B sites to induce high activity due to change in electronic structure.[73]

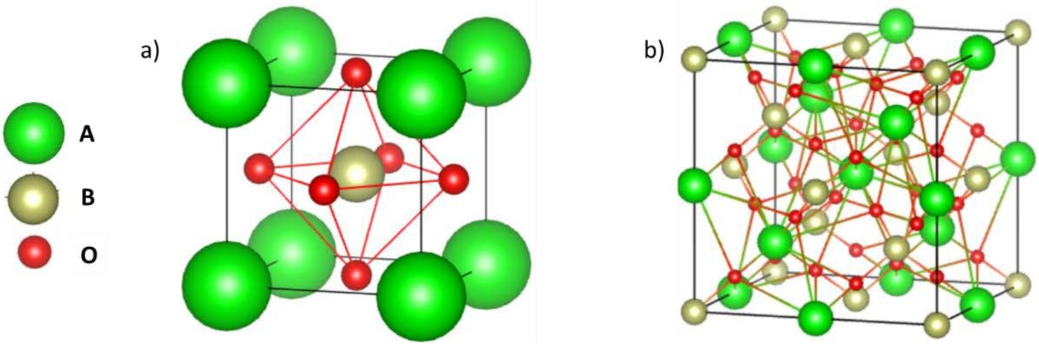

Figure 1.4: Schematic of a) Perovskite and b) Pyrochlore crystal structures.[76]

1.8.1.1 Perovskite

The A and B sites in perovskites can be tuned to form different compositions to obtain active and stable OER electrocatalysts. Specifically, Ir-based perovskites have been synthesised with varied A-sites (eg. Sr,[46,77–82] Ba,[46,83,84], SrCo[85], Ca[86]) for the OER. The synthesis of perovskite catalysts typically requires high temperature (> 800 °C) for long periods of time.[78,87] The high temperatures applied to form perovskite nanopowders is a potentially expensive process and typically has a negative impact on the catalyst surface area, leading to the synthesis of large particles (>50 nm).[85,88] Therefore, there is a need to produce cost-effective perovskites with high surface areas. Alternative solution-based syntheses (e.g., sol gel) have been performed with increased surface areas but still require similarly high temperatures (700 °C) for long periods of time (> 6 h).[77,79,80]

Perovskites are highly prone to A-site leaching which coincides with improved OER activity.[82] However, A-site leaching enhances Ir leaching and leads to degradation of the perovskite structure.[46] Solution-based syntheses have shown reduced leaching of A-sites compared to solid state syntheses.[80,86] Additional efforts to enhance stability of perovskites has focused on synthesising double perovskites however long term stability measurements have not been investigated.[84] Therefore, there is a need to investigate the long term stability (> 30 h) of perovskite materials.

1.8.1.2 Pyrochlores

Ir-based pyrochlore oxides have also been reported as active and stable OER electrocatalysts. The pyrochlore structure allows for the A and B sites to be tuned to obtain different compositions (e.g. A = Bi,[89–92] Gd,[93–95] Pr,[94] Nd,[93–95] Y,[89,96] etc.,). For OER catalysis, Ir and Ru can be deployed at the B-site. However, Ru-based catalysts are active but not stable for OER. Similar to perovskite syntheses, pyrochlores can be synthesised via solid state syntheses[90] which results in low surface area materials.[90,97] Other synthesis routes to synthesise pyrochlores have included hydrothermal,[91,92] Adams fusion[89] and sol-gel[94] however, these still result in relatively low surface area materials < 30 m^2/g.

The increase in OER activity for pyrochlores occurs under operando conditions as a result of leached A-sites.[82,89,98] However, leached A-sites can induce rapid degradation of B-sites (Ir) enhancing the degradation of the pyrochlore structure.[89,99] Therefore, the stability of pyrochlores requires further investigation to obtain active and stable pyrochlores for the OER in acidic environment.

1.8.2 Alloys

Alloying or synthesising bimetallic Ir materials offers a promising route to enhance the OER activity due to the synergistic effect that can occur between bi or multi-metallic metals.[100,101] The modification of the electronic structure through alloying, has shown to be a promising method for tuning the intrinsic activity of an OER catalyst. Alloys or bimetallic Ir materials are typically synthesised via wet chemistry (eg.,sol-gel),[101–107] thermal decomposition,[108,109] microwave-assisted,[110,111] and vapour deposition[112] to form Ir-M materials where M = Sn,[103,112] Ta,[103,109] Ni,[105,106,112–114] Ru,[107,115] Cu,[104,116] and Cr.[112]

Bimetallic oxides have been widely studied due to their increased intrinsic OER activity compared to pure Ir oxides.[112–114] Studies have shown that the addition of non-noble metal can improve the OER activity.[113] However the stability of the material is reduced with increasing non-noble metal content correlating with the increased leaching of the non-noble metal.[112] Additionally, varied morphologies of bimetallic materials (eg.,nanocages,[106,116] nanotubes[101] nanorods,[117118119] nanowires[120] and microspheres[104]) have been investigated and exhibited high stability and activity during the acidic OER. The enhanced OER performance has been attributed to synergistic effects between Ir and the non-noble metal and the increase in active sites available for the OER. However, long-term stability measurements of these nanostructures have not been thoroughly investigated.

High-entropy alloys (HEAs) containing 5 or more elements have also been explored for the OER.[111,121,122] HEAs typically exhibit enhanced physical properties which increases their stability and corrosion resistance making them ideal from a stability point of view as an electrocatalyst for OER. The OER activity shows overpotentials of 32 - 300 mV at 10 mA/cm^2 for HEAs, showing high activity compared to Ir (352 mV at 10 mA/cm^2). Short term chronopotentiometry measurements (< 15 h) were conducted and showed that HEAs are stable for up to 14 h at 10 mA/cm^2 with minimal changes in activity.[122,123] When combined with the elemental dissolution analysis, the low concentration of dissolved metals (< 10 µg) further corroborates the high stability of the HEA.[111] The stability of HEAs was attributed to the formation of an Ir-rich surface due to the dissolution of the metals during the OER (Figure 1.5).

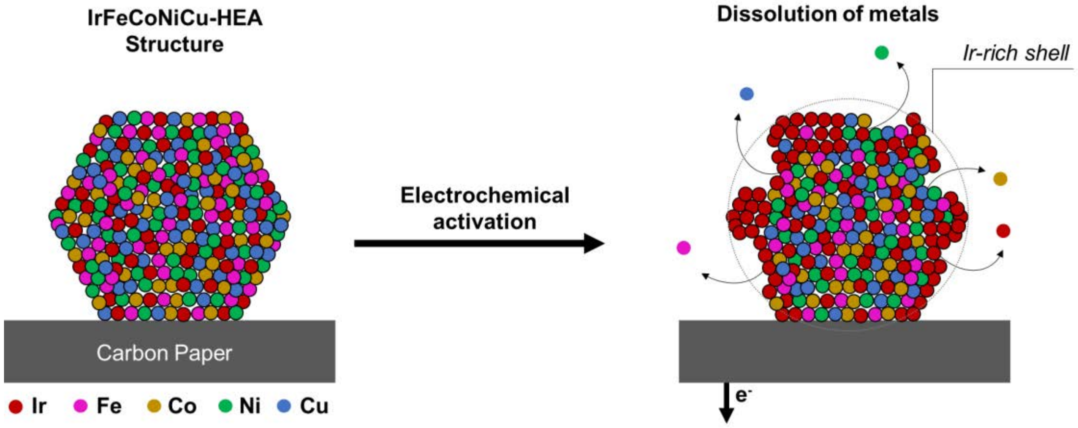

Figure 1.5: Schematic of the IrFeCoNiCu-HEA nanoparticle and the dissolution of the 3d metals leading to an Ir-rich surface adapted from ref. [111].

The ability to increase the number of elements used to form a HEA is an optimistic pathway to enhance the structural stability and the activity of alloyed materials.[123,124] However, minimal research currently exists on HEAs for the acidic OER to fully understand the structure-activity relationship. It is also important to note that the electrochemical testing of alloys has been shown to occur whilst being supported onto carbon based material in order to improve the conductivity of the alloy.[105,110,125]

1.8.3 Precious Metal Free OER Catalysts

To reduce the capital cost of an electrolyser, researchers have also investigated the complete removal of platinum group metals (PGM) from OER catalysts. However, the majority of this research has focused on alkaline conditions.[126–128] There is a substantial gap in catalyst performance (activity and stability) between PGM-free catalysts for acidic and alkaline environment. A few notable exceptions where promising acidic OER activity has been reported are briefly reviewed below.

Nickel and manganese antimontates[129–131] and tantalum-based intermetallic alloys[132] have shown promising results with overpotentials of 570 mV – 770 mV. However, the lack of Ir leads to enhanced leaching of the non-noble metal under acidic environment. Although these catalysts are promising, both the activity and stability are not currently sufficient for long-term PEM-WEs applications and therefore require further investigation.

1.8.4 Core-Shell

Core-shell nanomaterials vary by size, morphology and composition. They consist of a core with an outer shell. When deployed for the OER, the core is typically a non-PGM metal, while the shell is an active PGM containing material. Thus, the PGM loading is reduced compared to many other nanomaterial structures. Beyond reducing the PGM loading, varying the elemental compositions of the core or the shell can also have important consequences for the conductivity of the catalyst.[133,134] Notable Ir-based core-shells have included Ni,[135–138] Fe,[135] Co,[135] Cu,[138,139] Pd[139,140] and Ti[141,142] as metal cores.

Core-shells are utilised as they provide increased coverage of Ir onto the metallic core attribute to the high electrochemical surface area which improves electrocatalytic activity.[67,142–144] The interaction between Ir and the metal core can induce synergistic effects which leads to improved electronic effects that can improve the OER activity.[135,138] Ligand and strain effects are also a contributing factor to increased electrochemical activity.[145] DFT analysis has been conducted to evaluate the effect of compressive strain and determined that the strain on the Ir shell lowers adsorption strength of oxygen intermediates facilitating the generation of oxygen.[139] Additionally, there is also an interest in identifying the optimum Ir shell layer for improved OER activity and stability. A study identified that increasing the Ir shell layer would weaken the core.[135] However, the presence of a single layer protects the core from oxidation. It was also determined that increasing the atomic layer led to an increase in the OER activity with 3 Ir atomic layers being the optimum number of layer to achieve high OER activity.[140] The increased number of Ir layers improved the durability of the catalyst due to the increased presence of stable Ir^{4+} thus protecting the core from being oxidised during the OER.

Short-term (< 20 h)[69] and long term (~ 100 h)[70] stability measurements of core-shells have highlighted their potential as stable electrocatalysts for OER.

However, studies have shown that the core can be prone to oxidation correlated with the incomplete Ir coverage leading to deactivated material.[135] In addition, catalyst delamination can also induce core dissolution which results in an unstable electrocatalyst.[137]

1.8.5 Supported Catalysts

Supported catalysts are structures that disperse the catalytically active material (e.g., iridium oxide) onto a high surface area support material such that the total catalyst loading is decreased compared to bulk catalysts (Figure 1.6).[146] Alongside stability under the operating OER conditions, catalyst supports should be conductive, have a high surface area, and be made from economically viable and abundant element(s). It is vital for these characteristics to be present in a support to enable the catalyst to achieve high activity and stability whilst simultaneously reducing the PGM catalyst load. The increased surface area will increase Ir utilisation thus reducing Ir loading whilst simultaneously improving mass activity. Additionally, catalyst-support interactions could be used to tune the catalytic performance for the OER, enhancing the activity and/or stability of the catalyst.[147,148] The development of supported Ir catalysts represents a relatively unexplored route for the development of high-performance catalysts with the potential for low Ir loadings.[149]

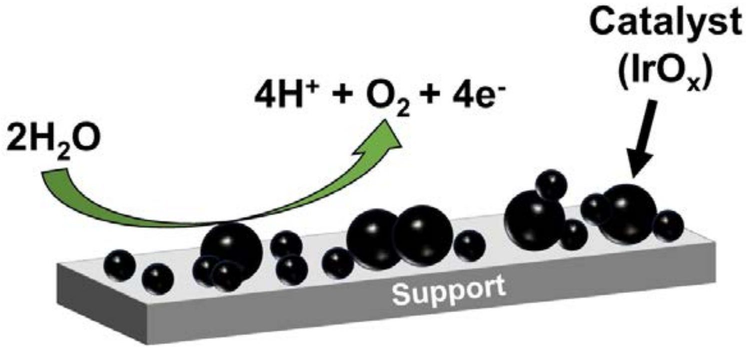

Figure 1.6: Schematic of IrO_x dispersed on support material. The OER reaction is shown to occur on the IrO_x surface.

1.8.5.1Selection of Support Material

As discussed above, the primary considerations for a potential catalysts support are, high surface area, high conductivity and low cost. Pourbaix diagrams have proven a useful tool for selecting transition metal oxides that would be stable at pH 0 and above 2 V_{RHE}. Han *et al.,*[150] discovered that Mo, Sb, W, Nb and Ta are cost-effective transition metal oxides which are stable at the aforementioned conditions. This section will provide an overview of the most commonly deployed metal oxide supports deployed for acidic OER (C, TiO_2, SnO_2 and Ta_2O_5).

One common limitation of metal oxide-based catalyst supports is their low conductivity. While several strategies have been explored towards improving the conductivity of metal oxide supports, doping is the most commonly deployed strategy. Similar to selecting a metal oxide support, it is important to choose dopants that are stable during PEM-WEs operation to reduce the dissolution of the support and thus catalyst degradation. Therefore, dopants must be able to withstand the corrosive and oxidising environment of a PEM-WE. This section will focus on possible dopants for the acidic OER and their activity and stability.

1.8.5.1.1 Carbon-based Supports

Carbon supports with different morphologies such as carbon nanotubes[151–153] and nanoparticles[154] have been studied as support materials for the OER under alkaline conditions. Carbon materials have a high surface area, excellent electrical conductivity, and robust mechanical strength.[155,156] Similar to transition metal oxide supports, carbon supports can facilitate the dispersion of active metal catalysts or their oxides, thereby increasing the number of active sites available for the OER and enhancing the overall catalytic performance.[157,158]

Despite these benefits, maintaining stability in acidic media remains a key challenge for carbon-based supported catalysts due to the highly oxidising and corrosive environment, which can lead to rapid degradation of the carbon support producing unwanted products (CO and CO_2) and hence the breakdown of the supported catalyst.[159,160] Recent advances have thus focused on doping carbon based materials with nitrogen to enhance the long-term stability of the support.[161,162]

1.8.5.1.2 Titanium Dioxide

Amongst metal oxides, titanium dioxide (TiO_2) is a very attractive catalyst-support owing to its high chemical and electrochemical resistance to corrosion and the existence of highly optimised syntheses to form high surface area nanostructures as well as various commercial sources of TiO_2 nanoparticles.[163]

Mazur *et al.*,[164] synthesised an IrO_2 catalyst supported on 3 different commercial TiO_2 powders, each with a different surface area (10, 50 and 90 m^2/g). It was shown that the support surface area influenced the crystallite size of IrO_2, electrical conductivity, and the electrochemical activity of the prepared supported catalyst. Furthermore, it was speculated that supports with a lower surface area led to the formation of an interconnected IrO_2 conductive film on the surface of the support leading to a higher catalyst performance. In a recent study, the correlation between electronic conductivity and Ir wt% in IrO_2-TiO_2 showed that the optimum Ir content is > 40 mol_M%, to provide an electrically conductive path between TiO_2 and IrO_2 .[165]

Despite these positive attributes of TiO_2, the low conductivity is a hinderance to achieving high OER performance as a catalyst-support requiring Ir loadings of > 50 wt%. Various strategies to increase the conductivity of TiO_2 have been investigated, including the synthesis of substochiometric oxides.[166–168] Nanostructuring strategies such as core-shells[67,142–144] and high surface area TiO_2[164] have also been utilised to maximise Ir utilisation. Conductive layer coated supports (CCSs), where a conductive Pt interlayer is introduced between the TiO_2 core and Ir catalyst, have recently shown 141% higher OER mass activity compared to commercial 75 wt% IrO_2-TiO_2 in a rotating disk electrode (RDE).[169] The nanostructured conductive interlayer allows for a lower total platinum-group metal (PGM) loading and simultaneously enhanced conductivity and is thus a promising approach for lowering Ir catalyst loading in PEM-WEs.

Molybdenum has oxidation states that vary from +2 to +6.[170] During OER molybdenum will likely be oxidised to +4 or +6 due to pH of electrolyte and potential applied.[171] We can determine that molybdenum would become a stable MoO_3 at high potentials and acidic pH.[172] Theoretically, molybdenum would be a stable dopant for OER between 1-1.8 V_{RHE}. However, the use of molybdenum as a dopant for water oxidation has not been widely researched. Nanoparticles of Mo doped TiO_2 were synthesised for lithium batteries.[173] It was determined that Mo reduces the agglomeration of TiO_2 and forms uniform particles with high surface area. Additionally, the conductivity is significantly improved due to the Mo dopant. Therefore, Mo may be an interesting material to use as a dopant due to its' ability to enhance physical and electrical properties of a metal oxide.

1.8.5.1.3 Tin Oxide

Beyond TiO_2, tin oxides have also received significant attention as promising catalyst supports for the acidic OER owing to the claimed stability under the operating conditions of a PEM anode.[174] However, tin content must be tightly controlled as this has been found to affect the resistivity and influence the catalytic activity.[175] Similarly to TiO_2, the conductivity of SnO_2 is typically low thus reducing catalytic activity.[174] However, irrespective of the conductivity, using SnO_2 as a support has led to promising OER activity at low Ir mass activities.[176] This could be attributed to tin content of < 50 wt% increasing the surface area of the support leading to enhanced catalytic activity.[177]

There have been multiple studies investigating Sb-doped SnO_2 (ATO) due to its enhanced conductivity, chemical and thermal stability.[148,178–181] Although ATO is beneficial as a support, there are stability issues due to the leaching of antimony from the support lattice leading to support degradation and subsequently catalyst dissolution.[182] Da Silva *et al.*,[174] highlighted similar catalytic activity for unsupported and doped SnO_2 supported Ir catalysts. Additionally, it is observed that IrO_x has greater instability than IrO_2 in the supported catalyst. Proving that annealing supported catalysts can enhance stability. However, Ir-doped SnO_2 catalysts can be more unstable than Ir-SnO_2.

There have been many studies focused on alternative (Nb and Ta) doped SnO_2 as a route to enhance catalyst-support stability. Stöwe *et al.,*[183] synthesised a range of doped tin oxides as support materials for Ir. One of those dopants was Ta due to its stable nature as an oxide. It was discovered that Ta-doped SnO_2 had pronounced lattice parameter changes attributed to the substitution of Ta^{4+} into the tin dioxide crystal lattice. Furthermore, they established that varied compositions of Ta led to differences in mass loss upon heating in air/nitrogen. Additionally, Ta doped SnO_2 has shown promising conductivity of 10^{-2} S/cm.[184] Tantalum doped supports have been shown to be more stable and active as the Ta content increases compared to ATO supports, showing promise as a stable support material.[155,185]

Niobium (Nb) based materials are promising as support materials due to the cost effective synthesis of the thermodynamic stable form (Nb_2O_5).[186] Niobium has been shown to be corrosion resistant in low concentration acidic solutions (high pH) at lower temperatures (< 95 °C).[187] A study utilised Nb as a dopant within SnO_2 and observed a range of conductivity (0.02 – 1.1 x 10 $^{-4}$ S/cm) as a function of Nb content.[188] The variation in conductivity was attributed to the homogeneity of Nb distribution within the SnO_2 lattice. Further research has identified that the increase in Nb content decreases the crystallite size of Ir allowing for increased dispersion of Ir particles.[189] Additionally, when doped with SnO_2, Nb showed that it was stable for ~ 60 hours during a 20 mA/cm^2 hold.[184]

1.8.5.1.4 Tantalum Oxide

The most important benefits of a tantalum oxide support is its predicted stability under highly oxidising electrochemical condition over a wide potential range.[190] In one study, the stability and conductivity of Ir/Ta_2O_5 was investigated, and it was observed that the conductivity of Ta_2O_5 was improved upon the addition of Ir.[191] Additionally, stability testing showed Ir/Ta_2O_5 to be highly stable with minimal dissolution of Ir and Ta (evaluated by ICP-MS). Specifically, no Ta species were observed in the electrolyte after stability testing, whereas 6.3 ppb of Ir was detected. Thus, showing the stable nature of Ta_2O_5.

In another study, $Ir_{0.1}Ta_{0.9}O_{2.45}$ nanoparticles of 1 – 6 nm were deposited onto gold electrode and evaluated for their OER activity and stability.[192] High mass activities of 1.2 kA_{O2}/g_{Ir} at an overpotential of 320 mV overpotential were obtained for $Ir_{0.1}Ta_{0.9}O_{2.45}$ of < 2 nm. It was observed that an increase in the particle diameter > 2 nm led to lower OER activity which was hypothesised to correlate with the reduced conductivity due to larger particle size or segregation of TaO_x. The stability of $Ir_{0.1}Ta_{0.9}O_{2.45}$ showed an initial decrease in activity during the first few minutes, then showed stability for the remaining 24 h. The initial decrease in activity was attributed to the formation of gold oxide acting as an insulator. It was shown that the morphology of the catalyst did not change during the stability testing. Thus, highlighting that Ta oxides are potentially stable as supports for OER.

Ternary mixed oxides such as IrO_2-SnO_2-Ta_2O_5 have also been synthesised as supports for the OER.[103] The addition of a Ta_2O_5 support to SnO_2 was shown to reduce crystallite size which provided an increase in surface area and conductivity. The enhanced properties of the IrO_2-SnO_2-Ta_2O_5 catalyst promoted an enriched Ir surface leading to high activity at lower loadings of Ir (15 mol%). However, stability testing was not conducted for this material.

1.8.6 Summary of strategies deployed to reduce the Ir content in electrocatalysts for the 4e-water oxidation reaction

In summary, there are multiple strategies that have been investigated towards reducing the Ir content at PEM anodes. Figure 1.7 shows a plot of current density vs. overpotential and mass activity vs. potential of the state-of-the-art catalysts discussed within this chapter. The current density plot highlights perovskites, pyrochlores and core-shells as the best performing catalysts with low overpotentials of < 350 mV, conversely the mass activity plot shows that the best performing catalysts are core-shells and supported catalysts with high mass activities (> 825 A/g$_{Ir}$) at less than 350 mV. We highlight the importance of choosing the right combination of materials to ensure that the physical and electronic properties of the supported catalyst are appropriate for the OER. While several of the strategies discussed in this section exhibit relatively good OER performance (excluding PGM free catalysts), there are still properties that need to be improved for these materials to be translatable into a commercial PEM-WE. For example, catalyst stability, cost, and activity. Many of these materials therefore require fine tuning to obtain an anode that exhibits the desired properties to obtain a high performing and stable OER catalyst.

In this thesis, we focus on two different strategies towards developing supported catalysts for the acidic OER. In Chapters 3 - 5, we evaluate the activity and stability of hollow TiO_2 and doped SnO_2 as catalyst-supports in a three-electrode configuration and a 5 cm^2 PEM-WE for the acidic OER.

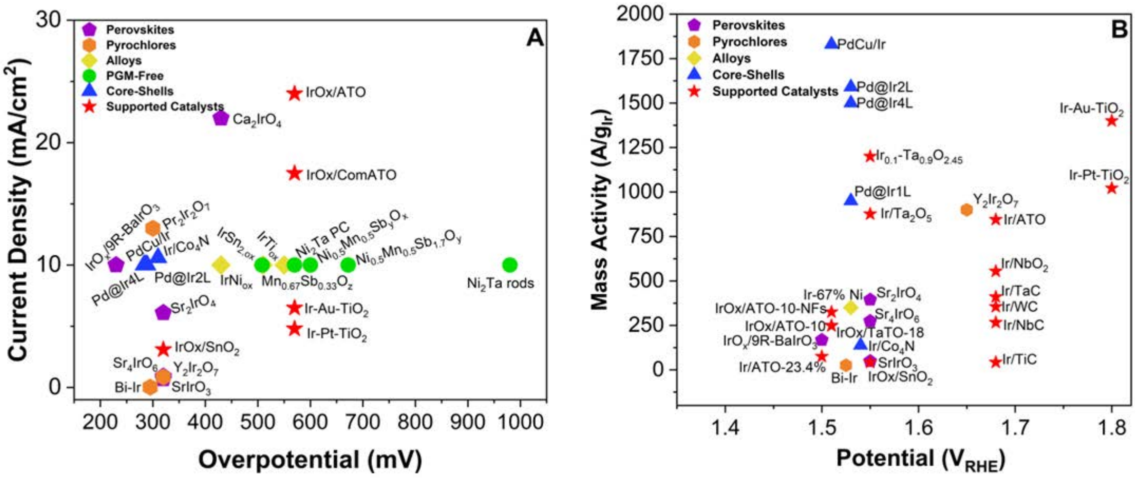

Figure 1.7: Summary plots to show the performance of numerous literature state-of-the-art OER electrocatalysts referenced in section 1.8. A) current density plotted against overpotential and b) Ir-normalised mass activity plotted against potential.

1.9 Investigating the Selectivity of 2-Electron Water Oxidation Reaction

1.9.1 Electrochemical Production of H_2O_2

Hydrogen peroxide is a strong oxidising agent that is widely used in multiple industries such as textiles, paper and chemical.[193] Currently, H_2O_2 is produced via an energy-intensive anthraquinone oxidation (AO) process. The production of H_2O_2 via the AO process has major safety concerns due to the large amounts of organic solvents used under high pressure producing highly concentrated (> 40 %) H_2O_2.[194] The transportation and storage of large volumes of highly concentrated H_2O_2 also poses a safety risk, thus motivating the development of a delocalised H_2O_2 production technology.

H_2O_2 can be produced via the 2-electron oxygen reduction reaction (ORR, (equation. 1.14)[195] and the 2-electron water oxidation (2e-WOR, (equation. 1.15) [61]. Interest in the 2e-WOR has increased due to the promise of utilising water as a reactant which is not dependant on the solubility of O_2 in water potentially increasing the efficiency.[16] It is also an anodic reaction which can therefore be coupled with the cathodic ORR in a device that produced H_2O_2 at both the anode and cathode of a working device. However, the majority of 2e-WOR electrocatalysts suffer from low selectivity and activity due to the competing 4-electron water oxidation reaction known as the oxygen evolution reaction (OER, (equation. 1.16). Indeed, the 2e-WOR is thermodynamically less favourable (1.76 V_{RHE}) than the OER (1.23 V_{RHE}).

$$O_2 + 2H^+ + 2e^- \rightarrow H_2O_2 \qquad \text{(equation. 1.14)}$$

$$2H_2O \rightarrow H_2O_2 + 2H^+ + 2e^- \qquad \text{(equation. 1.15)}$$

$$2H_2O \rightarrow O_2 + 4H^+ + 4e^- \qquad \text{(equation. 1.16)}$$

Therefore, when attempting to turn over the water oxidation reaction to H_2O_2 there is a high risk of also turning over 4e-WOR leading to less than 100 % Faradaic efficiency (FE) for the 2e-WOR. Owing to the highly oxidising potential (1.76 V_{RHE}) required to turn over the 2e-WOR, there are relatively few materials capable of turning over this reaction. However, some metal oxides have been investigated and shown promise for this reaction.

1.9.2 Materials with Selectivity for H_2O_2

Thin films of MnO_x was one of the earliest metal oxides shown to electrochemically oxidise water to H_2O_2 was reported by Izgorodin *et al*[196]. The MnO_x exhibited low overpotential of 150 mV to achieve 1 mA/cm^2. Subsequently, density functional theory (DFT) has been used to identify alternative materials with a potential to produce H_2O_2.[38,197] Specifically TiO_2, WO_3 and SnO_2 have been shown as candidates for H_2O_2, However, the FE of these catalysts was shown to be <50 % for all of these materials except $BiVO_4$ with 70 %.[198] Therefore, the majority of studies have investigated approaches to enhance the FE of $BiVO_4$. For example, doping $BiVO_4$ with gadolinium, which increased the FE to ~ 99.5 % due to a shift in the OH adsorption energy to a thermodynamically favourable value.[199] In another study $BiVO_4$ was made into a composite with WO_3 and showed a FE of 30 %.[200] It is of note that the majority of these works have investigated $BiVO_4$ as a photocatalyst rather than electrocatalyst.

Recent studies have increased the known list of active materials for WOR to H_2O_2 to include ZnO and $CaSnO_3$. ZnO has shown promise for photochemical production of H_2O_2. The analysis of ZnO as a WOR catalyst has shown a FE of 70 % at 3 V_{RHE} and an onset potential of 1.95 V_{RHE}.[201] $CaSnO_3$ has also shown promise as a WOR catalyst with an onset potential of 1.90 V_{RHE} and a peak FE of 76 % at 3.20 V_{RHE}.[202]

As well as the activity of the catalyst, the stability of the material must also be investigated especially due to the highly oxidising potentials used to form H_2O_2. Boron-doped diamond has been investigated and been able to achieve stability for 10 h at 200 mA/cm^2 and producing ~ 71 % FE.[61] Similarly, the stability of $CaSnO_3$ has shown promise with minimal change in activity over 12 h at 2.2 V_{RHE}. In summary, there remains a need to design alternative catalysts for 2e-WOR catalysts.

1.9.3 Influence of Electrolyte on H_2O_2 Production

In addition to investigating alternative catalysts for 2e-WOR, other factors such as the electrolyte are known to also influence the electrocatalysts activity and selectivity. A study conducted by Fuku *et al.,*[203] investigated the effect of electrolytes by utilising $BiVO_4$ coated on fluorine doped tin oxide (FTO) as a photoanode in $KHCO_3$ to form H_2O_2. The influence of Li_2SO_4, $NaClO_4$, K_2CO_3, $KHCO_3$, H_3BO_3+KOH and phosphate buffer on the production of H_2O_2 highlighted that $KHCO_3$ produced the highest concentration of H_2O_2 overall, leading to highest selectivity of 35 %. Gill *et al.,*[204] suggested that HCO_3^- enhances H_2O_2 production, rather than stabilise (or prevent the consumption) of H_2O_2. Specifically, HCO_3^-/HCO_4^- acts as a redox catalyst for H_2O_2 production in $KHCO_3$ electrolyte. Indeed, it is suggested that H_2O_2 is not directly produced from the catalyst but instead as a product of oxidising the electrolyte supporting the hypothesis laid out by Fuku *et al.*,[203] The pH of the electrolyte must also be taken into consideration as studies have suggested that H_2O_2 is unstable in high pH (> 12) for long periods of time (> 1 h).[204] In summary, it has been shown that pH near neutral with high CO_3^- content (2M) is the optimum electrolyte for H_2O_2 production.[41]

1.9.4 Quantification Techniques for H_2O_2

Due to the competing 2e$^-$ and 4e$^-$ WOR, it is important to be able to distinguish whether the recorded electrochemical current is due to the formation of H_2O_2 or O_2. Therefore, it is vital that the H_2O_2 can be quantified during the electrochemical experiment. As such, there are a range of methods which have been identified as reliable quantification techniques for H_2O_2, these are split into *in-situ* and *ex-situ* measurements.

1.9.4.1 In-Situ Quantification

In-situ quantification of H_2O_2 can be conducted by through rotating ring disk electrode (RRDE) experiments. Specifically, the disk electrode undergoes potential sweeping or a potential hold where H_2O is oxidised to H_2O_2 and O_2 (e.g., CV, LSV, CA or CP). Conversely, the ring is held at a potential whereby H_2O_2 is oxidised to O_2. The current produced at both the ring and the disk electrode are used to calculate the FE for H_2O_2 (equation. 1.17)[205] To improve the accuracy of these results, the collection efficiency of the ring must be calibrated prior to testing in the chosen electrolyte.[206] *In-situ* methods avoid error due to H_2O_2 degradation during the course of the WOR. Although this method is typically used for 2e-oxygen reduction reaction (ORR) it can be applied to the 2e-WOR so long as the disk is made from a material that is stable under the relevant applied potentials.

$$\text{FE of } H_2O_2 = 100\ \% \times \frac{i_{ring} \div N_{H2O2}}{i_{disk}} \qquad \text{(equation. 1.17)}$$

where, i is the current at the respective electrode and N is the collection efficiency.

1.9.4.2 Ex-Situ Measurements

The *ex-situ* measurements also known as accumulation methods, determine the concentration of H_2O_2 by collecting and analysing aliquots of electrolyte after 2e-WOR. Three methods have been commonly deployed in the literature: titration, colorimetry strips and UV-vis spectrophotometry, which are commonly used.

Quantifying H_2O_2 via titration involves dropwise addition of titrant to H_2O_2 containing solution. The titrant is subsequently oxidised or reduced by H_2O_2 inducing a colour change in the titrant, indicating that the H_2O_2 can no longer react with the titrant (endpoint). The concentration of H_2O_2 can then be calculated using the endpoint value of the reaction, concentration of titrant and known stoichiometric ratio between the titrant and H_2O_2. $KMnO_4$,[207,208] $Ce(SO_4)_2$[209] and iodine[210] have all been shown as effective titrants for H_2O_2 quantification. The titration method is typically used for high concentrations of H_2O_2 and does not require extensive equipment. One limitation of titration methods is that typically, low concentrations of analyte can induce signficant errors and uncertainty when determining the endpoint. However, Izgorodin *et al.*,[196] was able to combine titration and UV-vis spectrometry to determine µmoles of H_2O_2.

UV-vis spectrometry can be used to quantify the concentration of H_2O_2. Although H_2O_2 does not absorb light, when combined with other reagents that absorb light in the UV range the concentration can be determined.[211,212] Similar to titration, UV spectrometry relies on a colour change and requires the formation of a calibration curve of a known H_2O_2 to determine the concentration of H_2O_2 generated. Utilising the Beer-Lambert law (equation. 1.18) where the absorbance of a sample at a specified wavelength is proportional to concentration, the concentration of H_2O_2 can be determined via calibration curves.[213] The accuracy of this method is dependent on the calibration curve produced and the stability of the colour change can be a source of error. However, if the calibration curve and the colour is stable, UV-vis exhibit low detection limits (0.3-4 ppm) making this method a desired method to quantify low concentrations of H_2O_2.[214]

$$A = \epsilon l c \qquad \text{(equation. 1.18)}$$

where, A is absorbance, ε is molar absorptivity, c is concentration.

The use of H_2O_2 strips is a colorimetry detection technique. The colour change occurs by a similar principal to titration method whereby redox reactions occur and leads to colour change over time.[55] The strip is immersed into solution and the H_2O_2 reacts with the indicator present on the strip. Different concentrations of H_2O_2 will appear as different colours and can be compared against the given colorimetry card (like pH paper) or electronic strip reader to detect the concentration. Colorimetry strips can have a low detection limit of 0.5 ppm, however the error can reach +/- 20 % and are also influenced by interference species such as organic solvents.[41,214]

As discussed, each ex-situ method has a different limit of detection for H_2O_2 and thus the maximum concentration of H_2O_2 must be calculated prior to choosing an *ex-situ* quantification method (Table 1.3).

Table 1.3: Comparison of detection limits for ex-situ quantification methods adapted from ref. [41].

Method	Lower Detection Limit (ppm)
Titration	1,000 – 10,000
UV-vis	0.3 - 4
Colorimetry Strips	0.5 – 1,000

In addition to the detection limit, the H_2O_2 quantification method is influenced by the choice of electrolyte and pH. Gill *et al.,*[214] investigated the effects of pH and electrolyte on the quantification technique and determined that the error for colorimetry techniques is reduced when the electrolyte is between pH 2 – 12. Conversely, pH has negligible impact on error for UV-vis and titration methods across pH 0 – 14. However, large errors were found using the colorimetry method in the majority of electrolytes. UV-vis showed minimal error (< 5 %) in all electrolytes.

1.9.5 Summary

The development of materials and electrochemical conditions that promote the selective 2e-WOR to H_2O_2 under highly oxidising potentials is a complex problem that requires extensive attention. Figure *1.8* highlights the activity and selectivity of catalysts with selectivity for H_2O_2. The current density plot shows that $BiVO_4$

and ZnO catalysts produce high current which correlates with the high faradaic efficiencies (> 60%). However, $BiVO_4$ performed as a photocatalysts and has yet to be investigated as a electrocatalyst. Therefore, it is important to investigate the selectivity of other materials to obtain the best performing electrocatalyst. Furthermore, careful development of methodologies for the quantification of H_2O_2 requires thorough investigation to obtain accurate measurements of H_2O_2 selectivity. The subsequent ex-situ quantification of the generated H_2O_2 is also a bottleneck at low concentrations of H_2O_2 and must be strictly controlled to ensure accurate detection of the H_2O_2 produced.

In this thesis, Chapter 6 focuses on the development metal stannates and composite Au-$CaSnO_3$ as thin films and nanoparticles and the *ex-situ* quantification of the electrochemically produced H_2O_2.

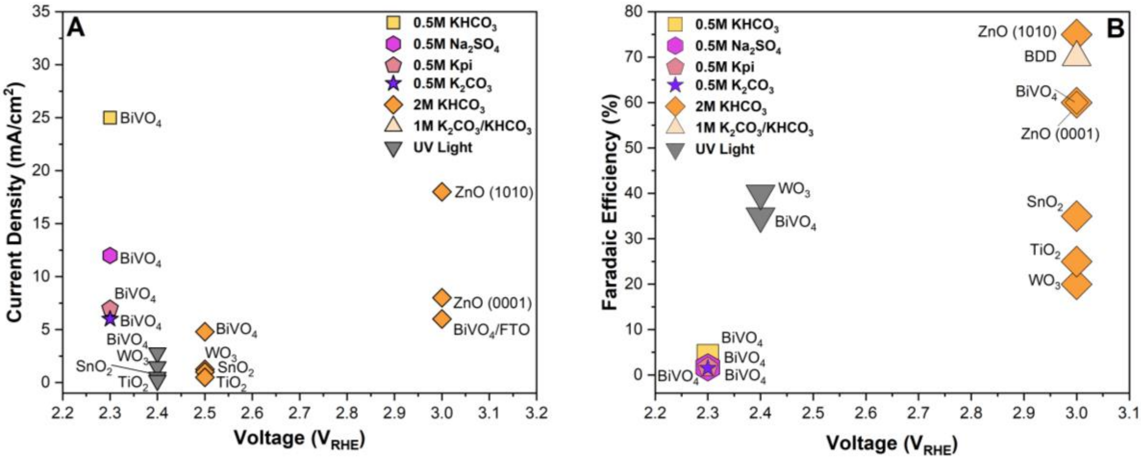

Figure 1.8: Summary of a) current density and b) faradaic efficiency performance of numerous literature state-of-the-art 2e-WOR electrocatalysts referenced in section 1.9.

1.10 Research Aims and Objectives

The broad focus of this thesis is to develop cost-effective electrocatalysts that can withstand the acidic and oxidising environments during the 2e and 4e WORs. The overall aims of the research is to synthesise cost-effective, active and stable supported catalysts that can obtain similar performance to the current state of the art catalyst (IrO_x) with low Ir loading (< 75 wt%) for the 4e WORs. Additionally, this work will aim to develop selective and active catalysts for the electrochemical production of hydrogen peroxide via the 2e WOR.

The electrochemical performance of the synthesised electrocatalysts will be evaluated via half-cell and MEA testing for long term activity and stability. The electrochemically produced hydrogen peroxide will be quantified using *ex-situ* techniques. Physical characterisations of the synthesised electrocatalysts will be conducted to investigate how the physical properties such as morphology and structure of the synthesised electrocatalysts influences the electrochemical activity, stability and selectivity.

2 Experimental Techniques

A critical part of this research involves the analysis of crystallite size, particle size, crystal phases, microstructure, morphology, elemental composition, elemental distribution, and oxidation states prior to (and sometimes post) electrochemical analysis. The techniques described in this chapter have been utilised to assess these materials and physical properties as well as the electrochemical performance of the prepared electrocatalysts.

2.1 Microscopy Techniques

2.1.1 Scanning Electron Microscopy

Scanning electron microscopy (SEM) is widely used in material characterisation as it provides highly magnified images of the surface and composition of materials when combined with energy dispersive x-rays (EDX).[215] The electron beam is focused and scanned across the surface of the sample. An electron beam reaches the sample leading to electron-sample interactions which produces a range of different signals. These signals include backscattered electrons (BSE), secondary electrons (SE) and characteristic x-rays. BSEs are due to inelastic interaction between the primary electrons and the sample. The primary electrons are then scattered inelastically at large angles and re-emerge from the surface, they provide information on the material composition. SE are emitted from an outer shell or valence electrons at energies below 50 eV and provide high resolution topographical images as only electrons within 10 nm depth are detected. These signals are collected and used to generate high resolution images of materials.[215,216]

In this work, the morphology of the synthesised materials were determined with a Zeiss Supra 40VP SEM fitted with an EDAX 40VP energy dispersive x-ray analyser.

2.1.2 (Scanning) Transmission Electron Microscopy

(Scanning) transmission electron microscopy ((S)TEM) provides high resolution images of the internal structural of a material, diffraction patterns and elemental distribution maps. TEM consists of a wide beam that covers a large sample area whereas STEM uses a focused beam that scans the sample surface.[217] Both (S)TEM utilise an electron beam to produce primary and secondary electrons that are detected. The high kinetic energy (80 – 300 kV) of the electron beam in (S)TEM enables electrons to penetrate through materials of < 200 nm. However, lower energy < 100 keV is used for light elements such as carbon to reduce damage. The thin samples and high kinetic energy allows for high lateral spatial resolution, limiting the spread of the probe and thus producing high resolution images.[218,219]

There are a range of imaging modes in (S)TEM such as, high resolution TEM (HRTEM) and high angle annular dark field (HAADF). HR-TEM occurs due to the use of a large aperture which allows for many diffracted beams to pass through. At high magnification, lattice fringes are visible in crystalline materials due to Bragg diffracting planes. HAADF imaging is formed by incoherently scattered electrons passing through the sample at high angles. The contrast of HAADF images depends on the atomic number of a sample due to the inelastically scattered electrons at high angles.[216,217]

In this work, two different TEM instruments were utilised. Samples were prepared by dry powder and liquid deposition onto holey carbon coated copper support grids and analysed using the FEI Talos 200x (conducted by Matthew Smith, University of Manchester) and the Titan HR-TEM imaging of the catalysts was performed using an FEI Talos F200X and scanning TEM was acquired using a probe abberation corrected FEI Titan G2 80-200 ChemiSTEM, with both microscopes operated at 200 kV. STEM elemental mapping was performed by EDX spectroscopy using a Super-X quad silicon drift detector (conducted by Dr. Matthew Lindley) at University of Manchester.

2.1.3 Energy Dispersive X-ray

SEM, TEM and STEM can be combined with energy dispersive X-ray (EDX) to show elemental composition and distribution of elements in a material. Specifically, a high energy primary electron ejects an electron from an inner shell.[216] A second electron subsequently moves from higher to lower energy state to fill the vacancy and emits an X-ray with specific energy. The X-ray is subsequently detected, producing a signal that is plotted as a spectrum which can be used to identify specific elements.[220]

2.2 X-Ray Techniques

2.2.1 X-Ray Diffraction

X-ray diffraction (XRD) is a method used to probe the crystallinity and phase of a material. It can also provide information such as crystalline size.[221]

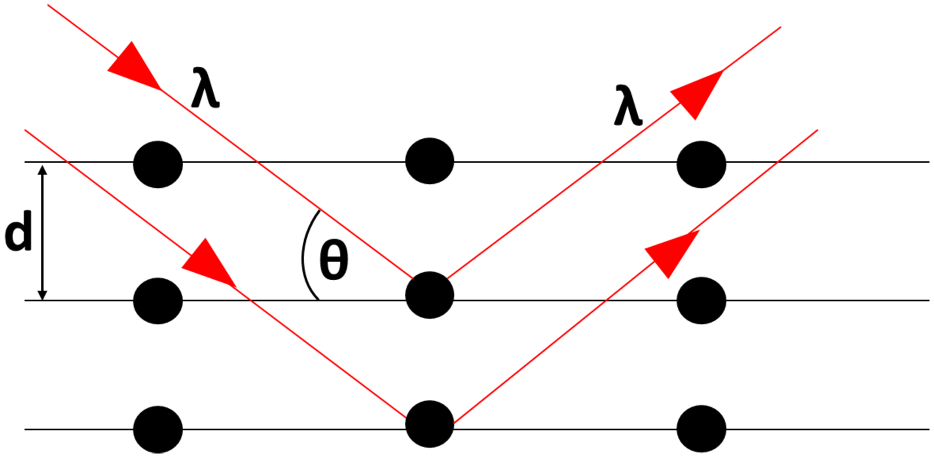

Figure 2.1: Schematic of Braggs Law, where d is the lattice plane spacing, θ is half of the diffraction angle, λ is the X-ray wavelength. The black circles correspond to an atom on parallel planes and the red lines show the direction of the x-ray at a specific wavelength.

When monochromatic in-phase X-rays are incident on a crystalline sample (Figure 2.1), they can be diffracted (undergo constructive interference) when conditions satisfy Bragg's Law (equation. 2.1). Specifically, this is dependent on the wavelength of the X-ray (λ), diffraction angle (θ) and the lattice spacing (d) in a crystalline sample. The sample can subsequently be identified by converting the diffraction peaks to d-spacings, and using a reference library to match the d-spacing to the sample pattern.[222] Crystallite size can be estimated by applying the Scherrer equation (equation. 2.2) to diffraction peaks.[221]

$$n\lambda = 2d \sin\theta \qquad \text{(equation. 2.1)}$$

$$D = \frac{K\lambda}{\beta\cos\theta} \qquad \text{(equation. 2.2)}$$

Where D is crystallite size, K is the Scherrer constant (0.9 for a spherical crystallite), λ is the x-ray wavelength, β is line broadening of diffracted peak at half the maximum intensity known as full width half max and θ is the diffraction angle.

This work utilised a PANalytical X'pert Powder X-ray diffractometer with a Cu Kα source (λ=1.54 Å) to identify the crystal structure of the synthesised nanopowders. The thin films crystal structure was analysed using Bruker D8 Advance with a Cu Kα radiation (λ= 1.54 Å). All diffraction peaks were recorded in the range 2θ = 20° – 60° and conducted by Dr. Gary Miller. The XRD peaks were identified using Inorganic Crystal Structure Database (ICSD) and Scherrer analysis was performed on highest intensity 2θ peaks to identify crystallite sizes.

2.2.2 X-Ray Photoelectron Spectroscopy

X-ray photoelectron spectroscopy (XPS) is a surface analysis technique that is used to determine elemental composition, chemical state and electronic state of elements in a material. This is achieved with typically MgKα radiation. The incident X-rays reacts with core electrons resulting in ionised states which emits photoelectrons once the minimum energy required to emit a photoelectron is reached.[223] These photoelectrons are detected and intensity plotted vs. binding energy (eV), the peaks are attributed to core-level electrons which preserved their original energy. Additionally, a high energy secondary electron fills the vacancy and emits enough energy to eject a tertiary electron from higher shell.[219] The tertiary electron is known as an Auger electron. The binding energies are calculated by measuring the kinetic energy of detected photoelectrons (equation. 2.3).[224]

$$\mathrm{E_B} = \mathrm{hv} - \mathrm{E_{Kin}} \qquad \text{(equation. 2.3)}$$

Where E_B is core level binding energy, *hv* is energy of incident photons and E_{kin} is kinetic energy of detected photoelectrons.

In this work, XPS data was collected using a Kratos Axis Supra system with a monochromated Al kα1 radiation (*hv* = 1486.6 eV). The survey spectra were collected with a pass energy of 160 eV and region scans with a pass energy of 40 eV. All spectra were shifted such that the C 1s was at 284.8 eV. The binding energies were confirmed using NIST database.[225] All XPS data was conducted by Dr. Gary Miller.

2.2.3 X-Ray Fluorescence

X-ray Fluorescence (XRF) is a fast and accurate method to determine elemental composition of materials. X-rays are applied to a sample from an x-ray source leading to an irradiated sample. Energy is released in the form of incident photons with sufficient energy to remove a core electron from an element.[226] During relaxation, the core hole at energy level E_0 is refilled by an electron from a higher energy shell with energy E_i. This process releases energy (equation. 2.4) in the form of a fluorescent photon (Figure 2.2).[227] The energy released from the photon is measured by a detector and analysed to provide the quantity of each element present in the sample.

$$Energy\ of\ photon = \mathrm{E_i} - \mathrm{E_0} \qquad \text{(equation. 2.4)}$$

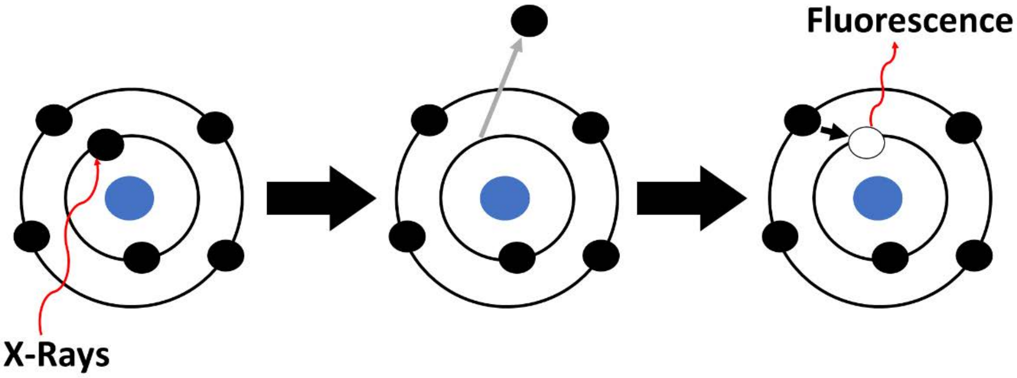

Figure 2.2: Formation of fluorescent x-rays, where the filled in circles correspond to nucleus (blue), electron (black) and electron vacancy (white).

The elemental composition of the synthesised materials was analysed using a Rigaku NEX-CG energy-dispersive X-ray fluorescence spectrometer. The samples were presented as loose powders. Due to the low yield of powder containing iridium, each powder was mixed with a backing material (Cerox, Fluxana) and analysed under vacuum (< 0.5Pa). The semi-quantitative results were calculated using the Rigaku Profile Fitting- Spectra Quant X (RPF-SQX).

2.3 Physical Techniques

2.3.1 Conductivity Measurements

Electrical properties of a material is an important consideration for electrocatalyst design. Electrical conductivity determines how electrons flow through a material. Resistivity is a value that describes how strong a material opposes flow of electrons.[228] It is directly proportional to resistance (equation. 2.5) and therefore we can determine the resistance of the material by using Ohm's law (equation. 2.6), and subsequently calculate the conductivity using (equation. 2.7).[229]

$$\sigma = \frac{1}{\rho} \qquad \text{(equation. 2.5)}$$

Where σ is the electrical conductivity and ρ is the resistivity.

$$R = \frac{V}{I} \qquad \text{(equation. 2.6)}$$

Where R is resistance, V is voltage and I is current.

$$\sigma = \frac{l}{AR} \qquad \text{(equation. 2.7)}$$

Where σ is the electrical conductivity, *l* is the sample thickness and *A* is geometric area.

The main two methods of measuring the resistivity of powders and thin films are two-point probe and four-point probe methodologies (Figure 2.3). The two-point probe method is a fast and easy method to determine resistivity in compressed powders. Typically, powders are placed between two electrodes and compressed. As the electrical resistance of a material depends on the particle contact, the powders must be measured under pressure to ensure the presence of sufficient electrical contact.[230] The electrodes are isolated from each other using polymer based films. Voltage is applied to the electrodes and produces a current which is used to determine resistance using (equation. 2.6).[231]

A four-point probe measurements reduces the effects of contact resistance between the electrode and material which increases resistance.[232] It is typically used for thin materials and assumes that the shape is rectangular.[228] The measurement consists of 4 electrical probes placed equidistance of each other.[233] A current is applied through first and last probe and a voltage is measured between probe 2 and 3 producing the resistance calculated using (equation. 2.8).[228,234]

$$\rho = \frac{Vwh}{I\ell'} \qquad \text{(equation. 2.8)}$$

Where, ρ is resistivity, V is voltage measured, w is width of material, h is height of material, I is the current and ℓ' is the distance between probe 2 and 3.

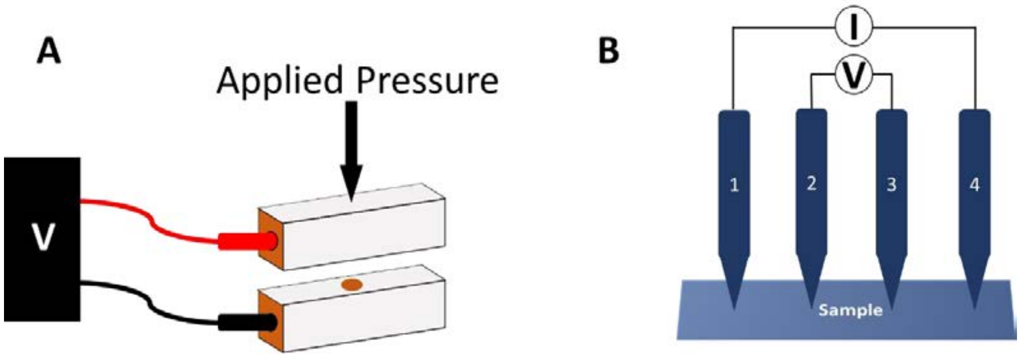

Figure 2.3: Schematic of a) 2-point and b) 4-point conductivity measurement, where V and I are voltage and current, respectively.

The conductivity of synthesised powders in this work was measured in a homemade 2-point probe setup similar to those previously reported in the literature.[150,229,230] Powder samples were compressed under constant pressure of 500 psi between two copper electrodes and isolated from each other using PTFE (Polyfon, thickness of 5 mm). The conductivity cell was connected to Metrohm, PGSTAT 204 potentiostat and an I-V curve was produced on Nova 2.1 software. The resistance and conductivity was determined using (equation. 2.6 and(equation. 2.7).

2.3.2 Brunauer-Emmett Teller Surface Area Analysis

Brunauer-Emmett-Teller (BET) is a model that can be used to determine the surface area of materials from adsorption isotherm data. Adsorption occurs when a gas (adsorbate) attaches to a solid surface (adsorbent). The gas (e.g. nitrogen) adsorption is measured at constant temperature as a function of pressure until saturation pressure is reached to collect adsorption isotherm data.[235,236] Prior to nitrogen adsorption isotherm measurements, samples are degassed to remove any adsorbed contaminants from the surface. This typically involves heating the sample under vacuum.[235] Adsorption can be physical or chemical.

The BET equation is valid in the range of relative pressures between 0.05 – 0.2. The number of molecules required to form a monolayer (monolayer capacity) is determined from the BET linear graph (equation. 2.9), from which the surface area (m^2/g) of the material can be calculated (equation. 2.10).

$$\frac{p}{V\left[\left(\frac{p_0}{p}\right)-1)\right]}=\frac{1}{V_\infty C}+\frac{C-1}{V_\infty C}\left(\frac{p}{p_0}\right) \qquad \text{(equation. 2.9)}$$

$$S = \frac{V_\infty \sigma N_A}{m V_o} \qquad \text{(equation. 2.10)}$$

Where, p_0/p is the relative pressure, V_∞ is the monolayer capacity, V is volume of gas adsorbed and C is BET constant, σ is the area occupied by a single adsorbate molecule on the surface (16.2 $Å^2$ for N_2), N_A is the Avagadro's number, V_o is the molar volume of the gas at standard temperature and pressure (22.414 cm^3) and m is the mass of the sample.

In this work, nitrogen adsorption isotherm measurements at −196 °C were conducted by Dr Lubomira Tosheva using a Micromeritics ASAP2020 instrument. The samples were degassed at 150 °C for 12 h prior to measurements. Surface areas were calculated using the BET equation.

2.4 Analytical Techniques

2.4.1 Inductively coupled plasma-mass spectrometry

Inductively coupled plasma – mass spectrometry (ICP-MS) is a multielement analysis technique widely used in the electrochemistry field to detect dissolved elements in electrolyte.[237] ICP-MS uses high temperature plasma to form positively charged ions. Liquid samples are introduced into the spray chamber via a nebuliser, which generates an aerosol. The aerosol travels through the sample injector of the plasma torch and undergoes desolvation, vaporisation, atomisation and ionisation as it travels through the different heating zones of the plasma.[238] The ion travels through a sampler and skimmer cone to reduce the heat of the ion before being transported to the ion optics which stops unwanted particulates from entering the mass analyser. The ions are separated by mass-to-charge ratio by the mass analysers and measured at the ion detector.[239]

In this work, the elemental dissolution was determined by analysing the concentration of dissolved elements in electrolytes using an Agilent 7900 ICP-MS system.

2.4.2 UV-VIS

UV-visible (UV-Vis) spectroscopy is a technique used to measure the light absorbed by a sample as a function of incident wavelength.[213] A monochromator is used to disperse the incident light into separate wavelength, which is then passed through the sample. When the light passes through the sample it can be absorbed, transmitted or reflected. The ratio of incident light (I_o) and transmitted light (I) is known as transmittance (T), typically given as a percentage (equation. 2.11). From transmittance, the absorbance can be defined (equation. 2.12). The absorbance can then be expressed using Beer-Lambert Law to obtain the concentration of a sample (equation. 2.13)

$$\%T = \frac{I}{I_o} \times 100 \qquad \text{(equation. 2.11)}$$

$$A = -logT \qquad \text{(equation. 2.12)}$$

$$A = \varepsilon cl \qquad \text{(equation. 2.13)}$$

In this work, UV-Vis was performed to quantify the production of H_2O_2 during electrochemical measurements using a UV-2600, Shimadzu.

2.5 Electrochemical Techniques

To probe the electrochemical performance of a material, a potentiostat is used to accurately measure potential, charge and current. For powdered samples, the evaluation of electrochemical reaction can be carried out by using a rotating disk electrode (RDE).[240] A typical set-up of the RDE utilises a 3-electrode configuration (Figure 2.4) consisting of working electrode (WE), counter electrode (CE) and reference electrode (RE).

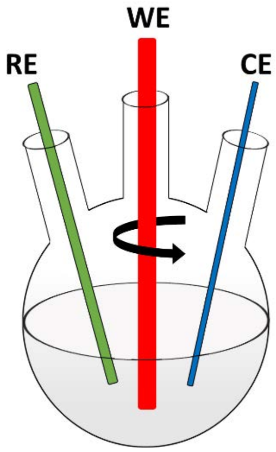

Figure 2.4: Schematic of 3-electrode electrochemical cell set-up.

Catalyst inks are composed of catalysts dispersed in solvents to probe the electrocatalytic activity of materials, for powder samples the ink is deposited onto an RDE. For thin films, the catalyst is deposited onto a conductive substrate that is not rotated. Nafion is added to the catalyst ink to act as a binder, improve catalyst dispersion and uniformity during rotation.[241] The ionomer to catalyst ratio is optimised to improve electrocatalysis performance.[242] The catalyst of interest is investigated at the WE by drop-casting the catalyst ink onto an inert and chemically stable and conductive material such as gold or glassy carbon.[243] Platinum or graphite is typically used as the CE, in this work a graphite rod is used as CE. The RE by definition has a fixed reversible potential that remains unchanged during the electrochemical experimental, which enables for accurate determination of the potential at the WE.[244] The measured potentials vs. reference during electrochemical testing are converted to the reversible hydrogen electrode (RHE) according to Nernst equation (equation. 2.14).

$$E_{RHE} = E_{WE} + E_{REF} + 0.059\,pH \qquad \text{(equation. 2.14)}$$

Where E_{RHE} is potential vs. RHE, E_{WE} is the measured potential of the WE against specified reference and E_{REF} is the standard potential of the reference electrode.

Electrochemical reactions occur in an electrolyte which provides a path for ions to flow between the electrodes (WE and CE) to balance the charge.[245] The concentration of the electrolyte influences the resistivity of the cell (ability for the current to flow between electrodes) in a 3-electrode configuration. Therefore, the concentration of the electrolyte must be carefully selected to provide sufficient ionic conductivity to the cell.[246] The RDE allows for a constant flux of bulk electrolyte to be present at the electrode. In this work, 0.05M H_2SO_4, 0.1M $HClO_4$ and 2M $KHCO_3$ are used as electrolytes. Sulfonate groups are similar to the Nafion membrane in PEM-WEs however, they are known to poison the surface of some Ir-based catalysts during half-cell reactions due to the strong adsorption of SO_4^- ions to catalyst surface.[247,248] Hence, the use of $HClO_4$ due to its' weak adsorption on the catalyst surface. However, $HClO_4$ is a stronger acid than H_2SO_4 and as such chapters 4 and 5 utilised H_2SO_4 due to weak catalyst stability. The use of different electrolyte can lead to altered performance due to changes in the adsorption energy leading to lower adsorption energies as seen for $HClO_4^-$ and thus higher OER activity.[249] A variety of electrochemical characterisation techniques can be performed using this electrochemical set-up which are discussed further in this section.

2.5.1 Voltammetry

Voltammetry is the evaluation of the current passed through an electrode as a function of the potential difference applied to the WE. This can be studied through techniques such as linear sweep (LSV) and cyclic voltammetry (CV).[236] Both LSV and CV are considered potential sweep techniques as the current is measured while the potential applied is changed over time.[246] For OER, potentials are typically swept from starting potential of 1.2 V_{RHE} (E_i) to final potential of 1.8 V_{RHE} (E_f) at a defined scan rate. In LSV, the potential is swept from E_i to E_f. For CV, the potential is reversed back to E_i once it reaches E_f (E_i to E_f to E_i). Multiple cycles (CVs) and LSVs can be conducted to observe the change in current as a function of potential.

When conducting CVs in an unstirred solution without a catalyst on the electrode, diffusion-controlled electron transfer is observed and a “duck-shaped” voltammogram is formed (Figure 2.5).[246] When undertaking a sweep in the positive direction (1.2 V_{RHE} to 2 V_{RHE}), the electrolyte is oxidised at the electrode surface, producing an oxidation peak. However, a reverse sweep (2 V_{RHE} to 1.2 V_{RHE}) leads to a reduction of the electrolyte and hence a reductive peak is displayed.[245] Conversely, a CV conducted in a stirred electrolyte such as using RDE, results in a decrease of the reduction peak due to increased mass transport.

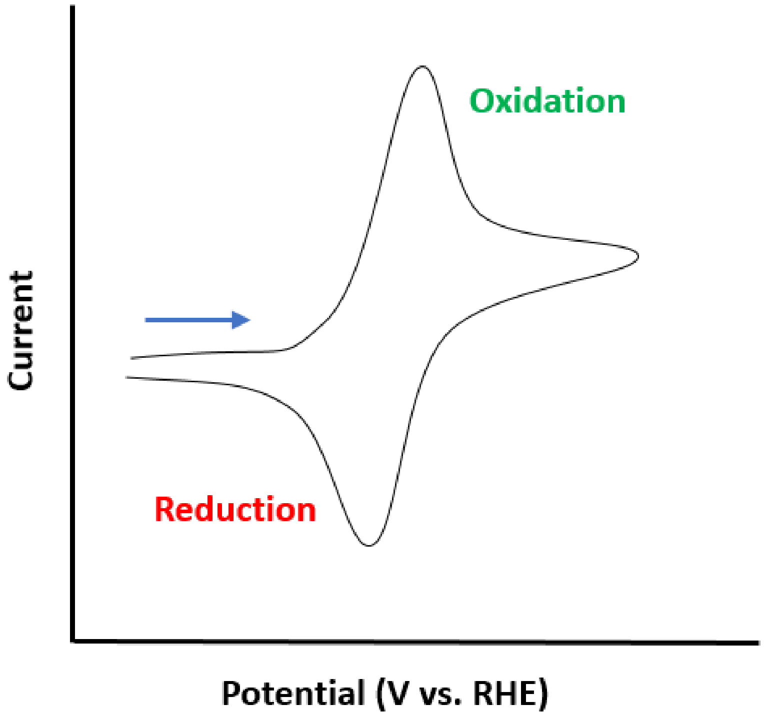

Figure 2.5: Cyclic voltammogram in an unstirred environment (diffusion-controlled) with an arrow indicating the potential sweep direction adapted from ref. [250].

To compare the electrochemical performance between catalysts in this work, the currents (I) were normalised to either the geometric surface area or catalyst (or precious metal) mass loading. The geometric activity normalises the current produced during voltammetry by the surface area of the working electrode to obtain current density (I_d, mA/cm^2) as shown in (equation. 2.15). When the catalytic current is normalised to the mass of catalyst (or Ir), we obtain mass activities (I_m, A/g$_{Ir}$). By normalising to the geometric surface area of the working electrode (0.196 cm^2 for a 5 mm diameter RDE) and the mass of Ir (determined by XRF or SEM), the Ir-mass activity can be calculated as shown in (equation. 2.16).

$$I_d = \mathrm{I} \div \text{surface area of WE} \qquad \text{(equation. 2.15)}$$

$$I_m = \frac{I_d \times surface\ area\ of\ WE}{mass\ of\ Ir} \qquad \text{(equation. 2.16)}$$

2.5.2 Chronoamperometry and Chronopotentiometry

Chronoamperometry (CA) and chronopotentiometry (CP) are electrochemical techniques that can be used to evaluate the stability of a material over time in electrocatalysis.[251] Prior to running CA and CP, a CV/LSV is typically generated to select the current/potential to analyse the stability of the electrocatalyst. During CA, a constant potential is applied to the WE and a current is measured as a function of time.[252] On the other hand, during CP a constant current is maintained at the WE and the potential is measured as a function of time.[251] Using these techniques we can evaluate the stability of the material by observing the rate at which the current (or potential) maintains the set potential (or current) over time.

2.5.3 Electrochemical Impedance Spectroscopy

Electrochemical impedance spectroscopy (EIS) investigates the material properties that influences mass-transfer, charge-transfer and diffusion processes in an electrochemical system.[250,253] EIS uses alternating current (AC) to generate an electrochemical reaction on the working electrode. A small amplitude sinusoidal AC voltage is applied to the working electrode and the impedance is measured as a function of frequency.[250] An impedance spectrum is generated when sweeping frequencies from mHz to MHz producing two types of plots (Figure 2.6). Nyquist plot is represented by plotting imaginary complex, *Z"* over the real complex *Z'* at different frequencies. At high frequencies the intercept at the x-axis provides the electrolyte resistance and at low frequencies the x-axis intercept provides the charge-transfer, electrolyte and resistance from other aspects of the electrochemical system.[254] In order to deconvolute the contribution from each component of the system, one has to fit the data to an equivalent circuit. This can be an extremely complex exercise in a multi-phase, multi-interface system such as a water electrolyser generating oxygen and hydrogen gases.

Similar information is also found using Bode plot, which is represented by absolute impedance vs. log frequency or phase shift φ versus the logarithmic frequency, it is typically used to investigate the capacitance in a system.[253] Both Nyquist and Bode plot provides the same information however Bode plot depicts the frequency unlike the Nyquist plot.[254]

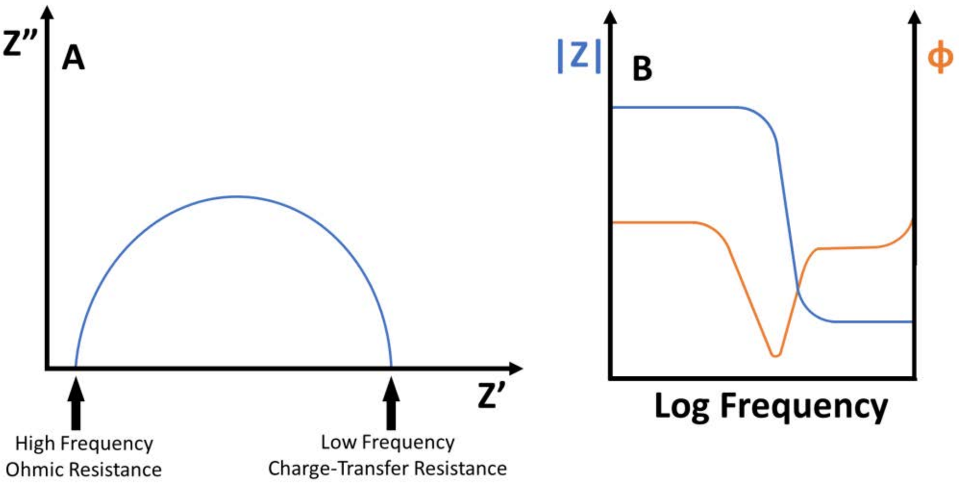

Figure 2.6: Representation of EIS spectrums a) Nyquist b) Bode plot

Using Nyquist plot, we can correct the voltage loss caused by ohmic resistance to obtain voltage associated with electrochemical activities of the working electrode (equation. 2.17).[255]

$$E_{iR} = E_{RHE} - \left(\left(\frac{I}{1000}\right) \times iR\right) \qquad \text{(equation. 2.17)}$$

Where E_{iR} is the iR corrected potential, E_{RHE} is the measured potential vs. RHE, I is the current in mA and iR is the ohmic resistance in ohm determined from Nyqiust plot.

In this work, half-cell electrochemical measurements were conducted with a rotating disk electrode (RDE, Pine Research) and VSP-3e potentiostat from

BioLogic Science Instruments. All measured potentials in this work are converted to RHE potential. The catalyst coated membrane was implemented into a single cell electrolyser. The testing was conducted with the VSP-3e potentiostat and a 20 A booster (VMP3B-20, BioLogic Science Instruments).

2.5.4 Tafel Analysis

During electrochemical reactions, current is measured as a function of applied potential. Many electrochemical reactions involve multiple mechanistic steps and inevitably, one of these steps is rate limiting. To evaluate the relationship between the activity and the reaction mechanism, the current of a redox reaction at a specific overpotential is analysed.[246] The current produced is determined in a non-Faradaic region where there are no mass transfer limitations and is known as Tafel analysis. Tafel analysis provides insight into the electrode kinetics and reaction mechanism. By determining the exchange current density, transfer coefficient, Tafel constant and Tafel slope we can relate activity to kinetics of the reaction. The Tafel slope is the main information that is used when doing Tafel analysis.[256] Tafel slope aids to determine the rate determining step of a mechanism and the kinetics of the reaction.[257] From the Butler-Volmer equation (equation. 2.18), we can derive the Tafel equation (equation. 2.19).

$$j = j_0 \left\{ \exp\,(-\alpha \left(\frac{nF}{RT}\right) \eta - \exp\,(1 - \alpha(\frac{nF}{RT})\eta \right\} \qquad \text{(equation. 2.18)}$$

$$\eta = \frac{RT}{\alpha F} ln j_0 - \frac{RT}{\alpha F} \log j \qquad \text{(equation. 2.19)}$$

Where j is the current, j_0 is the exchange current density, α is the transfer coefficient, n is the number of electrons transferred, η is the overpotential, F, R and T are Faraday's constant, gas constant and temperature, respectively.

The Tafel equation can be simplified to (equation. 2.20) at high overpotentials (> 100 mV), where *a* relates to the first term in (equation. 2.19) and *b* relates to the second term in (equation. 2.19) also known as the Tafel slope. Therefore, by plotting the overpotential v. log j, we can determine the Tafel slope from the gradient of the line.[258]

$$\eta = a + b \log j \qquad \text{(equation. 2.20)}$$

2.5.5 Activity-Stability Metrics

Recent work has focused on investigating the relationship between activity and stability of Ir-based catalysts for the OER. [46,67] The two metrics used to correlate this relationship is the activity-stability factor (ASF) and the stability number (S-number). ASF is defined as the ratio between rate of oxygen production at a specified overpotential and the rate of metal dissolution of the material during OER (equation. 2.21). The materials that are best for OER will produce high amount of oxygen with minimal dissolution of the metal to produce a high ASF value.[65]

$$ASF = \frac{\mathrm{j} - S}{S} \qquad \text{(equation. 2.21)}$$

Where, j is current density and S is the rate of dissolution.

Conversely S-number relates the ratio of moles of oxygen evolved against moles of metal dissolved in the electrolyte solution. It is independent of active sites, surface area and catalyst loading and thus can be used as a metric to compare the stability of a range of catalysts. The higher the S-number the more stable the material.[46] The S-number can also be used to determine the lifetime of a catalyst (equation. 2.22).

$$t = \frac{S \times z \times F \times m}{j \times M} \qquad \text{(equation. 2.22)}$$

Where, S is the stability number, z is the number of electrons per evolved O_2, F is Faraday's constant, m is mass of metal, j is the applied current density and M is the molar mass of the metal.

2.5.6 Accelerated Stress Tests

In proton exchange membrane water electrolysers (PEM-WEs), the catalyst is deployed within the membrane electrode assembly (MEA) which consists of the catalyst layer, gas diffusion layer and porous transport layer. Each of these components must withstand long-term operation to be viable as an energy storage technology.

Accelerated stress tests (ASTs) are conducted to understand the lifetime of single cell electrolyser. The principle of ASTs is to apply stressors and observe the performance loss over time to determine the durability of the cell or a desired component. There are multiple AST methods (i.e. triangle wave, square wave, sawtooth and hold) that are used to determine the stability of a catalyst.[259,260]

ASTs involve either potential/current cycling, hold or a combination of cycling/holding. These tests focus on understanding the degradation of catalysts and components under dynamic operating conditions.[261]

2.5.7 Polarisation Curves

PEM-WEs are electrochemically characterised by measuring a polarisation curve. Polarisation curve consists of a plot of cell voltage against current density (Figure 2.7). A polarisation curve has three regions, activation, ohmic and concentration.[262] The activation region is attributed to the rate of reaction at the electrode surface. The second region represents the ohmic losses and is influenced by the resistance of the cell. The concentration region is influenced by the transfer of reactants to the electrode surface and is therefore limited by mass-transport. Each of these regions is affected by the cells' operating conditions (eg,. membrane thickness, temperature etc.). A high performing electrolyser will exhibit low voltage at high current densities.[263]

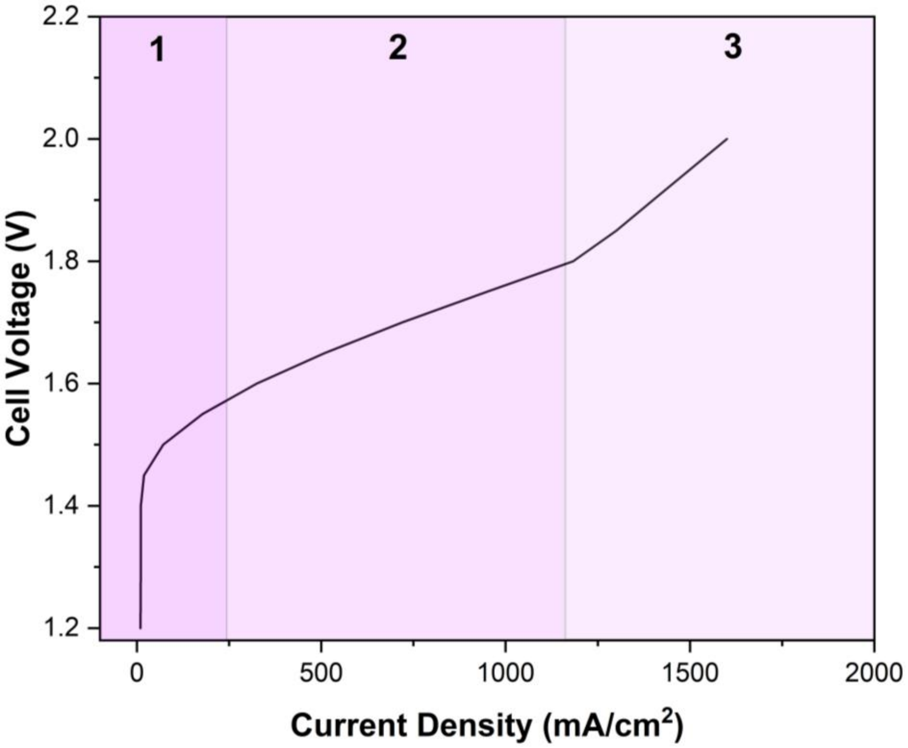

Figure 2.7: Graphical representation of a polarisation curve for PEM-WE highlighting three regions: 1) activation, 2) ohmic and 3) concentration region.

3 Hollow AuPd modified TiO_2 supports to achieve low Ir loading in water electrolyser anodes

The following chapter is a submitted manuscript written in collaboration with Matthew Lindley, Umesh S. Jonnalagadda, Annie Mae Goncalves Bullock, Qianwenhao Fan, Wen Liu, Sarah J. Haigh, James Kwan, Yagya N. Regmi and Laurie A. King.

3.1 Introduction

There have been many efforts focused on reducing Ir loading without compromising electrochemical activity and stability as shown in chapter 1.8. In this study, we investigate a new catalyst-support morphology, deploying a hollow TiO_2 support coated with alloyed AuPd nanoparticles (AuPd-TiO_2). We evaluate the effects of AuPd nanoparticles loading (1 wt% and 5 wt%), Ir loading (25 wt% and 50 wt%) and annealing environment (reducing and oxidised) to decipher how these factors correlate with catalyst conductivity and OER activity. The electrochemical performance is assessed in both RDE half-cell setup and in a membrane electrode assembly (MEA) enabling comparisons between these two distinct electrochemical testing configurations.

3.2 Experimental Section

3.2.1 Synthesis of hollow TiO2 and AuPd-TiO2

The synthesis of hollow TiO_2 and AuPd-TiO_2 nanostructures has been previously reported elsewhere.[264] In brief, the TiO_2 nanostructured supports were synthesised by a sol-gel templating method, whereby polystyrene beads were coated with TiOH gel and calcined at 500 °C. The TiO_2 supports were subsequently decorated with AuPd alloy nanoparticles (Au/Pd w/w = 5:1). To integrate AuPd alloy nanoparticles, Au nanoparticles were initially synthesised by reducing $HAuCl_4 \cdot 3H_2O$[265] followed by alloying with Pd via a modified seed-mediated process.[266] The AuPd nanoparticles were then added dropwise to a dispersion of the previously synthesised TiO_2 while stirring at room temperature. After 2 hours, the powder was recovered by centrifugation and dried at 70 °C overnight. Two different nanoparticle loadings were prepared, which we label "WH1" and "WH5". The AuPd loading was determined for each sample via ICP-OES with WH1 the lower loading of 1.17wt% Au and 0.26 wt% Pd and WH5 having the higher loading of 5.54 wt% Au and 1.08 wt% Pd.

3.2.2 Synthesis of Ir-WH1 and Ir-WH5

The deposition of iridium (Ir) onto the nanostructured TiO_2 and AuPd-TiO_2 supports (WH1 and WH5) was performed by a process adapted from a previously published incipient wetness impregnation synthesis.[142] In brief, 134 mg of dihydrogen hexachloroiridate (IV) hydrate ($H_2IrCl_6.6H_2O$, 40% Ir, Acros Organics) was mixed with 20 µL deionised H_2O (18.2 MΩ, Milli-Q) and 40 µL acetic acid (99.7%, Fisher Scientific). Separately, each support (hollow TiO_2, WH1 and WH5) was dispersed in 20 mL of ethanol to obtain a homogenous solution. The mass of the support was varied to enable control of Ir loading (25 wt% and 50 wt%). The prepared Ir and support dispersion were subsequently combined, bath sonicated for 10 mins, then stirred at 80 – 100 °C until dry.

Each dried supported catalyst powder was collected and finely ground using a pestle and mortar. Each powder was placed into a tube furnace, ramped to 500 °C at 10 °C/min and held for 2 hours at temperature under a reducing atmosphere (5 % H_2 and 95% N_2) at 50 sccm. The furnace was then allowed to cool to room temperature and a controlled passivation was conducted by flowing O_2 (50 sccm) for 20 secs. The resulting powders were then finely ground again. Each of the 50 wt% Ir supported catalysts were split into two batches and one half was subsequently annealed further in a box furnace (500 °C at 10 °C/min under atmospheric conditions for 30 minutes), cooled to room temperature and ground again using a pestle and mortar. The other half of these samples, which had only been annealed under a reducing atmosphere were tested as prepared.

3.2.3 Physical Characterisation

The crystal structure of the catalyst-supports was examined by XRD using PANalytical X'pert powder X-ray diffractometer with a Cu Kα source (λ=1.5406 Å). Diffraction peaks were recorded in the range 2θ = 20° – 60° with a step size of 0.013°, a measurement time of 89 seconds per step and a sample rotation rate of 60 rpm. The reference patterns were identified using the Inorganic Crystal Structure Database (ICSD) and Scherrer analysis was performed on the 2θ peaks at 25.0° and 40.8° for Ir and Ti, respectively. XPS was performed using a Kratos Axis Supra system with a monochromated Al $K\alpha_1$ radiation ($h\nu$ = 1486.6 eV). The survey spectra are collected with a pass energy of 160 eV and region scans with a pass energy of 40 eV. All spectra were energy shifted to align to the C 1s peak at 284.8 eV. The morphologies of the supports were determined on a Zeiss Supra

40VP scanning electron microscopy (SEM) with EDAX 40VP energy dispersive X-ray (EDX) analyser. High resolution transmission electron microscopy (HRTEM) imaging of the catalysts was performed using an FEI Talos F200X and scanning TEM (STEM) was acquired using a probe 69 aberration corrected FEI Titan G2 80-200 ChemiSTEM, with both microscopes operated at 200 kV. Particle sizes were determined using high-angle annular dark field (HAADF) STEM imaging, collected using 110 pA beam current, 21 mrad convergence angle, and a 48 mrad HAADF inner collection angle. STEM elemental mapping was performed by EDX spectroscopy using a Super-X quad silicon drift detector with a total collection angle of 0.7 sr. TEM samples were prepared by dry powder deposition onto holey carbon support films on 400 mesh Cu grids (Agar Scientific). The statistical analysis of Au and Ti particle sizes were determined using GraphPad Prism version 9.5.1 for Windows (GraphPad Software, San Diego, California USA). The statistical normally distributed data were compared with an unpaired t-test and non-normally distributed data were compared with Mann-Whitney U tests. The categorical frequency data were compared using the chi-squared test with post hoc Fisher's exact testing and results were deemed significant if $p < 0.05$. The elemental dissolution of the catalyst-supports was determined by analysing aliquots of electrolyte taken post electrochemical testing using inductively coupled plasma mass spectrometry (ICP-MS, Agilent 7900). The metal loading of the supports was determined by inductively coupled plasma optical emission spectrometry (ICP-OES, Agilent 5800), where 10 mg of AuPd-TiO_2 was digested in 10 mL of aqua regia, filtered and diluted to 50 mL.

3.2.4 Conductivity Measurements

The conductivities of the catalyst powders were measured in a 2-electrode conductivity cell developed in house, analogous to those previously reported in the literature.[150,229,230] In brief, two copper electrodes were wrapped in a hole punched PTFE (Polyfon, thickness of 5 mm) to isolate the two electrodes. The PTFE hole acted as a sample holder for powder samples. The powder samples were then compressed between the electrodes under constant pressure at 500 psi. The conductivity cell was connected to a potentiostat (Metrohm, PGSTAT 204) to generate I-V curves using linear sweep voltammetry (LSV) from -0.4 to 0.4 V, to determine the electrical resistance. The electrical conductivity was calculated using (equation. 3.1),[229] where σ is the electrical conductivity, l is the thickness of the PTFE (and the powder), *A* is the geometric area of the copper electrode and R is the electrical resistance.

$$\sigma = \frac{l}{AR} \qquad \text{(equation. 3.1)}$$

3.2.5 Half-Cell Electrochemical Characterisation

Half-cell electrochemical measurements were conducted on a RDE (Pine Research) and VSP-3e potentiostat from BioLogic Science Instruments in a three-electrode configuration. A 0.1 M $HClO_4$ electrolyte (pH 1.1), a gold disk working electrode (0.196 cm^2), graphite rod counter electrode and $Hg/HgSO_4$ reference electrode (OrigaSens, Alvatek) were used throughout. The synthesised supported catalysts were compared against commercial iridium (IV) oxide (IrO_2, Premion 99.99%, Alfa Aesar). All potentials were adjusted to the reversible hydrogen electrode (RHE) as detailed in Section 2.5.

Catalysts were deposited onto the gold disk working electrode using a previously reported modified method.[169,267] The catalyst inks were prepared by dispersing 2 mg of catalyst powder in 120 µL deionised water (18.2 MΩ, Milli-Q), 360 µL 1-propanol (NPA, 99%, Fisher Scientific) and 20 µL Nafion™ (5 wt%, Alfa Aesar). Inks were bath sonicated (FB15048, Fisherbrand) for 30 min prior to electrochemical testing followed by immediately drop casting onto the RDE Au disk at 200 rpm. The disk was subsequently rotated at 700 rpm for at least 30 minutes until dry. The theoretical Ir loading of each catalyst was 25.5 $\mu g_{Ir}/cm^2$. Each synthesised catalyst ink was deposited and tested 3 times. Between each deposition, the electrode was polished with 0.05 µm alumina slurry, rinsed and sonicated for 30 seconds in deionised water.

Prior to electrochemical OER testing, potentiostatic electrochemical impedance spectroscopy (PEIS) measurements with 85 % correction were conducted at 1.1 V_{RHE} (100 mHz to 200 kHz) and used to iR correct the reported potentials. The catalyst deposited working electrode was conditioned using cyclic voltammetry (CV) between 0.025 – 1.0 V_{RHE} for 50 cycles at 200 mV/s. The OER activity was subsequently assessed at 2500 rpm using CV by sweeping the potential between 1.0 – 1.8 V_{RHE} at 10 mV/s for 10 cycles. We used the performance of 10th CV cycle for analysis unless otherwise stated. To examine the stability in an RDE configuration, a CV was measured from 1.0 – 1.8 V_{RHE} for 30 cycles at 10 mV/s and 2500 rpm.

3.2.6 Membrane Electrode Assembly

Catalyst inks were prepared following a method described elsewhere.[268] Briefly, commercial 50 wt% Pt/C, deionised water, NPA and Nafion™ were mixed and bath sonicated for 30 minutes. The supported catalyst ink for the anode was mixed with deionised water, NPA and Nafion™ and horn sonicated (505, Fisherbrand) for 30 minutes. The vial was covered with parafilm and housed in an ice bath throughout sonication.

The catalyst coated membranes (CCMs) were prepared by drop casting the catalyst inks onto PTFE films on a vacuum hot plate at 53 °C and left to dry. Decal transfer was achieved by sandwiching the Nafion membrane (N212, Chemours) between the catalyst deposited PTFE films using a hot press under 1 metric ton pressure at 130 °C for 3 minutes.[269] The catalyst loading is determined via gravimetric measurements of the PTFE before and after the decal transfer. The anode catalyst loading ranged between 1.58 – 1.62 mg_{Cat}/cm^2 and cathode catalyst loading was 0.7 – 0.84 mg_{Cat}/cm^2.

The CCMs were integrated into a single cell electrolyser with Pt-plated single serpentine 5 cm^2 titanium flow field on the anode, single serpentine 5 cm^2 graphite flow field on the cathode, water feed at 120 mL/min on the anode and N_2 (100% RH) at 50 sccm at the cathode. Platinised sintered titanium porous transport layers (PTLs) from Mott corporation USA were used on the anode and carbon cloth gas diffusion layers (GDLs) with mesoporous layer (MPL) from FuelCellStore on the cathode. The cell was equilibrated at 60 °C for an hour prior to collecting polarisation curves using a BioLogic potentiostat (VSP-3e) with a 20 A booster (VMP3B-20). PEM-EL polarisation curves were generated via chronoamperometry (CA) steps collected for 3 minutes at increments of 0.05 V from 1.2 – 2.0 V. For each voltage step, the average current density of the last 30 s was used for the polarisation curve. For the saw-tooth voltage cycling accelerated stress tests (ASTs), 10k CVs were collected at 50 mV/s between 1.20 and 2.00 V. Polarisation curves were collected after each 1k cycles to assess performance degradation due to AST CVs. The concentration of dissolved Ir from the supported catalysts post-AST were evaluated by conducting inductively coupled plasma mass spectrometry (ICP-MS) on a 5 mL aliquot of the anode water outlet at the end of the ASTs.

3.3 Results and Discussions

3.3.1 Electrochemical Half-Cell Performance

In this study, nanostructured hollow TiO_2 catalyst supports were utilised as catalyst supports. The prepared nanostructures consisted of Ir deposited by wet impregnation using chloroiridic acid as the Ir precursor. The AuPd-TiO_2 supports (WH1 and WH5) and TiO_2 supports (without AuPd) were subsequently added to the Ir solution to form the supported catalysts. The catalyst powders were subjected to either: (1) a thermal reduction (5% H_2/95% N_2) (TiO_2-H_2, WH1-H_2 and WH5-H_2) or (2) a thermal reduction (5% H_2/95% N_2) followed by annealing in air (TiO_2-Air, WH1-Air and WH5-Air). For each catalyst prepared, two different Ir loadings (25 wt% and 50 wt%) were prepared. The samples are labelled as follows, “Ir wt%-catalyst support-annealing environment” as summarised in Table 3.1 alongside key synthetic details.

Table 3.1: Summary of supported catalysts prepared including sample names and brief synthetic details.

Sample Name	Ir wt%	Support	Annealing Environment	Annealing Programme
50-TiO_2- H_2	50	open nanoshell TiO_2	5% H_2 / 95% N_2	500 °C, 2 hours, 10 °C/min
50-WH1- H_2	50	1.1% Au/ 0.3% Pd- TiO_2	5% H_2 / 95% N_2	
50-WH5- H_2	50	5.5% Au/ 1.2% Pd- TiO_2	5% H_2 / 95% N_2	
25-WH1- H_2	25	1.1% Au/ 0.3% Pd- TiO_2	5% H_2 / 95% N_2	
25-WH5- H_2	25	5.5% Au/ 1.2% Pd- TiO_2	5% H_2 / 95% N_2	
50-TiO_2- Air	50	TiO_2	5% H_2 / 95% N_2 Air	500 °C, 2 hours, 10 °C /min 500 °C , 0.5 hours, 10 °C /min
50-WH1- Air	50	1.1% Au/ 0.3% Pd- TiO_2	5% H_2 / 95% N_2 Air	
50-WH5- Air	50	5.5% Au/ 1.2% Pd- TiO_2	5% H_2 / 95% N_2 Air	

The activity of the prepared catalyst-supports were initially assessed using a three-electrode RDE in acidic electrolyte (0.1 M $HClO_4$). Firstly, the supported catalysts were conditioned by cycling between 0.025 – 1.0 V_{RHE} at 200 mV/s for 50 cycles and subsequently by performing 10 CVs between 1.0 – 1.8 V_{RHE} at 10 mV/s (Figure 3.1). For the thermally reduced supported catalysts with 25 and 50 wt% Ir, we observed an increase in activity during the first 10 CVs, irrespective of the AuPd loading (Figure 3.1a). It is interesting to highlight that the thermally oxidised supported catalyst 50-WH5-air showed minimal changes in activity during the first 10 CVs (Figure 3.1b). Conversely, thermally oxidised supported catalysts 50-WH1-air and 50-TiO_2-air showed a deactivation of catalyst activity after 10 CV cycles. Similar dynamic behaviour of activation as a function of CV cycling has been observed in previously reported Ir-based OER catalysts, and has been attributed to the electrochemical growth of a hydrous Ir which can form during potential cycling.[270,174]

When catalysts are compared on a geometric current density basis, it is clear that the supported catalysts containing AuPd nanoparticles (WH1 and WH5) exhibited vastly superior OER performance over bare TiO_2 (Figure 3.1c). In addition to the presence of AuPd, thermal annealing conditions and iridium loading also had significant impacts on OER activities. Specifically, the average geometric current density at 1.65 V_{RHE} for 50 wt% Ir loaded supported catalysts annealed in H_2 is 21.22 mA/cm^2. When the same material is subsequently annealed in air, the current density is reduced to 0.47 mA/cm^2 (Figure 3.1c). This is in agreement with previous literature whereby the annealing environment (air) led to decreased activities.[155] Two distinct Ir loadings were synthesised and annealed under a reducing environment: 25 wt% and 50 wt% for both WH1 and WH5 supports. The average geometric area normalised current densities at 1.65 V_{RHE} for 25 wt% Ir are 1.35 mA/cm^2 and 21.22 mA/cm^2 for 50 wt% Ir, respectively (Figure 3.1c).

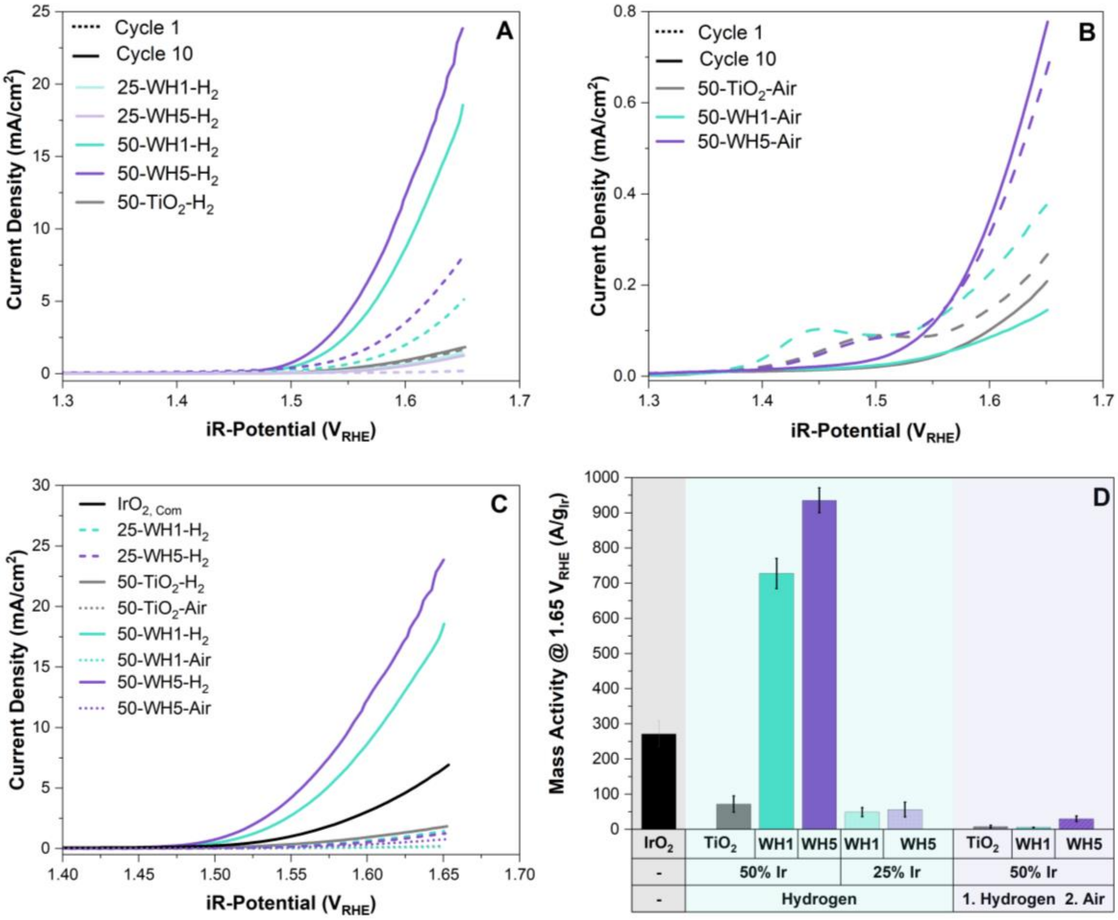

Figure 3.1: Comparison of cycle 1 and cycle 10 for supported catalysts a) thermally reduced, b) thermally oxidised, c) geometric area normalised OER activities of supported Ir catalysts and d) OER activities normalised to the mass of Ir. All experiments were conducted at least in triplicates to generate error bars. The electrolyte was 0.1 M $HClO_4$ electrolyte. Activities are reported for the 10th CV cycle with a theoretical Ir loading of 25.5 $\mu g_{Ir}/cm^2$ and compared against unsupported commercial rutile IrO_2 sample.

To assess Ir utilisation, mass activities (A/g_{Ir}) were calculated (Figure 3.1d) using the theoretical Ir loading. Overall, catalysts with 50 wt% Ir have much higher mass activities than 25 wt%. For example, 50-WH5-H_2 has a mass activity of 936 A/g_{Ir} compared to 25-WH5-H_2 with 49 A/g_{Ir} at 1.65 V_{RHE}. To evaluate the role of AuPd loading as a conductive additive to the support structure, two different AuPd loadings 1.1 Au: 0.3 Pd and 5.5 Au:1.2 Pd (WH1 and WH5, respectively) with 50 wt% Ir were compared at 1.65 V_{RHE}. We observed that 50-WH5-H_2 achieved a higher mass activity (936 A/g_{Ir}) than 50-WH1-H_2 (728 A/g_{Ir}). By comparing these mass activities to 50-TiO_2-H_2 (72 A/g_{Ir} at 1.65 V_{RHE}) we highlight that the AuPd significantly enhanced the electrochemical performance of our catalysts. When the prepared supported catalysts are benchmarked against unsupported commercial IrO_2, we observed higher mass activities for 50-WH1-H_2 and 50-

WH5-H_2 compared to commercial IrO_2 (Figure 3.1d). Furthermore, our highest performing OER catalysts demonstrated comparable mass activities to previously reported Ir-based catalysts prepared on TiO_2-based supports when assessed in an RDE (Figure 3.2a,b). The raw data values for Figure 3.2 are shown in the appendix (Figure A.1).

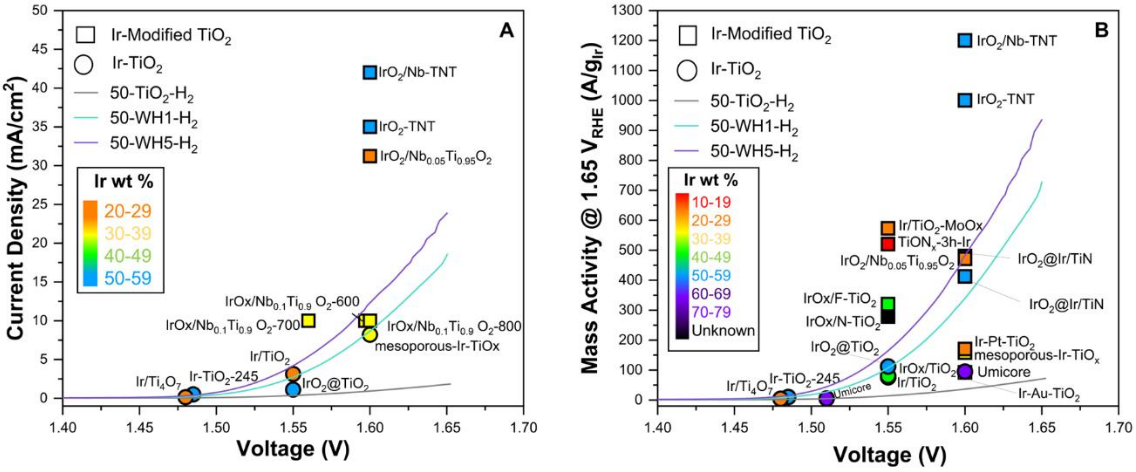

Figure 3.2: Comparison of various literature Ir catalysts supported on or integrated into titanium containing metal oxide supports where a) geometric activity[142,148,166,169,271–279] and b) mass activity[142,148,166,169,271,272,274–280] for the OER in acidic electrolyte. The circular symbols indicate Ir-TiO_2 catalysts only, whereas the square symbols represent Ir-Modified TiO_2 (e.g. the addition of either metal or non-metal elements to the TiO_2 support). The different colours detail the Ir wt%.

To assess the kinetics of the synthesised catalyst-support, Tafel analysis was performed (Figure 3.3). For each of the catalysts prepared, two distinct Tafel regions were observed corresponding to two distinct regions of the CV: low (< 300 mV) and high overpotentials (> 300 mV). This has previously been attributed to the presence of different active sites, or changes to the catalyst surface (reorganisation) at different applied potentials.[256,169] The Tafel slopes can also differ due to the OER mechanism that is being undertaken. The LOEM mechanism can lead to higher Tafel slopes due to the reorganisation of the lattice and multi-electron transfer processes with Tafel slopes exceeding 100 mV/decade.[281] Conversely, the AEM results in lower Tafel slopes (< 120 mV/decade) depending on the surface reaction and rate determining steps (eg. OH to OOH formation). Based on this information, it is probable that the synthesised supported catalysts are undergoing AEM mechanism due to the low Tafel slopes at high overpotentials.

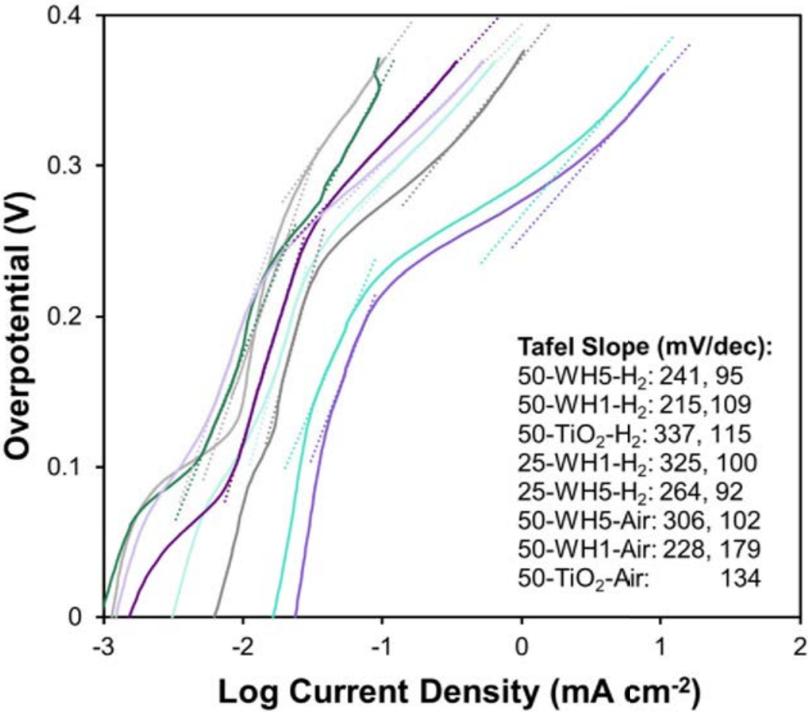

Figure 3.3: Tafel plots for the supported Ir catalysts with the calculated Tafel slopes.

3.3.2 Conductivity Measurements

To probe the role of conductivity on electrochemical OER activity, conductivity measurements of the synthesised supports and supported catalysts were conducted using an in-house developed cell (Figure 3.4). It is important to note that owing to the nature of the conductivity setup, these values are not absolute, but rather a method to enable in-house comparisons. All hollow TiO_2 supports were found to have low conductivities irrespective of the AuPd loading or thermal annealing conditions (10^{-8} – 10^{-9} S/cm). Interestingly, when Ir is deposited onto the catalyst-supports in combination with AuPd, a higher conductivity is observed for both Ir loadings (25 wt% and 50 wt%) and under both thermal treatments (reducing or oxidised) when compared to sibling samples prepared identically, but without AuPd. We also observe significantly higher conductivity (10^{-2} – 10^{-8}) for thermally reduced samples compared to the thermally oxidised supported catalysts (10^{-4} – 10^{-9} S/cm). Finally, when all other synthetic parameters remain constant, the catalysts with Ir deposited on WH5 have higher conductivities (10^{-2} – 10^{-7} S/cm) compared to those supported on WH1 (10^{-3} – 10^{-8} S/cm).

When analysing the OER performance (Figure 3.1c,d), it is noticeable that the two most conductive supported catalyst are indeed the two most active catalysts, suggesting that conductivity is a critical parameter for designing active OER catalysts. However, while the 50-WH1-air and 50-WH5-air samples have significantly higher conductivities compared to 25-WH1-H_2 and 25-WH5-H_2, their OER performance is rather similar. Thus, while reasonably high catalyst conductivity is essential for OER activity, such *ex-situ* powder conductivity measurements are not the sole predictor for OER activity trends in these supported catalysts.

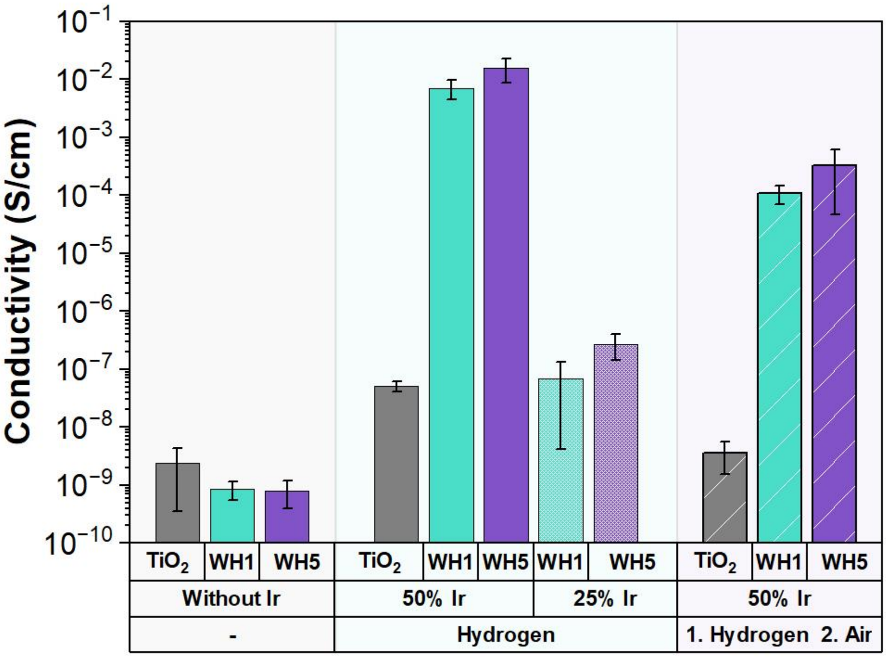

Figure 3.4: Conductivity of the various supports and catalyst-support motifs. Conductivities were measured with an in-house developed conductivity cell and are reported as averages of triplicate measurements.

3.3.3 Catalyst-Support Materials Characterisation

The presence of spherical TiO_2 motifs, and AuPd alloy nanoparticles non-uniformly distributed across TiO_2 for the as synthesised AuPd-TiO_2 supports (WH1 and WH5) was analysed via HAADF-STEM coupled with EDX (Figure 3.5). Analysis of lattice fringes visible in high resolution transmission electron microscopy (HRTEM) images of the AuPd nanoparticles on the WH1 support (Figure 3.5e), indicates a d-spacing of 0.24 nm, which can be attributed to the {111} lattice spacings of face centred cubic (FCC) AuPd alloy.[282]

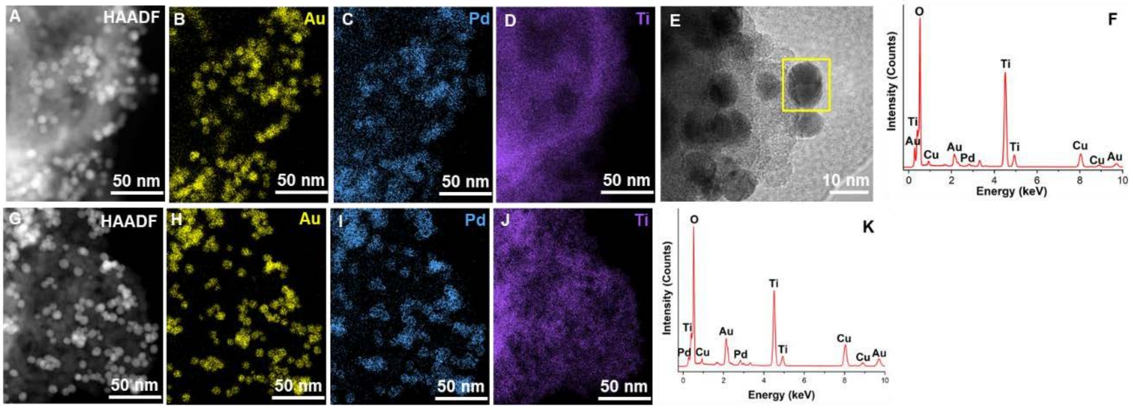

Figure 3.5: Morphology of WH1 (top row) and WH5 (bottom row) as synthesised (no annealing). a) HAADF STEM image, b-d) STEM-EDX elemental maps and e) High resolution TEM image and f) summed EDS spectra for the region shown for WH1. g) HAADF STEM image, h-j) STEM-EDX elemental maps and k) summed STEM EDX spectra for the region shown for WH5. Yellow box in (e) highlights the lattice fringe analysis region.

The average AuPd particle diameter in WH1 and WH5 is ~8 nm prior to Ir deposition (Figure 3.5). The Kolmogorov Smirnov tests of normality[283] indicated that the size of AuPd particles in WH1 (as prepared) were not normally distributed whereas particles in WH5 showed normal distribution (Figure 3.6a). Additional statistical analysis (chi-squared test) was used to identify the frequency of the particle sizes. By grouping the AuPd particles by size (<5, ≥5-<9, ≥9-<13, 13+), we observed a significant discrepancy (when $p < 0.05$) in the particle sizes distributions between WH1 and WH5 ($p = 0.01$). Therefore, post hoc Fisher's exact tests were conducted and identified that WH1 contained a significantly higher proportion of ≥5-<9 nm particles compared to WH5 which had a higher proportion of ≤5 nm particles ($p = 0.025$). The TiO_2 hollow sphere particle sizes were measured from SEM (~270 nm in diameter) and show comparable average diameters of 270 nm in WH1 and 275 nm in WH5 (Figure 3.6b). Chi-squared analysis on TiO_2 particle size proportion showed no significant difference ($p = 0.53$).

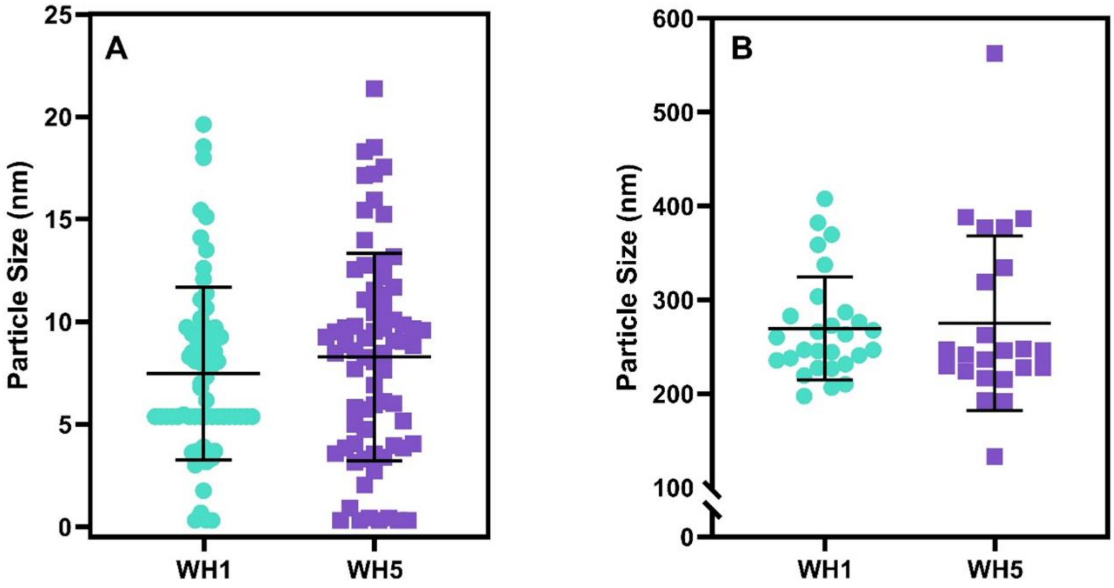

Figure 3.6: Particle diameter distribution obtained from (a) 67 and 72 measurements of AuPd nanoparticle size and (b) 28 and 23 measurements of the porous TiO_2 supports in WH1 and WH5, respectively. A Mann Whitney U test was used to compare the mean particle diameter between WH1 and WH5 in a) AuPd and b) TiO_2 supports. There was no significant difference between WH1 and WH5 particle size means for AuPd ($p = 0.27$) or for TiO_2 ($p = 0.59$).

The morphology of the thermally reduced 25 and 50 wt% Ir loaded catalysts and the Au, Pd, Ir and Ti distributions were determined via HAADF-STEM imaging and STEM-EDS mapping (Figure 3.7). A non-uniform distribution of Ir and AuPd particles across the TiO_2 supports is observed post annealing. Generally, the AuPd nanoparticles appear to be co-located with Ir, while there are also some Ir agglomerates isolated from the AuPd. Additionally, we observe that some of the Ir appears to be coated on the inside of the TiO_2 open nanoshell, which may also affect the conductivity or activity of the supported catalyst.

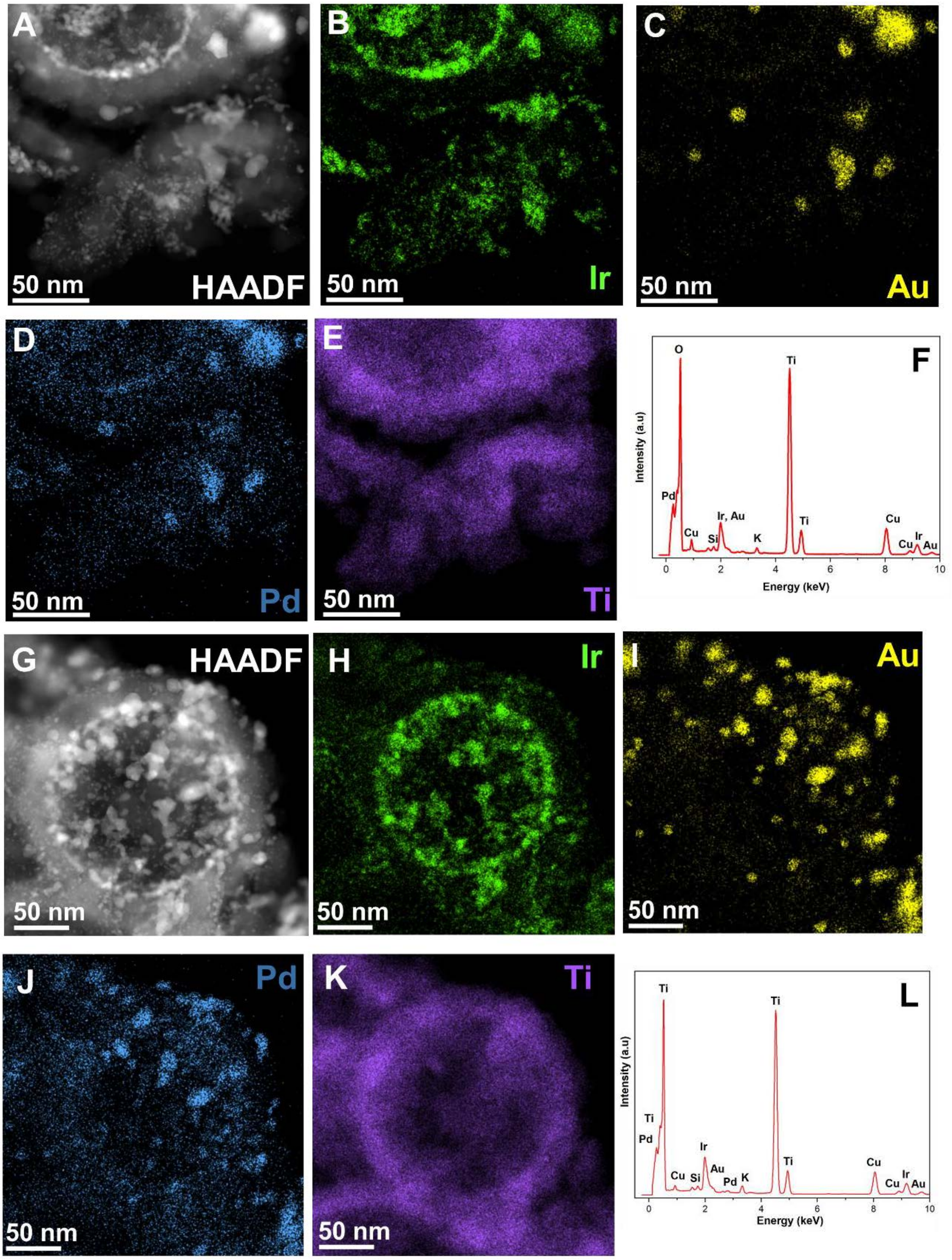

Figure 3.7: Morphology of supported catalysts via a) HAADF-STEM image for 50-WH5-H$_2$ b-e) STEM-EDS elemental maps for Ir, Au, Pd and Ti, respectively and f) summed STEM EDX spectra for the region shown and g) HAADF-STEM image of 25-WH5-H$_2$, h-k) STEM-EDS elemental maps for Ir, Au, Pd and Ti, respectively and l) summed STEM EDX spectra for the region shown.

The crystallinity of the supports and supported catalysts was assessed by XRD (Figure 3.8). For all samples, we observed 2θ peaks for crystalline anatase TiO$_2$ at 25°, 48, 54° and 55°. In all AuPd containing samples, peaks are observed at

38° and 44° corresponding to a FCC AuPd alloy. The thermally reduced samples contain a peak at 40° corresponding to FCC metallic Ir, whereas samples that were first reduced and subsequently thermally oxidised exhibited a mixture of FCC metallic Ir and low intensity rutile IrO_2 (28° and 34.7°) (Figure 3.8c).

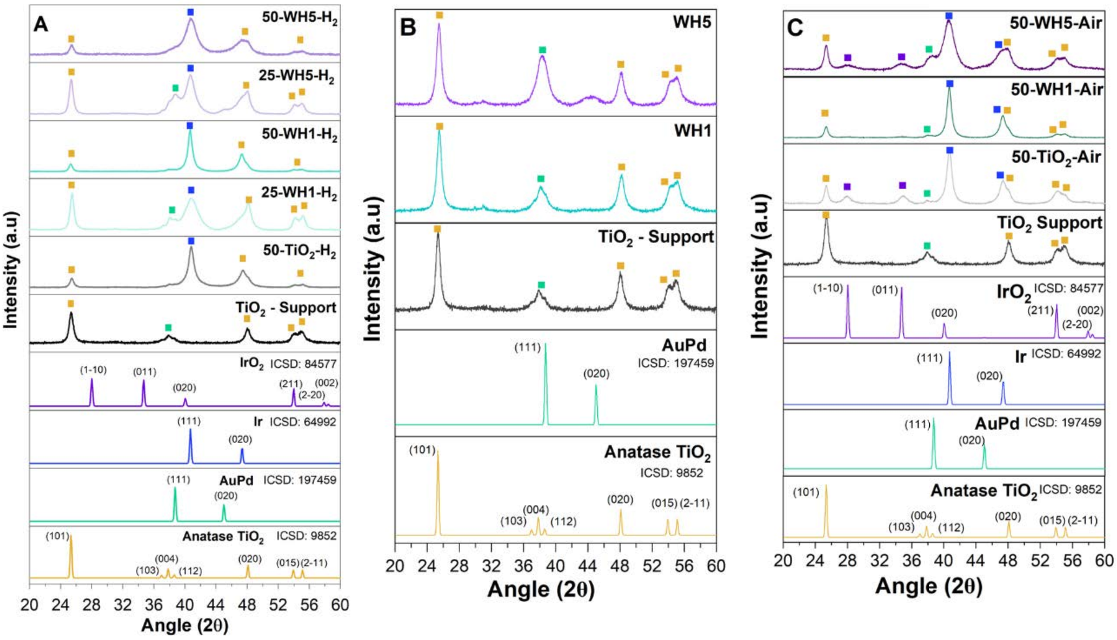

Figure 3.8: XRD of the a) supported catalysts annealed in H_2/N_2 atmosphere, b) supports prior to Ir deposition and c) supported catalysts annealed in air atmosphere with reference patterns corresponding to anatase TiO_2 (yellow), AuPd (green) and metallic Ir (blue) and IrO_2 (purple) as shown by the symbols. The relevant ICSD collection codes and planes are also provided.

The crystallite size of the TiO_2 support was assessed by the Scherrer equation and was shown to correspond approximately to the width of walls of the TiO_2 nanospheres (~14 – 16 nm). This remained constant irrespective of the composition or the synthesis environments (Table 3.2). Conversely, the crystallite size for Ir was found to vary across the samples. In both annealing environments (H_2 and air), broader metallic Ir peaks for 50-WH5 samples indicated the presence of smaller Ir crystallites (< 5 nm). Narrower Ir XRD peaks were observed for 50-WH1 and 50-TiO_2 indicating larger Ir metal crystallites of 10 – 14 nm. We speculate that at the lower 25 wt% Ir, provides sufficient anchor (or seeding) sites in both WH1 and WH5 to support these smaller Ir crystalline growth. Conversely, at the higher 50 wt% Ir loading, only WH5 has sufficient sites to maintain the smaller crystallite size.

Table 3.2: Crystallite sizes (calculated by Scherrer analysis) of Ir metal and TiO_2 for the supported catalysts.

Samples	**Crystallite Size (nm)**	
	Ir	TiO_2
25-WH1-H_2	4	16
25-WH5-H_2	5	15
50-TiO_2-H_2	10	14
50-TiO_2-Air	12	16
50-WH1-H_2	13	16
50-WH1-Air	14	16
50-WH5-H_2	5	14
50-WH5-Air	5	14

XPS analysis was performed on the as-synthesised supported catalysts and a commercial rutile IrO_2 catalyst to probe the Ir oxidation state (Figure 3.9a). For all of the synthesised samples, the observed Ir 4f doublets are shifted to lower binding energies compared to a typical rutile IrO_2.[284] Consistent with the XRD findings, the Ir in the thermally reduced samples is more metallic in nature (lower binding energies) compared to thermally oxidised samples. Furthermore, the thermally oxidised (air) samples show the clear presence of at least two doublets corresponding to a more oxidised (e.g., 4+) as well as reduced (metallic) Ir. Interestingly, no significant shift is observed in the Ir 4f region as a function of AuPd loading. The Au 4f region was also analysed. Typically, metallic Au $4f_{7/2}$ has a binding energy of 84.0 eV.[285] A slight shift towards lower binding energies was observed for AuPd loaded supports (83.4 eV and 83.2 eV for WH1 and WH5, respectively) (Figure 3.9b). Upon addition of 25 wt% Ir (25-WH5-H_2 and 25-WH1-air), the Au 4f region remains largely unchanged. However, with a higher Ir loading (50-WH5-H_2 and 50-WH5-Air) a shift to lower Au binding energy < 83.0 eV is observed, with 50-WH5 being slightly more oxidised compared to 50-WH1.

Across all samples, the Ti 2p region remains unchanged, irrespective of AuPd, Ir loading and annealing environment (Figure 3.9c).[286]

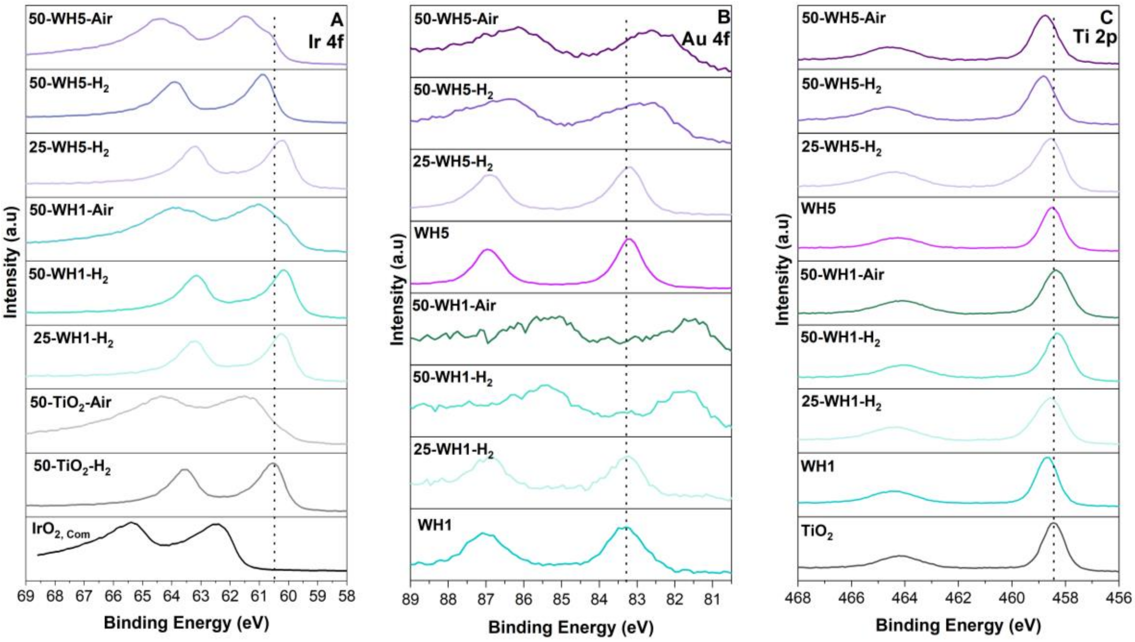

Figure 3.9: XPS spectra of a) Ir 4f includes comparison to IrO_2, b) Au 4f and c) Ti 2p for the synthesised supported catalysts. Dashed lines are added as a guide for the reader.

3.3.4 Membrane Electrode Assembly Performance

To understand the relevance of our catalyst design and RDE OER performance for PEM-ELs, we integrated our highest performing catalysts (50-WH1-H_2 and 50-WH5-H_2) into MEAs. The samples were benchmarked against an unsupported commercial IrO_2 (Figure 3.10). Nafion 212 membrane and a commercial 50 wt% platinum on carbon (Pt/C) cathode catalysts were used throughout. The anode catalyst loadings were 1.62 mg_{cat}/cm^2 for 50-WH1-H_2 and 1.58 mg_{cat}/cm^2 for 50-WH5-H_2. The unsupported IrO_2 had a loading of 3 mg_{IrO2}/cm^2. Figure 3.10a shows the beginning of life (BoL) and end of life (EoL) polarization curves prior to AST potential cycling for the supported and unsupported catalysts. To reach 1 A/cm^2, 1.79 V is required at the BoL for 50-WH5-H_2 whereas 50-WH1-H_2 requires 1.91 V. The commercial IrO_2 only required 1.63 V to reach 1 A/cm^2. The Ir utilisation was further evaluated by calculating Ir-mass activity (Figure 3.10b). We observe that both supported catalysts achieved superior mass activity compared to unsupported commercial IrO_2 at 2 V (1.09 A/mg_{IrO2}). Specifically, 50-WH5-H_2 achieved higher mass activities (2.42 A/mg_{Ir} at 2 V) compared to 50-WH1-H_2 (1.60 A/mg_{Ir} at 2 V), indicating the critical role of the higher AuPd loading for OER activity. More critically, these mass activity trends in MEA agree with RDE mass activity measurements (Figure 3.1 and

Table 3.3) where both supported catalysts exhibited higher mass activity than commercial IrO_2.

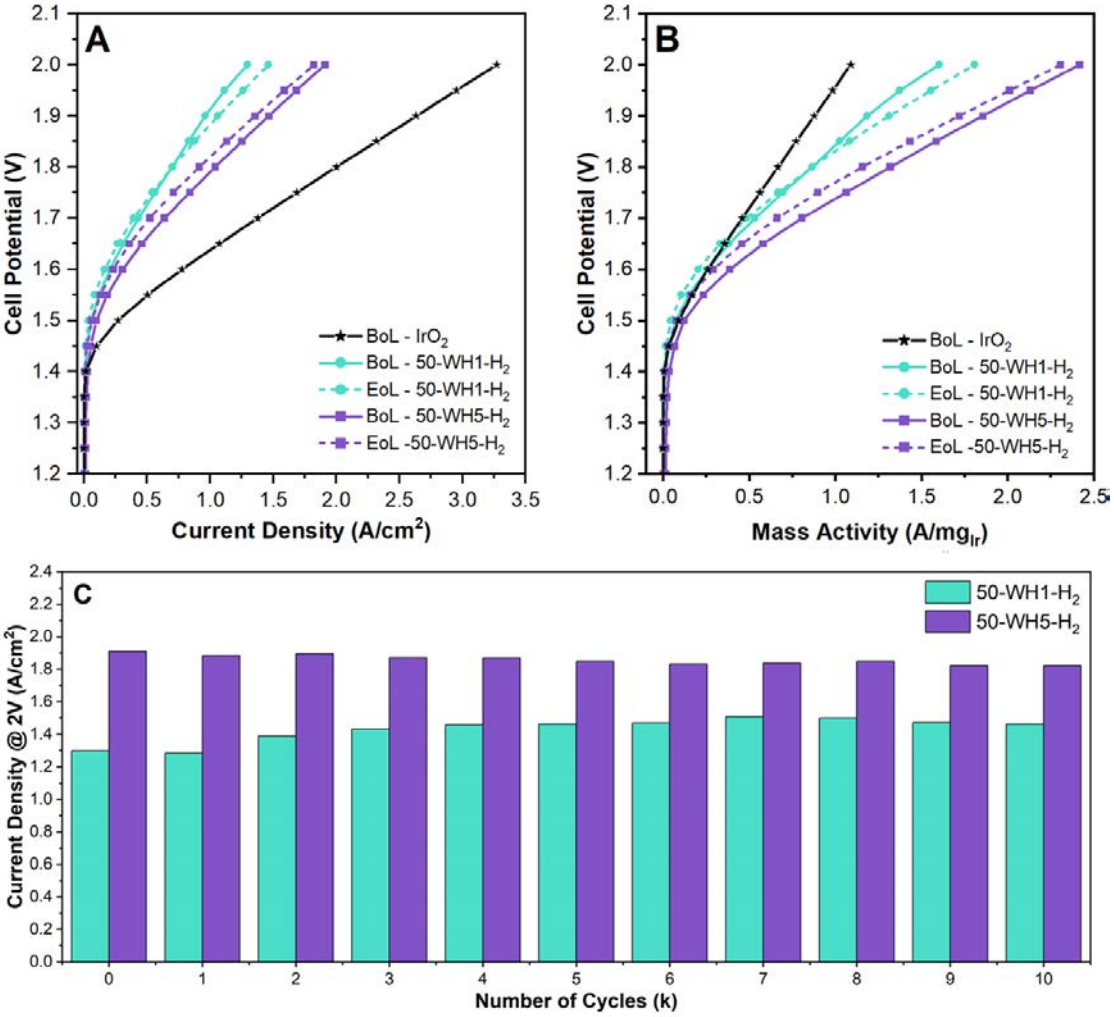

Figure 3.10: Beginning of life and end of life Polarisation curve of proton exchange membrane water electrolyser deploying 50-WH1-H_2 and 50-WH5-H_2 anode catalysts alongside a commercial rutile IrO_2 where a) geometric activity, b) Mass activity of the same catalysts and c) Performance of supported catalysts at 2 V after each thousandth cycle. Cell parameters: N212 membrane, 60 ^{o}C and N_2 gas flow. OER catalyst loadings: 3 mg_{IrO2}/cm^2 for IrO_2, 0.81 mg_{Ir}/cm^2 for 50-WH1-H_2 and 0.79 mg_{Ir}/cm^2 for 50-WH5-H_2.

To assess catalyst stability in the single-cell MEA, we performed saw-tooth voltage cycling at 50 mV/s from 1.2 – 2 V for 10,000 cycles (Figure 3.10c). The current density at 2.0 cell potential (V) was compared for both 50-WH1-H_2 and 50-WH5-H2. 50-WH5-H2 showed a BoL current density of 1.91 A/cm^2 and 1.82 A/cm^2 after 10,000 cycles (EoL). Conversely, 50-WH1-H2 at 2.0 V showed a BoL of 1.30 A/cm2 and EoL of 1.46 A/cm^2 at 2.0 V. Interestingly, the performance for 50-WH1-improved at potentials >1.8 V after 10k cycles. This could be due to either increase in Ir surface area or improved mass transport within the catalyst layer during AST potential cycling. Conversely, 50-WH5-H2 shows increased potential across current densities post AST. However, a voltage decay of 3 μV/cycle at 1 A/cm^2 indicates minimal performance loss during the AST, suggesting that this catalyst is highly stable even in a MEA configuration subjected to harsh operational conditions. Direct comparison of MEA decay rates from literature are complicated by the differences in cell setup and AST profiles. The desired degradation rate for potential GW scale application of electrolysers is < 6 μV/h and our results indicate that these TiO_2 supported Ir catalysts have the potential to meet the desired degradation rates.[287]

The higher AuPd content in the support clearly has a positive influence on the performance and durability of the Ir catalysts when assessed in both MEA and RDE configurations. When benchmarked against previously reported supported Ir catalysts tested in an MEA (

Table 3.3), we observed that our catalysts required lower potentials to reach 1 A/cm^2 compared to majority of the other catalysts, some with even higher anode catalyst loadings (> 2 mg$_{Ir}$/cm^2). However, we note that variations in cell temperature, membrane and testing conditions have a significant impact on the performance and thus a direct comparison (as we have done for RDE testing) is not possible.

The voltage applied during the ASTs is within range of the formation of H_2O_2 (1.76 V_{RHE}). Additionally, AuPd catalysts have been found to be selective for H_2O_2 production.[288–290] It is probable that H_2O_2 is also being formed in addition to O_2. However, the quantity formed is likely to be relatively low as the 4e-WOR is the more favourable reaction compared to 2e-WOR, as discussed in section 1.5.2. To quantify the production of H_2O_2 within this system, the water outlet would be collected and tested using *ex-situ* quantification methods such as titration, colorimetry and UV-vis spectrophotometry could be conducted (see section 1.9.4.2).

Table 3.3: 50-WH1-H2 and 50-WH5-H2 accelerated stress test conditions presented alongside various literature Ir-TiO_2 based electrocatalysts. CP is chronopotentiometry and CA is chronoamperometry. References for each catalyst are shown in the material column, * indicates catalysts from this work.

Materials	**Temperature (°C)**	**Membrane**	**Anode Catalyst Loading (mg_{Ir}/cm^2)**	**Potential at 1 A/cm^2**		**Stability Test Conditions**
				Beginning of Life (V)	*End of Life (V)*	
50-WH1-H_2 *	60	212	0.81	1.91	1.88	Saw-tooth
50-WH5-H_2 *	60	212	0.79	1.79	1.82	Saw-tooth
Ir/TiO_2-MoO_x [272]	80	115	0.50	1.74	1.85	Hold
IrO_x/F-TiO_2 [166]	80	115	1.00	1.66	1.68	Hold
Ir-Pt-TiO_2-PC-ann [169]	80	117	0.25	1.87	-	-
IrO_2@TiO_2 [142]	80	212	1.20	1.67	1.85	Hold
40I/TN-20 [189]	80	117	2.50	2.03	-	-
40Ir/V doped Ti [291]	80	117	2.50	2.03	2.13	Saw-tooth
IrO_2/TNO-H750 [292]	80	117	2.50	1.83	1.83	Hold
40IrO_2/$Ti_{0.7}Ta_{0.3}O_2$ [293]	80	117	1.50	1.95	-	-
TiO_2-R200M [164]	120	117	0.90	1.67	-	-
TiO_2-P25 [164]	120	117	0.90	1.75	-	-
F68-$Ir_{0.6}Sn_{0.4}O$ [294]	80	115	0.88	1.62	-	Hold

To evaluate Ir dissolution in the MEAs, a sample of the test water was collected at the end of the AST and analysed using ICP-MS. We observed that Ir dissolution was highest for better performing 50-WH5-H_2 (3.6 µg/L) compared to 50-WH1-H_2 (1.8 µg/L) after 10k cycles. The increased Ir dissolution for 50-WH5-H_2 may, at least to some extent, account for the decrease in activity during the AST 10k cycles (Figure 3.10c). We hypothesise that the larger Ir crystallite size (10 – 13 nm) in 50-WH1-H_2 could leach at slower rate than smaller particles in 50-WH5-H_2 which has a smaller crystallite size. It is also plausible that the larger Ir particles in 50-WH1-H_2 could be undergoing nanostructuring leading to increased surface area under the prevailing electrochemical conditions, and thus may explain the observed improved performance post-AST. We note that Ir is potentially redeposited on various components within the MEA rather than irreversible leaching.[295] It has been shown previously that most of the leached Ir is likely trapped within the membrane, transport layers and catalyst layers rather than exiting with the outlet water, meaning that the majority of the trapped Ir will not be detected in our ICP analysis.[296]

To assess any changes in the oxidation state during the AST, we conducted EoL XPS analysis of the tested MEAs (post AST) which were compared to the as synthesised catalyst powders (Figure 3.11). As discussed previously, the Ir surface of the as synthesised 50-WH1-H_2 and 50-WH5-H_2 was predominantly metallic in nature (Figure 3.9a). However, a slightly lower binding energy was observed for 50-WH1-H_2 (~60.2 eV) compared to 50-WH5-H_2 (~60.8 eV). Post AST, 50-WH1-H_2 was shown to have shifted slightly to higher binding energy (~0.2 eV) indicating the presence of IrO_2 on the surface of the catalyst which can increase catalyst stability. Conversely, 50-WH5-H_2 Ir 4f peaks were shifted to lower binding energy (~0.7 eV) suggesting a more reduced catalyst surface.

The O 1s was deconvoluted to gain insight into the reaction mechanism. The 3 peaks for oxygen - lattice oxygen (~ 529 eV), chemisorbed OH^- (~ 530 eV) and surface adsorbed H_2O (~ 533 eV) were identified during the analysis. We observed a similar trend for both, 50-WH1-H_2 and 50-WH5-H_2 with a slight decrease in lattice oxygen and OH^- after AST compared to prior AST measurements. This could indicate that the OER mechanism is undergoing a combination of AEM and LOEM. As during the AEM mechanism, the O^* is bond with H_2O or OH^- compared to the LOEM where O^* couples with lattice oxygen. [42–

[44] Taking into account the Tafel slopes (Figure 3.3), it is more likely that the AEM mechanism is the dominant mechanism. However, more *in-situ* analysis such as raman, XPS and theoretical modelling such as density functional theory should be conducted to accurately confirm this hypothesis. Interestingly, the Au $4f_{7/2}$ (Figure 3.11c) region showed lower binding energies (more metallic) for 50-WH1-H_2 compared to 50-WH5-H_2 in the as prepared powders as well as post AST. For both samples, the peaks shift to a higher binding energy post AST indicating that the Au is oxidised. In both supported catalysts, the Ti 2p region remains unchanged post AST when compared to the as synthesised catalyst powder (Figure 3.11d).

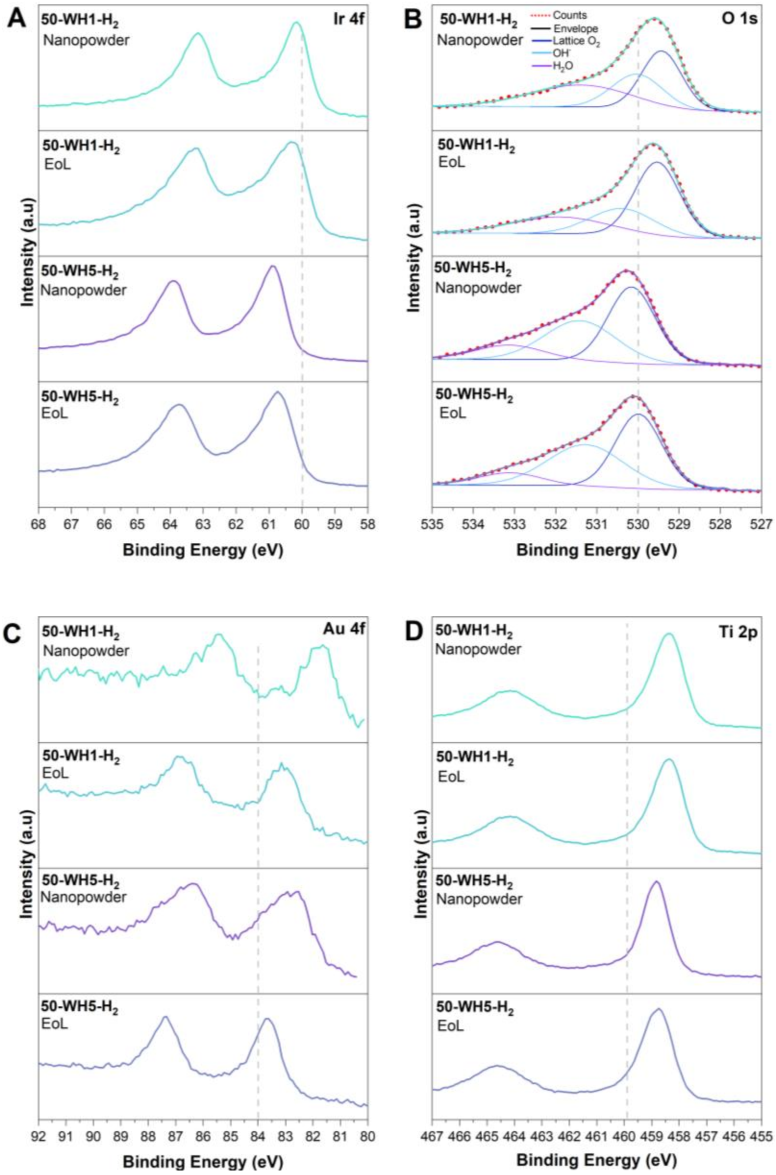

Figure 3.11: XPS spectra for a) Ir 4f, b) O 1s c) Au 4f and c) Ti 2p regions of the 50-WH1-H_2 and 50-WH5-H_2 in the form of nanopowder and post 10k AST catalyst coated membranes (EoL). The O 1s deconvolution shows lattice oxygen (dark

blue), adsorbed OH^- (light blue) and adsorbed water (purple). Grey dashed lines are provided to guide the eye.

3.4 Conclusion

We demonstrate for the first time a unique, hollow TiO_2 particles decorated with AuPd nanoparticles as a high-performance catalyst-support for iridium-based OER electrocatalysts. We show that the AuPd and Ir loadings and thermal annealing environment are critical to OER performance. Specifically, catalysts prepared with a higher AuPd and Ir loading (WH5, 50 wt% Ir) outperform those prepared with lower loadings (WH1, 25 wt% Ir). Furthermore, the highest performing catalyst-support (50 wt% Ir on TiO_2 coated with 5.5 wt% Au and 1.2 wt% Pd) (50-WH5-H_2) exhibited 3-times higher mass activity at 1.65 V_{RHE} (936 A/g_{Ir}) compared to commercial IrO_2 (271 A/g_{Ir}) in half-cell RDE testing. The highest performing catalysts were integrated into a membrane electrode assembly and subjected to 10k accelerated stress test consisting of saw-tooth potential sweep cycles. The same trends in OER activity were found to translate from the half-cell measurements to full devices (50-WH5-H_2 > 50-WH1-H_2). Furthermore, 50-WH5-H_2 showed the highest mass activity in an electrolyser achieving 2.42 A/mg_{Ir} at cell potential of 2 V compared to 1.09 A/mg_{IrO2} for commercial IrO_2. Through various materials characterisations of the surface oxidation state, crystallinity, morphology and conductivity, we demonstrate that there is no single parameter that correlates with OER performance. Rather, a complex interplay exists between conductivity, Ir oxidation state, crystallite and particle sizes which influence the acidic OER activity and durability of these hollow supported catalysts.

4 The role of iridium deposition methods on M-SnO_2 supported catalysts

4.1 Introduction

As discussed in section 1.8.5, supported Ir-based catalysts have shown promise as a strategy to reduce Ir loading for OER catalysis.[135,169,184,271,276,297,298] However, as well as the choice of support as discussed in chapter 3. The Ir deposition synthesis route is an important parameter to consider as it can control the chemical composition, oxidation state and crystallinity of Ir on the support. Currently, there are a range of Ir deposition techniques utilised to prepare supported Ir catalysts for the OER. For example, organometallic chemical deposition (OMCD),[299] colloidal,[148,174,300,301] Adams fusion[164,175,271,291,293,298,302–305] and wetness impregnation.[169,189] For each of these deposition techniques, the crystallinity and particle size is influenced by the temperature and duration of synthesis.[304] However, not all of their physical or electronic properties will be similar.

This chapter aims to focus on a systematic comparison between two iridium deposition techniques (polyol and acid modified polyol) on Sb doped SnO_2 supports to probe how the synthetic methodology influences the OER activity and stability. The conductivity, structure, composition and oxidation states of the prepared catalysts are investigated to determine how physical and electronic properties influence OER activity and stability.

4.2 Experimental

4.2.1 Synthesis of Doped SnO2 Supports

Doped (Sb, Ta, Nb and Mo) SnO_2 supports were synthesised using a previously reported method.[147] In brief, 1.28g of 1-tetradecylamine (TDA, 98%, Fisher Scientific) was mixed with 65 mL deionised water and 160 mL of ethanol for 3 h at room temperature. A separate mixture of 4.79 g of tin (IV) chloride (99%, anhydrous, Fisher Scientific) and 0.0016 moles of dopant precursor (antimony acetate 99.99% Sigma Aldrich, $TaCl_5$ 99.8 %, $NbCl_5$ 99%, $MoCl_5$ 99.6 %, Alfa Aesar) was dissolved in 20 mL of ethanol and added to the TDA solution. The mixture was stirred for 1 h at room temperature. An ammonium hydroxide (5 wt%, Fisher Scientific) solution was made using 0.102 ml in 200 mL deionised water.

The TDA solution was added dropwise to the ammonium hydroxide solution and refluxed at 80 °C for 72 h without stirring and cooled to room temperature. The yellow precipitate was collected via centrifugation and washed 5 times with deionised water. The precipitate was placed into an autoclave with 10 mL of water and hydrothermally treated at 120 °C for 24 h. The product was washed 5 times via centrifugation with 40 mL of 1:1 ethanol to water mixture and subsequently freeze dried for 24 h then calcinated at 400 °C for 3 h. For the synthesis of SnO_2, the same protocol was followed but without a dopant precursor. Commercial ATO (< 50 nm, Sigma Aldrich) was also used as a support.

4.2.2 Synthesis of Supported Catalysts

Iridium was deposited onto the prepared (and commercial ATO) catalyst supports through two different literature methods with an Ir loading target of 20 wt%. Specifically, we ascribe the two methods as polyol[147] and acid-modified polyol (AMP)[155] syntheses. In brief, the AMP syntheses were conducted as follows, 107.2 mg of hydrogen hexachloroiridate (IV) hexahydrate (40 % Ir, Acros Organics) was mixed with 5.76 mL of deionised water. 80 mL of ethylene glycol and 40 mL deionised water was subsequently added to the iridium solution and stirred. The solution pH was adjusted to pH 12 by dropwise addition of 25 mL of 0.5 M NaOH diluted in 25 mL of water and 25 mL of ethylene glycol solution. Subsequently, the solution was refluxed at 160 °C for 3 h and cooled to room temperature under constant stirring and under argon. To achieve 20 wt% Ir on the support, 160 mg of each support was dispersed in 40 mL deionised water and 40 mL ethylene glycol, this support solution was added to iridium solution. The pH was adjusted to pH 1 by adding 35 mL of 1M H_2SO_4 diluted in 35 mL deionised water and 35 mL ethylene glycol. The solution was stirred for 20 h at room temperature and separated via centrifugation then washed three times with deionised water and dried at 100 °C in air.

For the polyol synthesis, 74 mg of iridium acetate hydrate (< 50 % Ir, ChemPur) and 80 mg of sodium hydroxide (98 %, Fisher Scientific) were dissolved in 20 mL of ethylene glycol and stirred vigorously for 30 mins. To produce 20 wt % Ir on the support, 152 mg of support was added to the iridium solution. The solution was sonicated for 20 mins, subsequently stirred for 15 mins under argon and refluxed at 160 °C for 30 mins. The solution was rapidly cooled to room temperature and stirred for 24 h. The supported catalyst was separated from the solution via centrifugation and washed 3 times with deionised water. The collected material was freeze dried for 24 h and annealed at 250 °C in air for 2 h.

4.3 Material Characterisation

Full experimental and instrumentation details are shown in Chapter 2. In brief, to evaluate the surface area, crystal structure, oxidation state, composition, morphology and particle sizes by conducting BET, XRD, XPS, XRF, TEM and STEM-EDX. Aliquots of electrolyte (5 mL) was collected during stability testing to quantify the concentration of dissolved elements in supported catalysts using Inductively coupled plasma mass spectrometry (ICP-MS).

4.4 Conductivity Measurement

Based on previously reported literature,[150,229,230] an in-house developed 2-electrode conductivity cell comprised of two copper electrodes isolated from each other with 5 mm thick, PTFE (Polyfon) was connected to a Metrohm PGSTAT 204 potentiostat. Each catalyst powder was compressed under constant pressure of 500 psi during testing. The electrical resistance was determined by generating an I-V curve with a potential range of 0 to 0.2 V using cyclic voltammetry (CV). Using (equation. 4.1),[229] the electrical conductivity was calculated.

$$\sigma = \frac{l}{AR} \qquad \text{(equation. 4.1)}$$

where σ is the electrical conductivity, *l* is the thickness of the PTFE, *A* is the geometric area of the copper electrode and R is the electrical resistance.

4.5 Electrochemical Characterisation

Electrochemical measurements were performed in a three-electrode electrochemical cell configuration with a rotating disk electrode (RDE, Pine Research) and VSP-3e potentiostat from BioLogic Science Instruments. A gold working electrode (0.196 cm^2), graphite rod as the counter electrode, Hg/$HgSO_4$ reference electrode and 0.05 M H_2SO_4 electrolyte was used throughout. To deposit the synthesised catalyst-supports onto the gold working electrode, inks were prepared by dispersing 3.5 mg of catalyst powder in 1 mL 2-propanol (IPA, 99%, Fisher Scientific), 3.98 mL deionised water (18.2 MΩ, Milli-Q) and 20 µL Nafion™ (5 wt%, Alfa Aesar). Prior to electrochemical testing, inks were bath sonicated for 30 mins. The electrodes were subsequently prepared by dropcasting onto the Au RDE and rotating the disk at 700 rpm for 30 minutes until dry. All electrodes were prepared with a total catalyst loading of 20 $\mu g_{Cat}/cm^2$. Each catalyst ink was deposited in triplicate.

Potentiostatic electrochemical impedance spectroscopy (PEIS) measurements were conducted at 1.1 V_{RHE} (100 mHz to 200 kHz) to correct for ohmic losses. The surface of the catalyst was conditioned using cyclic voltammetry (CV) between 0.025 - 1 V_{RHE} for 50 cycles at a scan rate of 200 mV s^{-1}. The OER activity was assessed using CV by sweeping the potential between 1 – 1.8 V_{RHE} with a scan rate of 10 mV s^{-1} for 10 cycles under rotation at 2500 rpm. The 4th cycle of each measurement was used to determine the mass activity.

As described in Section 2.5 the potentials measured (vs. $Hg/HgSO_4$ reference) during electrochemical testing were converted to the reversible hydrogen electrode (RHE). The stability was measured using chronoamperometry (CA) held at 1.6 V_{RHE} for 18 hours. The CA was interrupted every hour to conduct one CV and PEIS measurement. PEIS was conducted at 1.1 V_{RHE} (100 mHz to 200 kHz). The dissolution of Ir, Sn, Sb, Mo, Ta and Nb was monitored throughout the stability measurements through collecting 5 mL aliquots of electrolyte at 0 min, 1 h, 2 h, 4 h and 18 h for ICP-MS analysis. The S-number was calculated using (equation. 4.2 - equation. 4.4).

$$\text{moles of oxygen} = \frac{\text{Q (C)}}{4 \times 96{,}485\ \text{C/mol}} \qquad \text{(equation. 4.2)}$$

$$\text{moles of Ir dissolved} = \frac{\text{Mass of Ir dissolved (g, from ICP)}}{\text{Mr of Ir }(\frac{\text{g}}{\text{mol}})} \qquad \text{(equation. 4.3)}$$

$$\text{S} - \text{number} = \frac{\text{moles of oxygen}}{\text{moles of Ir dissolved}} \qquad \text{(equation. 4.4)}$$

Where, Q is the cumulative charge at 18 h chronoamperometry and 4 is the number of electrons to drive the OER.

4.6 Results and Discussion

4.6.1 Characterisation of supports and supported catalysts.

Electrocatalyst supports were synthesised following a literature adapted mesoporous synthesis method[147,181] to prepare $M\text{-}SnO_2$ (where M = Sb, Ta, Nb and Mo additives) as well as an unmodified SnO_2. The synthesised supports in this chapter will be referred as MTO (where TO = SnO_2), the synthesised ATO will be referred to as ATO_{Meso} to distinguish between synthesised and commercial ATO (ATO_{Com}). XRD of the prepared supports (Figure 4.1) evidence a tetragonal rutile-SnO_2 whereby all the observed peaks at 2θ = 26.6°, 34.1°, 38.0°, 51.9° and 54.8° can be indexed to (110), (101), (200), (211) and (220) planes respectively. All peaks are accounted for in the diffractograms and hence no crystalline impurities are found to be present in the prepared supports.

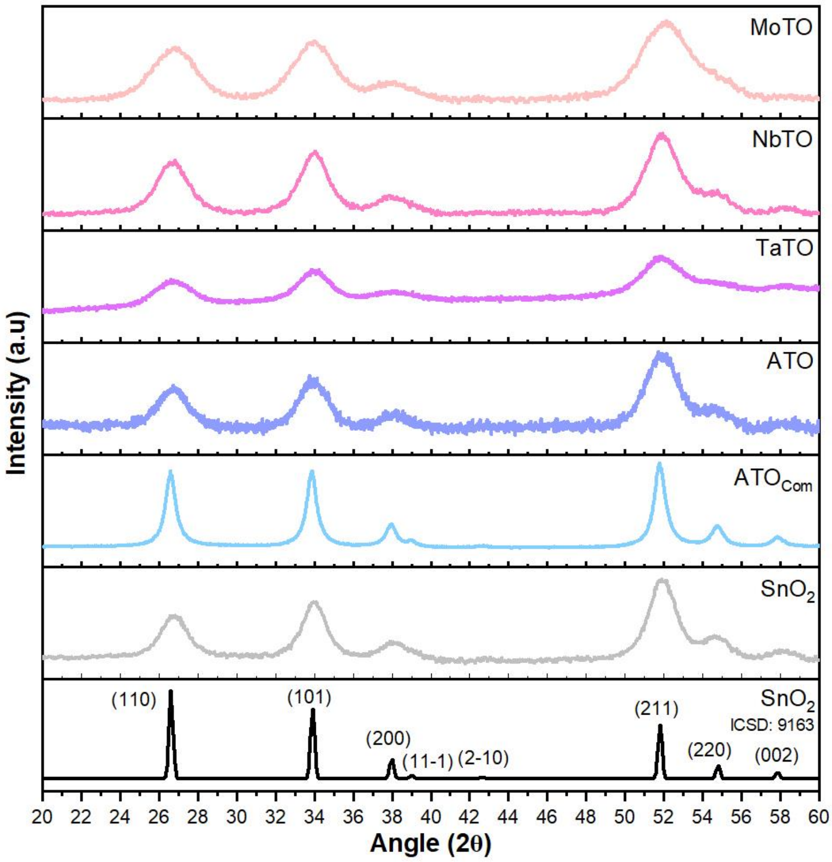

Figure 4.1: XRD peaks of the synthesised and ATO_{Com} supports.

Scherrer analysis of peaks at 2θ < 40° showed a similar crystallite size of 4 – 5 nm for all synthesised support compositions (Table 4.1). Conversely, ATO_{Com} was shown to have a crystallite size of 13 nm. XRF confirmed the presence of the additives (M = Sb, Ta, Nb and Mo) with weight fractions varying between 5 – 17 wt % (Table 4.1). The surface area of each support was analysed using BET analysis (Table 4.1). The supports containing additives resulted in high surface areas (94 – 143 m^2/g) in comparison to pure SnO_2 (74 m^2/g). ATO_{Com} had a low

BET surface area of 56 m^2/g, as expected due to the large SnO_2 crystallite size (13 nm) compared to the synthesised supports.

Table 4.1: XRF determined weight fraction of additives in supports, BET surface area, Scherrer determined crystallite size of supports and XRF determined weight fractions of Ir in supported catalysts for polyol and acid modified polyol syntheses.

Sample	**Additive weight fractions (wt%)**	**BET (m^2/g)**	**SnO_2 Crystallite Size of Supports (nm)**	**Ir weight fractions (wt%)**	
				Polyol	**Acid Modified Polyol**
SnO_2	-	74	5	2	4
ATO_{Com}	16	56	13	25	10
ATO_{Meso}	9	94	5	24	9
TaTO	17	124	3	2	13
NbTO	5	111	4	3	3
MoTO	8	143	3	1	4

For all catalysts, an Ir loading of 20 wt% on the supports was targeted synthetically. Interestingly, a wide range of Ir wt% was observed for the supported catalysts despite following identical synthetic parameters (Table 4.1). Specifically, the polyol Ir deposition resulted in a large range of 1 – 25 wt% Ir, whereas the AMP synthesis led to a lower but narrower Ir wt% (4 – 13 wt%).

The conventional polyol synthetic methodology is a one-step process that requires an alkaline environment to reduce the Ir precursor to metallic Ir and form glycolate anion which acts as a stabiliser for the Ir colloids.[306] Research has shown that an additional pH adjustment step after the reduction of Ir and addition of the support can increase the surface charge of the catalyst-support as a function of decreasing pH.[142,307] By increasing the surface charge on the support, an Ir colloid is electrostatically attracted to the support surface and subsequently acts as seeds for further growth of Ir, increasing the dispersion of Ir on the surface of the support.[36] A study focusing on the effect of support surface charge, highlighted that decreasing the pH during Ir deposition techniques results in an increase in Ir loading due to an increase in surface charge on the support.[301] We hypothesise that the increase in Ir content for Ir-SnO_2-AMP, Ir-TaTO-AMP and Ir-MoTO-AMP compared to its polyol counterpart could be due to an increase in surface charge during AMP process.

In addition to the differences in polyol and AMP syntheses we highlight that different precursors were used to prepare the various different catalyst supports. Specifically, ATO_{Meso} was synthesised with acetate precursor and the remaining supports (SnO_2, TaTO, NbTO and MoTO) were synthesised with a chloride precursor. Although the synthesised materials were washed extensively prior to Ir deposition, we hypothesise that residual chloride ions (Cl^-) present on the support hinders uniform dispersion of Ir due to Cl^- blocking surface sites of the support which are no longer available for Ir. Therefore, the use of acetate precursor compared to the use of chloride precursor is also a contributing factor to the reduced Ir wt% in polyol deposition technique.

We observe that the choice of support precursor combined with Ir deposition technique influences Ir wt% leading to differences in interactions between Ir and the support during the deposition process. We must note that the reductions in Ir wt% for AMP and polyol samples is also due to very small Ir particle size, that were too small to centrifuge and hence remained in the supernatant during the washing process. Due to the non-uniform Ir wt% in each supported catalyst, the following discussion will compare ATO_{Meso} and ATO_{Com} based supported catalysts in both Ir deposition techniques. The similar Ir wt% of the supports ~ 25 wt% for polyol and ~ 10 wt% in AMP for both ATO_{Meso} and ATO_{Com} will enable the comparison of the Ir deposition technique without taking the non-uniform Ir wt% into consideration. The supported catalysts are ascribed with P or AMP (polyol and acid modified polyol, respectively) to depict the Ir deposition technique used to synthesise the supported catalyst.

XRD (Figure 4.2a), was used to assess the crystallinity of the supported catalysts. No additional crystalline phases (e.g., Ir or IrO_2) were observed when compared to the as synthesised rutile M-SnO_2 supports (Figure 4.1). This suggests that the particle size of the Ir deposition is either very small, or that the deposited Ir is amorphous. The crystallite size of tetragonal rutile SnO_2 in supported catalysts post-Ir deposition was evaluated by Scherrer analysis (Table 4.2). We observed no change in crystallite size as a function of Ir deposition.

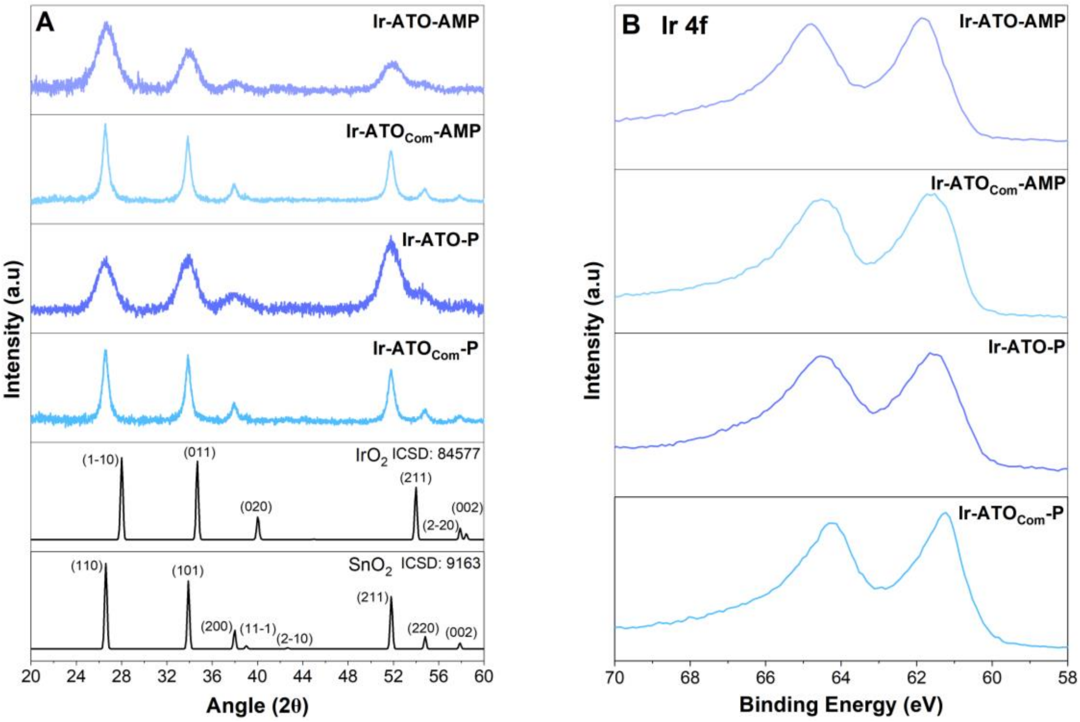

Figure 4.2: a) XRD peaks of all synthesised supported catalysts via polyol and AMP techniques with reference patterns below together with the relevant ICSD collection codes and b) XPS of Ir 4f spectra for supported catalysts.

Table 4.2: Average crystallite size of ATO$_{Com}$ and ATO$_{Meso}$-based supported catalysts determined by Scherrer analysis.

Samples	**Average SnO$_2$ Crystallite Size of supported catalysts (nm)**	
	Polyol	**Acid Polyol**
Ir-ATO$_{Com}$	13	13
Ir-ATO$_{Meso}$	4	5

To probe the oxidation state of Ir in the supported catalysts, we conducted XPS and analysed the Ir 4f$_{7/2}$ region (Figure 4.2b). Typically, metallic Ir peaks are observed at ~ 60.9 eV[308] and rutile IrO$_2$ at ~ 61.8 eV[309]. For polyol supported catalysts we observed Ir 4f$_{7/2}$ peaks at 61.2 eV for Ir-ATO$_{Com}$ while Ir-ATO$_{Meso}$ was shifted to higher binding energy (61.6 eV). The AMP supported catalysts exhibited a Ir $4f_{7/2}$ peak at 61.6 eV for Ir-ATO$_{Com}$ and a binding energy increase to 61.8 eV for Ir-ATO$_{Meso}$. For both Ir deposition techniques, the Ir-ATO$_{Meso}$ Ir $4f_{7/2}$ peak is observed at slightly higher (~ 0.2-0.4 eV) binding energies compared to their Ir-ATO$_{Com}$ counterparts. However, given the small differences observed, we conclude that the as prepared catalysts are predominantly in the Ir^{4+} oxidation state (IrO_2) irrespective of the Ir deposition technique. Interestingly, the Ir-ATO$_{Com}$-P Sn $3d_{5/2}$ and Sb $3d_{3/2}$ peaks are shifted to lower binding energies (~ 486.6 eV and 539.9 eV, respectively) compared to the other synthesised supported catalysts (487.3 eV and ~ 540.5 eV, respectively) (Figure 4.3a). However, the oxidation states all correspond to SnO_2 (486.0 – 488.0 eV)[225,308] and Sb_2O_5 (~ 540.0 – 541.0 eV for Sb $3d_{3/2}$).[310]

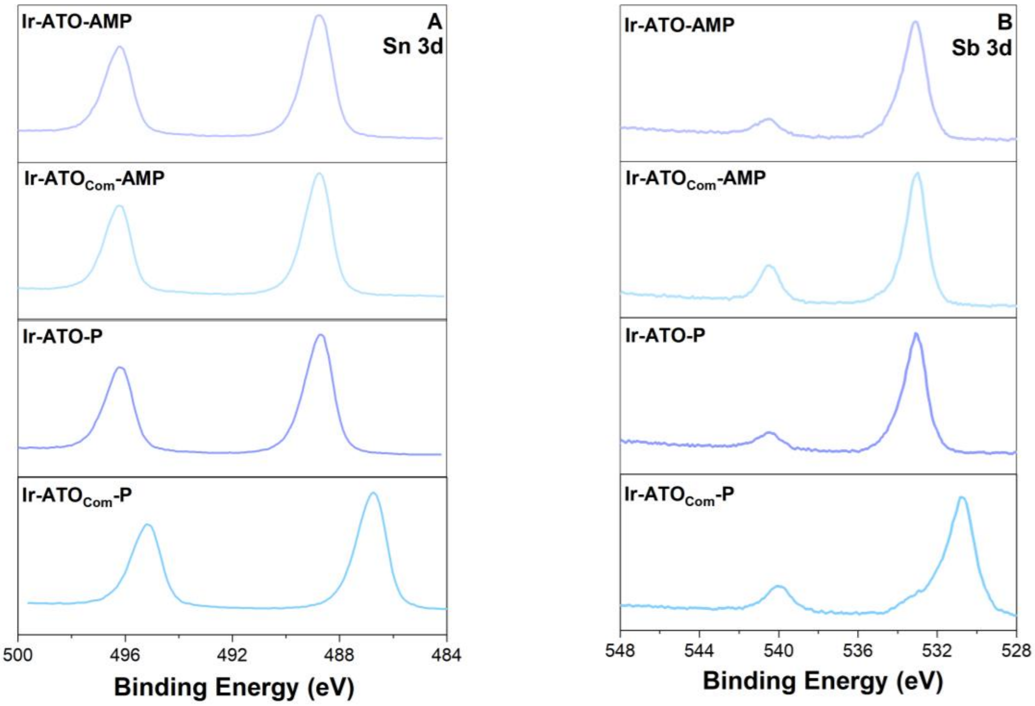

Figure 4.3: XPS spectra of a) Sn 3d and b) Sb 3d for all the supported catalysts.

4.6.2 Electrochemical OER activity and conductivity of ATO-based supported catalysts.

The electrochemical OER performance of the supported catalysts was assessed in acidic electrolyte (0.05 M H_2SO_4) using a three-electrode configuration with a RDE as a working electrode. When comparing the geometric current density of the supported catalyst at 1.7 V_{RHE} (Figure 4.4a) we observe current densities of 0.98 – 5.28 mA/cm^2 with a trend of Ir-ATO$_{Com}$-P > Ir-ATO$_{Meso}$-AMP > Ir-ATO$_{Com}$-AMP > Ir-ATO$_{Meso}$-P.

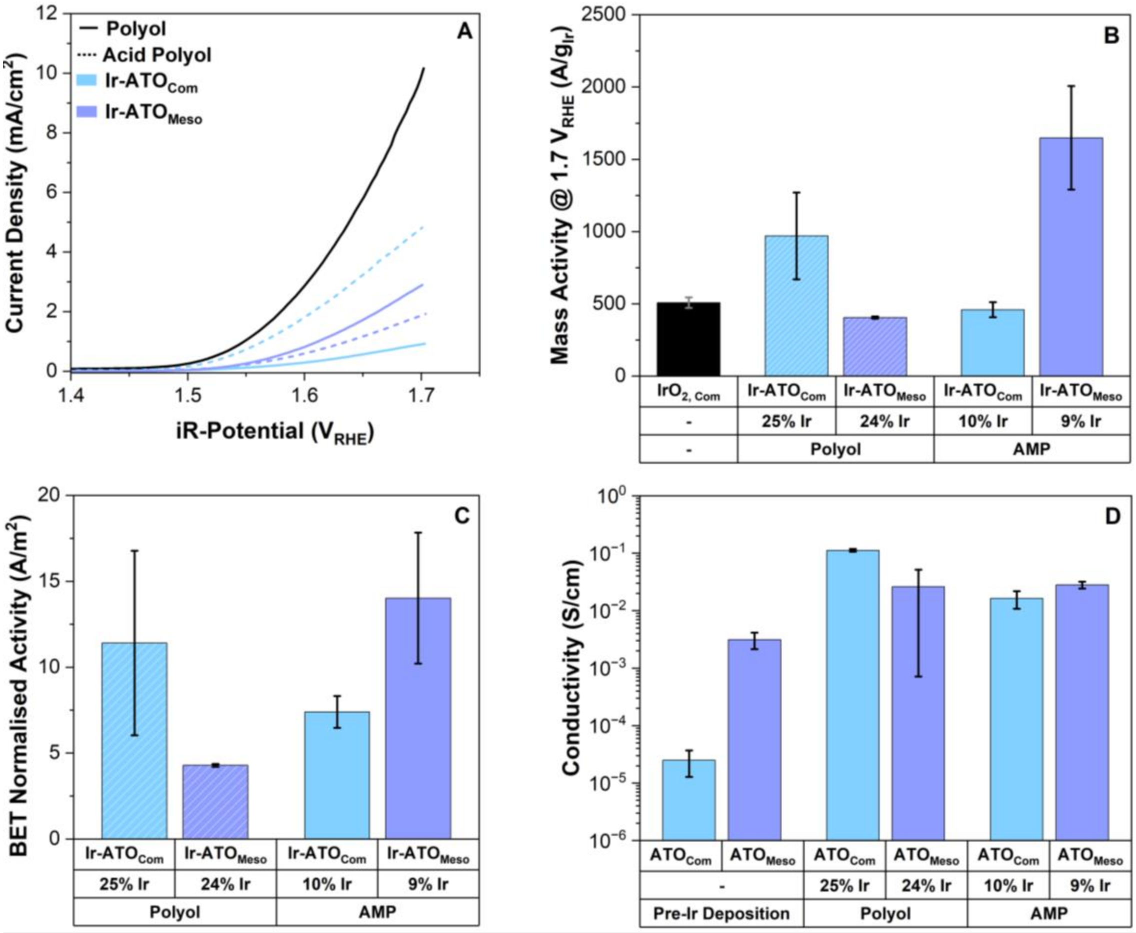

Figure 4.4: Electrochemical performance of the supported catalysts a) geometric surface area, b) Ir-mass normalised activity, c) BET surface area normalised activity and d) conductivities of the as-synthesised supports (Pre-Ir deposition) and supported catalysts. The electrochemical analysis was conducted in triplicate to produce error bars and the 5th CV cycle was used to obtain these results. All tests were conducted in 0.05 M H_2SO_4 with a total supported catalyst loading of 20 $\mu g_{Cat}/cm^2$.

To assess Ir utilisation, the current density at 1.7 V_{RHE} was normalised to mass of Ir, to obtain mass activities (Figure 4.4b). For all supported iridium catalysts, we observe an increase in mass activity compared to unsupported IrO_2 irrespective of Ir deposition technique. When comparing the effects of Ir deposition technique on the mass activity, we observe that polyol deposited, Ir-ATO$_{com}$ has the highest mass activity of 1062 A/g$_{Ir}$ compared to 419 A/g$_{Ir}$ for Ir-ATO$_{Meso}$-Polyol. The converse effect is seen for AMP supported catalysts with Ir-ATO$_{Meso}$-AMP obtaining the higher mass activity of 1794 A/g$_{Ir}$. Although we cannot compare the two Ir depositions with the same support directly (due to the disparity in Ir wt%), it is interesting to note that Ir-ATO$_{Meso}$-AMP with just 9 wt% Ir has higher mass activity overall compared to Ir-ATO$_{Com}$-Polyol with Ir wt% of 25.

The increase in mass activity for Ir-ATO$_{Meso}$-AMP is potentially due to the influence of high surface area for ATO$_{Meso}$ compared to ATO$_{Com}$ (Table 4.1)

To investigate the role of surface area on the OER activity, the catalyst activity at 1.7 V$_{RHE}$ of the four supported catalysts were normalised to BET surface areas (Figure 4.4c). For polyol synthesised supported catalysts, ATO$_{Com}$ obtained the highest activity of 12 A/m$_{BET}^2$. The converse was obtained for AMP supported catalysts with ATO$_{Meso}$ exhibiting 15 A/m$_{BET}^2$. The same trend as mass activities (Figure 4.4b) is observed and thus, implies that both Ir deposition techniques are influenced by the surface area of the support. Specifically, the increase in OER activity as the surface area increases is seen for AMP supported catalysts where the high electrochemical activities of Ir-ATO$_{Meso}$ correlates with the high surface area of ATO$_{Meso}$ (94 m^2/g) compared to the low activity seen for Ir-ATO$_{Com}$ with a low surface area of 56 m^2/g. The positive correlation between support surface area and OER activity for supported catalysts has been reported to be due to increased Ir utilisation on the support.[148] Therefore, we can deduce that the increased surface area in ATO$_{Meso}$ has improved Ir utilisation resulting in high mass activity for Ir-ATO-AMP. Interestingly, the opposite effect is seen for polyol supported catalysts, where an increase in the surface area of the support led to decreased activity of the supported catalyst. Subsequently, highlighting the disparities between the Ir deposition techniques.

The conductivities of the ATO supports and supported catalysts were analysed using a homemade conductivity cell and measured in triplicate (Figure 4.4d). The resulting conductivities are a guide to internally benchmark our materials and are not appropriate for comparison with literature conductivity values owing the experimental setup. The conductivity of the supports was 10^{-3} S/cm for ATO$_{Meso}$ and 10^{-5} S/cm for ATO$_{Com}$. Upon addition of Ir, the conductivity of ATO$_{Com}$ exhibits an increase of 3 and 4 orders of magnitudes for AMP (10^{-2} S/cm) and polyol (10^{-1} S/cm) supported catalysts, respectively. However, we observe only a marginal increase in conductivity for Ir-ATO$_{Meso}$ in both Ir deposition techniques (10^{-2} S/cm). This suggests that the Ir loadings onto the higher surface area ATO$_{Meso}$ (94 m^2/g) does not provide a very electrically conductive network compared to ATO$_{Com}$ (56 m^2/g). Such differences in conductivity have previously been attributed to the increased dispersion of isolated Ir particles on the surface of high surface area supports while low surface area supports have a higher density of Ir particles that agglomerate and form a conductive path.[164] Therefore, the higher geometric, mass and BET normalised activities (Figure 4.4a, b and c) for Ir-ATO$_{Com}$-P with low surface area support (56 m^2/g) compared to Ir-ATO$_{Meso}$-P (94 m^2/g) with low OER activities can be correlated to the conductive nature of Ir-ATO$_{Com}$-P. Conversely, for AMP supported catalysts, high OER activities occur for Ir-ATO$_{Meso}$, suggesting that the differences in conductivity and particle interconnectivity does not provide the full explanation for the OER performance trends.

To assess the kinetics of each supported catalyst, Tafel analysis (Figure 4.5) was performed at overpotentials of more than 200 mV. Our results showed that AMP supported catalysts exhibit faster kinetics (90 - 120 mV/dec) compared to polyol supported catalysts (60 – 300 mV/dec). Interestingly, the highest performing polyol supported catalyst Ir-ATO$_{Com}$ exhibited the lowest slope of 60 mV/dec. The mechanism that is most likely to be occurring for the SnO$_2$ based supported catalysts synthesised by AMP and Ir-ATO$_{Com}$-P is the AEM mechanism due to the low Tafel slopes (< 120 mV/dec). Conversely, the polyol supported catalysts could be undergoing LOEM mechanism as this mechanism has been reported to obtain higher Tafel slopes.[281]

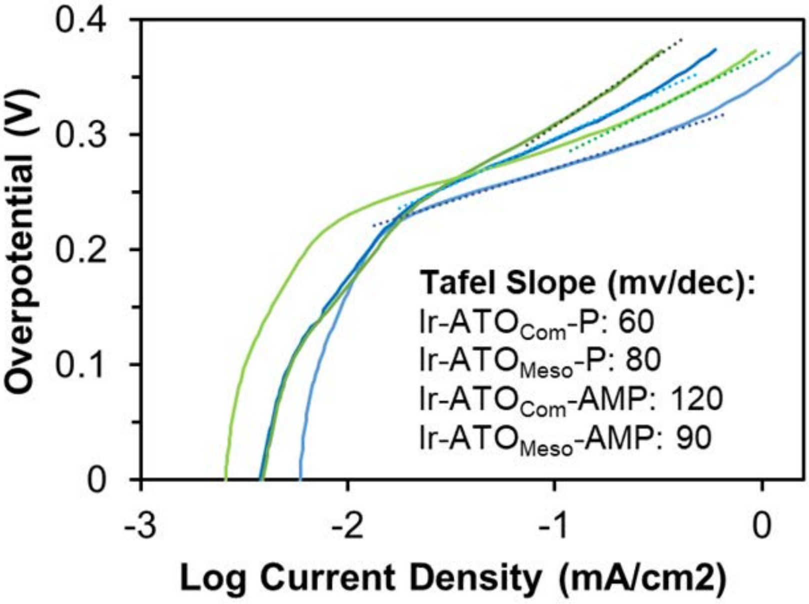

Figure 4.5: Tafel slopes of polyol and acid modified polyol supported catalysts at η = > 200 mV.

4.6.3 Morphology of the ATO supported catalysts.

The morphology and elemental distribution of Ir as a function of Ir deposition techniques were probed by high-resolution TEM (HR-TEM) imaging and EDX mapping. Both Ir deposition techniques show agglomerated particles for Ir-ATO$_{\text{Meso}}$-AMP/P and Ir-ATO$_{\text{Com}}$-P (Figure 4.6a,g and m) High-angle annular dark field scanning transmission electron microscopy (HAADF-STEM) imaging coupled with EDX was utilised to determine the distribution of Ir on the ATO supports. Ir-ATO$_{\text{Meso}}$-AP and Ir-ATO$_{\text{Com}}$-P shows small clusters of Ir (< ~ 5 nm) on ATO surface (Figure 4.6c and o). Conversely, Ir-ATO$_{\text{Meso}}$-P showed large area of non-uniform distribution of Ir (Figure 4.6i). EDS maps for Sb and Sn showed large agglomerates in both polyol and AMP (Figure 4.6d, e, j, k, p and q). It is interesting to note that the highest performing supported catalyst, Ir-ATO$_{\text{Meso}}$-AMP (1794 A/g$_{\text{Ir}}$) exhibited similar conductivity of 10^{-2} S/cm to its polyol counterpart (419 A/g$_{\text{Ir}}$) with different observed Ir dispersion. The agglomerates in Ir-ATO$_{\text{Meso}}$-AMP appear to be isolated Ir agglomerates (Figure 4.6c) compared to Ir-ATO$_{\text{Meso}}$-P with large, connected Ir cluster (Figure 4.6i). Suggesting that isolated Ir clusters aid in boosting OER activity.

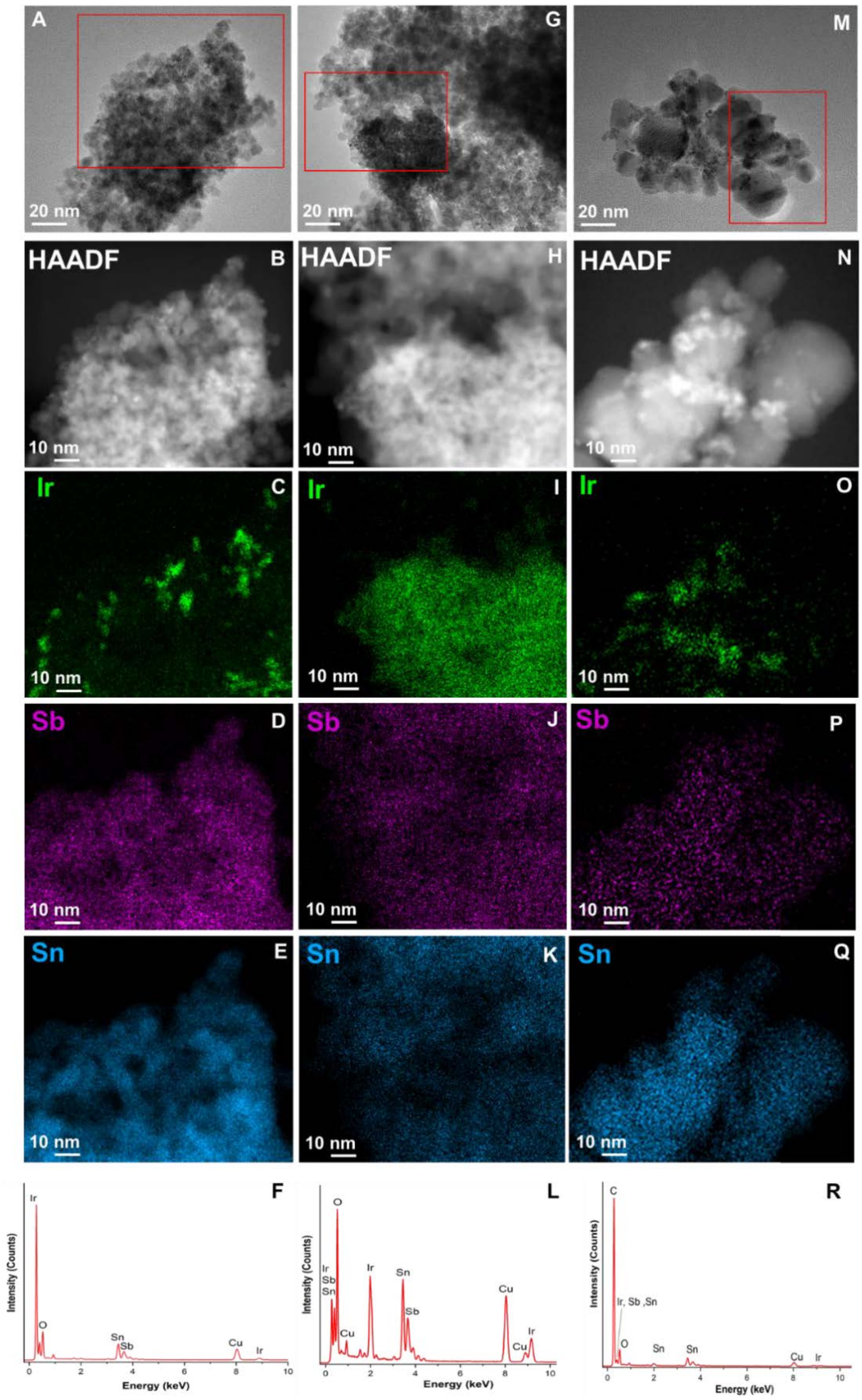

Figure 4.6: HR-TEM imaging a) HR-TEM of Ir-ATO-AMP b) HAADF-STEM image, c-e) STEM-EDS maps for Ir, Sb and Sn, respectively and f) EDS spectra. HR-TEM imaging of Ir-ATO-P (g), h) HAADF-STEM, i-k) STEM-EDS maps for Ir, Sb and Sn, respectively and l) EDS spectra. HR-TEM imaging of Ir-ATO$_{\text{Com}}$-P (m), n) HAADF-STEM, o-q) STEM-EDS maps for Ir, Sb and Sn and r) EDS spectra. Red box indicates the EDS maps area of analysis.

4.6.4 Evaluating the stability of ATO-based supported catalysts.

The electrochemical stability of the synthesised supported catalysts were screened by conducting a potential hold at 1.6 V_{RHE} for 18 hours. CVs were conducted at hourly intervals throughout the CA and the current density from CA at each hour is shown in Figure 4.7a. Aliquots of electrolyte were taken at 1, 2, 4 and 18 h for ICP analysis to quantify the dissolution of Ir, Sn and Sb. We observed a slight increase in activity for Ir-ATO_{Meso}-P in the first hour of testing, with a subsequent degradation in performance. Similarly, a gradual and small increase in activity is observed for Ir-ATO_{Com}-P after ~ 7 h. The increase in activity may be due to surface restructuring or due to the removal of accumulated microbubbles from the surface of the working electrode exposing more Ir active sites which is commonly observed for Ir OER electrocatalysts.[311,312] Typically, conditioning of a catalyst occurs by voltage cycling in non-faradaic regions (< 1.23 V) for > 50 times to obtain a steady-state catalyst surface.[247] The initial rapid loss of activity for the remaining supported catalysts is possibly due to the lack of conditioning of the catalyst prior to stability measurements. Additionally, the formation of hydrous IrO_x occurring from the electrochemical oxidation of amorphous IrO_x is typically unstable leading to increased dissolution in the first hour.[270] After the first hour, the remaining supported catalysts show a gradual decline in current density over the course of 18 h, indicating the degradation of the supported catalysts as a function of OER potential.

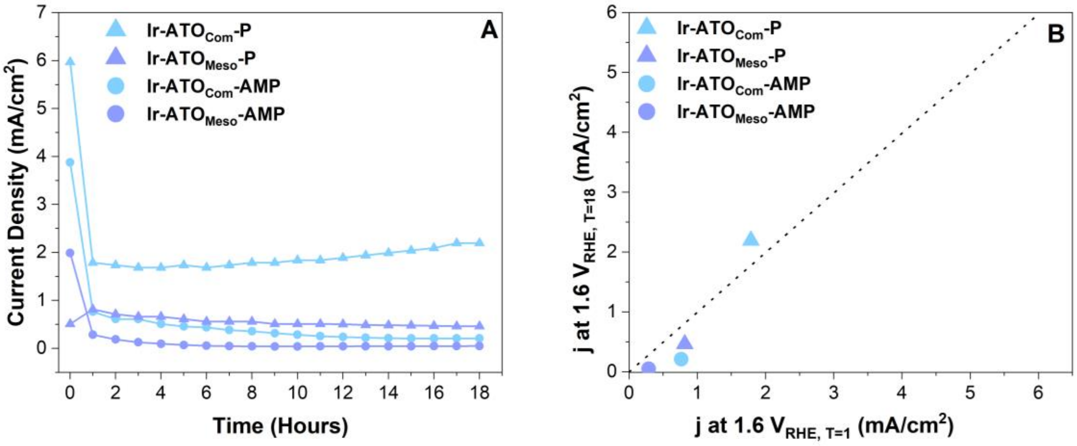

Figure 4.7: a) Hourly current density measurements at 1.6 V_{RHE} of the supported catalysts over the course of 18 h (obtained from CA data) and b) current density (j) of supported catalysts at 1.6 V_{RHE} before (T = 1) and after 18 hours stability test (T = 18). Line in (b) indicates y = x.

To further quantify the stability of the prepared supported catalysts over the course of stability measurements, the current density at 1.6 V_{RHE} at the end of the 18 h measurement was plotted against the current density at 1.6 V_{RHE} at 1 h of the experiment (Figure 4.7b). The dashed line in Figure 4.7b indicates y = x, as a guide to show the expected performance of a stable catalyst. Interestingly, for both polyol and AMP methodologies, Ir-ATO_{Meso} is the most stable supported catalyst with a relatively low current density loss of 0.4 mA/cm^2 (polyol) and 0.2 mA/cm^2 (AMP) over the course of 18 h. For ATO_{Com} supported catalysts, the AMP synthesis showed a loss of ~ 0.6 mA/cm^2 however, the polyol synthesised supported catalyst showed an increase in current density from 1.8 mA/cm^2 to 2.2 mA/cm^2 post-18 h CA. This increase in performance highlights the dynamic nature of Ir-ATO_{Com}-P.

The dissolution of the supported catalysts as a function of applied potential to the working electrode was evaluated by performing a CA at 1.6 V_{RHE}. Aliquots of the electrolyte at 1, 2, 4 and 18 h were taken and analysed by ICP-MS to determine the dissolved fraction (Figure 4.8a). Both Ir deposition methods exhibit similar trends during the course of electrochemical dissolution. The lowest dissolved fraction for all supported catalysts irrespective of Ir deposition technique is attributed to Sn (0.0006 – 0.06 %) compared to Ir dissolution of 0.01 – 3.84 % and 0.01 – 1.05 % for Sb over the course of 18 h. Additionally, most of the dissolved Ir and Sb occurs in the first hour. Ir has been reported to exhibit high transient dissolution, due to surface restructuring leading to high dissolution rates at the start of stability measurements.[313] The increased Sb dissolution in comparison to Sn has previously been attributed to Sb being less stable than Sn in acidic environment.[174,182] Although, Ir is the outermost surface the lack of Ir coverage across the whole support evidenced by TEM (Figure 4.6). The support remains exposed to the acidic environment and subsequently increases Sb dissolution. We also observe an initial increase and subsequent decrease in Sn dissolution for Ir-ATO_{Com} in both Ir deposition methods over the course of 18 h. We hypothesise that some of the Sn dissolved and redeposited onto the catalyst surface during the hourly CV cycles.[314]

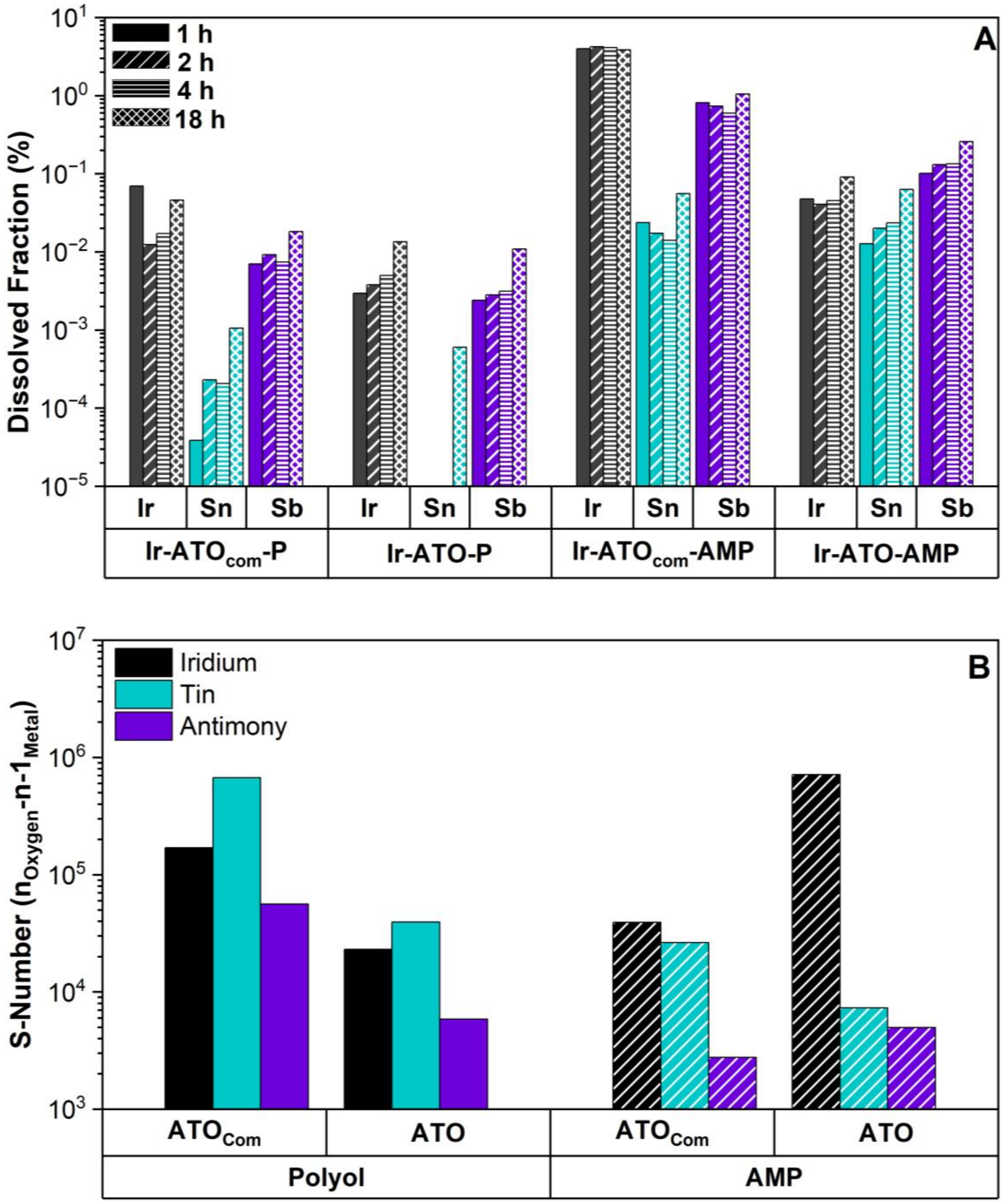

Figure 4.8: Elemental dissolution analysis of supported catalysts with a) dissolved fraction (percentage of element leached determined by ICP-MS) / element wt% measured by XRF) and b) S-number for Ir, Sn and Sb in the supported catalysts.

We observe a correlation between dissolution and electrochemical degradation for Ir-ATO$_{Com}$-AMP. Specifically, a steep decline in current density is observed (Figure 4.7a) and when compared against the dissolution (Figure 4.8a), Ir-ATO$_{Com}$-AMP has the highest dissolution of Ir and Sb (3.8 % and 1.0 %, respectively). Conversely, for polyol synthesised catalysts, the increase in current density observed for Ir-ATO$_{Com}$ (Figure 4.7a) does not correlate with the dissolution observed. The dissolution of Ir and Sb is highest for Ir-ATO$_{Com}$ (0.05

% and 0.02%, respectively) than Ir-ATO$_{Meso}$ with 0.01 % Ir and Sb dissolution after 18 h. Further confirming the dynamic nature of Ir-ATO$_{Com}$-P.

To correlate the activity and stability relationships in electrocatalysts, there are two main metrics known as the activity-stability factor (ASF)[67] and the stability number (S-number)[46] that can be calculated. ASF is defined as the ratio between rate of oxygen production and the rate of metal dissolution, conversely S-number relates the ratio of moles of oxygen evolved against moles of Ir dissolved. This work utilised the S-number metric to evaluate the correlation between activity and stability for Ir, Sn and Sb where the higher the S-number the more stable the catalyst (Figure 4.8b). We observe that Ir (10^4) and Sb (10^3) in Ir-ATO$_{Com}$-AMP has lower stability number compared to its ATO$_{Meso}$ counterpart with 10^5 for Ir and 10^3 for Sb. When combined with the observed dissolution and OER activity, we can deduce that Ir-ATO$_{Meso}$-AMP is the most stable AMP supported catalyst. However, for polyol supported catalysts (Figure 4.8b), we observe that Ir, Sn and Sb is more stable in Ir-ATO$_{Com}$ than Ir-ATO$_{Meso}$, contradicting the observed dissolution.

When comparing S-numbers for IrO_2 catalysts from literature, we observed that our synthesised Ir-ATO supported catalysts are similar orders of magnitude (10^4 - 10^6) to unsupported IrO_2 (10^4).[142,155] However, we must note that these values for IrO_2 were based on a galvanostatic hold and this work conducted a potentiostatic hold. The S-numbers from this work highlight that the presence of a support leads to increased stability compared to unsupported IrO_2 and low Ir content. Interestingly, in both Ir deposition techniques Sn shows the highest stability in ATO$_{Com}$ with 10^6 for polyol and 10^5 for AMP. Although, we cannot directly compare the Ir deposition techniques due to the dissimilar Ir wt%. It is interesting to note that the Ir S-number for Ir-ATO$_{Meso}$-AMP is 2 orders of magnitude higher (10^6) than Ir-ATO$_{Meso}$-P (10^4) despite its low Ir content (9 %), further highlighting the importance of Ir deposition methods and the influence of high surface area supports.

4.7 Conclusion

In this work, the synthesis of doped (Nb, Ta, Mo and Sb) SnO_2 supports was shown to have high surface area (> 74 m^2/g) compared to commercially purchased antimony tin oxide (56 m^2/g). Two Ir deposition techniques (polyol and acid modified polyol) were evaluated for their effect on OER performance. The polyol deposition method led to low Ir content < 2% for undoped SnO_2, Ta, Nb and Mo-SnO_2 supports. The acidic pH adjustment in acid modified polyol increased the Ir loading to > 2 wt%. The effect of Ir deposition was investigated by comparing the performance of as-synthesised antimony doped tin oxide (ATO_{Meso}) against commercial antimony doped tin oxide (ATO_{Com}) for each Ir deposition technique. The polyol synthesis showed high mass activity for Ir-ATO_{Com}-P (1062 A/g_{Ir}) due to high conductivity while acid modified polyol showed high mass activity for Ir-ATO_{Meso}-AMP (1794 A/g_{Ir}) due to the high surface area support. The difference in OER performance as a function of Ir deposition highlights that Ir wt% is not the only factor that enhances OER activity. Further confirming the conclusion made in chapter 3, that the combination of high surface area and conductivity and other physical properties factors contribute to the observed high mass activities.

5 The effect of dopants on SnO_2-based catalyst supports

5.1 Introduction

As mentioned in section 1.8.5.1.3, antimony tin oxide is a widely used catalyst support. However, antimony is susceptible to leaching over time, thereby reducing the lifetime of the support and leading to Ir dissolution.[259,315] Many dopants for Ti and Sn oxides have been explored beyond Sb. Specifically, W,[300,316] Ta,[155,293] Nb,[188,189,275] Ti[317] and Mo oxides have been identified as potentially stable dopants under acidic conditions.[183,318] The dopant content can lead to improved conductivities upon the addition of Ir which enhances the intrinsic activity of Ir.[189] Short term (< 50 hours) stability measurements have shown that doped supports can increase the stability of the supported catalyst, however the dopant is susceptible to leaching over time.[185] Therefore, the choice and composition of doped supports must be investigated to produce conductive and stable supports that can lead to high performing supported catalysts for the OER.

This chapter will act as an extension of chapter 4 by focusing on the activity and stability of alternative dopants for the acidic OER reaction. Due to the low Ir wt% obtained from the polyol and acid modified polyol (AMP) synthesis in the previous chapter. An accurate comparison between all the synthesised dopants and the Ir deposition technique could not be made. However, Nb-SnO_2, Mo-SnO_2 and undoped SnO_2 AMP synthesised supported catalysts obtained similar Ir wt% therefore those 3 supports will be investigated. Similar to previous results chapter, the conductivity, structure, composition and oxidation states of the prepared catalysts are investigated to determine how physical and electronic properties influences the OER activity and stability.

5.2 Synthesis of SnO_2 supports and supported catalysts

The undoped SnO_2 and doped (Nb and Mo) SnO_2 supports, and the subsequent AMP supported catalysts were synthesised using methods described in chapter 4.

5.3 Material Characterisation

The characterisation techniques including conductivity measurements and electrochemical measurements utilised in this chapter are described in chapter

4. In brief, XRF, BET, XRD and XPS were conducted to confirm the composition, surface area and oxidation state of the supports and supported catalysts. Conductivity measurements were undertaken to determine the electrical properties of the supported catalysts. The electrochemical activity measurements ware performed in 0.05 M H_2SO_4 with a target Ir loading of 20 wt% onto the support. The stability measurements were also conducted in 0.05 M H_2SO_4 with a potential hold (CA) at 1.6 V_{RHE} and aliquots of electrolyte were obtained to perform ICP-MS to determine the elemental dissolution of the supported catalysts.

5.4 Results and Discussion

5.4.1 Characterisation of supports and supported catalysts.

The synthesised supports Nb and Mo-SnO_2 (NbTO and MoTO, respectively) and undoped SnO_2, show evidence of rutile SnO_2 from XRD. XRD of the prepared supports (Figure 5.1a) evidence a tetragonal rutile-SnO_2 whereby the observed peaks and planes at 2θ = 26.6° (110), 34.1° (101), 38.0° (200), 51.9° (211), and 54.8° (220).

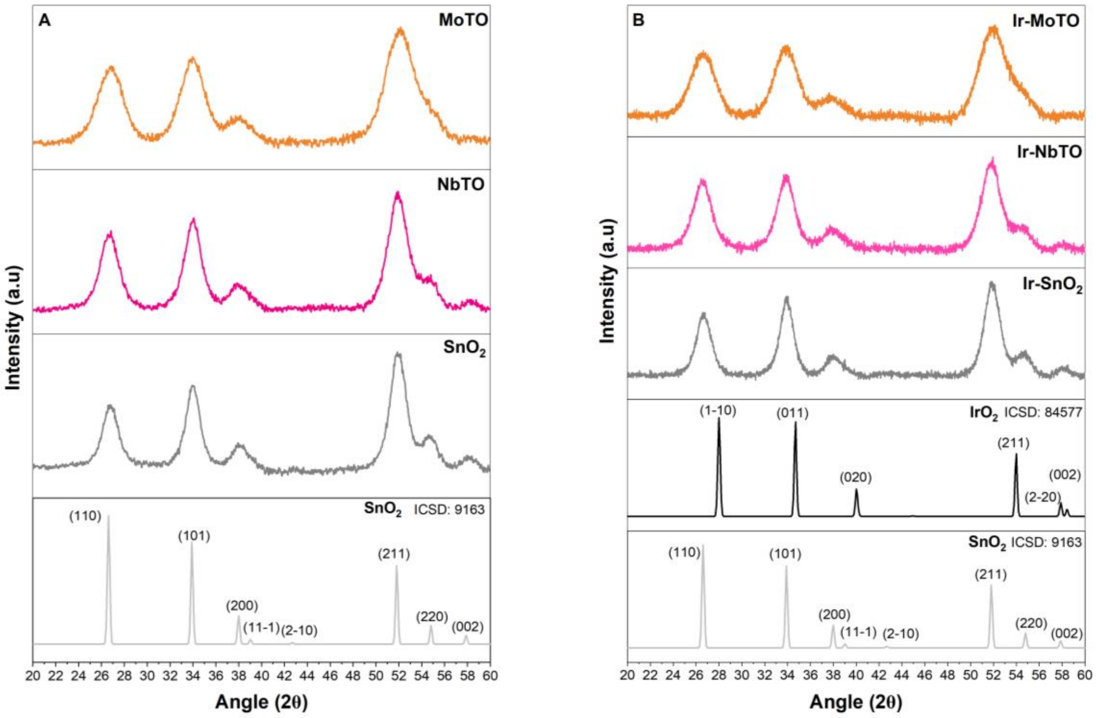

Figure 5.1: XRD peaks of a) as-synthesised supports and b) supported catalysts.

For all synthesised support compositions, the Scherrer analysis of peaks at 2θ < 40° was conducted and showed crystallite sizes of 3 – 5 nm for all support compositions (Table 5.1). To quantify the composition of the supports, XRF measurements were conducted confirming the presence of the additives (Nb and Mo) with weight fractions of 5 wt % and 8 wt% for NbTO and MoTO, respectively (Table 5.1). The surface area of each support was determined using BET analysis (Table 5.1). The supports containing an additive exhibit higher surface areas (111 and 143 m^2/g) in comparison to undoped SnO_2 (74 m^2/g). Although the crystallite size for SnO_2 (5 nm) is similar to NbTO and MoTO (4 and 3 nm, respectively), the addition of the additives increased the surface area. The addition of additives to the SnO_2 lattice can result in peak broadening due to lattice distortion which results in low crystallite sizes during Scherrer analysis. Similar results have been reported between ATO and FTO supports and attributed to differences in hydrolysis and condensation rates during synthesis of the support resulting in disordered mesopores that can increase d-spacing.[181]

Table 5.1:XRF determined weight fraction of additives in supports, BET surface area, crystallite size of supports and XRF determined weight fractions of Ir in supported catalysts for acid modified polyol syntheses.

Sample	**Additive weight fractions (wt%)**	**BET (m^2/g)**	**SnO_2 crystallite size of supports (nm)**	**Ir weight fractions (wt%)**	**SnO_2 crystallite size of supported catalysts (nm)**
SnO_2	-	74	5	4	5
NbTO	5	111	4	3	5
MoTO	8	143	3	4	3

The Ir catalysts were deposited on the supports to prepare supported catalysts using an acid modified polyol method adapted from literature.[155] The crystallinity of the supported catalysts were analysed by XRD and it was observed that there were no additional peaks for Ir species (IrO_2, Ir etc) post deposition (Figure 5.1b). This indicates that Ir is either not present, Ir crystallites are extremely small or the deposited Ir is amorphous. To confirm the presence of Ir, we analysed the supported catalysts using XRF. We obtained Ir with wt% of 3-4 nm (Table 5.1). Therefore, Ir must be present as amorphous or small crystallites.

The oxidation states of Ir and Sn were analysed with XPS on the supported catalysts. Typically, Sn $3d_{5/2}$ binding energies for Sn^{4+} occur between 486 – 488 eV[225]. In this work the Sn $3d_{5/2}$ peaks (Figure 5.2a) show binding energies of 487, 486.7 and 486.8 eV for Ir-SnO_2, Ir-NbTO and Ir-MoTO respectively. Thus, confirming the presence of Sn^{4+} oxidation state for Sn. Obtaining accurate Ir oxidation states is difficult due to Ir species (+3 and +4) that occur at similar binding energies.[284,309,319] For Ir $4f_{7/2}$, we typically see IrO_2 binding energies at 61.1 – 62.9 eV.[225] Our supported catalysts obtained binding energies of 61.4, 61.3 and 61.2 eV for Ir-SnO_2, Ir-NbTO and Ir-MoTO respectively confirming the presence of an IrO_2 and Ir oxidation state of 4+.

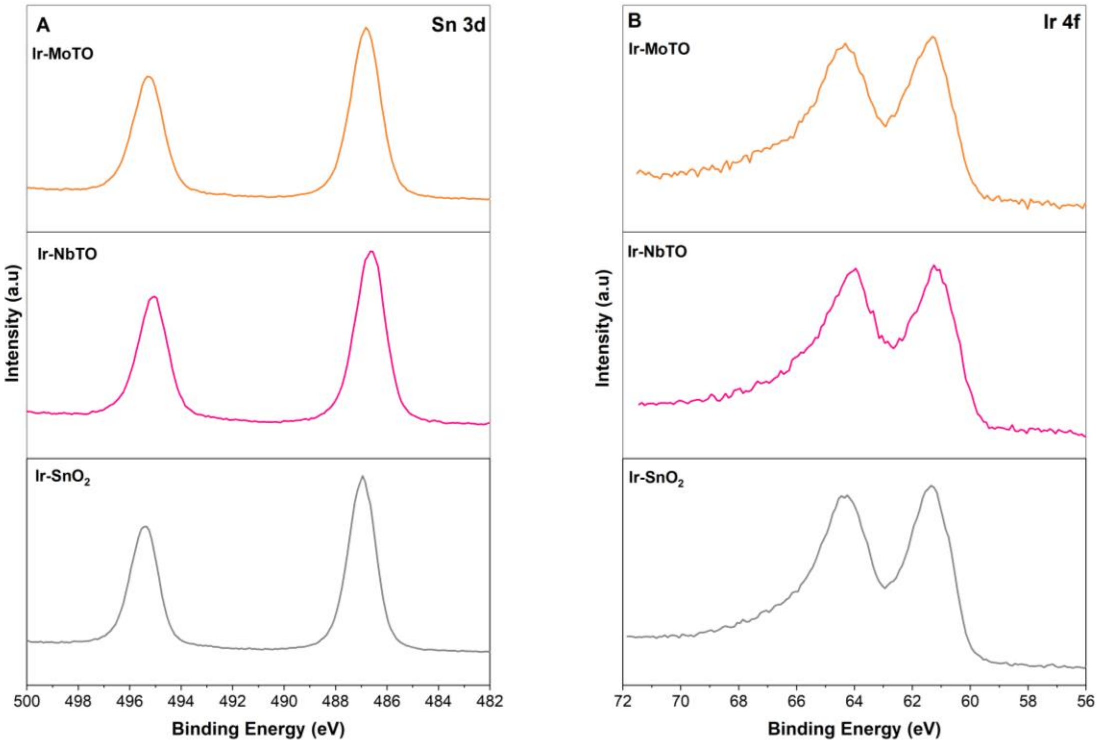

Figure 5.2: XPS spectra of supported catalysts a) Sn 3d and b) Ir 4f.

5.4.2 Electrochemical OER activity and conductivity of supported catalysts

The OER activity of the supported Ir catalysts was measured by potential cycling between 1 – 1.8 V_{RHE} in 0.05M H_2SO_4. The positive sweep (oxidative) was plotted to determine the OER performance of the supported catalysts (Figure 5.3a). The supported catalysts obtained geometric surface areas normalised activities of 0.93 – 1.59 mA/cm^2 at 1.7 V_{RHE}. The additive containing supported catalysts (Ir-NbTO and Ir-MoTO) obtained higher geometric area normalised activities than Ir-SnO_2. However, the unsupported IrO_2 exhibited the highest geometric area normalised activity overall with 10.17 mA/cm^2 at 1.7 V_{RHE}.

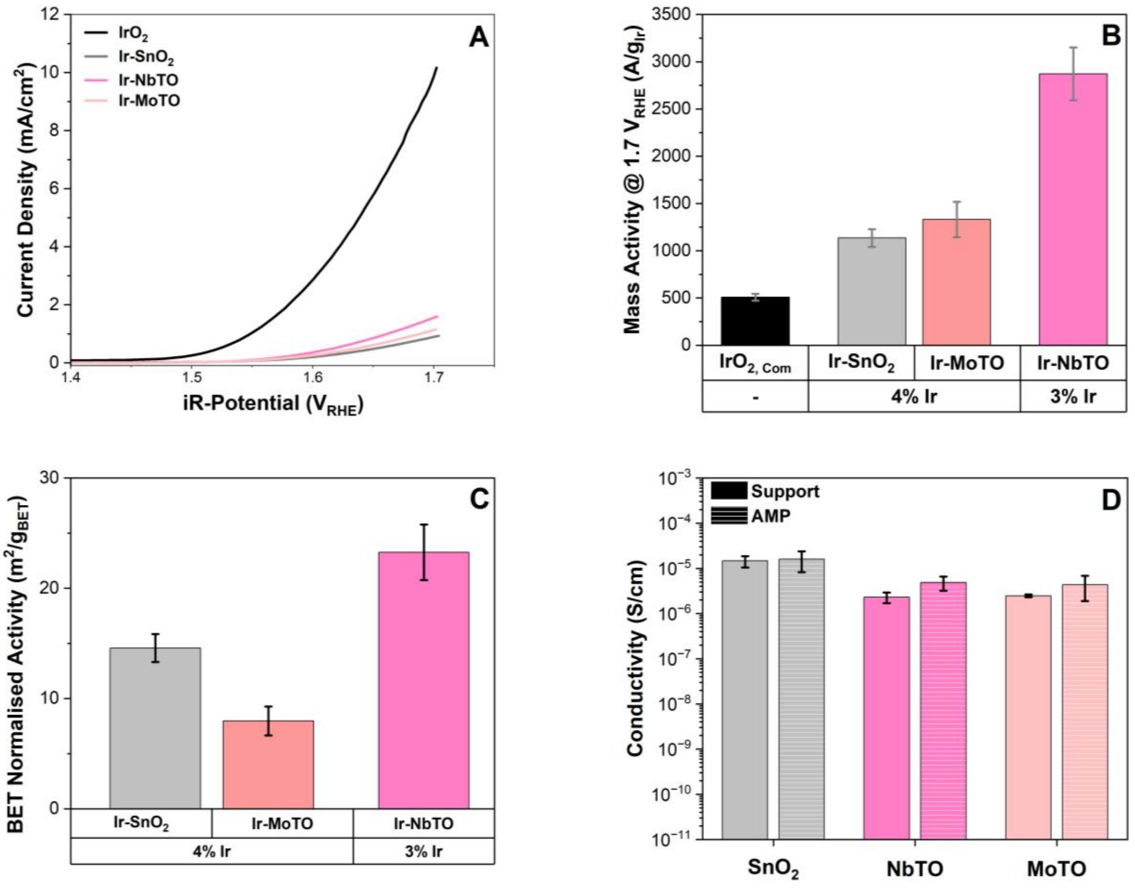

Figure 5.3: Electrochemical analysis of supported catalysts a) geometric surface area, b) Ir-mass activity, c) surface area normalised activity and d) conductivity. All electrochemical analyses were conducted in 0.05 M H_2SO_4 in triplicate to produce error bars and the 5th cycle was used to obtain these results with a total supported catalyst loading of 20 $\mu g_{Cat}/cm^2$.

Electrocatalysts are known to have rough surfaces with high surface area. Normalising the current solely by the geometric surface area overestimates the performance of an electrocatalyst as it assumes that the surface is smooth.[320] To accurately measure the current response of an electrocatalyst, the current must be normalised by the mass of catalyst loaded onto the working electrode. In addition, the Ir utilisation for Ir-based supported catalysts can be measured. The mass activities in this work were analysed by normalising the current at 1.7 V_{RHE} to the mass of Ir (0.10 – 0.16 μg) in each supported catalyst (Figure 5.3b). We observed that all the supported catalysts obtained higher mass activities than unsupported IrO_2 (508 A/g_{Ir}). When comparing the supported catalysts as a function of the additives, we observe that Ir-NbTO obtains the highest mass activity of 2871 A/g_{Ir} at low Ir loading of 3 wt% compared to Ir-SnO_2 (1135 A/g_{Ir}) with similar Ir content of 4 wt%. This increased mass activity directly correlates to higher BET surface area, however it is difficult to evaluate the effects of additive on Ir mass activity.

Interestingly, Ir-MoTO with a higher surface area (143 m^2/g) than Ir-NbTO (111 m^2/g) achieves mass activities in a similar range to Ir-SnO_2 (74 m^2/g). Therefore, we normalised the current at 1.7 V_{RHE} with the BET surface area to determine the effects of surface area on the resulting mass activities (Figure 5.3c). The highest performing supported catalyst is shown to be Ir-NbTO with 26 A/m^2, following the same trend as mass activities. Although, the highest surface area support was Ir-MoTO (143 m^2/g) it did not produce higher BET surface area normalised activity than Ir-NbTO or Ir-SnO_2. This shows that there is a potential interaction between the NbTO support and Ir leading to improved OER performance, irrespective of support surface area.

The relationship between activity and reaction mechanism can be investigated by analysing the current produced as a function of potential applied to the working electrode. As a result, information on the rate determining steps of the reaction can be found by conducting Tafel analysis. In this work, Tafel analysis was conducted at overpotentials of more than 200 mV to assess the kinetics of each supported catalyst (Figure 5.4). The supported catalysts containing an additive (Nb and Mo) resulted in slopes of <100 mV/dec indicating faster kinetics compared to Ir-SnO_2 with a Tafel slope of 100 mV/dec. Interestingly, Ir-MoTO with similar mass activity to Ir-SnO_2 showed the lowest slope of 70 mV/dec. Similar to previous chapters, the low Tafel slopes potentially indicate the occurrence of the adsorbate evolution mechanism.

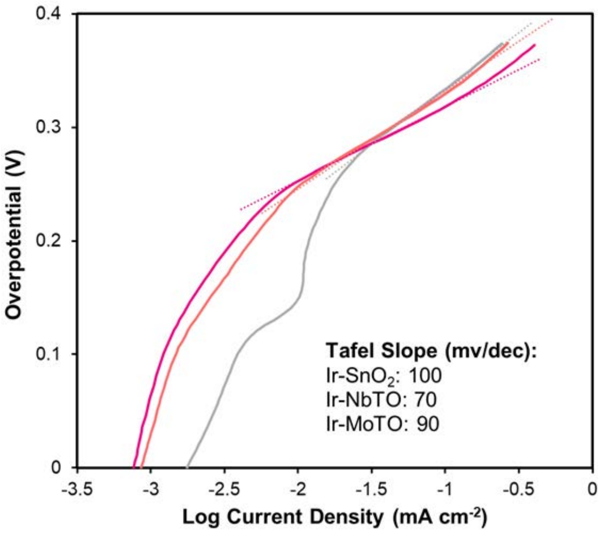

Figure 5.4: Tafel slopes of supported catalysts at η = > 200 mV.

The conductivities of the supports and supported catalysts were measured in triplicate in a homemade conductivity cell (Figure 5.3d). The SnO_2 support achieved 10^{-5} S/cm compared to both NbTO and MoTO reaching 10^{-6} S/cm. Upon Ir deposition, the supported catalysts had a marginal increase in conductivity, but the trend was still maintained with 10^{-5} S/cm for Ir-SnO_2 and 10^{-6} S/cm for Ir-NbTO and Ir-MoTO. Ir deposition was expected to lead to an increase in conductivities because Ir (and IrO_2) are more conductive than other transition metal oxides. However, these supported catalysts only contain 3-4 Ir wt% and thus, there is not enough Ir to provide a conductive pathway that can lead to an increase in conductivity. A previous report has shown that 40 mol % of Ir (~ 50 wt%) on TiO_2 is required to provide a significant enhancement on conductivities.[165]

However, the low Ir loading (and low conductivities) has not hindered the mass activities of the supported catalysts (Figure 5.3b). Therefore, we can deduce that supported catalyst have maximised Ir utilisation leading to increased mass activities despite the low conductivities. This highlights that conductivity is not the only factor that influences OER performance but the potential interaction between additive and Ir may enhance OER performance.

5.4.3 Stability of supported catalysts

The stability of the supported catalysts was evaluated by conducting CA at 1.6 V_{RHE} for 18 hours. An aliquot of the electrolyte was taken at 1, 2, 4 and 18 h and analysed using ICP-MS to determine the elemental dissolution of each supported catalyst. The current density during the CA measurements was plotted at hourly intervals (Figure 5.5). We observed a rapid decrease in current density in the first hour of the CA measurement. This can potentially be attributed to the catalyst surface restructuring.[247] Additionally, amorphous IrO_x which may be present within this sample is known to undergo dissolution faster than crystalline Ir, however this is still a debated topic in the field.[270,321] Activity losses during CA have also been attributed to microscopic bubble formation hindering the increase of current density due to blocked activity site, thus may not necessarily indicate an unstable supported catalyst.[311] We also observe a steep decline in current density for Ir-NbTO over the course of 18 h in comparison to Ir-MoTO and Ir-SnO_2 which both show stabilisation after ~ 12 hours with a slight increase in current density at 18 hours. This highlights the dynamic nature of all supported catalysts with Ir-NbTO appearing to be the most unstable.

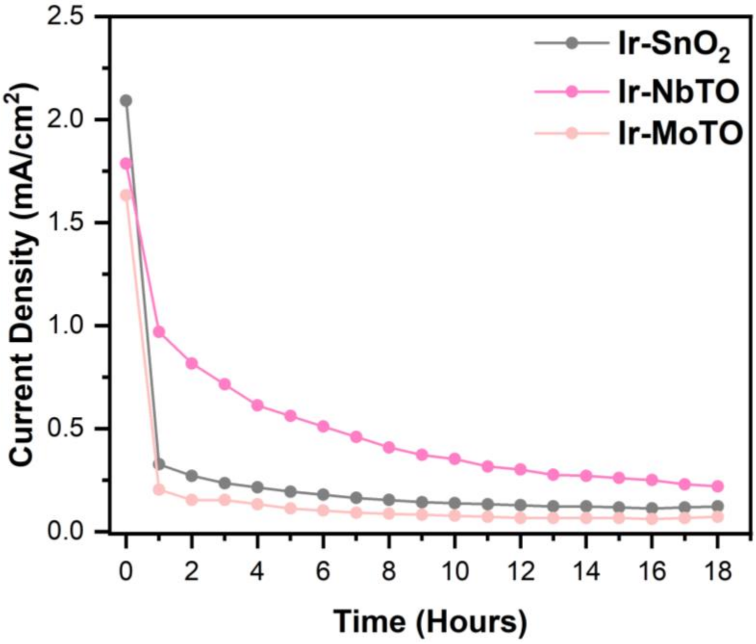

Figure 5.5: Current density of each supported catalyst at hourly intervals of the stability measurements.

Due to the initial rapid decrease in current density and the uncertainty in the degradation mechanism in the first hour, we opted to plot the first hour against the last hour to observe change in stability over the course of 18 hours (Figure 5.6a). For the supported catalyst to be seen as "stable", the activities should lie along the diagonal (y = x). We observe that Ir-MoTO exhibits a loss of 0.13 mA/cm^2 over the course of 18 h compared to 0.20 and 0.75 mA/cm^2 for Ir-SnO$_2$ and Ir-NbTO, respectively. Overall, we deduce a trend of MoTO > SnO$_2$ > NbTO, thus we observe that MoTO is less active but more stable supported catalyst.

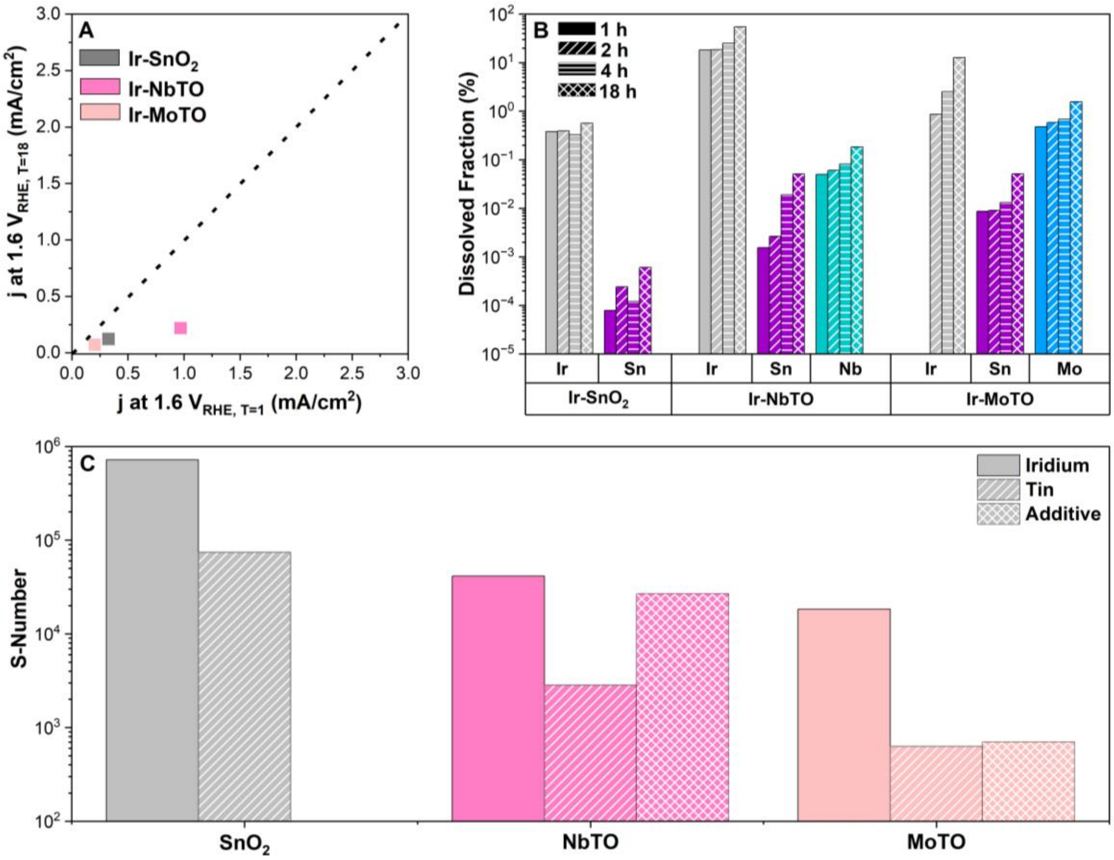

Figure 5.6: Stability analysis of supported catalysts a) current density (j) at 1 hour and 18 hours of chronoamperometry with a line of y = x to guide the eye, b) dissolved fraction of Ir, Sn, Nb and Mo (percentage of element leached determined by ICP-MS / element wt% measured by XRF) and c) stability numbers of Ir and Sn.

When observing the dissolution of the supported catalysts (Figure 5.6b), we determined that most of the dissolution occurred in the first hour as seen in Figure 5.5 potentially due to electrochemical degradation of the supported catalysts. Additionally, the highest dissolved element is Ir in all supported catalysts with a dissolved fraction of 0.6 – 55.0 % after 18 h CA compared to 0.0006 – 0.05 % for Sn and 0.2 – 1.6 % for additives. Interestingly, Ir-MoTO does not show any degradation of Ir until the second hour of dissolution although Ir-MoTO exhibits steep decrease in the first hour (Figure 5.5), indicating that another factor may have influenced the degradation in the first hour. When analysing Sn dissolution in in Ir-NbTO and Ir-MoTO, we observe an increase in dissolution over time with both supported catalysts exhibiting a dissolution of 0.05 % (Figure 5.6b). However, Ir-SnO_2 shows a decrease in dissolution from 2 to 4 hours, highlighting that Sn is possibly repositing onto the catalyst surface.[314] The Ir-NbTO and Ir-MoTO show that Mo dissolution is higher (1.6 %) than Nb dissolution (0.2 %) over 18 h. The high dissolution of Mo compared to Nb, does not correlate with the observed steep decline in current density for Ir-NbTO (Figure 5.5). Therefore, we can hypothesise that the additive is not the main cause of the observed electrochemical degradation in Ir-NbTO.

When normalising the dissolution by the OER activity, known as the S-number, a metric that correlates ratio of moles of oxygen formed and dissolved Ir.[46] Where a high S-number equates to a stable catalyst. We observe that Ir-SnO_2 achieves the highest Ir S-number (10^5) compared to Ir-NbTO and Ir-MoTO (10^4), this correlates with the observed dissolution of Ir (Figure 5.6b). Suggesting that the presence of additives reduces the stability of the supported catalysts. This can be further confirmed when observing the S-number of Sn and additives in Ir-NbTO and Ir-MoTO. Specifically, Ir-MoTO has the lowest S-number of Sn and additive of all the supported catalysts with 10^3 for Sn and 10^2 Mo. This correlates with the observed dissolved fraction (Figure 5.6b), however it does not correlate with the observed electrochemical degradation (Figure 5.5), where Ir-NbTO shows higher degradation despite showing higher stability with S-number of 10^3 for Sn and 10^4 for Nb. Thus, highlighting that the Mo additive, enhances the instability of the supported catalyst. The lack of stability in doped SnO_2 supported catalysts compared to undoped SnO_2 has been reported to occur due to support degradation as a result of dopant leaching.[174] Overall, we observe a stability trend of SnO_2 > NbTO and MoTO.

5.5 Conclusions

In this work, we evaluated the OER activity and stability of SnO_2, NbTO and MoTO supported Ir catalysts in a rotating disk electrode configuration and determined the elemental dissolution using ICP-MS. We observed that supporting Ir on high BET surface area supports enhances the OER activities (1135 – 3000 A/g_{Ir}) at low Ir wt% (3 – 4 wt%) despite obtaining low conductivities. The instability of the supported catalyst can be attributed to the presence of dopants as undoped supported catalyst show higher stability than doped supported catalysts. This work highlights that not one factor is responsible for the enhancement of OER performance as has been discussed in the previous results chapters. The development of highly active and stable supported catalysts relies on balancing the optimum structural and physical properties of each catalyst and catalyst-support.

6 The Synthesis and Characterisation of Metal Stannates for the 2-electron Water Oxidation to Form H_2O_2

6.1 Introduction

In addition to focusing on the OER, the electrochemical production of hydrogen peroxide (H_2O_2) is an important reaction to consider due to the 4e-WOR reaching similar potentials to the 2e-WOR and its industrial benefits. As discussed in section 1.9.2, various different catalysts have shown promising activity and selectivity for the 2e-WOR, including, ZnO,[201] WO_3,[38,197] SnO_2,[38,202] TiO_2[38,197,322], $BiVO_4$,[38,203], $CaSnO_3$[16,18,202] and boron-doped diamond (BDD)[61]. However, despite showing promising results further investigation is required to synthesise alternative catalysts that can yield high selectivity, production rate, stability and activity for the 2e-WOR.

Owing to the aqueous nature of H_2O_2, accurate and appropriate analytical methods are required to quantify the performance (e.g., selectivity) of 2e-WOR electrocatalysts. To date, studies have utilised a range of *in-situ* (rotating ring disk electrodes[204]) and *ex-situ* (titration[38,61,214,323], colorimetry[18,194,202,214], test strips[201,214]) measurements to quantify H_2O_2 production. However, the challenge lies in quantifying very low concentrations of H_2O_2 (< 0.3 ppm), making it difficult to gain an accurate measurement of selectivity.[214]

This chapter focuses on the development of electrocatalysts for the 2e-WOR to electrochemically produce H_2O_2 by synthesising metal stannates ($CaSnO_3$ and $BaSnO_3$). Additionally, nanopowders of Au-$CaSnO_3$ composites were synthesised to investigate the influence of Au on 2e-WOR. The quantification of the electrochemically produced H_2O_2 was performed on each of the synthesised catalysts following a literature method which combined titration with UV-vis absorption spectroscopy technique.

6.2 Experimental Syntheses

6.2.1 Stannate thin films

$CaSnO_3$ and $BaSnO_3$ thin films were synthesised following a previously reported literature protocol.[202] 0.1 M $SnCl_4$, 0.1 M $CaCl_2$ and 0.1 M $BaCl_2$ solutions were prepared from $SnCl_4{\bullet}5H_2O$ (Fisher Scientific), $CaCl_2{\bullet}6H_2O$ (98%+ for Analysis, Fisher Scientific) and $BaCl_2{\bullet}2H_2O$ (Alfa Aesar), respectively. 25 µL of $SnCl_4$ was spin coated onto fluorine doped tin oxide (FTO) glass (~7 Ω/sq, Sigma Aldrich) and dried on a hot plate for 2 minutes at ~ 80 °C. Once dried, 25 µL $CaCl_2$ was spin coated onto the same FTO glass and dried on a hot plate for 2 minutes at ~ 80 °C. Further cycles of spin coating and drying were repeated until a total of 4 layer were deposited per precursor solution. The same process was reported for spin coated deposition of $BaSnO_x$ films. Once all the layers are deposited, the samples were annealed at 700 °C for 5 h.

6.2.2 Stannate nanoparticles

Nanoparticles of $CaSnO_3$ were synthesised following literature.[202] In brief, 3 mmol of $CaCl_2•6H_2O$, 0.57 g $SnCl_4•5H_2O$ and 0.961 g citric acid (99+%, Alfa Aesar) were dissolved in 30 mL of 30 wt% H_2O_2 (30-32%, Fisher Scientific). The solution was stirred, and 30 wt% ammonia hydroxide solution (33%, Fisher Scientific) was added dropwise until a pH of 10 was obtained. The solution was refluxed at 50 °C for 5 h. The precipitates were washed twice using 50 mL deionised water and 50 mL ethanol and annealed in air for 2 h at 600 °C, 650 °C, 700 °C and 750 °C. The nanoparticles annealed at 750 °C were dispersed in solvents (water, IPA and cation-exchange Nafion) and spin coated onto FTO glass to form thin films as described in section 6.3.2.

6.2.3 Au nanoparticles

Two synthesis techniques were adapted from literature to prepare 3 nm[144,324] and 15 nm[325] diameter Au nanoparticles. To form 3 nm Au, 100 mg hydrogen tetrachloroaurate (III) hydrate (49 wt% Au, Alfa Aesar), 10 mL 1,2,3,4-tetrahydronaphthalene (97%, Alfa Aesar), 10 mL oleylamine (80-90% C18, Fisher Scientific) were mixed. In a separate beaker, 43.5 mg borane tert-butylamine complex (TBAB) (97%, Alfa Aesar), 1 mL oleylamine and 1 mL 1,2,3,4-tetrahydronaphthalene was sonicated until dissolved. This solution was quickly injected into the previous solution and vigorously stirred at 22 °C for 1 h. The Au particles were centrifuged in methanol (1:3 gold solution to methanol ratio), dried with Ar and stored in hexane.

To form 15 nm Au particles, a pH optimised mixture of sodium citrate and citric acid was formed by mixing 2.2 mM solutions of sodium citrate and citric acid to obtain a ratio of 75:25. 150 mL of the pH optimised mixture was refluxed at 100 °C (~ 30 mins). 25 mM of hydrogen tetrachloroaurate (III) hydrate was added to the pH optimised mixture and rapidly stirred. The Au mixture was continuous stirred until a deep red colour occurred (~ 2 mins). The heat was then switched off and continuously stirring until the solution's temperature reached 70 °C.

6.2.4 Au-CaSnO$_3$ nanopowders

6.2.4.1 Citrate synthesis

A ligand exchange was performed on 3 nm Au particles prior to the formation of Au-CaSnO$_3$ to replace the oleylamine ligand with citric acid. In brief, following a previously reported synthesis,[326] 10 mg of 3 nm Au particles were suspended in 1.05 mL toluene. A separate mixture of 0.26 mL dimethyl sulfoxide (DMSO, Fisher Scientific) and 0.065 mmol mercaptosuccinic acid (98%, Alfa Aesar) was mixed. The Au/toluene mixture was mixed with the DMSO/mercaptosuccinic acid solution and purged with nitrogen for 20 mins before sonicating for 4 h, forming a black precipitate. The precipitate was washed with 1:3 precipitate to 2-methoxyethanol ratio then suspended in 1.31 mL 0.1 M sodium citrate solution and sonicated overnight (~ 19 h).

Following the ligand exchange, a molar ratio of 1 Au : 5 Ca/Sn was synthesised by mixing 0.02 mmol of ligand exchange Au nanoparticles with 0.1 mmol of $CaCl_2•6H_2O$, 0.1 mmol $SnCl_4•5H_2O$ and 0.166 mmol citric acid (99+%, Alfa Aesar). This solution was dissolved in 1 mL of 30 wt% H_2O_2 (30-32%, Fisher Scientific). The solution was stirred, and 30 wt% ammonia hydroxide solution (33%, Fisher Scientific) was added dropwise until a pH of 10 was obtained. The solution was refluxed at 50 °C for 5 h. The precipitates were washed twice using 4 mL deionised water and 4 mL ethanol and dried at 80 °C for 2 h in air.

For 15 nm Au, to achieve 1:5 molar ratio of Au:Ca/Sn, the same method as above was followed except 90 mL of the Au in 75:25 citrate solution was added in place of citric acid.

6.2.4.2 Oleylamine synthesis

Using the 3 nm Au particles (prior to ligand exchange) stored in hexane from section 6.2.3 and adapting previous literature,[144] a molar ratio of 1 Au : 5 Ca/Sn was achieved by mixing 0.02 mmol of gold (in hexane solution) with 0.1 mmol calcium 2,4-pentanedionate hydrate (99%, Fisher Scientific), 0.1 mmol tin (II) acetylacetonate (99.9% Sigma Aldrich), 0.2 mmol oleic acid and 3 mL oleylamine. The mixture was heated for 1 h at 100 °C under argon. Separately, 0.8 mmol TBAB and 400 μL oleylamine was mixed and injected into the Au/Ca solution and stirred for 1 h.

For both syntheses, the nanoparticles were dispersed in solvents (water, IPA and cation-exchange Nafion) and spin coated onto FTO glass to form thin films. Full experimental details are provided in section 6.3.2.

6.3 Material Characterisation

6.3.1 Physical characterisation

Full details of the instruments and experimental setup is described in Chapter 2. In brief, the crystal structure of the nanopowders and thin films were analysed by X-ray diffraction (XRD). X-ray photoelectron spectroscopy (XPS) was utilised to determine the oxidation state of the catalysts. The morphology, composition and elemental maps of the stannate catalysts were determined by scanning electron microscopy (SEM) coupled to an energy dispersive X-ray spectroscopy (EDX). The morphology, particle sizes and elemental distribution maps of the Au containing catalysts was determined by transmission electron microscopy (TEM) and scanning transmission electron microscopy coupled to energy dispersive X-ray spectroscopy (STEM-EDX). TEM sample preparation was conducted by dispersing the catalysts in hexane and dropcasting 10 µL onto holey carbon coated copper support grids (400 mesh Cu grids, Agar Scientific). Ultraviolet–visible spectroscopy (UV-vis) was conducted to determine H_2O_2 quantification.

6.3.2 Electrochemical characterisation

Electrochemical measurements were performed in a 3-electrode configuration in a Teflon beaker. FTO glass was used as the substrate/working electrode for the catalysts, graphite rod as the counter electrode, Ag/AgCl reference electrode and 2 M $KHCO_3$ (pH ~ 8.3) throughout. The stannate and Au-$CaSnO_3$ nanopowder inks were synthesised by dispersing 3.5 mg catalyst in 1.6 mL deionised water (18.2 MΩ, Milli-Q) and 0.5 mL cation exchanged Nafion. The cation-exchanged Nafion was prepared by dissolving 2 mL Nafion (D-520 dispersion, Alfa Aesar) into 1 mL 0.1 M KOH.[327] The inks were sonicated for 30 mins in a horn sonicator (505, Fisherbrand). The ink was spin coated in 10 µL increments until 50 µL was deposited onto the FTO glass. The FTO glass was dried for 2 mins at ~ 80 °C after each 10 µL deposition. The stannate thin films were used as-synthesised. The catalyst coated FTO glass was made into electrodes by placing a drop gallium indium eutectic (99.99%, Alfa Aesar) onto the top of the FTO and covering with copper tape. The copper tape was isolated by covering with PTFE tape (RS Components). Exposed FTO (that was free of catalyst) was isolated using

Locite™ EA 9461 epoxy (RS Components) and left to dry for >12 hours prior to running electrochemistry.

Prior to measuring the OER activity, ohmic resistance was measured by potentiostatic electrochemical impedance spectroscopy (PEIS) with 85% correction at 1.7 V_{RHE} (200 kHz). The OER activity was determined by using cyclic voltammetry (CV) to sweep potential between 1.7 – 2.4 V_{RHE} at 10 mV/s for 10 cycles, the oxidation sweep was plotted to observe the electrochemical performance. The 4th cycle was used to evaluate the current density. Stability measurements were conducted using chronoamperometry (CA) to hold potential at 3.4 V_{RHE} for 5 hours. At hourly intervals, 1.5 mL of electrolyte was collected to quantify H_2O_2 produced.

6.3.3 H_2O_2 quantification

Following literature methods,[196] a combination of titration and UV-vis analysis was conducted to determine the concentration and selectivity of H_2O_2 for each electrode. An aliquot of electrolyte (1.5 mL) was collected hourly and replaced with fresh 2 M $KHCO_3$. The aliquot was mixed with 1 M H_2SO_4 (1.5 mL) and the UV-vis absorbance collected (500 – 700 nm, Figure 6.1a) to obtain the blank spectrum. 0.4 mM $KMnO_4$ was added in 100 µL increments to the aliquot, and the absorbance spectrum collected after each 100 µL addition. The absorbance at λ_{max} = 526 nm was plotted against volume of $KMnO_4$ (Figure 6.1b), a tangent line is added to obtain the endpoint. Based on the stoichiometric reaction between $KMnO_4$ and H_2O_2 (equation. 6.1),[207] the endpoint can be used to measure the concentration of H_2O_2 (equation. 6.2 - (equation. 6.5) and subsequently the selectivity (equation. 6.6).

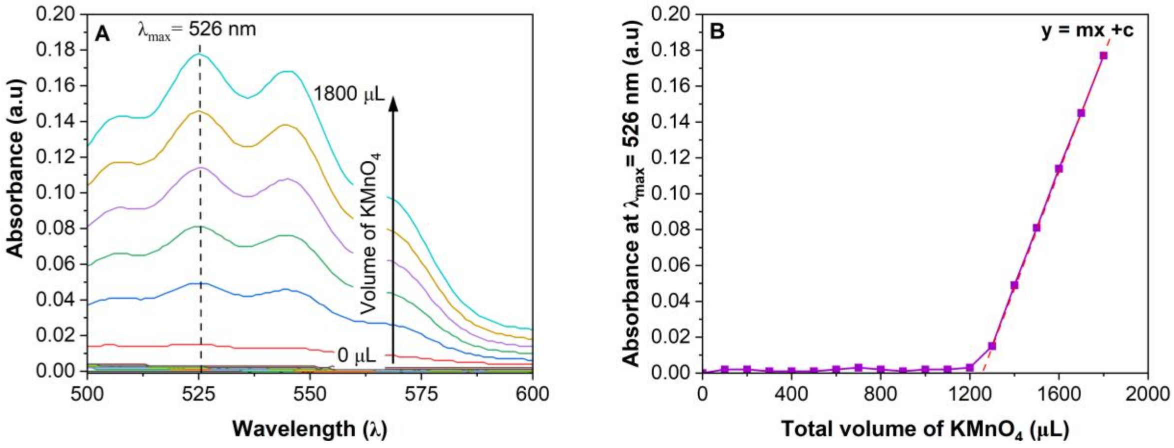

Figure 6.1: a) Absorbance spectra of blank FTO after 1 h CA and b) Absorbance at λ_{max} of blank FTO after 1 h CA against total volume of $KMnO_4$ added to aliquot. Red line indicates tangent line.

$$2MnO_4^- + 5H_2O_2 + 6H^+ \rightarrow 2Mn^{2+} + 5O_2 + 8H_2O \qquad \text{(equation. 6.1)}$$

$$mol\ of\ KMnO_4 = conc\ of\ KMnO_4\ \times vol\ of\ KMnO_4 \qquad \text{(equation. 6.2)}$$

$$mol\ of\ H_2O_2\ in\ aliquot\ = \left(\frac{mol\ of\ KMnO_4}{vol\ of\ aliquot}\right) \times \frac{5}{2} \qquad \text{(equation. 6.3)}$$

$$mol\ of\ H_2O_2\ in\ electrolyte = \left(\frac{vol\ of\ total\ soln}{vol\ of\ aliquot}\right) \times\ mol\ of\ H_2O_2\ aliquot \qquad \text{(equation. 6.4)}$$

$$conc\ of\ H_2O_2\ = \frac{mol\ H_2O_2\ in\ total\ electrolyte}{vol\ of\ total\ soln} \qquad \text{(equation. 6.5)}$$

$$Selectivity\ (\%) = \left(\frac{mol\ of\ H_2O_2\ \times 96485\ C/mol \times 2e^-}{Total\ charge\ passed\ (C)}\right) \times 100 \qquad \text{(equation. 6.6)}$$

6.4 Results and Discussion

6.4.1 Thin Films: Materials Characterisation

Thin films of $CaSnO_3$ and $BaSnO_3$ were synthesised by spin coating $CaSnO_3$ and $BaSnO_3$ nanoparticles onto FTO. XRD was performed to determine the crystallinity of the thin films (Figure 6.2a). The diffracted peaks evidence a cubic perovskite structure for $BaSnO_3$ when prepared at 700 °C with peaks at 30.6° and 54.5° indexed to (110) and (211), respectively.[328] The remaining peaks at 26.6°, 33.8°, 37.9°, 51.7° and 54.8° were attributed to rutile SnO_2. Additional peaks at < 24° are attributed to $BaCO_3$.[329] The expected XRD peaks associated with perovskite $CaSnO_3$ were not detected, indicating that the annealing temperature was not high enough to form a perovskite structure. The annealing temperature could not be further increased due to the thermal limitations of FTO. Rather, the prepared $CaSnO_3$ thin film shows only peaks which can be ascribed to an uncoated FTO with peaks at 26.6°, 33.8°, 37.9°, 51.7° and 54.7° attributed to rutile SnO_2 and indexed to (110), (101), (200), (211) and (220) (Figure 6.2a). These prepared films will henceforth be named $CaSnO_x$.

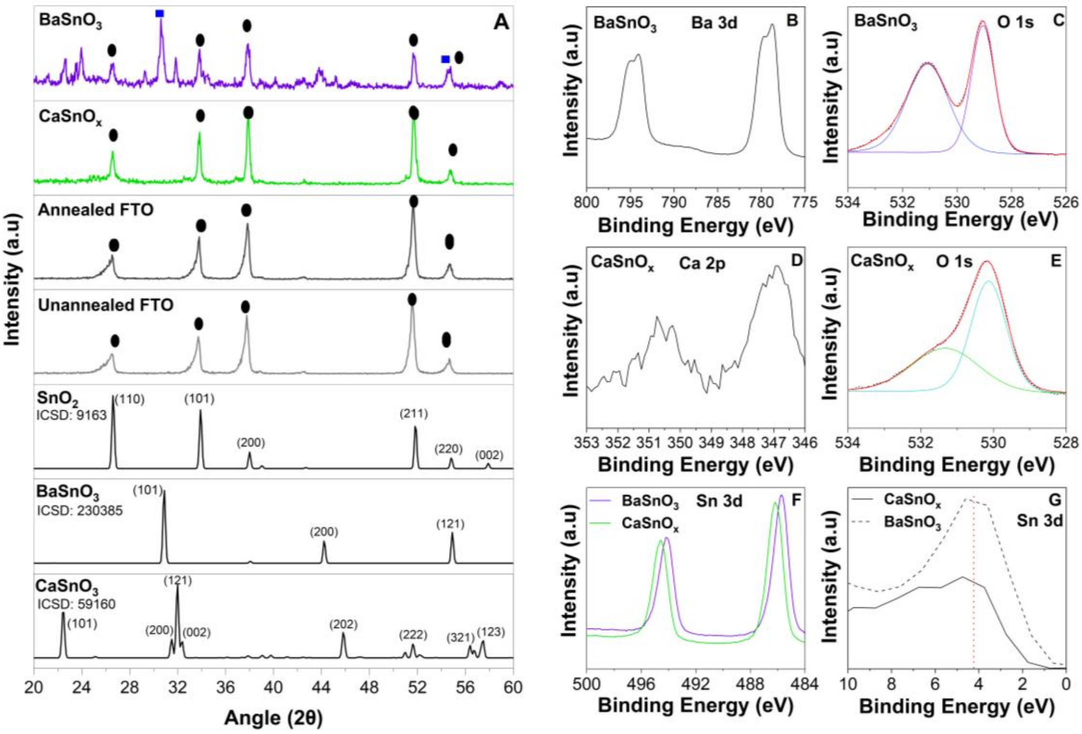

Figure 6.2: a) XRD peaks of unannealed FTO, annealed FTO, $CaSnO_x$ and $BaSnO_3$ alongside the relevant ICSD reference patterns. Blue symbol indicates $BaSnO_3$ peaks and black indicates SnO_2 and XPS spectra of b) Ba 3d, c) O 1s for $BaSnO_3$, d) Ca 2p, e) O 1s for $CaSnO_x$, f) Sn 3d spectra and g) Sn 3d valence bands of $BaSnO_3$ and $CaSnO_x$.

The oxidation states of the thin film surfaces were investigated by X-ray photoelectron spectroscopy (XPS). Specifically, XPS spectra of Ba 3d, Sn 3d and O 1s for $BaSnO_3$ were analysed, Ba 3d region shows two sets of doublets (778.8 eV and 779.7 eV) indicating the presence of two different Ba oxidation species, likely due to the presence of both $BaSnO_3$ and $BaCO_3$ (Figure 6.2b).[330] The O 1s spectra for $BaSnO_3$ was deconvoluted and analysed, peaks at 529.0 eV and 531.0 eV are attributed to lattice oxygen (oxygen-metal bond) and defective oxygen, respectively (Figure 6.2c).[331] Although there was no observed $CaSnO_3$ perovskite structure by XRD (Figure 6.2a), XPS analysis clearly indicates the presence of calcium at the surface of the thin film (Figure 6.2d). Specifically, the Ca 2p region showed a doublet with peaks at 347.0 eV and 350.5 eV. The peak positions and separation of peaks ~3.5 eV suggests the presence of Ca^{2+}.[332] The O 1s region was analysed and showed a more oxidised surface for $CaSnO_3$ than $BaSnO_3$ with the lattice oxygen (530.1 eV) and defective oxygen (531.4 eV) peaks shifting to slightly higher binding energies (Figure 6.2e). The Sn 3d region for both $BaSnO_3$ and $CaSnO_x$ was analysed and showed $CaSnO_x$ at a higher binding energy (486.2 eV) compared to $BaSnO_3$ (485.7 eV) (Figure 6.2f). Due to the overlapping binding energies of SnO and SnO_2 (~ 486 – 487 eV),[333] the valence band spectra (< 10 eV) of each catalyst was analysed and showed peaks at ~ 4 eV which is attributed to SnO_2 (Figure 6.2g).[334]

6.4.2 Thin Films: Electrochemical Performance

The electrochemical performance of the thin films was assessed in 2 M $KHCO_3$ electrolyte in a three-electrode configuration, with catalyst coated FTO glass as the working electrode. During CA measurements, 1.5 mL aliquots of electrolyte were taken at 1, 2, 4 and 18 h and titrated with $KMnO_4$. The colour change was detected using UV-vis to determine the endpoint from which the concentration and selectivity to H_2O_2 production were calculated. Two controls were also investigated for the 2e-WOR, unannealed FTO (UA-FTO) and annealed FTO (A-FTO). The linear sweep voltammogram (LSV) between 1.7 – 2.4 V_{RHE} showed that UA-FTO obtained the highest geometric current density of 1.36 mA/cm^2 at 2.38 V_{RHE} compared to 0.46 mA/cm^2 for $BaSnO_3$ and 0.35 mA/cm^2 $CaSnO_x$ (Figure 6.3a). It has previously been reported that FTO is active for 2e-WOR at high overpotentials (> 1240 mV) leading to high current densities (>20 mA/cm^2).[203,323] We show that this is an underestimation of FTO performance in this potential window.

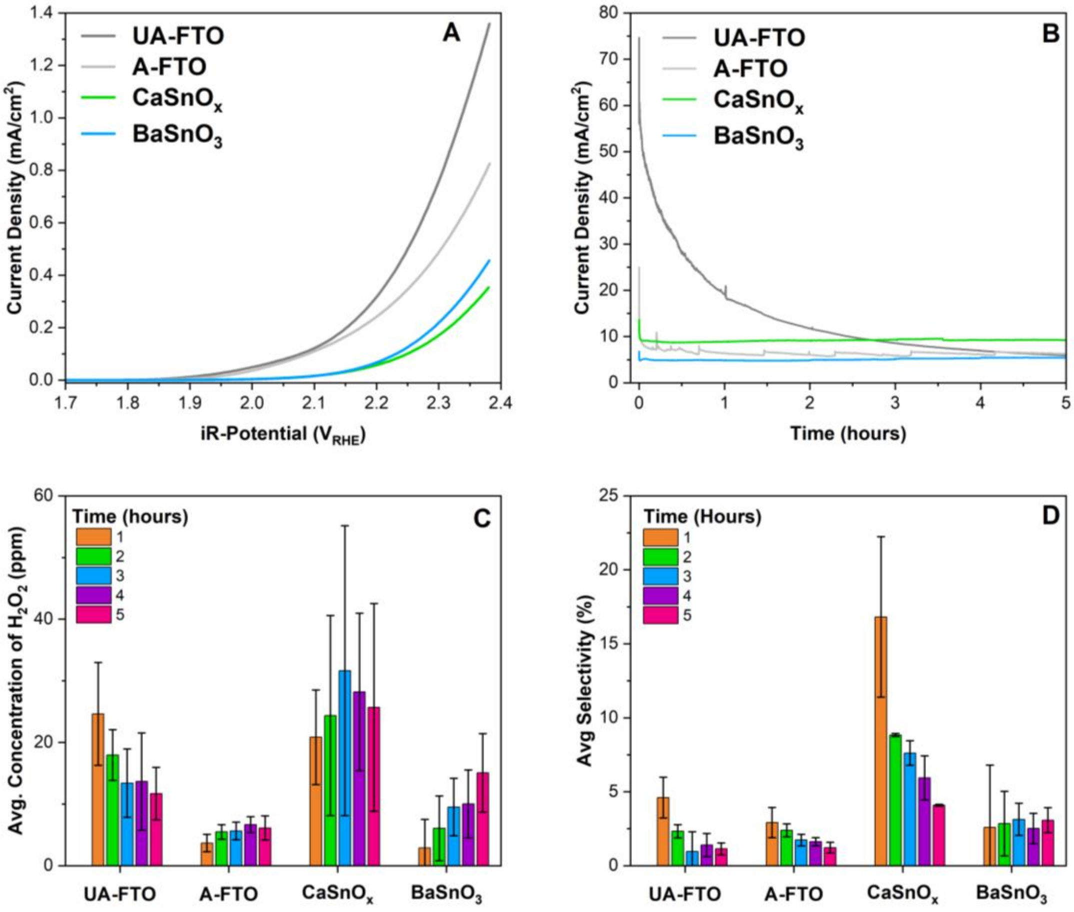

Figure 6.3: Electrochemical performance of the uncoated and catalyst coated FTO substrates a) geometric current density, b) chronoamperometry at 3.4 V_{RHE}, c) average concentration of produced H_2O_2 and d) selectivity of H_2O_2. All electrochemical analyses were undertaken in 2 M $KHCO_3$ (pH ~ 8.3) in a 3-electrode configuration.

Due to the low current density at 2.4 V_{RHE}, low concentrations of H_2O_2 are likely to be produced and therefore the CA was performed at higher potential. The production of H_2O_2 was evaluated by holding potential at 3.4 V_{RHE} (CA) for 5 h. Conditioning of the electrode to achieve steady state catalyst surface was not performed prior to CA in line with literature protocols.[247] The initial steep decrease in electrode performance at 0 – 0.05 h for all electrodes is possibly due to the lack of conditioning of the catalyst prior to stability measurements (Figure 6.3b). After 0.05 h, uncoated FTO (UA and A-FTO) initially exhibited the highest current density of > 25 mA/cm^2 at 0.05 hours compared to 9 mA/cm^2 for $BaSnO_3$ and 5 mA/cm^2 for $CaSnO_x$ (Figure 6.3b). Over the duration of the 5-hour stability test, we observe a steep decline in current density for UA-FTO and A-FTO. Conversely, after 5 h CA, $CaSnO_x$ maintains a current density of ~ 9.2 mA/cm^2 for 3 hours. Although $BaSnO_3$ exhibits lower current density than uncoated FTO, the catalyst maintained ~ 5 mA/cm^2 for 5 hours. We speculate that the hourly increase in current density is due to accumulated bubbles, leading to blocked active sites due to bubble accumulation.[312] The hourly collection and replenishment of electrolyte for H_2O_2 quantification dispelled the bubbles and exposed more of the active sites on the surface leading to increased current density.

6.4.3 Thin Films: H_2O_2 Quantification

Through electrolyte aliquoting, the concentration of H_2O_2 throughout the CA stability test was monitored (Figure 6.3c), UA-FTO and $CaSnO_x$ produced similar concentrations of H_2O_2 in the first hour (~ 25 ppm). It is important to note that the presence of carbonate electrolyte can enhance H_2O_2 production due to the electrochemical oxidation of HCO_3^- to HCO_4^- at 1.80 V_{RHE} initiating the formation of H_2O_2 via HCO_4^- decomposition.[193] Over 3 hours, the concentration of H_2O_2 decreased for UA-FTO while the concentration increased to 32 ppm for $CaSnO_x$. After 3 h, we observed a decrease in H_2O_2 concentration for $CaSnO_x$ to 26 ppm at 5 h. The decrease in concentration over time has previously been reported for $CaSnO_3$ and attributed to the electrochemical decomposition of H_2O_2.[16,202] The thermodynamic potential for H_2O_2 oxidation (0.67 V_{RHE}) is lower than the applied potential during the CA, likely leading to decomposition of H_2O_2 occurring before water oxidation.[61] In addition, the known instability of H_2O_2 in alkaline media likely further degrades H_2O_2 with time.[335] $BaSnO_3$ showed a steady increase in concentration during 5 h measurements. However, the concentrations did not exceed concentrations seen in $CaSnO_x$, indicating that $CaSnO_x$ is more active for H_2O_2 production.

The selectivity of the prepared thin films was calculated each hour based on the moles of H_2O_2 produced during the stability measurement and the cumulative charge passed at each hour during the CAs (Figure 6.3d). We observe that the first hour produces the highest selectivity for UA-FTO, A-FTO and $CaSnO_x$ followed by a decrease in selectivity over time. $CaSnO_x$ was found to have the highest selectivity to H_2O_2 with 17 % at 1 h compared to 3 % for $BaSnO_3$ and 3 – 5 % for uncoated FTO. Similar to the observed changes in H_2O_2 concentration over the 5 h CA testing, the selectivity of uncoated FTO and $CaSnO_x$ decreases over time. For $BaSnO_3$, the selectivity is maintained at ~ 3 % irrespective of the increase in H_2O_2 concentration, highlighting that $BaSnO_3$ is not highly selective for H_2O_2 production.

It is also important to note that the conductivity of the thin film can also hinder the performance of an electrode. A study of 0.5 wt% $CaSnO_3$ thin films with 1 – 7 layers of $CaSnO_3$ were electrochemical tested for H_2O_2.[202] A decrease in current density and selectivity as a function of increasing catalyst layer was observed. In this chapter, 5 layers of 0.3 w/v% $CaSnO_x$ and 0.4 w/v% $BaSnO_3$ were synthesised. We suggest that future experiments can focus on tuning the concentration of catalyst solution and number of spin coated layers, potentially improving our observed electrochemical performance and production of H_2O_2.

6.4.4 Nanoparticles of $CaSnO_3$

Nanoparticles of $CaSnO_3$ were synthesised by the thermal decomposition of peroxo-precursors adapted from literature.[202] The crystal structure of the $CaSnO_3$ was analysed by XRD. It was observed that calcination temperature (600 – 750 °C) influenced the crystal structure of $CaSnO_3$ (Figure 6.4). Calcination temperatures of > 700 °C showed the presence of $CaSnO_3$ with a perovskite structure with peaks at 22.6°, 32.0°, 46.0°, 51.8°, 56.7° and 57.7°.[336] Similar effects of annealing temperature on crystallinity have been previously reported for $CaSnO_3$ nanoparticles.[16]

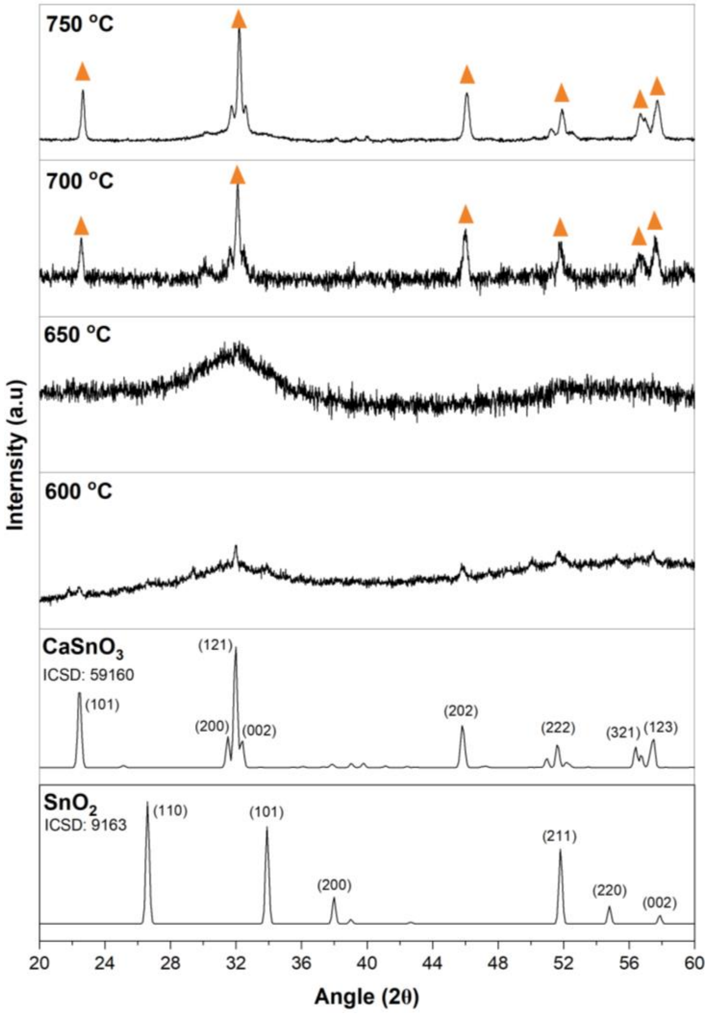

Figure 6.4: XRD patterns of $CaSnO_3$ annealed at 600, 700 and 750 °C and relevant reference patterns from ICSD. Orange symbols represent the $CaSnO_3$ peaks.

The perovskite structure of $CaSnO_3$ at 750 °C was further characterised and will be ascribed as $CaSnO_3$-750 in this chapter. The morphology of $CaSnO_3$-750 was characterised by SEM (Figure 6.5). We observed agglomerated clusters of $CaSnO_3$ particles of >20 nm. Although, the catalyst was thoroughly washed prior to annealing, the weight fractions obtained from SEM-EDX showed the presence of residual Cl^- (0.3 wt%).

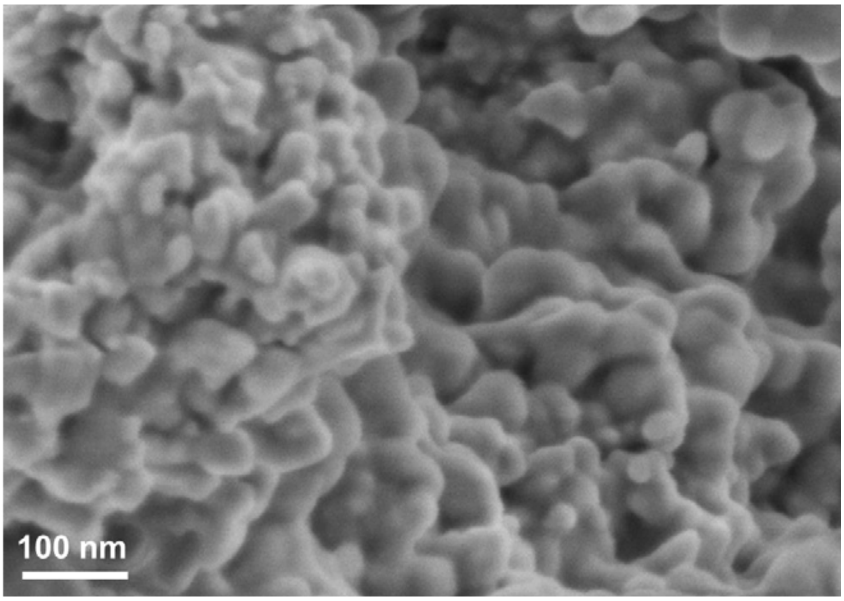

Figure 6.5: Micrograph of $CaSnO_3$-750 collected by SEM.

The electrochemical performance of $CaSnO_3$-750 was assessed in a 3-electrode configuration with FTO as the working electrode. The nanoparticles ($CaSnO_3$-750) were spin coated onto FTO with a catalyst loading of 0.1 mg_{Cat}/cm^2 (0.2 w/v%). The $CaSnO_3$-750 were compared against unannealed FTO (UA-FTO) and $CaSnO_x$ (Figure 6.6). The increase in crystallinity has been reported to enhance catalytic activity and H_2O_2 production rates.[16] Interestingly, we observe that the LSV for $CaSnO_3$-750 and $CaSnO_x$ are very similar, despite the differences in crystallinity. Additionally, when comparing the geometric activity at 2.37 V_{RHE} we observe lower current densities in both nanoparticle $CaSnO_3$-750 and thin films of $CaSnO_x$, compared to UA-FTO (1.27 mA/cm^2). We hypothesise that the lack of conductivity results in low current densities. $CaSnO_3$ is a wide band gap semiconductor (E_g = ~ 4.4 eV) which likely also results in low conductivity.[337] Indeed, a recent study reported that $CaSnO_3$ encapsulated in carbon fibre (CF) increased in conductivity compared to bare $CaSnO_3$.[18] This was attributed to sufficient contact between conductive CF and $CaSnO_3$ leading to improved activity and high Faradaic efficiency at low potentials (~ 90 % at 2.9 V_{RHE}).

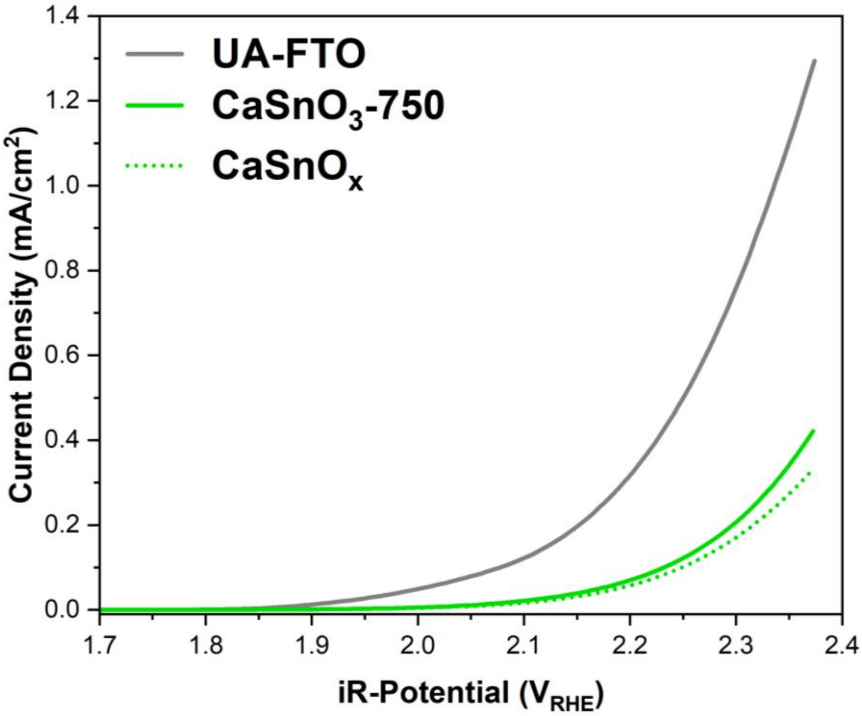

Figure 6.6: Geometric activity of unannealed FTO, $CaSnO_x$ thin films and $CaSnO_3$-750 nanoparticles. All electrochemical analyses were undertaken in 2 M $KHCO_3$ (pH ~ 8.3).

6.4.5 Au-$CaSnO_3$ Nanoparticles: Material Characterisation

Au is known to be thermodynamically stable at potentials above water oxidation (1.23 V)[338] and has been reported as an efficient catalyst for the 2-electron oxygen reduction reaction to form H_2O_2.[21,339] Owing to the low conductivity in $CaSnO_3$, we investigated Au-$CaSnO_3$ and Au-SnO_2 nanoparticles as a potential strategy to improve the electrochemical 2e-WOR performance of these materials.

We synthesised Au nanoparticles from two synthetic techniques (labelled “optimised mixing” and “oleylamine based”) to obtain two different Au particle sizes. Using high resolution TEM (HR-TEM), we analysed the morphology and particle size of the Au particles and Au-$CaSnO_3$ (Figure 6.7). Both Au syntheses showed spherical Au particles, irrespective of the synthesis methodology. The oleylamine synthesis resulted in smaller Au particles of 3 nm whereas the optimised mixing synthesis obtained Au particles of 15 nm (Figure 6.7a and d, respectively). The incorporation of Au into the $CaSnO_3$ synthesis produced agglomerated Au-$CaSnO_3$ irrespective of Au particle size (Figure 6.7c,d). Specifically, Au-$CaSnO_3$ from 3 nm Au (Au-$CaSnO_3$-OA) showed large, agglomerated Au particles attached to large $CaSnO_3$ agglomerates (Figure 6.7e). Conversely Au-$CaSnO_3$ synthesised with 15 nm Au particles (Au-$CaSnO_3$-OM) showed a more homogeneous distribution of Au clusters across large $CaSnO_3$ agglomerates (Figure 6.7f).

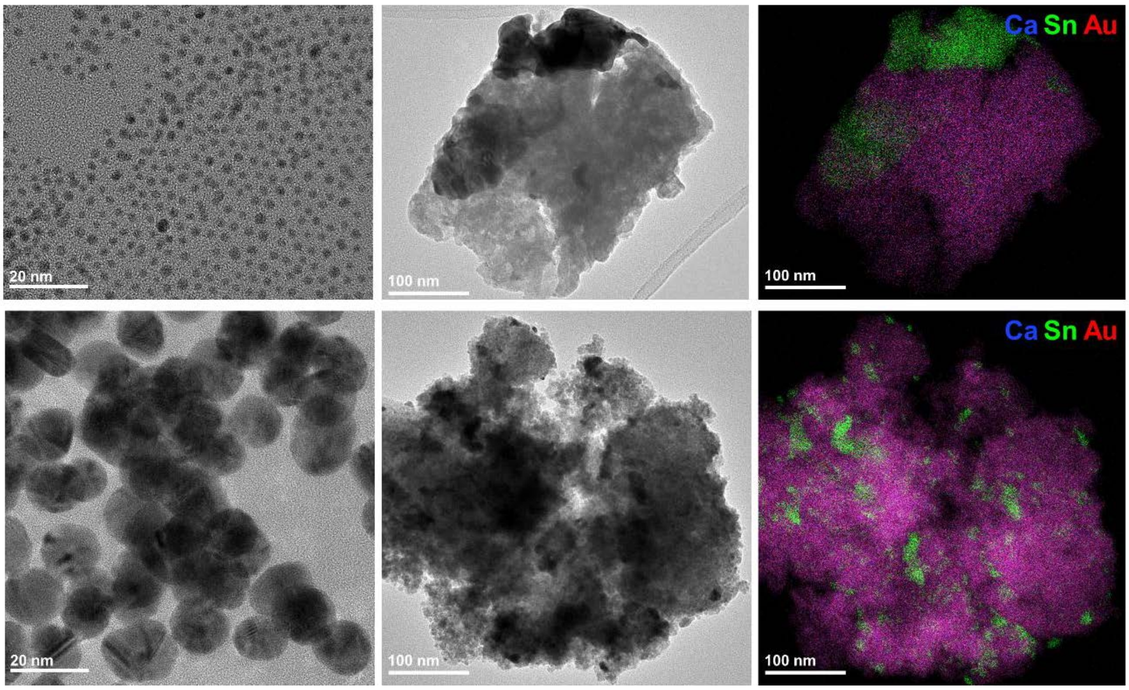

Figure 6.7: HR-TEM images of Au synthesised by a) oleylamine, b) optimised mixing, HR-TEM images of c) Au-$CaSnO_3$-OA, d) Au-$CaSnO_3$-OM, elemental distribution maps of Ca, Sn and Au for e) Au-$CaSnO_3$-OA and f) Au-$CaSnO_3$-OM.

We also synthesised Au-$CaSnO_3$ solution using the 3 nm Au nanoparticles (oleylamine synthesis) as described in Section 6.2.4.2. Using HR-TEM, we observed the formation of Janus-type nanoparticles (Figure 1.8a). The elemental distribution maps (Figure 1.8c) showed that despite the inclusion of a calcium precursory, Au-SnO_x were prepared rather than the expected Au-$CaSnO_3$. We hypothesise that the synthesis required longer reaction time to form Au-$CaSnO_3$ particles.

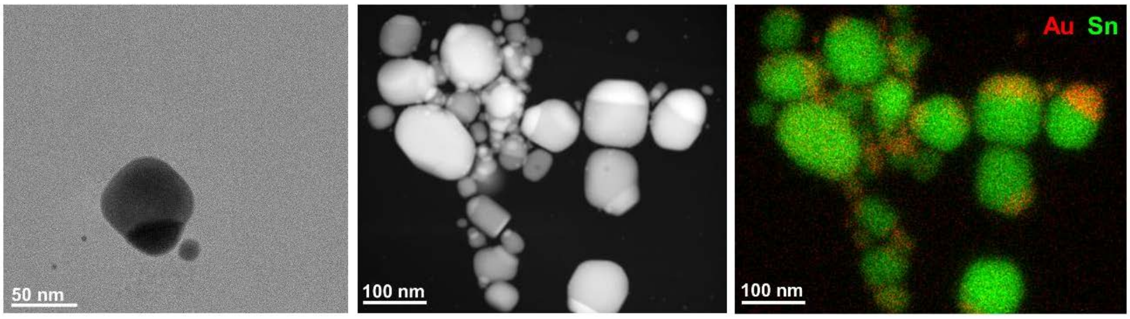

Figure 6.8: a) HR-TEM images of Au-SnO_x, b) High angular annular dark field (HAADF) and c) elemental distribution maps of Sn and Au.

6.4.6 Au-$CaSnO_3$ and Au-SnO_x Nanoparticles: Electrochemical Performance

Although, we were able to analyse the morphology of Au-SnO_x via TEM (Figure 6.8), the oleylamine synthesis route did not produce a high enough yield (< 1 mg) to prepare an ink and assess the electrochemical activity of the material. Therefore, the following electrochemical performance is based on the citrate synthesised Au-$CaSnO_3$ (Figure 6.7c, d). The electrochemical measurements were undertaken in 2 M $KHCO_3$ (pH ~ 8.3) in a 3-electrode configuration. The Au-$CaSnO_3$-OA and Au-$CaSnO_3$-OM were dispersed in water, IPA and nafion and spin coated onto FTO glass to form working electrodes (as described in Section 6.3.2) with a catalyst loading of 0.1 mg_{Cat}/cm^2.

The electrochemical performance was assessed by conducting a LSV from 1.7 to 2.4 V_{RHE} followed by CA at 3.4 V_{RHE}. The geometric activity of Au-$CaSnO_3$ was compared against $CaSnO_3$-750, the results showed that the addition of Au to $CaSnO_3$ did not improve the current density. Specifically, at 2.37 V_{RHE}, nanoparticles of $CaSnO_3$-750 exhibited 0.42 mA/cm^2 compared to lower current densities achieved for Au-$CaSnO_3$-OA (0.34 mA/cm^2) and Au-$CaSnO_3$-OM (0.31 mA/cm^2) (Figure 6.9a). Future experiments should seek to quantify the effect of catalyst loading on the electrochemical performance (LSV and CA).

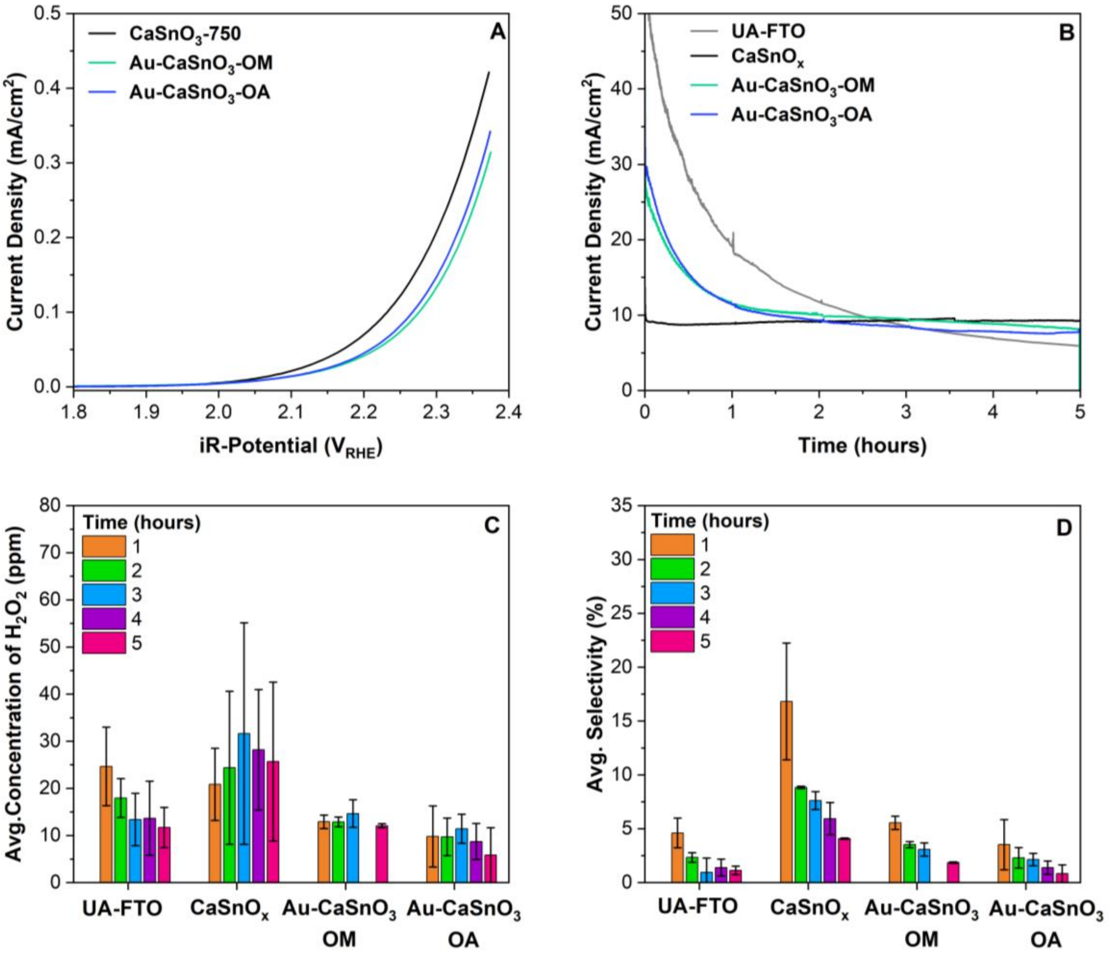

Figure 6.9: Electrochemical analysis as a) geometric activity of Au-$CaSnO_3$ from inorganic synthesis and $CaSnO_3$, b) chronoamperometry at 3.4 V_{RHE} of Au-$CaSnO_3$, $CaSnO_3$-TF and UA-FTO, c) average concentration of H_2O_2 produced and d) average selectivity of H_2O_2. All electrochemical analyses were undertaken in 2 M $KHCO_3$ (pH ~ 8.3).

Stability measurements were again conducted by CA holds at 3.4 V_{RHE} coupled to electrolyte aliquoting to determine whether the presence of Au would increase the production of H_2O_2 irrespective of the low current densities (Figure 6.9b). Upon, visual inspection of the coated FTO after CA measurements no catalyst remained on the FTO (Figure 6.10). Hence the observed decline in current density for Au-$CaSnO_3$ is potentially due to the dissolution/delamination of the catalysts. After 5 h, we observe similar trend to geometric activity with both Au-$CaSnO_3$ catalysts obtaining low current densities of 7.51 mA/cm^2 for Au-$CaSnO_3$-OM and 8.13 mA/cm^2 for Au-$CaSnO_3$-OM compared to $CaSnO_x$ (9.23 mA/cm^2).

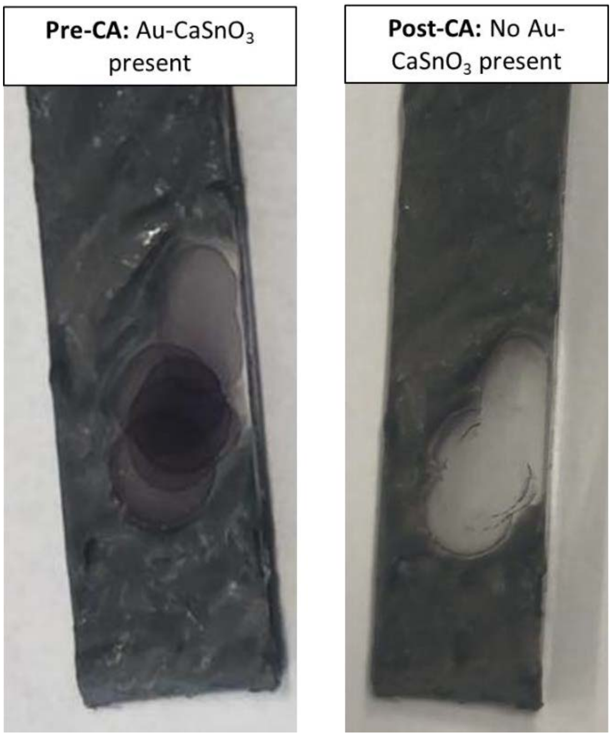

Figure 6.10: Image of Au-$CaSnO_3$ coated FTO prior to CA measurements and post CA measurements.

The concentration and selectivity of H_2O_2 was assessed during the stability measurements. The trend in concentrations of H_2O_2 for Au-$CaSnO_3$ is similar to $CaSnO_x$ with an initial increase and subsequent decrease over time (Figure 6.9c). However, the observed H_2O_2 concentrations are significantly lower for Au-$CaSnO_3$ compared to $CaSnO_x$ for all samples investigated (as expected due to the low geometric current densities observed in Figure 6.9a. As previously described, this could be due to the electrochemical decomposition of H_2O_2 or a result of catalyst dissolving or delaminating as seen in Figure 6.10. After 5 h, the concentration of Au-$CaSnO_3$-OM is 12 ppm compared to Au-$CaSnO_3$-OA with 6 ppm.

Similar to the measured concentrations of H_2O_2, the selectivity of Au-$CaSnO_3$ showed high selectivity in the first hour followed by a decrease over time, confirming the potential of electrochemical decomposition of H_2O_2 (Figure 6.9d). As expected, the selectivity of Au-$CaSnO_3$-OM is higher than Au-$CaSnO_3$-OA. Specifically, Au-$CaSnO_3$-OM achieves 6 % selectivity compared to 4 % for Au-$CaSnO_3$-OA at 1 h. Overall, the addition of Au to $CaSnO_3$ did not improve the activity or selectivity of $CaSnO_x$ potentially correlated to the lack of Au content or catalyst degradation.

6.5 Conclusion

In summary, a titration/UV-vis quantification method was adopted to determine the concentrations and electrochemical selectivity of various electrocatalysts ($CaSnO_3$, $BaSnO_3$ and Au-$CaSnO_3$) as thin films and nanopowders for the 2e-WOR to H_2O_2. Unfortunately, compared to literature catalysts, we find very low yields and selectivity. We speculate that the reaction time was not substantial to produce high yields and the conductivity of the material was not sufficient to improve electrochemical performance. In addition, the composite Au-$CaSnO_3$ did not provide an increase in electrochemical performance. We hypothesise that the catalyst dissolution or delamination from the substrate, hindered the electrochemical performance of Au-$CaSnO_3$. We suggest that an investigation into the degradation mechanism of the catalyst would provide information on the viability of Au-$CaSnO_3$ as an electrocatalyst for the 2e-WOR. Furthermore, we show that the majority of H_2O_2 produced electrochemically decomposed after the first hour, highlighting the highly unstable nature of H_2O_2 after 1 h. It is also important to note that benchmarking using FTO substrate is complex due to FTO also turning over the 2e-WOR.

7 Conclusions and Future Work

7.1 Overall Conclusions

The synthesis of electrocatalyst is vital towards the decarbonisation of transportation and chemical industries using electrolysis. This thesis focused on synthesising and characterising cost-effective electrocatalysts for the 2-electron and 4-electron water oxidation reactions (2e-WOR and 4e-WOR, respectively). Specifically, by synthesising doped-SnO_x and titanium dioxide (TiO_2) supported iridium catalysts and metal stannate catalysts. The overall aims and objectives of this thesis were to investigate the electrochemical activity, selectivity and stability of the synthesised electrocatalysts and determine how their physical and electronic properties influenced the electrochemical performance. The first three project chapters of this thesis Chapters 3 – 5 focused on synthesising Ir-based supported catalysts for the oxygen evolution reaction (OER, 4e-WOR). The final project chapter (Chapter 6) focused on synthesising metal stannates and quantifying the electrochemical production of H_2O_2 via the 2e-WOR.

In Chapter 3, hollow TiO_2 coated with AuPd nanoparticles were synthesised as supports for Ir. The supported catalysts showed high OER activity and stability in a rotating disk electrode configuration and a membrane electrode assembly (MEA). The work highlights the effect of AuPd and Ir loading as well as thermal annealing environment on the OER performance. Specifically, the high AuPd and Ir loading leads to a highly active and stable supported catalyst. Through various material characterisation techniques, this work demonstrated that there is not one single parameter that influences the high OER performance. However, the combination of conductivity, Ir oxidation state, crystallite size and particle sizes of the hollow TiO_2 coated AuPd influenced the OER performance.

Chapter 4 and 5 focused on the influence of doped SnO_x as catalysts-supports. Chapter 4 investigated the influence of Ir deposition techniques on antimony tin oxide (ATO) supported Ir catalysts. Specifically, the polyol and acid-modified polyol (AMP) deposition techniques were utilised to synthesis Ir-ATO supported catalysts. The AMP synthesis requires a pH adjustment which we hypothesise can lead to an increase in the surface charge on the support and aids Ir loadings compared to polyol synthesis. The influence of ATO surface area was also investigated and found that the AMP deposition technique combined with high surface area support improves the OER activity, highlighting the enhanced Ir utilisation for AMP synthesised supported catalysts. This work highlights the influence that Ir deposition techniques have on conductivity, support surface area and Ir loading of supported catalyst to improve OER performance.

Chapter 5 investigated the effect of additives to SnO_2 support and its influence on the OER performance. Specifically, Nb-SnO_2 and Mo-SnO_2 were synthesised and evaluated as catalysts-supports for Ir. It was determined that the synthesis of high surface area supports aids in enhancing the OER performance of the supported catalyst. However, the low Ir content (< 4 %) reduced the conductivity and stability of the supported catalyst. Therefore, similar to all the supported catalyst chapters (3 - 5), a combination of high Ir content, conductivity and surface area support is required to achieve both an active and stable supported catalyst. Overall, the supported catalyst chapters showed that the use of supported catalysts outperforms unsupported IrO_2.

Chapter 6 focused on synthesising and characterising metal stannates ($CaSnO_3$ and $BaSnO_3$) and composites of Au-$CaSnO_3$ as thin films and nanopowder catalysts for the electrochemical production of H_2O_2 via the 2e-WOR. A quantification method involving titration and UV-Visible spectroscopy technique was utilised to quantify the concentration and electrochemical selectivity of the electrocatalysts for the 2e-WOR to H_2O_2. Overall, none of the synthesised catalysts exhibited high performance for 2e-WOR, however the metal stannate thin films showed stable performance. Upon quantifying the H_2O_2 produced, low H_2O_2 concentrations and electrochemical selectivities were calculated, which can potentially be attributed to a combination of H_2O_2 instability in alkaline electrolyte and electrochemical oxidation of H_2O_2. The Au-$CaSnO_3$ composites obtained lower current densities, concentrations and selectivities than the thin film metal stannates. The lack of high performance for the Au-$CaSnO_3$ composites correlates with the observed mechanical instability of the catalyst on the substrate. This project also highlights that utilising fluorine doped tin oxide (FTO) glass as a substrate is intricate due to FTO also turning over the 2e-WOR, leading to high activities observed for FTO than the synthesised metal stannates and Au-$CaSnO_3$.

Overall, this thesis has achieved its aims and objectives by investigating the electrochemical performance of the electrocatalyst in a half-cell and MEA configuration and characterising the materials. The results from this thesis show promising results of utilising AuPd coated TiO_2 as a catalyst support to enhance electrochemical performance at lower loading of 50 wt% Ir compared to the current state of the art (75 wt% Ir). Additionally, the observation that different Ir deposition techniques can influence the electrochemical performance is an important additional factor to consider when developing electrocatalysts. Similar to current research, the stability of dopants requires further optimisation to obtain a stable and cost-effective dopant for catalyst-supports. This thesis highlights that fine tuning the composition, dopant, morphology, Ir deposition technique of supported catalysts can lead to viable 4e-WOR electrocatalysts with enhanced activity, selectivity and stability. The design of catalysts and substrates for the 2e-WOR requires substantial investigation to obtain highly active, selective and stable materials. Moreover, the work on H_2O_2 within this thesis has highlighted that there is a need to investigation quantification techniques for low concentrations of H_2O_2 to project the development of this technology.

7.2 Future Works

The electrocatalyst designs for the 2e-WOR and the 4e-WOR in this thesis have shown promising results thus far. However, for the electrocatalysts to be viable in a commercial PEM-WEs further work to boost the electrochemical activity, stability and selectivity could be conducted. This section describes the improvements that could be made to the synthesised electrocatalysts in each chapter with the potential of enhancing the electrochemical performance.

The synthesis of the hollow TiO_2 achieved high mass activities compared to IrO_x in an RDE and MEA. However, further investigations to potentially improve the OER performance such as tuning the size and thickness of the AuPd nanoparticles could be evaluated. In addition, *in-situ* characterisations should be investigated to evaluate how the catalyst behaves during the OER measurements and why there is preferential nucleation of Ir inside the hollow TiO_2. AuPd catalysts are known to be active for 2-electron oxygen reduction reaction, a H_2O_2 selective cell could potentially be produced which could generate H_2O_2 from both the anode and cathode electrodes. Therefore, it would be interesting to evaluate these hollow TiO_2 coated AuPd catalysts for the 2e-WOR.

For the doped SnO_2 chapters, the Ir loadings onto the supports should be increased and the optimum dopant : SnO_2 ratio in the catalyst-support should be investigated to potentially improve the OER performance. The long-term stability of dopants in catalyst supports is currently under-researched. It would be advantageous to evaluate the supported catalysts in an MEA coupled with *in*-situ characterisation techniques such as a flow-cell to determine the elemental dissolution and supported catalyst degradation mechanism during long-term stability measurements.

In addition, further experimental work should be conducted to calculate the turnover frequency (TOF) and electrochemical surface area to determine the intrinsic activity of each catalyst. Theoretical modelling should be conducted to accurately determine the mechanisms that are undergoing for all synthesised electrocatalysts.

The 2e-WOR requires the synthesis of active, selective and stable electrocatalysts with low overpotentials that can compete with the 4e-WOR. The role of catalyst conductivity for the metal stannates must be investigated further to evaluate its effect on H_2O_2 production. In this work, the addition of conductive Au resulted in the dissolution/delamination of the Au-$CaSnO_3$ which led to reduced current densities and stability. Therefore, the degradation mechanism must be investigated to determine the viability of Au-$CaSnO_3$ as a 2e-WOR catalyst. The influence of carbonate electrolyte on H_2O_2 is widely researched for electrochemical H_2O_2 by 2e-WOR. In this work, the 2e-WOR performance was conducted in 2 M $KHCO_3$, however it has been reported that the combination of HCO_3^-/CO_3^- in electrolyte would substantially increase H_2O_2 production. A repeat of the catalysts in this work in a combined electrolyte (HCO_3^-/CO_3^-) could lead to an increase in H_2O_2 production. Identifying alternative substrates would also be advantageous as FTO has thermal limitations and turns over 2e-WOR which increases the complexity of benchmarking these electrocatalysts.

Overall, the electrochemical production of H_2 and H_2O_2 using proton exchange membrane water electrolysis is an expanding field that has the potential to decarbonise transportation/chemical industries. For the technology to become economically viable, the synthesis of cost-effective electrocatalysts must be considered. Specifically, by understanding how to maintain highly active, stable and selective electrocatalysts, the production of economic proton-exchange membrane electrolysers can be amplified.

A. Appendix

Figure A.1: Comparison of the OER activities from rotating disk electrode from the literature with mass activities and geometric area normalised current densities where available. References for each material shown in the first column, * indicates the materials from Chapter 3.

Sample Name	**Ir wt%**	**Ir Loading (µg/cm^2)**	**Electrolyte**	**Mass Activity (A/g$_{Ir}$)**	**Current Density (mA/cm^2)**	**Voltage at given current density (V)**
50-TiO_2-H_2*	50	25.5	0.1 M $HClO_4$	72	1.84	1.65
50-WH1-H_2*	50	25.5	0.1 M $HClO_4$	728	18.57	1.65
50-WH5-H_2*	50	25.5	0.1 M $HClO_4$	936	23.87	1.65
Ir/TiO_2-MoO_x [272]	26	37.5	0.05 M H_2SO_4	573	-	1.55
Ir/TiO_2 [272]	26	37.5	0.05 M H_2SO_4	76	3.13	1.55
Ir-TiO_2-245 [271]	55	50	0.1 M $HClO_4$	10	0.5	1.49
IrO_x/$Nb_{0.1}Ti_{0.9}O_2$-600 [273]	30	-	0.5 M H_2SO_4	-	10	1.60
IrO_x/$Nb_{0.1}Ti_{0.9}O_2$-700 [273]	30	-	0.5 M H_2SO_4	-	10	1.56
IrO_x/$Nb_{0.1}Ti_{0.9}O_2$-800 [273]	30	-	0.5 M H_2SO_4	-	10	1.60
IrO_x/F-TiO_2 [166]	40	0.3	0.5 M H_2SO_4	320.2	-	1.55

IrO_x/TiO_2 166	40	0.3	0.5 M H_2SO_4	80.8	-	1.55
IrO_2-TNT 277	50	35	0.5 M H_2SO_4	-	35	1.60
IrO_2/Nb-TNT 277	50	35	0.5 M H_2SO_4	-	42	1.60
$IrO_2@TiO_2$ 142	50	10	0.1 M $HClO_4$	112	1.12	1.55
IrO_2@Ir/TiN 278	50	379	0.5 M H_2SO_4	412.7	-	1.60
IrO_2@Ir/TiN 278	60	379	0.5 M H_2SO_4	480.4	-	1.60
Ir/Ti_4O_7 279	25	33.33	0.5 M H_2SO_4	4.2	0.14	1.48
Mesoporous-Ir-TiO_x 274	30	-	0.5 M H_2SO_4	158.3	8.2	1.60
Ir-Pt-TiO_2 169	25	3.49	0.1 M $HClO_4$	170	-	1.60
$IrO_2/Nb_{0.05}Ti_{0.95}O_2$ 275	26	66.3	0.5 M H_2SO_4	471	31.23	1.60
IrO_x/N-TiO_2 280	-	-	0.5 M H_2SO_4	278.7	-	1.55
$TiON_x$-3h-Ir 276	11	-	0.1 M $HClO_4$	520.3	-	1.55
Umicore 148	75	3.7	0.1 M $HClO_4$	5	-	1.50

References

1 B. M. Hunter, H. B. Gray and A. M. Müller, Earth-Abundant Heterogeneous Water Oxidation Catalysts, *Chem. Rev.*, 2016, **116**, 14120–14136.

2 A. Kalair, N. Abas, M. S. Saleem, A. R. Kalair and N. Khan, Role of energy storage systems in energy transition from fossil fuels to renewables, *Energy Storage*, , DOI:10.1002/est2.135.

3 E. Commission, *A Roadmap for moving to a competitive low carbon economy in 2050*, 2011.

4 M. Carmo, D. L. Fritz, J. Mergel and D. Stolten, A comprehensive review on PEM water electrolysis, *Int. J. Hydrogen Energy*, 2013, **38**, 4901–4934.

5 N. energy W. Industry, *Fuel Cell and Hydrogen technologies in Europe 2014 - 2020*, 2011.

6 T. Wilberforce, A. Alaswad, A. Palumbo, M. Dassisti and A. G. Olabi, Advances in stationary and portable fuel cell applications, *Int. J. Hydrogen Energy*, 2016, **41**, 16509–16522.

7 K. A. Kavadias, D. Apostolou and J. K. Kaldellis, Modelling and optimisation of a hydrogen-based energy storage system in an autonomous electrical network, *Appl. Energy*, 2018, **227**, 574–586.

8 L. Moriau, M. Smiljanić, A. Lončar and N. Hodnik, Supported Iridium-based Oxygen Evolution Reaction Electrocatalysts - Recent Developments, *ChemCatChem*, 2022, **14**, 1–23.

9 I. E. . Stephens and N. Athanassopoulou, *Materials for the Energy Transition roadmap: Materials for Low-Carbon Production of Hydrogen and Related Energy Carriers and Chemical Feedstocks*, England, 2020.

10 REN21, *Renewables 2021 Global Status Report*, 2017.

11 P. Nikolaidis and A. Poullikkas, A comparative overview of hydrogen production processes, *Renew. Sustain. Energy Rev.*, 2017, **67**, 597–611.

12 A. Kusoglu, Chalkboard 1 - The Many Colors of Hydrogen, *Electrochem. Soc. Interface*, 2021, **30**, 44–48.

13 K. Scott, in *Electrochemical Methods for Hydrogen Production*, ed. K. Scott, Royal Society of Chemistry, 25th edn., 2020, pp. 1–27.

14 F. N. Khatib, T. Wilberforce, O. Ijaodola, E. Ogungbemi, Z. El-Hassan, A. Durrant, J. Thompson and A. G. Olabi, Material degradation of components in polymer electrolyte membrane (PEM)electrolytic cell and mitigation mechanisms: A review, *Renew. Sustain. Energy Rev.*, 2019, **111**, 1.

15 S. Yang, A. Verdaguer-Casadevall, L. Arnarson, L. Silvioli, V. Čolić, R. Frydendal, J. Rossmeisl, I. Chorkendorff and I. E. L. Stephens, Toward the Decentralized Electrochemical Production of H2O2: A Focus on the Catalysis, *ACS Catal.*, 2018, **8**, 4064–4081.

16 T. Kang, B. Li, Q. Hao, W. Gao, F. Bin, K. N. Hui, D. Fu and B. Dou, Efficient Hydrogen Peroxide (H2O2) Synthesis by CaSnO3via Two-Electron Water Oxidation Reaction, *ACS Sustain. Chem. Eng.*, 2020, **8**, 15005–15012.

17 S. Mavrikis, S. C. Perry, P. K. Leung, L. Wang and C. Ponce De León, Recent Advances in Electrochemical Water Oxidation to Produce Hydrogen Peroxide: A Mechanistic Perspective, *ACS Sustain. Chem. Eng.*, 2021, **9**, 76–91.

18 C. Zhang, R. Lu, C. Liu, L. Yuan, J. Wang, Y. Zhao and C. Yu, High Yield Electrosynthesis of Hydrogen Peroxide from Water Using Electrospun CaSnO3@Carbon Fiber Membrane Catalysts with Abundant Oxygen Vacancy, *Adv. Funct. Mater.*, 2021, **31**, 1–9.

19 S. C. Perry, D. Pangotra, L. Vieira, L. I. Csepei, V. Sieber, L. Wang, C. Ponce de León and F. C. Walsh, Electrochemical synthesis of hydrogen peroxide from water and oxygen, *Nat. Rev. Chem.*, 2019, **3**, 442–458.

20 I. Yamanaka, T. Hashimoto, R. Ichihashi and K. Otsuka, Direct synthesis of H2O2 acid solutions on carbon cathode prepared from activated carbon and vapor-growing-carbon-fiber by a H2/O2 fuel cell, *Electrochim. Acta*, 2008, **53**, 4824–4832.

21 C. M. Sánchez-Sánchez and A. J. Bard, Hydrogen peroxide production in the oxygen reduction reaction at different electrocatalysts as quantified by scanning electrochemical microscopy, *Anal. Chem.*, 2009, **81**, 8094–8100.

22 Z. Lu, G. Chen, S. Siahrostami, Z. Chen, K. Liu, J. Xie, L. Liao, T. Wu, Di. Lin, Y. Liu, T. F. Jaramillo, J. K. Nørskov and Y. Cui, High-efficiency oxygen reduction to hydrogen peroxide catalysed by oxidized carbon materials, *Nat. Catal.*, 2018, **1**, 156–162.

23 H. Tüysüz, Alkaline Water Electrolysis for Green Hydrogen Production, *Acc. Chem. Res.*, , DOI:10.1021/acs.accounts.3c00709.

24 J. Chi and H. Yu, Water electrolysis based on renewable energy for hydrogen production, *Cuihua Xuebao/Chinese J. Catal.*, 2018, **39**, 390–394.

25 A. Keçebaş, M. Kayfeci and M. Bayat, in *Solar Hydrogen Production: Processes, Systems and Technologies*, eds. F. Calise, M. D. D'Accadia, M. Santarelli, A. Lanzini and D. Ferrero, Academic Press, Cambridge, 1st edn., 2019, pp. 299–317.

26 K. Ayers, N. Danilovic, R. Ouimet, M. Carmo, B. Pivovar and M. Bornstein, Perspectives on low-temperature electrolysis and potential for renewable hydrogen at scale, *Annu. Rev. Chem. Biomol. Eng.*, 2019, **10**, 219–239.

27 C. Spöri, J. T. H. Kwan, A. Bonakdarpour, D. P. Wilkinson and P. Strasser, The Stability

Challenges of Oxygen Evolving Catalysts: Towards a Common Fundamental Understanding and Mitigation of Catalyst Degradation, *Angew. Chemie - Int. Ed.*, 2017, **56**, 5996, 6004.

28 T. Hibino, K. Kobayashi, M. Ito, Q. Ma, M. Nagao, M. Fukui and S. Teranishi, Efficient Hydrogen Production by Direct Electrolysis of Waste Biomass at Intermediate Temperatures, *ACS Sustain. Chem. Eng.*, 2018, **6**, 9360–9368.

29 S. S. Kumar and V. Himabindu, Hydrogen production by PEM water electrolysis – A review, *Mater. Sci. Energy Technol.*, 2019, **2**, 442–454.

30 Y. Zhao, B. Jin, A. Vasileff, Y. Jiao and S. Z. Qiao, Interfacial nickel nitride/sulfide as a bifunctional electrode for highly efficient overall water/seawater electrolysis, *J. Mater. Chem. A*, 2019, **7**, 8117–8121.

31 D. H. Marin, J. T. Perryman, M. A. Hubert, G. A. Lindquist, L. Chen, A. M. Aleman, G. A. Kamat, V. A. Niemann, M. B. Stevens, Y. N. Regmi, S. W. Boettcher, A. C. Nielander and T. F. Jaramillo, Hydrogen production with seawater-resilient bipolar membrane electrolyzers, *Joule*, 2023, **7**, 765–781.

32 J. E. Huang, F. Li, A. Ozden, A. S. Rasouli, F. P. G. de Arquer, S. Liu, S. Zhang, M. Luo, X. Wang, Y. Lum, Y. Xu, K. Bertens, R. K. Miao, C. T. Dinh, D. Sinton and E. H. Sargent, CO2 electrolysis to multicarbon products in strong acid, *Science (80-.).*, 2021, **372**, 1074–1078.

33 S. Alia, D. Ding, A. Mcdaniel, F. M. Toma and H. N. Dinh, Chalkboard - 2: How to Make Clean Hydrogen, *Electrochem. Soc. interface*, 2021, **30**, 49–56.

34 H. A. Miller, K. Bouzek, J. Hnat, S. Loos, C. I. Bernäcker, T. Weißgärber, L. Röntzsch and J. Meier-Haack, Green hydrogen from anion exchange membrane water electrolysis: A review of recent developments in critical materials and operating conditions, *Sustain. Energy Fuels*, 2020, **4**, 2114–2133.

35 S. Shiva Kumar, V. Himabindu, S. S. Kumar and V. Himabindu, Hydrogen production by PEM water electrolysis – A review, *Mater. Sci. Energy Technol.*, 2019, **2**, 443–454.

36 Ö. F. Selamet, F. Becerikli, M. D. Mat and Y. Kaplan, Development and testing of a highly efficient proton exchange membrane (PEM) electrolyzer stack, *Int. J. Hydrogen Energy*, 2011, **36**, 11480–11487.

37 Y. Ando and T. Tanaka, Proposal for a new system for simultaneous production of hydrogen and hydrogen peroxide by water electrolysis, *Int. J. Hydrogen Energy*, 2004, **29**, 1349–1354.

38 X. Shi, S. Siahrostami, G. L. Li, Y. Zhang, P. Chakthranont, F. Studt, T. F. Jaramillo, X. Zheng and J. K. Nørskov, Understanding activity trends in electrochemical water oxidation to form hydrogen peroxide, *Nat. Commun.*, 2017, **8**, 1–12.

39 S. Cherevko, S. Geiger, O. Kasian, N. Kulyk, J. P. Grote, A. Savan, B. R. Shrestha, S. Merzlikin, B. Breitbach, A. Ludwig and K. J. J. Mayrhofer, Oxygen and hydrogen evolution reactions on Ru, RuO2, Ir, and IrO2 thin film electrodes in acidic and alkaline electrolytes: A comparative study on activity and stability, *Catal. Today*, 2016, **262**, 170–180.

40 Y. Guo, G. Li, J. Zhou and Y. Liu, Comparison between hydrogen production by alkaline water electrolysis and hydrogen production by PEM electrolysis, *IOP Conf. Ser. Earth Environ. Sci.*, 2019, **371**, 2–7.

41 X. Shi, S. Back, T. M. Gill, S. Siahrostami and X. Zheng, Electrochemical Synthesis of H2O2 by Two-Electron Water Oxidation Reaction, *Chem*, 2021, **7**, 38–63.

42 Q. Liang, G. Brocks and A. Bieberle-Hütter, Oxygen evolution reaction (OER) mechanism under alkaline and acidic conditions, *J. Phys. Energy*, 2021, **3**, 1–8.

43 S. Hu, S. Ge, H. Liu, X. Kang, Q. Yu and B. Liu, *Adv. Funct. Mater.*, 2022, 32, 1–21.

44 J. S. Yoo, X. Rong, Y. Liu and A. M. Kolpak, Role of Lattice Oxygen Participation in Understanding Trends in the Oxygen Evolution Reaction on Perovskites, *ACS Catal.*, 2018, **8**, 4628–4636.

45 Z. Shi, X. Wang, J. Ge, C. Liu and W. Xing, Fundamental understanding of the acidic oxygen evolution reaction: mechanism study and state-of-the-art catalysts, *Nanoscale*, 2020, **12**, 13249–13275.

46 S. Geiger, O. Kasian, M. Ledendecker, E. Pizzutilo, A. M. Mingers, W. T. Fu, O. Diaz-Morales, Z. Li, T. Oellers, L. Fruchter, A. Ludwig, K. J. J. Mayrhofer, M. T. M. Koper and S. Cherevko, The stability number as a metric for electrocatalyst stability benchmarking, *Nat. Catal.*, 2018, **1**, 508–515.

47 T. Binninger and M. L. Doublet, The Ir-OOOO-Ir transition state and the mechanism of the oxygen evolution reaction on IrO2(110), *Energy Environ. Sci.*, 2022, **15**, 2519–2528.

48 K. Schweinar, B. Gault, I. Mouton and O. Kasian, Lattice Oxygen Exchange in Rutile IrO2 during the Oxygen Evolution Reaction, *J. Phys. Chem. Lett.*, 2020, **11**, 5008–5014.

49 F. Godínez-Salomón, L. Albiter, S. M. Alia, B. S. Pivovar, L. E. Camacho-Forero, P. B. Balbuena, R. Mendoza-Cruz, M. J. Arellano-Jimenez and C. P. Rhodes, Self-Supported Hydrous Iridium-Nickel Oxide Two-Dimensional Nanoframes for High Activity Oxygen Evolution Electrocatalysts, *ACS Catal.*, 2018, **8**, 10498–10520.

50 H. Wu, Y. Wang, Z. Shi, X. Wang, J. Yang, M. Xiao, J. Ge, W. Xing and C. Liu, Recent developments of iridium-based catalysts for the oxygen evolution reaction in acidic water electrolysis, *J. Mater. Chem. A*, 2022, **10**, 13170–13189.

51 Y. Pan, X. Xu, Y. Zhong, L. Ge, Y. Chen, J. P. M. Veder, D. Guan, R. O'Hayre, M. Li, G. Wang, H. Wang, W. Zhou and Z. Shao, Direct evidence of boosted oxygen evolution over perovskite by enhanced lattice oxygen participation, *Nat. Commun.*, 2020, **11**, 1–10.

52 A. Zagalskaya and V. Alexandrov, Role of Defects in the Interplay between Adsorbate Evolving and Lattice Oxygen Mechanisms of the Oxygen Evolution Reaction in RuO2 and IrO2, *ACS Catal.*, 2020, **10**, 3650–3657.

53 O. Kasian, S. Geiger, T. Li, J. P. Grote, K. Schweinar, S. Zhang, C. Scheu, D. Raabe, S. Cherevko, B. Gault and K. J. J. Mayrhofer, Degradation of iridium oxides via oxygen evolution from the lattice: Correlating atomic scale structure with reaction mechanisms, *Energy Environ. Sci.*, 2019, **12**, 3548–3555.

54 Z. Ma, Y. Zhang, S. Liu, W. Xu, L. Wu, Y. C. Hsieh, P. Liu, Y. Zhu, K. Sasaki, J. N. Renner, K. E. Ayers, R. R. Adzic and J. X. Wang, Reaction mechanism for oxygen evolution on RuO2, IrO2, and RuO2@IrO2 core-shell nanocatalysts, *J. Electroanal. Chem.*, 2018, **819**, 296–305.

55 X. Hu, Z. Sun, G. Mei, X. Zhao, B. Y. Xia and B. You, Engineering Nonprecious Metal Oxides Electrocatalysts for Two-Electron Water Oxidation to H2O2, *Adv. Energy Mater.*, , DOI:10.1002/aenm.202201466.

56 C. Xia, S. Back, S. Ringe, K. Jiang, F. Chen, X. Sun, S. Siahrostami, K. Chan and H. Wang, Confined local oxygen gas promotes electrochemical water oxidation to hydrogen peroxide, *Nat. Catal.*, 2020, **3**, 125–134.

57 Y. Li, Y. Sun, Y. Qin, W. Zhang, L. Wang, M. Luo, H. Yang and S. Guo, Recent Advances on Water-Splitting Electrocatalysis Mediated by Noble-Metal-Based Nanostructured Materials, *Adv. Energy Mater.*, 2020, **10**, 1–20.

58 Q. Guo, J. Mao, J. Huang, Z. Wang, Y. Zhang, J. Hu and J. Dong, Reducing Oxygen Evolution Reaction Overpotential in Cobalt-Based Electrocatalysts via Optimizing the “ Microparticles-in-Spider Web ” Electrode Configurations, *Nano Micro Small*, 2020, **16**, 1.

59 K. Ayers, The potential of proton exchange membrane–based electrolysis technology, *Curr. Opin. Electrochem.*, 2019, **18**, 9–15.

60 M. A. Hubert, L. A. King and T. F. Jaramillo, Evaluating the Case for Reduced Precious Metal Catalysts in Proton Exchange Membrane Electrolyzers, *ACS Energy Lett.*, 2022, **7**, 17–23.

61 S. Mavrikis, M. Göltz, S. C. Perry, F. Bogdan, P. K. Leung, S. Rosiwal, L. Wang and C. Ponce de León, Effective Hydrogen Peroxide Production from Electrochemical Water Oxidation, *ACS Energy Lett.*, 2021, **6**, 2369–2377.

62 G. Rothenberg, in *Catalysis: Concepts and Green Applications*, John Wiley & Sons, Amsterdam, 2nd edn., 2017, pp. 74–75.

63 O. T. Holton and J. W. Stevenson, The Role of Platinum in Proton Exchange Membrane Fuel Cells Evaluation of platinum’s unique properties for use in both the anode and cathode of a proton exchange membrane fuel cell, *Platin. Met. Rev.*, 2013, **57**, 259–271.

64 E. Fabbri, A. Habereder, K. Waltar, R. Kötz and T. J. Schmidt, Developments and perspectives of oxide-based catalysts for the oxygen evolution reaction, *Catal. Sci. Technol.*, 2014, **4**, 3800–3821.

65 J. Masa, C. Andronescu and W. Schuhmann, Electrocatalysis as the Nexus for Sustainable Renewable Energy: The Gordian Knot of Activity, Stability, and Selectivity, *Angew. Chemie - Int. Ed.*, 2020, **59**, 15298–15312.

66 F. Song, L. Bai, A. Moysiadou, S. Lee, C. Hu, L. Liardet and X. Hu, Transition Metal Oxides as Electrocatalysts for the Oxygen Evolution Reaction in Alkaline Solutions: An Application-Inspired Renaissance, *J. Am. Chem. Soc.*, 2018, **140**, 7748–7759.

67 Y. T. Kim, P. P. Lopes, S. A. Park, A. Y. Lee, J. Lim, H. Lee, S. Back, Y. Jung, N. Danilovic, V. Stamenkovic, J. Erlebacher, J. Snyder and N. M. Markovic, Balancing activity, stability and conductivity of nanoporous core-shell iridium/iridium oxide oxygen evolution catalysts, *Nat. Commun.*, 2017, **8**, 1–8.

68 G. A. Somorjai and Y. G. Borodko, Research in nanosciences - Great opportunity for catalysis science, *Catal. Letters*, 2001, **76**, 1–5.

69 J. Rehbein and B. K. Carpenter, Do we fully understand what controls chemical selectivity?, *Phys. Chem. Chem. Phys.*, 2011, **13**, 20906–20922.

70 F. Zaera, Outstanding mechanistic questions in heterogeneous catalysis, *J. Phys. Chem. B*, 2002, **106**, 4043–4052.

71 G. A. Somorjai and J. Y. Park, Molecular factors of catalytic selectivity, *Angew. Chemie - Int. Ed.*, 2008, **47**, 9212–9228.

72 A. A. Eskandrani, S. M. Ali and H. M. Al-Otaibi, Study of the oxygen evolution reaction at strontium palladium perovskite electrocatalyst in acidic medium, *Int. J. Mol. Sci.*, 2020, **21**, 1–12.

73 J. Xu, C. Chen, Z. Han, Y. Yang, J. Li and Q. Deng, Recent advances in oxygen electrocatalysts based on perovskite oxides, *Nanomaterials*, 2019, **9**, 1–19.

74 X. K. Gu, J. C. A. Camayang, S. Samira and E. Nikolla, Oxygen evolution electrocatalysis using mixed metal oxides under acidic conditions: Challenges and opportunities, *J. Catal.*, 2020, **388**, 130–140.

75 M. Kim, J. Park, M. Kang, J. Y. Kim and S. W. Lee, Toward Efficient Electrocatalytic Oxygen Evolution: Emerging Opportunities with Metallic Pyrochlore Oxides for Electrocatalysts and Conductive Supports, *ACS Cent. Sci.*, 2020, **6**, 880–891.

76 K. Momma and F. Izumi, VESTA 3 for three-dimensional visualization of crystal, volumetric and morphology data, *J. Appl. Crystallogr.*, 2011, **44**, 1272–1276.

77 L. Yang, G. Yu, X. Ai, W. Yan, H. Duan, W. Chen, X. Li, T. Wang, C. Zhang, X. Huang, J. S. Chen and X. Zou, Efficient oxygen evolution electrocatalysis in acid by a perovskite with

face-sharing IrO6 octahedral dimers, *Nat. Commun.*, 2018, **9**, 1–9.

78 J. Yu, J. Yu, X. Wu, D. Guan, Z. Hu, S. C. Weng, H. Sun, Y. Song, R. Ran, W. Zhou, M. Ni, Z. Shao and Z. Shao, Monoclinic SrIrO3: An Easily Synthesized Conductive Perovskite Oxide with Outstanding Performance for Overall Water Splitting in Alkaline Solution, *Chem. Mater.*, 2020, **32**, 4514.

79 M. Retuerto, L. Pascual, J. Torrero, M. A. Salam, Á. Tolosana-Moranchel, D. Gianolio, P. Ferrer, P. Kayser, V. Wilke, S. Stiber, V. Celorrio, M. Mokthar, D. G. Sanchez, A. S. Gago, K. A. Friedrich, M. A. Peña, J. A. Alonso and S. Rojas, Highly active and stable OER electrocatalysts derived from Sr2MIrO6 for proton exchange membrane water electrolyzers, *Nat. Commun.*, , DOI:10.1038/s41467-022-35631-5.

80 L. Yang, K. Zhang, H. Chen, L. Shi, X. Liang, X. Wang, Y. Liu, Q. Feng, M. Liu and X. Zou, An ultrathin two-dimensional iridium-based perovskite oxide electrocatalyst with highly efficient {001} facets for acidic water oxidation, *J. Energy Chem.*, 2022, **66**, 619–627.

81 M. You, L. Gui, X. Ma, Z. Wang, Y. Xu, J. Zhang, J. Sun, B. He and L. Zhao, Electronic tuning of SrIrO3 perovskite nanosheets by sulfur incorporation to induce highly efficient and long-lasting oxygen evolution in acidic media, *Appl. Catal. B Environ.*, 2021, **298**, 120562.

82 L. C. Seitz, C. F. Dickens, K. Nishio, Y. Hikita, J. Montoya, A. Doyle, C. Kirk, A. Vojvodic, H. Y. Hwang, J. K. Norskov and T. F. Jaramillo, A highly active and stable IrOx/SrIrO3catalyst for the Oxygen evolution reaction, *Science (80-.).*, 2016, **353**, 1011–1014.

83 N. Li, L. Cai, C. Wang, Y. Lin, J. Huang, H. Sheng, H. Pan, W. Zhang, Q. Ji, H. Duan, W. Hu, W. Zhang, F. Hu, H. Tan, Z. Sun, B. Song, S. Jin, W. Yan and L. Cai, Identification of the Active-Layer Structures for Acidic Oxygen Evolution from 9R-BaIrO3Electrocatalyst with Enhanced Iridium Mass Activity, *J. Am. Chem. Soc.*, 2021, **143**, 18001–18009.

84 O. Diaz-Morales, S. Raaijman, R. Kortlever, P. J. Kooyman, T. Wezendonk, J. Gascon, W. T. Fu and M. T. M. Koper, Iridium-based double perovskites for efficient water oxidation in acid media, *Nat. Commun.*, 2016, **7**, 1–6.

85 Y. Chen, H. Li, J. Wang, Y. Du, S. Xi, Y. Sun, M. Sherburne, J. W. Ager, A. C. Fisher and Z. J. Xu, Exceptionally active iridium evolved from a pseudo-cubic perovskite for oxygen evolution in acid, *Nat. Commun.*, 2019, **10**, 1–10.

86 Y. Wu, W. Sun, Z. Zhou, W. Q. Zaman, M. Tariq, L. Cao and J. Yang, Highly Efficient Oxygen Evolution Activity of Ca2IrO4 in an Acidic Environment due to Its Crystal Configuration, *ACS Omega*, 2018, **3**, 2902–2908.

87 J. G. Vos, Z. Liu, F. D. Speck, N. Perini, W. Fu, S. Cherevko and M. T. M. Koper, Selectivity Trends between Oxygen Evolution and Chlorine Evolution on Iridium-Based Double Perovskites in Acidic Media, *ACS Catal.*, 2019, **9**, 8561–8574.

88 X. Liang, L. Shi, R. Cao, G. Wan, W. Yan, H. Chen, Y. Liu and X. Zou, Perovskite-Type Solid Solution Nano-Electrocatalysts Enable Simultaneously Enhanced Activity and Stability for Oxygen Evolution, *Adv. Mater.*, 2020, **32**, 1–8.

89 D. Lebedev, M. Povia, K. Waltar, P. M. Abdala, I. E. Castelli, E. Fabbri, M. V. Blanco, A. Fedorov, C. Copéret, N. Marzari and T. J. Schmidt, Highly Active and Stable Iridium Pyrochlores for Oxygen Evolution Reaction, *Chem. Mater.*, 2017, **29**, 5182–5191.

90 J. Parrondo, M. George, C. Capuano, K. E. Ayers and V. Ramani, Pyrochlore electrocatalysts for efficient alkaline water electrolysis, *J. Mater. Chem. A*, 2015, **3**, 10819–10828.

91 W. Sun, J. Y. Liu, X. Q. Gong, W. Q. Zaman, L. M. Cao and J. Yang, OER activity manipulated by IrO 6 coordination geometry: An insight from pyrochlore iridates, *Sci. Rep.*, 2016, **6**, 1–10.

92 K. Sardar, S. C. Ball, J. D. B. Sharman, D. Thompsett, J. M. Fisher, R. A. P. Smith, P. K. Biswas, M. R. Lees, R. J. Kashtiban, J. Sloan and R. I. Walton, Bismuth iridium oxide oxygen evolution catalyst from hydrothermal synthesis, *Chem. Mater.*, 2012, **24**, 4192–4200.

93 D. F. Abbott, R. K. Pittkowski, K. MacOunová, R. Nebel, E. Marelli, E. Fabbri, I. E. Castelli, P. Krtil and T. J. Schmidt, Design and Synthesis of Ir/Ru Pyrochlore Catalysts for the Oxygen Evolution Reaction Based on Their Bulk Thermodynamic Properties, *ACS Appl. Mater. Interfaces*, 2019, **11**, 37748–37760.

94 C. Shang, C. Cao, D. Yu, Y. Yan, Y. Lin, H. Li, T. Zheng, X. Yan, W. Yu, S. Zhou and J. Zeng, Electron Correlations Engineer Catalytic Activity of Pyrochlore Iridates for Acidic Water Oxidation, *Adv. Mater.*, 2019, **31**, 1–6.

95 K. Matsuhira, M. Wakeshima, Y. Hinatsu and S. Takagi, Metal-insulator transitions in pyrochlore oxides Ln2Ir 2O7, *J. Phys. Soc. Japan*, 2011, **80**, 1–14.

96 P. C. Shih, J. Kim, C. J. Sun and H. Yang, Single-Phase Pyrochlore Y2Ir2O7 Electrocatalyst on the Activity of Oxygen Evolution Reaction, *ACS Appl. Energy Mater.*, 2018, **1**, 3992–3998.

97 K. Sardar, E. Petrucco, C. I. Hiley, J. D. B. Sharman, P. P. Wells, A. E. Russell, R. J. Kashtiban, J. Sloan and R. I. Walton, Water-Splitting Electrocatalysis in Acid Conditions Using Ruthenate-Iridate Pyrochlores, *Angew. Chemie*, 2014, **126**, 11140–11144.

98 M. A. Hubert, A. Gallo, Y. Liu, E. Valle, J. Sanchez, D. Sokaras, R. Sinclair, L. A. King and T. F. Jaramillo, Characterization of a Dynamic Y2Ir2O7Catalyst during the Oxygen Evolution Reaction in Acid, *J. Phys. Chem. C*, 2022, **126**, 1751–1760.

99 C. W. Song, J. Lim, H. Bin Bae and S.-Y. Chung, Discovery of crystal structure–stability correlation in iridates for oxygen evolution electrocatalysis in acid, *Energy Environ. Sci.*, 2020, **13**, 4178–4188.

100 H. Li, C. Ren, S. Xu, L. Wang, Q. Yue, R. Li, Y. Zhang, Q. Xue and J. Liu, Te-template approach to fabricating ternary TeCuPt alloy nanowires with enhanced catalytic performance towards oxygen reduction reaction and methanol oxidation reaction, *J. Mater. Chem. A*, 2015, **3**, 5850–5858.

101 M. Zhu, Q. Shao, Y. Qian and X. Huang, Superior overall water splitting electrocatalysis in acidic conditions enabled by bimetallic Ir-Ag nanotubes, *Nano Energy*, 2019, **56**, 330–337.

102 K. MacOunová, J. Jirkovský, M. V. Makarova, J. Franc and P. Krtil, Oxygen evolution on Ru1−xNixO2−y nanocrystalline electrodes, *J. Solid State Electrochem.*, 2009, **13**, 959–965.

103 S. Ardizzone, C. L. Bianchi, G. Cappelletti, M. Ionita, A. Minguzzi, S. Rondinini and A. Vertova, Composite ternary SnO2-IrO2-Ta2O5 oxide electrocatalysts, *J. Electroanal. Chem.*, 2006, **589**, 160–166.

104 L. Zhou, X. Liu, K. Wang, X. Zhao, H. Pu, T. Zhang, J. Jia, K. Dong and Y. Deng, One-Pot Synthesis of Alloy Ir-Cu Microspheres with Excellent Electro-Catalytic Activity Toward Oxygen Evolution Reaction under Acidic Conditions, *Energy and Fuels*, 2020, **34**, 9956–9962.

105 J. Lim, S. Yang, C. Kim, C. W. Roh, Y. Kwon, Y. T. Kim and H. Lee, Shaped Ir-Ni bimetallic nanoparticles for minimizing Ir utilization in oxygen evolution reaction, *Chem. Commun.*, 2016, **52**, 5641–5644.

106 C. Wang, Y. Sui, M. Xu, C. Liu, G. Xiao and B. Zou, Synthesis of Ni-Ir Nanocages with Improved Electrocatalytic Performance for the Oxygen Evolution Reaction, *ACS Sustain. Chem. Eng.*, 2017, **5**, 9787–9792.

107 N. Danilovic, R. Subbaraman, K. C. Chang, S. H. Chang, Y. Kang, J. Snyder, A. P. Paulikas, D. Strmcnik, Y. T. Kim, D. Myers, V. R. Stamenkovic and N. M. Markovic, Using Surface Segregation To Design Stable Ru-Ir Oxides for the Oxygen Evolution Reaction in Acidic Environments, *Angew. Chemie*, 2014, **126**, 14240–14245.

108 J. J. Zhang, J. M. Hu, J. Q. Zhang and C. N. Cao, IrO2-SiO2 binary oxide films: Geometric or kinetic interpretation of the improved electrocatalytic activity for the oxygen evolution reaction, *Int. J. Hydrogen Energy*, 2011, **36**, 5218–5226.

109 J. Hu, J. Zhang, H.-M. Meng and C.-N. Cao, Microstructure , electrochemical surface and electrocatalytic properties of IrO 2 + Ta 2 O 5, *J. Mater. Sci.*, 2003, **38**, 705–712.

110 H. Guo, Z. Fang, H. Li, D. Fernandez, G. Henkelman, S. M. Humphrey and G. Yu, Rational Design of Rhodium-Iridium Alloy Nanoparticles as Highly Active Catalysts for Acidic Oxygen Evolution, *ACS Nano*, 2019, **13**, 13225–13234.

111 A. L. Maulana, P. C. Chen, Z. Shi, Y. Yang, C. Lizandara-Pueyo, F. Seeler, H. D. Abruña, D. Muller, K. Schierle-Arndt and P. Yang, Understanding the Structural Evolution of

IrFeCoNiCu High-Entropy Alloy Nanoparticles under the Acidic Oxygen Evolution Reaction, *Nano Lett.*, 2023, **23**, 6637–6644.

112 A. L. Strickler, R. A. Flores, L. A. King, J. K. Nørskov, M. Bajdich and T. F. Jaramillo, Systematic Investigation of Iridium-Based Bimetallic Thin Film Catalysts for the Oxygen Evolution Reaction in Acidic Media, *ACS Appl. Mater. Interfaces*, 2019, **11**, 34059–34066.

113 T. Reier, Z. Pawolek, S. Cherevko, M. Bruns, T. Jones, D. Teschner, S. Selve, A. Bergmann, H. N. Nong, R. Schlögl, K. J. J. Mayrhofer and P. Strasser, Molecular insight in structure and activity of highly efficient, low-Ir Ir-Ni oxide catalysts for electrochemical water splitting (OER), *J. Am. Chem. Soc.*, 2015, **137**, 13031–13040.

114 Z. H. Zhou, W. H. Li, Z. Zhang, X. C. Zhao, W. Cao and Q. S. Huang, Ni optimizes Ir reaction pathway through IrNi alloy synergistic effect to improve overall water splitting efficiency, *Int. J. Hydrogen Energy*, 2023, **48**, 8440–8449.

115 O. Kasian, S. Geiger, P. Stock, G. Polymeros, B. Breitbach, A. Savan, A. Ludwig, S. Cherevko and K. J. J. Mayrhofer, On the Origin of the Improved Ruthenium Stability in RuO 2 –IrO 2 Mixed Oxides , *J. Electrochem. Soc.*, 2016, **163**, F3099–F3104.

116 C. Wang, Y. Sui, G. Xiao, X. Yang, Y. Wei, G. Zou and B. Zou, Synthesis of Cu-Ir nanocages with enhanced electrocatalytic activity for the oxygen evolution reaction, *J. Mater. Chem. A*, 2015, **3**, 19669–19673.

117 W. Lu, P. Yuan, F. Wei, K. Cheng, W. Li, Y. Zhou, W. Zheng and G. Zhang, Porous Ir-Sn binary oxide nanorod assembly as an efficient electrocatalyst for water oxidation, *Int. J. Electrochem. Sci.*, 2018, **13**, 3235–3245.

118 D. Jin, H. Yoo, Y. Lee, C. Lee and M. H. Kim, IrO2-ZnO Composite Nanorod Array as an Acid-Stable Electrocatalyst with Superior Activity for the Oxygen Evolution Reaction, *ACS Appl. Energy Mater.*, 2022, **5**, 3810–3820.

119 S. D. Ghadge, O. I. Velikokhatnyi, M. K. Datta, P. M. Shanthi, S. Tan, K. Damodaran and P. N. Kumta, *ACS Catal.*, 2019, 9, 2134–2157.

120 S. M. Alia, S. Shulda, C. Ngo, S. Pylypenko and B. S. Pivovar, Iridium-Based Nanowires as Highly Active, Oxygen Evolution Reaction Electrocatalysts, *ACS Catal.*, 2018, **8**, 2111–2120.

121 Z. Lei, X. Liu, Y. Wu, H. Wang, S. Jiang, S. Wang, X. Hui, Y. Wu, B. Gault, P. Kontis, D. Raabe, L. Gu, Q. Zhang, H. Chen, H. Wang, J. Liu, K. An, Q. Zeng, T. G. Nieh and Z. Lu, Enhanced strength and ductility in a high-entropy alloy via ordered oxygen complexes, *Nature*, 2018, **563**, 546–550.

122 H. Zhu, Z. Zhu, J. Hao, S. Sun, S. Lu, C. Wang, P. Ma, W. Dong and M. Du, High-entropy alloy stabilized active Ir for highly efficient acidic oxygen evolution, *Chem. Eng. J.*, 2022, **431**, 133251.

123 Z. X. Cai, H. Goou, Y. Ito, T. Tokunaga, M. Miyauchi, H. Abe and T. Fujita, Nanoporous ultra-high-entropy alloys containing fourteen elements for water splitting electrocatalysis, *Chem. Sci.*, 2021, **12**, 11306–11315.

124 Z. Jin, J. Lv, H. Jia, W. Liu, H. Li, Z. Chen, X. Lin, G. Xie, X. Liu, S. Sun and H. J. Qiu, Nanoporous Al-Ni-Co-Ir-Mo High-Entropy Alloy for Record-High Water Splitting Activity in Acidic Environments, *Small*, , DOI:10.1002/smll.201904180.

125 Y. Pi, Q. Shao, P. Wang, J. Guo and X. Huang, General Formation of Monodisperse IrM (M = Ni, Co, Fe) Bimetallic Nanoclusters as Bifunctional Electrocatalysts for Acidic Overall Water Splitting, *Adv. Funct. Mater.*, , DOI:10.1002/adfm.201700886.

126 Y. Yang, H. Fei, G. Ruan, C. Xiang and J. M. Tour, Efficient Electrocatalytic Oxygen Evolution on Amorphous Nickel-Cobalt Binary Oxide Nanoporous Layers, *ACS Nano*, 2014, **8**, 9518–9523.

127 G. Zhang, J. Yang, H. Wang, H. Chen, J. Yang and F. Pan, Co3O4-δ Quantum Dots As a Highly Efficient Oxygen Evolution Reaction Catalyst for Water Splitting, *ACS Appl. Mater. Interfaces*, 2017, **9**, 16159–16167.

128 Y. Li, F. M. Li, X. Y. Meng, S. N. Li, J. H. Zeng and Y. Chen, Ultrathin Co3O4 Nanomeshes for the Oxygen Evolution Reaction, *ACS Catal.*, 2018, **8**, 1913–1920.

129 L. Zhou, A. Shinde, J. H. Montoya, A. Singh, S. Gul, J. Yano, Y. Ye, E. J. Crumlin, M. H. Richter, J. K. Cooper, H. S. Stein, J. A. Haber, K. A. Persson and J. M. Gregoire, Rutile Alloys in the Mn-Sb-O System Stabilize Mn3+ to Enable Oxygen Evolution in Strong Acid, *ACS Catal.*, 2018, **8**, 10938–10948.

130 M. H. So, I. A. Moreno-hernandez, C. A. Macfarland, K. M. Papadantonakis, B. S. Brunschwig, C. G. Read and N. S. Lewis, Crystalline nickel manganese antimonate as a stable water-oxidation catalyst in aqueous 1.0 M H2SO4, *RSC Energy Environ. Sci.*, 2017, **10**, 2103–2108.

131 Z. Mahidashti, M. Rezaei, M. Borrelli and A. Shaygan Nia, Insight into the stability mechanism of nickel and manganese antimonate catalytic films during the oxygen evolution reaction in acidic media, *J. Electroanal. Chem.*, 2023, **937**, 117404.

132 J. S. Mondschein, K. Kumar, C. F. Holder, K. Seth, H. Kim and R. E. Schaak, Intermetallic Ni 2 Ta Electrocatalyst for the Oxygen Evolution Reaction in Highly Acidic Electrolytes, *Inorg. Chem.*, 2018, 6010–6015.

133 R. Ghosh Chaudhuri and S. Paria, Core/shell nanoparticles: Classes, properties, synthesis mechanisms, characterization, and applications, *Chem. Rev.*, 2012, **112**, 2373–2433.

134 M. Gawande, A. Goswami, T. Asefa, H. Guo, A. Biradar, D.-L. Peng, R. Zboril and R. Varma, Core – shell nanoparticles : synthesis and applications in catalysis and electrocatalysis, *Chem. Soc. Rev.*, 2015, **44**, 7540–7590.

135 B. M. Tackett, W. Sheng, S. Kattel, S. Yao, B. Yan, K. A. Kuttiyiel, Q. Wu and J. G. Chen, Reducing Iridium Loading in Oxygen Evolution Reaction Electrocatalysts Using Core-Shell Particles with Nitride Cores, *ACS Catal.*, 2018, **8**, 2615–2621.

136 C. Spöri, P. Briois, H. N. Nong, T. Reier, A. Billard, S. Kühl, D. Teschner and P. Strasser, Experimental Activity Descriptors for Iridium-Based Catalysts for the Electrochemical Oxygen Evolution Reaction (OER), *ACS Catal.*, 2019, **9**, 6653–6663.

137 J. R. Esquius, G. Algara-Siller, I. Spanos, S. J. Freakley, R. Schlögl and G. J. Hutchings, Preparation of solid solution and layered Irox−Ni(OH)2 oxygen evolution catalysts: Toward optimizing iridium efficiency for OER, *ACS Catal.*, 2020, **10**, 14640–14648.

138 J. Zhang, Z. Chen, C. Liu, J. Zhao, S. Liu, D. Rao, A. Nie, Y. Chen, Y. Deng and W. Hu, Hierarchical iridium-based multimetallic alloy with double-core-shell architecture for efficient overall water splitting, *Sci. China Mater.*, 2020, **63**, 249–257.

139 M. Li, Z. Zhao, Z. Xia, M. Luo, Q. Zhang, Y. Qin, L. Tao, K. Yin, Y. Chao, L. Gu, W. Yang, Y. Yu, G. Lu and S. Guo, Exclusive Strain Effect Boosts Overall Water Splitting in PdCu/Ir Core/Shell Nanocrystals, *Angew. Chemie*, 2021, **133**, 8324–8331.

140 J. Zhu, Z. Lyu, Z. Chen, M. Xie, M. Chi, W. Jin and Y. Xia, Facile Synthesis and Characterization of Pd@IrnL (n = 1-4) Core-Shell Nanocubes for Highly Efficient Oxygen Evolution in Acidic Media, *Chem. Mater.*, 2019, **31**, 5867–5875.

141 J. Chen, S. Jayabal, D. Geng and X. Hu, Monolayer Iridium Nanoparticles Coated TiO2 Core-Shell Architecture as Efficient Oxygen Evolution Reaction Electrocatalyst, *ChemistrySelect*, 2021, **6**, 9134–9138.

142 C. Van Pham, M. Bühler, J. Knöppel, M. Bierling, D. Seeberger, D. Escalera-López, K. J. J. Mayrhofer, S. Cherevko and S. Thiele, IrO2 coated TiO2 core-shell microparticles advance performance of low loading proton exchange membrane water electrolyzers, *Appl. Catal. B Environ.*, 2020, **269**, 118762.

143 Z. Zhuang, W. Sheng and Y. Yan, Synthesis of monodispere Au@Co3O4 core-shell nanocrystals and their enhanced catalytic activity for oxygen evolution reaction, *Adv. Mater.*, 2014, **26**, 3950–3955.

144 A. L. Strickler, M. Escudero-Escribano and T. F. Jaramillo, Core-Shell Au@Metal-Oxide Nanoparticle Electrocatalysts for Enhanced Oxygen Evolution, *Nano Lett.*, 2017, **17**, 6040–6046.

145 P. Strasser, S. Koh, T. Anniyev, J. Greeley, K. More, C. Yu, Z. Liu, S. Kaya, D. Nordlund, H. Ogasawara, M. F. Toney and A. Nilsson, Lattice-strain control of the activity in dealloyed core-shell fuel cell catalysts, *Nat. Chem.*, 2010, **2**, 454–460.

146 N. T. Suen, S. F. Hung, Q. Quan, N. Zhang, Y. J. Xu and H. M. Chen, Electrocatalysis for the oxygen evolution reaction: recent development and future perspectives, *Chem. Soc. Rev.*, 2017, **46**, 337–365.

147 H. S. Oh, H. N. Nong, T. Reier, A. Bergmann, M. Gliech, J. Ferreira De Araújo, E. Willinger, R. Schlögl, D. Teschner and P. Strasser, Electrochemical Catalyst-Support Effects and Their Stabilizing Role for IrOx Nanoparticle Catalysts during the Oxygen Evolution Reaction, *J. Am. Chem. Soc.*, 2016, **138**, 12552–12563.

148 A. Hartig-Weiss, M. Miller, H. Beyer, A. Schmitt, A. Siebel, A. T. S. Freiberg, H. A. Gasteiger and H. A. El-Sayed, Iridium Oxide Catalyst Supported on Antimony-Doped Tin Oxide for High Oxygen Evolution Reaction Activity in Acidic Media, *ACS Appl. Nano Mater.*, 2020, **3**, 2185–2196.

149 A. S. Pushkarev, I. V. Pushkareva and D. G. Bessarabov, Supported Ir-Based Oxygen Evolution Catalysts for Polymer Electrolyte Membrane Water Electrolysis: A Minireview, *Energy and Fuels*, 2022, **36**, 6613–6625.

150 B. Han, M. Risch, S. Belden, S. Lee, D. Bayer, E. Mutoro and Y. Shao-Horn, Screening oxide support materials for OER catalysts in acid, *J. Electrochem. Soc.*, 2018, **165**, F813–F820.

151 X. Zhou, X. Liu, J. Zhang, C. Zhang, S. J. Yoo, J. G. Kim, X. Chu, C. Song, P. Wang, Z. Zhao, D. Li, W. Zhang and W. Zheng, Highly-dispersed cobalt clusters decorated onto nitrogen-doped carbon nanotubes as multifunctional electrocatalysts for OER, HER and ORR, *Carbon N. Y.*, 2020, **166**, 284–290.

152 X. Xing, R. Liu, M. Anjass, K. Cao, U. Kaiser, G. Zhang and C. Streb, Bimetallic manganese-vanadium functionalized N,S-doped carbon nanotubes as efficient oxygen evolution and oxygen reduction electrocatalysts, *Appl. Catal. B Environ.*, 2020, **277**, 119195.

153 P. Babar, K. Patil, V. Karade, K. Gour, A. Lokhande, S. Pawar and J. H. Kim, In Situ Fabrication of Nickel-Iron Oxalate Catalysts for Electrochemical Water Oxidation at High Current Densities, *ACS Appl. Mater. Interfaces*, 2021, **13**, 52620–52628.

154 X. Gu, Z. Liu, M. Li, J. Tian and L. Feng, Surface structure regulation and evaluation of FeNi-based nanoparticles for oxygen evolution reaction, *Appl. Catal. B Environ.*, 2021, **297**, 120462.

155 C. Daiane Ferreira Da Silva, F. Claudel, V. Martin, R. Chattot, S. Abbou, K. Kumar, I. Jiménez-Morales, S. Cavaliere, D. Jones, J. Rozière, L. Solà-Hernandez, C. Beauger, M. Faustini, J. Peron, B. Gilles, T. Encinas, L. Piccolo, F. H. Barros De Lima, L. Dubau and F. Maillard, Oxygen Evolution Reaction Activity and Stability Benchmarks for Supported and Unsupported IrOxElectrocatalysts, *ACS Catal.*, 2021, **11**, 4107–4116.

156 F. Davodi, E. Mü, M. Tavakkoli, J. Sainio, H. Jiang, B. Gö, G. Marzun and T. Kallio, Catalyst Support Effect on the Activity and Durability of Magnetic Nanoparticles: toward Design of Advanced Electrocatalyst for Full Water Splitting, *Appl. Mater. interfaces*, 2018, **10**, 31300–31301.

157 S. Lim, J. Cho and S. Park, Elevating IrOx acidic oxygen evolution activity using SnO2-rGO hybrid support, *J. Electroanal. Chem.*, 2023, **928**, 116992.

158 X. Wen, L. Bai, M. Li and J. Guan, Ultrafine iridium oxide supported on carbon nanotubes for efficient catalysis of oxygen evolution and oxygen reduction reactions, *Mater. Today Energy*, 2018, **10**, 153–160.

159 S. J. Ashton and M. Arenz, A DEMS study on the electrochemical oxidation of a high surface area carbon black, *Electrochem. commun.*, 2011, **13**, 1473–1475.

160 J. L. Young, Z. Kang, F. Ganci, S. Madachy and G. Bender, PEM electrolyzer characterization with carbon-based hardware and material sets, *Electrochem. commun.*, 2021, **124**, 106941.

161 J. Sun, S. E. Lowe, L. Zhang, Y. Wang, K. Pang, Y. Wang, Y. Zhong, P. Liu, K. Zhao, Z. Tang and H. Zhao, Ultrathin Nitrogen-Doped Holey Carbon@Graphene Bifunctional Electrocatalyst for Oxygen Reduction and Evolution Reactions in Alkaline and Acidic Media, *Angew. Chemie - Int. Ed.*, 2018, **57**, 16511–16515.

162 X. Wu, B. Feng, W. Li, Y. Niu, Y. Yu, S. Lu, C. Zhong, P. Liu, Z. Tian, L. Chen, W. Hu and C. M. Li, Metal-support interaction boosted electrocatalysis of ultrasmall iridium nanoparticles supported on nitrogen doped graphene for highly efficient water electrolysis in acidic and alkaline media, *Nano Energy*, 2019, **62**, 117–126.

163 A. Lavacchi, M. Bellini, E. Berretti, Y. Chen, A. Marchionni, H. A. Miller and F. Vizza, Titanium dioxide nanomaterials in electrocatalysis for energy, *Curr. Opin. Electrochem.*, 2021, **28**, 100720.

164 P. Mazúr, J. Polonský, M. Paidar and K. Bouzek, Non-conductive TiO 2 as the anode catalyst support for PEM water electrolysis, *Int. J. Hydrogen Energy*, 2012, **37**, 12081–12088.

165 E. Oakton, D. Lebedev, A. Fedorov, F. Krumeich, J. Tillier, O. Sereda, T. J. Schmidt and C. Copéret, A simple one-pot Adams method route to conductive high surface area IrO2-TiO2 materials, *New J. Chem.*, 2016, **40**, 1834–1838.

166 G. Li, X. Xu, H. Liu, X. Yang and M. C. Lin, Enhanced Electrocatalytic Performance of IrOx by Employing F-Doped TiO2 as Support towards Acidic Oxygen Evolution Reaction, *ChemCatChem*, 2022, **14**, 1–7.

167 R. E. Fuentes, J. Farell and J. W. Weidner, Multimetallic electrocatalysts of Pt, Ru, and Ir supported on anatase and rutile TiO2 for oxygen evolution in an acid environment, *Electrochem. Solid-State Lett.*, 2011, **14**, 5–7.

168 F. C. Walsh and R. G. A. Wills, The continuing development of Magnéli phase titanium sub-oxides and Ebonex® electrodes, *Electrochim. Acta*, 2010, **55**, 6342–6351.

169 Y. N. Regmi, E. Tzanetopoulos, G. Zeng, X. Peng, D. I. Kushner, T. A. Kistler, L. A. King

and N. Danilovic, Supported Oxygen Evolution Catalysts by Design: Toward Lower Precious Metal Loading and Improved Conductivity in Proton Exchange Membrane Water Electrolyzers, *ACS Catal.*, 2020, **10**, 13125–13135.

170 A. P. Freitas, R. F. André, C. Poucin, T. K. C. Le, J. Imbao, B. Lassalle-Kaiser and S. Carenco, Guidelines for the Molybdenum Oxidation State and Geometry from X-ray Absorption Spectroscopy at the Mo L2,3-Edges, *J. Phys. Chem. C*, 2021, **125**, 17761–17773.

171 V. S. Saji and C. W. Lee, Molybdenum, molybdenum oxides, and their electrochemistry, *ChemSusChem*, 2012, **5**, 1146–1161.

172 M. Pourbaix, *Atlas of electrochemical equilibria in aqueous solutions*, 1974, vol. 1.

173 J. Zhang, T. Huang, L. Zhang and A. Yu, Molybdenum-doped titanium dioxide and its superior lithium storage performance, *J. Phys. Chem. C*, 2014, **118**, 25300–25309.

174 G. C. da Silva, S. I. Venturini, S. Zhang, M. Löffler, C. Scheu, K. J. J. Mayrhofer, E. A. Ticianelli and S. Cherevko, Oxygen Evolution Reaction on Tin Oxides Supported Iridium Catalysts: Do We Need Dopants?, *ChemElectroChem*, 2020, **7**, 2330–2339.

175 A. Marshall, B. Børresen, G. Hagen, M. Tsypkin and R. Tunold, Preparation and characterisation of nanocrystalline IrxSn 1-xO2 electrocatalytic powders, *Mater. Chem. Phys.*, 2005, **94**, 226–232.

176 P. Bhanja, B. Mohanty, A. K. Patra, S. Ghosh, B. K. Jena and A. Bhaumik, IrO2 and Pt Doped Mesoporous SnO2 Nanospheres as Efficient Electrocatalysts for the Facile OER and HER, *ChemCatChem*, 2019, **11**, 583–592.

177 J. Xu, G. Liu, J. Li and X. Wang, The electrocatalytic properties of an IrO 2/SnO 2 catalyst using SnO 2 as a support and an assisting reagent for the oxygen evolution reaction, *Electrochim. Acta*, 2012, **59**, 105–112.

178 V. A. Saveleva, L. Wang, O. Kasian, M. Batuk, J. Hadermann, J. J. Gallet, F. Bournel, N. Alonso-Vante, G. Ozouf, C. Beauger, K. J. J. Mayrhofer, S. Cherevko, A. S. Gago, K. A. Friedrich, S. Zafeiratos and E. R. Savinova, Insight into the Mechanisms of High Activity and Stability of Iridium Supported on Antimony-Doped Tin Oxide Aerogel for Anodes of Proton Exchange Membrane Water Electrolyzers, *ACS Catal.*, 2020, **10**, 2508–2516.

179 I. A. Khan, P. Morgen, S. Gyergyek, R. Sharma and S. M. Andersen, Selection on antimony-doped tin oxide (ATO) as an efficient support for iridium-based oxygen evolution reaction (OER) catalyst in acidic media, *Mater. Chem. Phys.*, 2023, **308**, 128192.

180 A. T. Marshall and R. G. Haverkamp, Electrocatalytic activity of IrO2-RuO2 supported on Sb-doped SnO2 nanoparticles, *Electrochim. Acta*, 2010, **55**, 1978–1984.

181 H. S. Oh, H. N. Nong and P. Strasser, Preparation of mesoporous Sb-, F-, and in-doped SnO2 bulk powder with high surface area for use as catalyst supports in electrolytic cells,

Adv. Funct. Mater., 2015, **25**, 1074–1081.

182 S. Geiger, O. Kasian, A. M. Mingers, K. J. J. Mayrhofer and S. Cherevko, Stability limits of tin-based electrocatalyst supports, *Sci. Rep.*, 2017, **7**, 3–9.

183 K. Stöwe and M. Weber, Niobium, Tantalum, and Tungsten Doped Tin Dioxides as Potential Support Materials for Fuel Cell Catalyst Applications, *Zeitschrift fur Anorg. und Allg. Chemie*, 2020, **646**, 1470–1480.

184 H. Ohno, S. Nohara, K. Kakinuma, M. Uchida, A. Miyake, S. Deki and H. Uchida, Remarkable Mass Activities for the Oxygen Evolution Reaction at Iridium Oxide Nanocatalysts Dispersed on Tin Oxides for Polymer Electrolyte Membrane Water Electrolysis, *J. Electrochem. Soc.*, 2017, **164**, F944–F947.

185 S. Abbou, R. Chattot, V. Martin, F. Claudel, L. Solà-Hernandez, C. Beauger, L. Dubau and F. Maillard, Manipulating the Corrosion Resistance of SnO2Aerogels through Doping for Efficient and Durable Oxygen Evolution Reaction Electrocatalysis in Acidic Media, *ACS Catal.*, 2020, **10**, 7283–7294.

186 J. Ma, X. Guo, H. Xue, K. Pan, C. Liu and H. Pang, Niobium/tantalum-based materials: Synthesis and applications in electrochemical energy storage, *Chem. Eng. J.*, 2020, **380**, 122428.

187 E. Asselin, T. M. Ahmed and A. Alfantazi, Corrosion of niobium in sulphuric and hydrochloric acid solutions at 75 and 95 °C, *Corros. Sci.*, 2007, **49**, 694–710.

188 E. Oakton, J. Tillier, G. Siddiqi, Z. Mickovic, O. Sereda, A. Fedorov and C. Copéret, Structural differences between Sb- and Nb-doped tin oxides and consequences for electrical conductivity, *New J. Chem.*, 2016, **40**, 2655–2660.

189 C. Hao, H. Lv, C. Mi, Y. Song and J. Ma, Investigation of Mesoporous Niobium-Doped TiO2 as an Oxygen Evolution Catalyst Support in an SPE Water Electrolyzer, *ACS Sustain. Chem. Eng.*, 2016, **4**, 746–756.

190 E. McCafferty, in *Introduction to Corrosion Science*, Springer, New York, NY, New York, 1st edn., 2010, p. 109.

191 C. Baik, J. Cho, J. I. Cha, Y. Cho, S. S. Jang and C. Pak, Electron-rich Ir nanostructure supported on mesoporous Ta2O5 for enhanced activity and stability of oxygen evolution reaction, *J. Power Sources*, 2023, **575**, 233174.

192 Y. R. Zheng, J. Vernieres, Z. Wang, K. Zhang, D. Hochfilzer, K. Krempl, T. W. Liao, F. Presel, T. Altantzis, J. Fatermans, S. B. Scott, N. M. Secher, C. Moon, P. Liu, S. Bals, S. Van Aert, A. Cao, M. Anand, J. K. Nørskov, J. Kibsgaard and I. Chorkendorff, Monitoring oxygen production on mass-selected iridium–tantalum oxide electrocatalysts, *Nat. Energy*, 2022, **7**, 55–64.

193 D. Pangotra, L. I. Csepei, A. Roth, C. Ponce de León, V. Sieber and L. Vieira, Anodic

production of hydrogen peroxide using commercial carbon materials, *Appl. Catal. B Environ.*, , DOI:10.1016/j.apcatb.2021.120848.

194 D. Pangotra, L. I. Csepei, A. Roth, V. Sieber and L. Vieira, Anodic generation of hydrogen peroxide in continuous flow, *Green Chem.*, 2022, **24**, 7931–7940.

195 H. W. Kim, V. J. Bukas, H. Park, S. Park, K. M. Diederichsen, J. Lim, Y. H. Cho, J. Kim, W. Kim, T. H. Han, J. Voss, A. C. Luntz and B. D. McCloskey, Mechanisms of two-electron and four-electron electrochemical oxygen reduction reactions at nitrogen-doped reduced graphene oxide, *ACS Catal.*, 2020, **10**, 852–863.

196 A. Izgorodin, E. Izgorodina and D. R. MacFarlane, Low overpotential water oxidation to hydrogen peroxide on a MnO x catalyst, *Energy Environ. Sci.*, 2012, **5**, 9496–9501.

197 S. Siahrostami, G. L. Li, V. Viswanathan and J. K. Nørskov, One- or Two-Electron Water Oxidation, Hydroxyl Radical, or H2O2 Evolution, *J. Phys. Chem. Lett.*, 2017, **8**, 1157–1160.

198 V. Viswanathan, H. A. Hansen and J. K. Nørskov, Selective Electrochemical Generation of Hydrogen Peroxide from Water Oxidation, *J. Phys. Chem. Lett.*, 2015, **6**, 4224–4228.

199 J. H. Baek, T. M. Gill, H. Abroshan, S. Park, X. Shi, J. Nørskov, H. S. Jung, S. Siahrostami and X. Zheng, Selective and Efficient Gd-Doped BiVO 4 Photoanode for Two-Electron Water Oxidation to H 2 O 2, *ACS Energy Lett.*, 2019, **4**, 720–728.

200 K. Fuku and K. Sayama, Efficient oxidative hydrogen peroxide production and accumulation in photoelectrochemical water splitting using a tungsten trioxide/bismuth vanadate photoanode, *Chem. Commun.*, 2016, **52**, 5406–5409.

201 S. R. Kelly, X. Shi, S. Back, L. Vallez, S. Y. Park, S. Siahrostami, X. Zheng and J. K. Nørskov, ZnO As an Active and Selective Catalyst for Electrochemical Water Oxidation to Hydrogen Peroxide, *ACS Catal.*, 2019, **9**, 4593–4599.

202 S. Y. Park, H. Abroshan, X. Shi, H. S. Jung, S. Siahrostami and X. Zheng, CaSnO 3 : An Electrocatalyst for Two-Electron Water Oxidation Reaction to Form H 2 O 2, *ACS Energy Lett.*, 2019, **4**, 352–357.

203 K. Fuku, Y. Miyase, Y. Miseki, T. Gunji and K. Sayama, Enhanced Oxidative Hydrogen Peroxide Production on Conducting Glass Anodes Modified with Metal Oxides, *ChemistrySelect*, 2016, **1**, 5721–5726.

204 T. M. Gill, L. Vallez and X. Zheng, The Role of Bicarbonate-Based Electrolytes in H2O2Production through Two-Electron Water Oxidation, *ACS Energy Lett.*, 2021, **6**, 2854–2862.

205 C. Xia, J. Y. (Timothy) Kim and H. Wang, Recommended practice to report selectivity in electrochemical synthesis of H2O2, *Nat. Catal.*, 2020, **3**, 605–607.

206 R. Zhou, Y. Zheng, M. Jaroniec and S. Z. Qiao, Determination of the Electron Transfer

Number for the Oxygen Reduction Reaction: From Theory to Experiment, *ACS Catal.*, 2016, **6**, 4720–4728.

207 Y. Wei, J. Zhang, Q. Zheng, J. Miao, P. J. J. Alvarez and M. Long, Quantification of photocatalytically-generated hydrogen peroxide in the presence of organic electron donors: Interference and reliability considerations, *Chemosphere*, 2021, **279**, 130556.

208 N. V. Klassen, D. Marchington and H. C. E. McGowan, H2O2 Determination by the I3− Method and by KMnO4 Titration, *Anal. Chem.*, 1994, **66**, 2921–2925.

209 K. Jiang, S. Back, A. J. Akey, C. Xia, Y. Hu, W. Liang, D. Schaak, E. Stavitski, J. K. Nørskov, S. Siahrostami and H. Wang, Highly selective oxygen reduction to hydrogen peroxide on transition metal single atom coordination, *Nat. Commun.*, , DOI:10.1038/s41467-019-11992-2.

210 G. Schmitz, The oxidation of iodine to iodate by hydrogen peroxide, *Phys. Chem. Chem. Phys.*, 2001, **3**, 4741–4746.

211 A. N. Baga, G. R. A. Johnson, N. B. Nazhat and R. A. Saadalla-Nazhat, A simple spectrophotometric determination of hydrogen peroxide at low concentrations in aqueous solution, *Anal. Chim. Acta*, 1988, **204**, 349–353.

212 G. K. Philip J. Brandhuber, *Methods for the Detection of Residual Concentrations of Hydrogen Peroxide in Advanced Oxidation Processes*, 2009.

213 F. S. Rocha, A. J. Gomes, C. N. Lunardi, S. Kaliaguine and G. S. Patience, Experimental methods in chemical engineering: Ultraviolet visible spectroscopy—UV-Vis, *Can. J. Chem. Eng.*, 2018, **96**, 2512–2517.

214 T. M. Gill and X. Zheng, Comparing Methods for Quantifying Electrochemically Accumulated H2O2, *Chem. Mater.*, 2020, **32**, 6285–6294.

215 K. D. Parry V, Scanning Electron Microscopy : An introduction, *III-Vs Rev.*, 2000, **13**, 40–44.

216 B. J. Inkson, *Scanning Electron Microscopy (SEM) and Transmission Electron Microscopy (TEM) for Materials Characterization*, Elsevier Ltd, 2016.

217 K. Akhtar, S. A. Khan, S. B. Khan and A. M. Asiri, *Scanning electron microscopy: Principle and applications in nanomaterials characterization*, 2018.

218 P. J. Goodhew, General Introduction to Transmission Electron Microscopy TEM, *Aberration-Corrected Anal. Transm. Electron Microsc.*, 2011, 1–19.

219 C. R. Brundle, C. A. Evans. Jr and S. Wilson, *Encyclopedia of Materials Characterization*, Manning Publication Co., 1992.

220 D. Shindo and T. Oikawa, in *Analytical Electron Microscopy for Materials Science*, 2002, pp. 81–102.

221 B. Ingham, *Crystallogr. Rev.*, 2015, 21, 229–303.

222 B. . Cullity, in *Elements of X-Ray Diffraction*, ed. M. Cohen, Addison-Wesley Publishing Company Inc, 2nd edn., 1977, pp. 81–105.

223 S. Hofmann, *Auger- and X-Ray Photoelectron Spectroscopy in Materials Science: A User Oriented Guide*, Springer Science & Business Media, 2012.

224 G. Greczynski and L. Hultman, X-ray photoelectron spectroscopy: Towards reliable binding energy referencing, *Prog. Mater. Sci.*, 2020, **107**, 4,7.

225 V. 5. . NIST Standard Reference Database 20, NIST X-ray Photoelectron Spectroscopy Database.

226 J. Baumann, Y. Kayser and B. Kanngießer, Grazing Emission X-Ray Fluorescence: Novel Concepts and Applications for Nano-Analytics, *Phys. Status Solidi Basic Res.*, 2021, **258**, 1–17.

227 P. Brouwer, *Theory of XRF*, 2010.

228 J. G. Webster and H. Eren, *Measurement, Instrumentation, and Sensors Handbook: Electromagnetic, Optical, Radiation, Chemical, and Biomedical Measurement, Second Edition*, .

229 D. Xu, M. B. Stevens, M. R. Cosby, S. Z. Oener, A. M. Smith, L. J. Enman, K. E. Ayers, C. B. Capuano, J. N. Renner, N. Danilovic, Y. Li, H. Wang, Q. Zhang and S. W. Boettcher, Earth-Abundant Oxygen Electrocatalysts for Alkaline Anion-Exchange-Membrane Water Electrolysis: Effects of Catalyst Conductivity and Comparison with Performance in Three-Electrode Cells, *ACS Catal.*, 2019, **9**, 7–15.

230 A. Celzard, J. F. Marêché, F. Payot and G. Furdin, Electrical conductivity of carbonaceous powders, *Carbon N. Y.*, 2002, **40**, 2801–2815.

231 F. Wudl and M. R. Bryce, Apparatus for two-probe conductivity measurements on compressed powders, *J. Chem. Educ.*, 1990, **67**, 717–718.

232 A. Fraser, Z. Zhang, G. Merle, J. Gostick and J. Barralet, Powder Conductivity Assessment Using a Disposable 3D Printed Device, *Electroanalysis*, 2018, **30**, 1897–1901.

233 Y. Lu, L. M. Santino, S. Acharya, H. Anandarajah and J. M. D'Arcy, Studying Electrical Conductivity Using a 3D Printed Four-Point Probe Station, *J. Chem. Educ.*, 2017, **94**, 950–955.

234 S. Thorsteinsson, F. Wang, D. H. Petersen, T. M. Hansen, D. Kjr, R. Lin, J. Y. Kim, P. F. Nielsen and O. Hansen, Accurate microfour-point probe sheet resistance measurements on small samples, *Rev. Sci. Instrum.*, , DOI:10.1063/1.3125050.

235 M. Naderi, in *Progress in Filtration and Separation*, 2015, pp. 585–608.

236 P. Atkins and J. Paula de, *Atkins' Physical Chemistry*, Oxford University Press, Oxford,

8th edn., 2006.

237 O. Kasian, S. Geiger, K. J. J. Mayrhofer and S. Cherevko, Electrochemical On-line ICP-MS in Electrocatalysis Research, *Chem. Rec.*, 2019, **19**, 2130–2142.

238 R. Thomas, *A Beginner's Guide to ICP-MS*, 2003, vol. 16.

239 S. C. Wilschefski and M. R. Baxter, Inductively Coupled Plasma Mass Spectrometry: Introduction to Analytical Aspects, *Clin. Biochem. Rev.*, 2019, **40**, 115–133.

240 J. L. Town, F. MacLaren and H. D. Dewald, Rotating disk voltammetry experiment, *J. Chem. Educ.*, 1991, **68**, 352–354.

241 J. Chlistunoff and J. M. Sansiñena, On the use of Nafion® in electrochemical studies of carbon supported oxygen reduction catalysts in aqueous media, *J. Electroanal. Chem.*, 2016, **780**, 134–146.

242 H. Zhang, X. Wang, J. Hang and J. Zhang, in *PEM Fuel Cell Electrocatalysts and Catalyst Layers: Fundamentals and Applications*, ed. J. Zhang, Springer, London, 1st edn., 2008, pp. 894–895.

243 P. Cassoux, L. Valade and L. . Fabre, in *Comprehensive Coordination Chemistry II*, eds. J. A. McCleverty and T. J. Meyer, Elsevier Science, Pergamon, 2003, vol. 1, pp. 761–773.

244 Y. S. Choudhary, L. Jothi and G. Nageswaran, in *Spectroscopic Methods for Nanomaterials Characterization*, eds. S. Thomas, R. Thomas, A. K. Zachariah and R. Mishra Kumar, Elsevier Inc., 1st edn., 2017, vol. 2, pp. 19–54.

245 N. Elgrishi, K. J. Rountree, B. D. McCarthy, E. S. Rountree, T. T. Eisenhart and J. L. Dempsey, A Practical Beginner's Guide to Cyclic Voltammetry, *J. Chem. Educ.*, 2018, **95**, 197–206.

246 C. G. Zoski, *Handbook of electrochemistry*, 2007.

247 J. A. Arminio-Ravelo, A. W. Jensen, K. D. Jensen, J. Quinson and M. Escudero-Escribano, Electrolyte Effects on the Electrocatalytic Performance of Iridium-Based Nanoparticles for Oxygen Evolution in Rotating Disc Electrodes, *ChemPhysChem*, 2019, **20**, 2956–2963.

248 A. L. Strickler, D. Higgins and T. F. Jaramillo, Crystalline Strontium Iridate Particle Catalysts for Enhanced Oxygen Evolution in Acid, *ACS Appl. Energy Mater.*, 2019, **2**, 5490–5498.

249 S. A. K. Navodye and G. T. K. K. Gunasooriya, Acid Electrolyte Anions Adsorption Effects on IrO2 Electrocatalysts for Oxygen Evolution Reaction, *J. Phys. Chem. C*, 2024, **128**, 6041–6052.

250 P. S. Nnamchi and C. S. Obayi, in *Characterization of Nanomaterials: Advances and Key Technologies*, eds. S. M. Bhagyaraj, O. S. Oluwafemi, N. Kalarikkal and S. Thomas, Woodhead Publishing, 1st edn., 2018, pp. 103–127.

251 G. Inzelt, *Chronoamperometry, Chronocoulometry, and Chronopotentiometry in Encyclopedia of Applied Electrochemistry*, Springer, New York, 2014.

252 R. K. Franklin, S. M. Martin, T. D. Strong and R. B. Brown, in *Reference Module in Materials Science and Materials Engineering*, Elsevier Ltd., 2016, pp. 2–30.

253 H. S. Magar, R. Y. A. Hassan and A. Mulchandani, Electrochemical impedance spectroscopy (Eis): Principles, construction, and biosensing applications, *Sensors*, , DOI:10.3390/s21196578.

254 S. M. Park and J. S. Yoo, *Anal. Chem.*, 2003, 75, 455–461.

255 W. Zheng, iR Compensation for Electrocatalysis Studies: Considerations and Recommendations, *ACS Energy Lett.*, 2023, **8**, 1952–1958.

256 T. Shinagawa, A. T. Garcia-Esparza and K. Takanabe, Insight on Tafel slopes from a microkinetic analysis of aqueous electrocatalysis for energy conversion, *Sci. Rep.*, 2015, **5**, 1–21.

257 S. Anantharaj, S. Noda, M. Driess and P. W. Menezes, The Pitfalls of Using Potentiodynamic Polarization Curves for Tafel Analysis in Electrocatalytic Water Splitting, *ACS Energy Lett.*, 2021, **6**, 1607–1611.

258 Y. H. Fang and Z. P. Liu, *ACS Catal.*, 2014, 4, 4364–4376.

259 S. Komini Babu, R. Mukundan, C. Wang, D. Langlois, D. A. Cullen, D. Papadias, K. L. More, R. Ahluwalia, J. Waldecker and R. Borup, Effect of Catalyst and Catalyst Layer Composition on Catalyst Support Durability, *J. Electrochem. Soc.*, 2021, **168**, 044502.

260 S. M. Alia, S. Stariha and R. L. Borup, Electrolyzer durability at low catalyst loading and with dynamic operation, *J. Electrochem. Soc.*, 2019, **166**, F1164,F1170.

261 P. Aßmann, A. S. Gago, P. Gazdzicki, K. A. Friedrich and M. Wark, Toward developing accelerated stress tests for proton exchange membrane electrolyzers, *Curr. Opin. Electrochem.*, 2020, **21**, 225–233.

262 A. S. Tijani, M. F. A. Ghani, A. H. A. Rahim, I. K. Muritala and F. A. Binti Mazlan, Electrochemical characteristics of (PEM) electrolyzer under influence of charge transfer coefficient, *Int. J. Hydrogen Energy*, 2019, **44**, 27177–27189.

263 J. Van Der Merwe, K. Uren, G. Van Schoor and D. Bessarabov, Characterisation tools development for PEM electrolysers, *Int. J. Hydrogen Energy*, 2014, **39**, 14212–14221.

264 U. S. Jonnalagadda, X. Su and J. J. Kwan, Nanostructured TiO2 cavitation agents for dual-modal sonophotocatalysis with pulsed ultrasound, *Ultrason. Sonochem.*, 2021, **73**, 1–9.

265 S. Liu, G. Chen, P. N. Prasad and M. T. Swihart, Synthesis of monodisperse Au, Ag, and Au-Ag alloy nanoparticles with tunable size and surface plasmon resonance frequency, *Chem. Mater.*, 2011, **23**, 4098–4101.

266 C. J. Wrasman, A. Boubnov, A. R. Riscoe, A. S. Hoffman, S. R. Bare and M. Cargnello, Synthesis of Colloidal Pd/Au Dilute Alloy Nanocrystals and Their Potential for Selective Catalytic Oxidations, *J. Am. Chem. Soc.*, 2018, **140**, 12930–12939.

267 S. M. Alia and N. Danilovic, Rotating Disk Electrode Standardization and Best Practices in Acidic Oxygen Evolution for Low-Temperature Electrolysis, *Front. Energy Res.*, 2022, **10**, 1–8.

268 Y. N. Regmi, X. Peng, J. C. Fornaciari, M. Wei, D. J. Myers, A. Z. Weber and N. Danilovic, A low temperature unitized regenerative fuel cell realizing 60% round trip efficiency and 10 000 cycles of durability for energy storage applications, *Energy Environ. Sci.*, 2020, **13**, 2096–2105.

269 S. Shahgaldi, I. Alaefour, G. Unsworth and X. Li, Development of a low temperature decal transfer method for the fabrication of proton exchange membrane fuel cells, *Int. J. Hydrogen Energy*, 2017, **42**, 11813–11822.

270 S. Cherevko, S. Geiger, O. Kasian, A. Mingers and K. J. J. Mayrhofer, Oxygen evolution activity and stability of iridium in acidic media. Part 2. - Electrochemically grown hydrous iridium oxide, *J. Electroanal. Chem.*, 2016, **774**, 102–110.

271 E. Oakton, D. Lebedev, M. Povia, D. F. Abbott, E. Fabbri, A. Fedorov, M. Nachtegaal, C. Copéret and T. J. Schmidt, IrO2-TiO2: A High-Surface-Area, Active, and Stable Electrocatalyst for the Oxygen Evolution Reaction, *ACS Catal.*, 2017, **7**, 2346–2352.

272 E. J. Kim, J. Shin, J. Bak, S. J. Lee, K. hyun Kim, D. H. Song, J. H. Roh, Y. Lee, H. W. Kim, K. S. Lee and E. A. Cho, Stabilizing role of Mo in TiO2-MoOx supported Ir catalyst toward oxygen evolution reaction, *Appl. Catal. B Environ.*, 2021, **280**, 1–10.

273 J. Liao, Y. Wang, M. Chen, M. Wang, J. Fan, H. Li, H. Wang, L. Zeng and T. Zhao, IrOXSupported onto Niobium-Doped Titanium Dioxide as an Anode Reversal Tolerant Electrocatalyst for Proton Exchange Membrane Fuel Cells, *ACS Appl. Energy Mater.*, 2022, **5**, 3259–3268.

274 D. Bernsmeier, M. Bernicke, R. Schmack, R. Sachse, B. Paul, A. Bergmann, P. Strasser, E. Ortel and R. Kraehnert, Oxygen Evolution Catalysts Based on Ir–Ti Mixed Oxides with Templated Mesopore Structure: Impact of Ir on Activity and Conductivity, *ChemSusChem*, 2018, **11**, 2367–2374.

275 W. Hu, S. Chen and Q. Xia, IrO2/Nb-TiO2 electrocatalyst for oxygen evolution reaction in acidic medium, *Int. J. Hydrogen Energy*, 2014, 6967–6976.

276 L. Moriau, M. Bele, Ž. Marinko, F. Ruiz-Zepeda, G. Koderman Podboršek, M. Šala, A. K. Šurca, J. Kovač, I. Arčon, P. Jovanovič, N. Hodnik and L. Suhadolnik, Effect of the Morphology of the High-Surface-Area Support on the Performance of the Oxygen-Evolution Reaction for Iridium Nanoparticles, *ACS Catal.*, 2021, **11**, 670–681.

277 R. V. Genova-Koleva, F. Alcaide, G. Álvarez, P. L. Cabot, H. J. Grande, M. V. Martínez-

Huerta and O. Miguel, Supporting IrO2 and IrRuOx nanoparticles on TiO2 and Nb-doped TiO2 nanotubes as electrocatalysts for the oxygen evolution reaction, *J. Energy Chem.*, 2019, **34**, 227–239.

278 G. Li, K. Li, L. Yang, J. Chang, R. Ma, Z. Wu, J. Ge, C. Liu and W. Xing, Boosted Performance of Ir Species by Employing TiN as the Support toward Oxygen Evolution Reaction, *ACS Appl. Mater. Interfaces*, 2018, **10**, 38117–38124.

279 L. Wang, P. Lettenmeier, U. Golla-Schindler, P. Gazdzicki, N. A. Cañas, T. Morawietz, R. Hiesgen, S. S. Hosseiny, A. S. Gago and K. A. Friedrich, Nanostructured Ir-supported on Ti4O7 as a cost-effective anode for proton exchange membrane (PEM) electrolyzers, *Phys. Chem. Chem. Phys.*, 2016, **18**, 4487–4495.

280 G. Li, H. Jia, H. Liu, X. Yang and M. C. Lin, Nanostructured IrOx supported on N-doped TiO2 as an efficient electrocatalyst towards acidic oxygen evolution reaction, *RSC Adv.*, 2022, **12**, 28929–28936.

281 Z. Wang, W. A. Goddard and H. Xiao, Potential-dependent transition of reaction mechanisms for oxygen evolution on layered double hydroxides, *Nat. Commun.*, 2023, **14**, 38–44.

282 L. Shi, A. Wang, T. Zhang, B. Zhang, D. Su, H. Li and Y. Song, One-step synthesis of Au-pd alloy nanodendrites and their catalytic activity, *J. Phys. Chem. C*, 2013, **117**, 12526–12536.

283 P. Mishra, C. M. Pandey, U. Singh, A. Gupta, C. Sahu and A. Keshri, Descriptive statistics and normality tests for statistical data, *Ann. Card. Anaesth.*, 2019, **22**, 67–72.

284 V. Pfeifer, T. E. Jones, J. J. Velasco Vélez, C. Massué, R. Arrigo, D. Teschner, F. Girgsdies, M. Scherzer, M. T. Greiner, J. Allan, M. Hashagen, G. Weinberg, S. Piccinin, M. Hävecker, A. Knop-Gericke and R. Schlögl, The electronic structure of iridium and its oxides, *Surf. Interface Anal.*, 2016, **48**, 261–273.

285 M. Khawaji and D. Chadwick, Au-Pd NPs immobilised on nanostructured ceria and titania: Impact of support morphology on the catalytic activity for selective oxidation, *Catal. Sci. Technol.*, 2018, **8**, 2529–2539.

286 J. E. Gonçalves, S. C. Castro, A. Y. Ramos, M. C. M. Alves and Y. Gushikem, X-ray absorption and XPS study of titanium mixed oxides synthesized by the sol-gel method, *J. Electron Spectros. Relat. Phenomena*, 2001, **114–116**, 307–311.

287 K. Ayers, A. Soleymani, J. Jankovic, H. Yu and G. Mirshekari, Degradation Mechanisms in Advanced MEAs for PEM Water Electrolyzers Fabricated by Reactive Spray Deposition Technology, *J. Electrochem. Soc.*, 2022, **169**, 1–26.

288 E. Pizzutilo, O. Kasian, C. Hyuck, S. Cherevko, G. J. Hutchings, K. J. J. Mayrhofer and S. J. Freakley, Electrocatalytic synthesis of hydrogen peroxide on Au-Pd nanoparticles : From fundamentals to continuous production, *Chem. Phys. Lett.*, 2017, **683**, 436–442.

289 J. K. Edwards, B. E. Solsona, P. Landon, A. F. Carley, A. Herzing, C. J. Kiely and G. J. Hutchings, Direct synthesis of hydrogen peroxide from H 2 and O 2 using TiO 2 -supported Au – Pd catalysts, 2005, **236**, 69–79.

290 R. B. Rankin, Trends in Selective Hydrogen Peroxide Production on Transition Metal Surfaces from First Principles.

291 C. Hao, H. Lv, Q. Zhao, B. Li, C. Zhang, C. Mi, Y. Song and J. Ma, Investigation of V-doped TiO2 as an anodic catalyst support for SPE water electrolysis, *Int. J. Hydrogen Energy*, 2017, **42**, 9384–9395.

292 H. Lv, S. Wang, C. Hao, W. Zhou, J. Li, M. Xue and C. Zhang, Oxygen-Deficient Ti 0.9 Nb 0.1 O 2-x as an Efficient Anodic Catalyst Support for PEM Water Electrolyzer, *ChemCatChem*, 2019, **11**, 2511–2519.

293 H. Lv, G. Zhang, C. Hao, C. Mi, W. Zhou, D. Yang, B. Li and C. Zhang, Activity of IrO2 supported on tantalum-doped TiO2 electrocatalyst for solid polymer electrolyte water electrolyzer, *RSC Adv.*, 2017, **7**, 40427–40436.

294 G. Li, H. Yu, D. Yang, J. Chi, X. Wang, S. Sun, Z. Shao and B. Yi, Iridium-Tin oxide solid-solution nanocatalysts with enhanced activity and stability for oxygen evolution, *J. Power Sources*, 2016, **325**, 15–24.

295 G. Bucci, K. Gadelrab and W. C. Carter, Mesoscale Model for Ostwald Ripening of Catalyst Nanoparticles, *J. Electrochem. Soc.*, 2021, **168**, 054515.

296 M. Milosevic, T. Böhm, A. Körner, M. Bierling, L. Winkelmann, K. Ehelebe, A. Hutzler, M. Suermann, S. Thiele and S. Cherevko, In Search of Lost Iridium : Quantification of anode Catalyst Layer Dissoluton in Proton Exchange Membrane Water Electrolyzers, *ACS Energy Lett.*, 2023, **8**, 2682–2688.

297 A. S. A. Pushkarev, S.A, Pushkareva, V.I, Du Preez, P.S, Ivanova A.N, Grigoriev, A.S, Slavcheva P.E, Bessarabov G.D, Fateev N.V, Iridium catalyst supported on conductive titanium oxides for polymer electrolyte membrane electrolysis, *Chem. Probl.*, 2019, **17**, 9–14.

298 S. B. Han, Y. H. Mo, Y. S. Lee, S. G. Lee, D. H. Park and K. W. Park, Mesoporous iridium oxide/Sb-doped SnO2 nanostructured electrodes for polymer electrolyte membrane water electrolysis, *Int. J. Hydrogen Energy*, 2019, **45**, 1409–1416.

299 Z. S. H. S. Rajan, T. Binninger, P. J. Kooyman, D. Susac and R. Mohamed, Organometallic chemical deposition of crystalline iridium oxide nanoparticles on antimony-doped tin oxide support with high-performance for the oxygen evolution reaction, *Catal. Sci. Technol.*, 2020, **10**, 3938–3948.

300 S. Zhao, A. Stocks, B. Rasimick, K. More and H. Xu, Highly Active, Durable Dispersed Iridium Nanocatalysts for PEM Water Electrolyzers, *J. Electrochem. Soc.*, 2018, **165**, F82–F89.

301 H. P. Tran, H. N. Nong, H. S. Oh, M. Klingenhof, M. Kroschel, B. Paul, J. Hübner, D. Teschner and P. Strasser, Catalyst-Support Surface Charge Effects on Structure and Activity of IrNi-Based Oxygen Evolution Reaction Catalysts Deposited on Tin-Oxide Supports, *Chem. Mater.*, 2022, **34**, 9350–9363.

302 E. Mayousse, F. Maillard, F. Fouda-Onana, O. Sicardy and N. Guillet, Synthesis and characterization of electrocatalysts for the oxygen evolution in PEM water electrolysis, *Int. J. Hydrogen Energy*, 2011, **36**, 10474–10481.

303 D. F. Abbott, D. Lebedev, K. Waltar, M. Povia, M. Nachtegaal, E. Fabbri, C. Copéret and T. J. Schmidt, Iridium oxide for the oxygen evolution reaction: Correlation between particle size, morphology, and the surface hydroxo layer from operando XAS, *Chem. Mater.*, 2016, **28**, 6591–6604.

304 C. Felix, T. Maiyalagan, S. Pasupathi, B. Bladergroen and V. Linkov, Synthesis and Optimisation of IrO2 Electrocatalysts by Adams Fusion Method for Solid Polymer Electrolyte Electrolysers, *Micro Nanosyst.*, 2012, **4**, 186–191.

305 C. Felix, B. J. Bladergroen, V. Linkov, B. G. Pollet and S. Pasupathi, Ex-situ electrochemical characterization of IrO 2 synthesized by a modified Adams fusion method for the oxygen evolution reaction, *Catalysts*, 2019, **9**, 1–16.

306 H. S. Oh, J. G. Oh, Y. G. Hong and H. Kim, Investigation of carbon-supported Pt nanocatalyst preparation by the polyol process for fuel cell applications, *Electrochim. Acta*, 2007, **52**, 7278–7285.

307 H. S. Oh, J. G. Oh and H. Kim, Modification of polyol process for synthesis of highly platinum loaded platinum-carbon catalysts for fuel cells, *J. Power Sources*, 2008, **183**, 600–603.

308 F. J. Moulder, F. W. Stickle, E. P. Sobol and D. K. Bomben, *Handbook of X-ray Photoelectron Spectroscopy*, Perkin-Elmer Corporation, Eden Prairie, Minnesota, 1992.

309 V. Pfeifer, T. E. Jones, J. J. Velasco Vélez, C. Massué, M. T. Greiner, R. Arrigo, D. Teschner, F. Girgsdies, M. Scherzer, J. Allan, M. Hashagen, G. Weinberg, S. Piccinin, M. Hävecker, A. Knop-Gericke and R. Schlögl, The electronic structure of iridium oxide electrodes active in water splitting, *Phys. Chem. Chem. Phys.*, 2016, **18**, 2292–2296.

310 F. Garbassi, XPS and AES study of antimony oxides, *Surf. Interface Anal.*, 1980, **2**, 165–169.

311 H. A. El-Sayed, A. Weiß, L. F. Olbrich, G. P. Putro and H. A. Gasteiger, OER Catalyst Stability Investigation Using RDE Technique: A Stability Measure or an Artifact?, *J. Electrochem. Soc.*, 2019, **166**, F458–F464.

312 M. Fathi Tovini, A. Hartig-Weiß, H. A. Gasteiger and H. A. El-Sayed, The Discrepancy in Oxygen Evolution Reaction Catalyst Lifetime Explained: RDE vs MEA - Dynamicity within the Catalyst Layer Matters, *J. Electrochem. Soc.*, 2021, **168**, 014512.

313 S. Cherevko, A. R. Zeradjanin, A. A. Topalov, N. Kulyk, I. Katsounaros and K. J. J. Mayrhofer, Dissolution of noble metals during oxygen evolution in acidic media, *ChemCatChem*, 2014, **6**, 2219–2223.

314 F. Y. Chen, Z. Y. Wu, Z. Adler and H. Wang, Stability challenges of electrocatalytic oxygen evolution reaction: From mechanistic understanding to reactor design, *Joule*, 2021, **5**, 1704–1731.

315 R. Mohamed, T. Binninger, P. J. Kooyman, A. Hoell, E. Fabbri, A. Patru, A. Heinritz, T. J. Schmidt and P. Levecque, Facile deposition of Pt nanoparticles on Sb-doped SnO2 support with outstanding active surface area for the oxygen reduction reaction, *Catal. Sci. Technol.*, 2018, **8**, 2672–2685.

316 X. Min, Y. Shi, Z. Lu, L. Shen, T. O. Ogundipe, P. Gupta, C. Wang, C. Guo, Z. Wang, H. Tan, S. Mukerjee and C. Yan, High performance and cost-effective supported IrOx catalyst for proton exchange membrane water electrolysis, *Electrochim. Acta*, 2021, **385**, 138391.

317 H. Li, Y. Xu, N. Lv, Q. Zhang, X. Zhang, Z. Wei, Y. Wang, H. Tang and H. Pan, Ti-Doped SnO2 Supports IrO2 Electrocatalysts for the Oxygen Evolution Reaction (OER) in PEM Water Electrolysis, *ACS Sustain. Chem. Eng.*, 2023, **11**, 1121–1132.

318 Z. Wang, Y. R. Zheng, I. Chorkendorff and J. K. Nørskov, Acid-Stable Oxides for Oxygen Electrocatalysis, *ACS Energy Lett.*, 2020, **5**, 2905–2908.

319 V. Pfeifer, T. E. Jones, J. J. Velasco Vélez, R. Arrigo, S. Piccinin, M. Hävecker, A. Knop-Gericke and R. Schlögl, In situ observation of reactive oxygen species forming on oxygen-evolving iridium surfaces, *Chem. Sci.*, 2017, **8**, 2143–2149.

320 S. Anantharaj, S. R. Ede, K. Karthick, S. Sam Sankar, K. Sangeetha, P. E. Karthik and S. Kundu, Precision and correctness in the evaluation of electrocatalytic water splitting: Revisiting activity parameters with a critical assessment, *Energy Environ. Sci.*, 2018, **11**, 744–771.

321 O. Kasian, J. P. Grote, S. Geiger, S. Cherevko and K. J. J. Mayrhofer, The Common Intermediates of Oxygen Evolution and Dissolution Reactions during Water Electrolysis on Iridium, *Angew. Chemie - Int. Ed.*, 2018, **57**, 2488–2491.

322 S. G. Xue, L. Tang, Y. K. Tang, C. X. Li, M. L. Li, J. J. Zhou, W. Chen, F. Zhu and J. Jiang, Selective Electrocatalytic Water Oxidation to Produce H2O2 Using a C,N Codoped TiO2 Electrode in an Acidic Electrolyte, *ACS Appl. Mater. Interfaces*, 2020, **12**, 4423–4431.

323 L. Fan, X. Bai, C. Xia, X. Zhang, X. Zhao, Y. Xia, Z. Y. Wu, Y. Lu, Y. Liu and H. Wang, CO2/carbonate-mediated electrochemical water oxidation to hydrogen peroxide, *Nat. Commun.*, 2022, **13**, 1–9.

324 S. Peng, Y. Lee, C. Wang, H. Yin, S. Dai and S. Sun, A facile synthesis of monodisperse Au nanoparticles and their catalysis of CO oxidation, *Nano Res.*, 2008, **1**, 229–234.

325 F. Schulz, T. Homolka, N. G. Bastús, V. Puntes, H. Weller and T. Vossmeyer, Little adjustments significantly improve the Turkevich synthesis of gold nanoparticles, *Langmuir*, 2014, **30**, 10779–10784.

326 M. Hatakeyama, H. Kishi, Y. Kita, K. Imai, K. Nishio, S. Karasawa, Y. Masaike, S. Sakamoto, A. Sandhu, A. Tanimoto, T. Gomi, E. Kohda, M. Abe and H. Handa, A two-step ligand exchange reaction generates highly water-dispersed magnetic nanoparticles for biomedical applications, *J. Mater. Chem.*, 2011, **21**, 5959–5966.

327 J. Sanchez, M. B. Stevens, A. R. Young, A. Gallo, M. Zhao, Y. Liu, M. V. Ramos-Garcés, M. Ben-Naim, J. L. Colón, R. Sinclair, L. A. King, M. Bajdich and T. F. Jaramillo, Isolating the Electrocatalytic Activity of a Confined NiFe Motif within Zirconium Phosphate, *Adv. Energy Mater.*, 2021, **11**, 1–15.

328 S. S. Shin, E. J. Yeom, W. S. Yang, S. Hur, M. G. Kim, J. Im, J. Seo, J. H. Noh and S. Il Seok, Colloidally prepared La-doped BaSnO3 electrodes for efficient, photostable perovskite solar cells, *Science (80-.).*, 2017, **356**, 167–171.

329 C. Huang, X. Wang, X. Liu, M. Tian and T. Zhang, Extensive analysis of the formation mechanism of BaSnO3 by solid-state reaction between BaCO3 and SnO2, *J. Eur. Ceram. Soc.*, 2016, **36**, 583–592.

330 J. D. Baniecki, M. Ishii, T. Shioga, K. Kurihara and S. Miyahara, Surface core-level shifts of strontium observed in photoemission of barium strontium titanate thin films, *Appl. Phys. Lett.*, 2006, **89**, 2004–2007.

331 F. Alema and K. Pokhodnya, Dielectric properties of BaMg1/3Nb2/3O3 doped Ba0.45Sr0.55TiO3 thin films for tunable microwave applications, *J. Adv. Dielectr.*, 2015, **5**, 1–9.

332 N. Sharma, K. M. Shaju, G. V. S. Rao and B. V. R. Chowdari, Anodic behaviour and X-ray photoelectron spectroscopy of ternary tin oxides, *J. Power Sources*, 2005, **139**, 250–260.

333 F. A. Akgul, C. Gumus, A. O. Er, A. H. Farha, G. Akgul, Y. Ufuktepe and Z. Liu, Structural and electronic properties of SnO2, *J. Alloys Compd.*, 2013, **579**, 50–56.

334 A. Y. Mohammed, S. J. Lee, Y. Jang, J. S. Kin, C. S. Hwang and D.-Y. Cho, X-ray spectroscopy study on the electronic structure of Sn-added p-type SnO films, *J. Phys. Condens. Matter*, 2018, **32**, 1–8.

335 Y. Lai, X. Liu, H. Ye, G. Ke, B. Lui, F. Dong and H. He, Objective Observations of the Electrochemical Production of H2O2 in KHCO3 Aqueous Electrolyte and Related Application Inspirations, *J. Phys. Chem. C*, 2021, **125**, 19831–19838.

336 Y. H. Ochoa-Muñoz, J. E. Rodríguez-Páez and R. Mejía de Gutiérrez, Structural and optical study of perovskite nanoparticles MSnO3 (M = Ba, Zn, Ca) obtained by a wet chemical route, *Mater. Chem. Phys.*, , DOI:10.1016/j.matchemphys.2021.124557.

337 H. Mizoguchi, H. W. Eng and P. M. Woodward, Probing the Electronic Structures of Ternary Perovskite and Pyrochlore Oxides Containing Sn4+ or Sb5+, *Inorg. Chem.*, 2004, **43**, 1667–1680.

338 O. Diaz-Morales, F. Calle-Vallejo, C. De Munck and M. T. M. Koper, Electrochemical water splitting by gold: Evidence for an oxide decomposition mechanism, *Chem. Sci.*, 2013, **4**, 2334–2343.

339 J. S. Jirkovský, M. Halasa and D. J. Schiffrin, Kinetics of electrocatalytic reduction of oxygen and hydrogen peroxide on dispersed gold nanoparticles, *Phys. Chem. Chem. Phys.*, 2010, **12**, 8042–8052.